Non-invasive assessment of the aortic pressure wave development and testing using in silico and in vivo data

Mariscal Harana, Jorge

Awarding institution:
King's College London

Non-Invasive Assessment of the Aortic Pressure Wave: Development And Testing Using *In Silico* and *In Vivo* Data

Jorge Mariscal Harana

Department of Biomedical Engineering
School of Biomedical Engineering and Imaging Sciences
Faculty of Life Sciences and Medicine

Supervised by

Dr. Jordi Alastruey Arimon
Prof. Spencer Sherwin
Dr. Peter H. Charlton

July 2020

A thesis submitted in fulfilment of the requirements for the degree of

Doctor of Philosophy

Abstract

Clinical evidence shows that central (aortic) blood pressure (cBP) is a better marker of cardiovascular risk than brachial pressure. However, cBP can only be accurately measured invasively, through catheterisation. Although medical imaging techniques such as magnetic resonance imaging and ultrasound provide good resolution aortic blood flow and geometry, they do not currently provide cBP.

This thesis presents a novel approach to measure cBP non-invasively from medical imaging data and a non-invasive peripheral pressure measurement, using zero and one-dimensional computational models of aortic haemodynamics. The studies reported used both *in silico* (simulated) and *in vivo* (clinical) data for algorithm development, testing, and validation. Firstly, three *in silico* datasets were created using computational models whose inputs were cardiovascular properties from the clinical literature for healthy humans. Secondly, existing and new methods to measure cardiovascular properties from clinical data were investigated. These properties have clinical value for assessing cardiovascular function and are also used as inputs to computational models to measure cBP non-invasively. Thirdly, the performance of three computational models of aortic haemodynamics for non-invasive cBP measurement was assessed. Three *in vivo* datasets were used to determine the preferred cBP algorithm: one containing invasive cBP measurements for aortic coarctation patients; and two containing non-invasive cBP measurements for hypertensive patients and normotensive volunteers, respectively. Finally, a 'cohort-specific' *in silico* dataset was created to study the individual effect of cardiovascular properties on the aortic pressure gradients – measured using magnetic resonance imaging – in dilated cardiomyopathy patients. Hence, the main contributions of this thesis were the development and testing of a range of tools to measure cardiovascular properties and cBP from non-invasive clinical measurements; and the study of the individual cardiovascular determinants of the aortic pressure gradients.

In the clinic, the preferred cBP algorithm could be used to augment, at no additional cost, the clinical data obtained from ultrasound and magnetic resonance imaging by providing an accurate, patient-specific, non-invasive measurement of cardiovascular parameters and cBP waves. Furthermore, the assessment of haemodynamic metrics (*e.g.* aortic pressure gradients, blood pressure or flow waves) using 'cohort-specific' *in silico* datasets could be applied to study other patient groups and to address alternative research questions.

Para Celia,
la fuerza motriz
del latir de mi corazón.

Acknowledgements

Firstly, I want to thank my supervisors: Jordi Alastruey, Spencer Sherwin and Peter Charlton, whose motivation, diligence and attention to detail I have always found utterly inspiring. Thank you for teaching me how to think critically, for your excellent mentoring and for your invaluable support and feedback during all these years.

I also want to thank the members of the HæMod research group for their help throughout the PhD: Arna van Engelen, Joaquín Flores, Jorge Aramburu, Marie Willemet, Nick Gaddum, Phil Chowienczyk, Sally Epstein, Samuel Vennin, Ye Li and Weiwei Jin. I must thank those who I had the pleasure to collaborate with: Alberto Figueroa, Ashraf Khir, Chris Arthurs, Dave Nordsletten, David Marlevi, Fede Cuomo, Fredrik Fossan, Isra Valverde, Leif Hellevik, Marija Marčan, Mateusz Florkow, Shima Abdullateef and Torben Schneider. I am also thankful to the colleagues who I have met at conferences around the world and who advised, helped, encouraged and criticised my work, particularly: Jonathan Mynard, Patrick Segers and Raoul van Loon.

Furthermore, I want to thank my examiners: Alun Hughes and Giovanni Biglino, for making my PhD viva a challenging yet enjoyable academic experience, and for their thorough revision of my work and advice on how to improve it.

This work was sponsored by the King's & Imperial EPSRC Centre for Doctoral Training in Medical Imaging. I am thankful for their financial support and for creating an interdisciplinary environment which I greatly benefited from. I am also thankful to Philips Healthcare, for sharing their prototype MRI software with me.

Thank you Julia, Nick, Rob and Valeria, for keeping the CDT gears turning. Thanks Matt, for teaching me the great value of science communication and for inspiring me to improve my presentation skills. I am grateful to my CDT colleagues for our enjoyable time together, especially during the MRes. I am also grateful to my friends from the first cohort: Adela, Esther, Giovanna, Marco and Marta, for paving the way for the rest of us. Thanks to my Lambeth wing (and later Becket House) family: Anna, Bram, Dan, Emily, Liya, Myria, Rene, Sandra and Sila. I thank everyone from the Tommies Social crew, and especially Des, whose mentoring in the arts of social networking I highly appreciate. I also thank my Comedy Club peeps: Alex, Laura, Milou and Veronika, for so many (nerd) nights.

I want to finish this section by expressing my infinite gratitude to the beautiful humans who have become my family far from home.

Thank you, Dédalo and Maxi, for a wonderful friendship and for convincing me of studying in the UK. You were the pioneers; I simply followed in your footsteps.

Thank you, Sam, for a once-in-a-lifetime kind of friendship which simply cannot be described with words. I am incredibly glad that I met you.

Thank you, Alex, Bene, Charlotte, Christian, Leo, Matte, Nika and Paolo, for welcoming me to the group from day one and for making my time in London matter.

And finally, ich danke Dir von ganzem Herzen, Kerstin. From the very first moment you have made my life shine ever brighter. Thank you 3000 times for your support, patience and understanding through the final push. This thesis is also yours.

Jorge Mariscal Harana, July 2020

Agradecimientos

Las páginas que siguen representan el trabajo de cuatro años de investigación. Sin embargo, este no ha sido un esfuerzo individual. Esta tesis os la dedico a vosotros, que habéis sido partícipes de su creación y a quienes agradezco vuestro apoyo, ánimo y paciencia.

Por encima de todo, a mis padres, Céline y Luis, por darme la vida. Sin vuestro amor, dedicación, educación y sacrificio nunca habría llegado hasta aquí. Sois mi modelo a seguir. A mis abuelos, Isabel y Manolo, que ya camináis entre las estrellas. Gracias por haberme enseñado el valor del amor incondicional, de la humildad y de la bondad. A mi abuela Berti, pues tu cariño estuvo siempre por encima de nuestras diferencias ideológicas. Tu pasión por la literatura, la historia, la música y las películas sigue viva en mí. A mis tíos, Yoli y Fernando, por estar ahí desde que tengo uso de razón. Acompaño cada momento en vuestra compañía con una sonrisa. A mis abuelos, Toñi y Luis, por acogerme cuando más lo necesitábamos. Gracias por vuestra hospitalidad y buen sentido del humor. A mis tíos, Sara, Isaac, Jacob e Israel, por compartir conmigo vuestra manera de disfrutar la vida desde pequeñito. Gran parte de lo que soy os lo debo a vosotros.

A mis queridos Koaleños, Ale, Edu, Félix, Guille, Jaime, Jorge, Moy, Nolo, Nuño, Olga, Pepe y Terry, por ser una fuente inagotable de felicidad y diversión (y salseo) desde siempre. A Javi, por todas las aventuras que hemos vivido juntos. Gracias por una larga lista de recuerdos inolvidables y por los que nos quedan. A Manchón, por entenderme mejor que nadie. Gracias por ser mi compañero de batalla y por compartir tantas inquietudes intelectuales y viajes conmigo. A Aurora, por tu apoyo emocional, el cual espero haber devuelto en similar medida, y por acercarme con tus conocimientos al fascinante mundo de la mente humana. A Marta y Amanda, por una amistad que ni el tiempo ni la distancia han sido capaces de erosionar. Volver a veros es siempre un auténtico placer. A MJ, una de esas bellísimas personas que suman y que me ha enseñado el inmenso poder de la fuerza de voluntad y de la constancia.

Y finalmente, a mi hermana Celia, porque te mereces todo y más. Eres amor infinito y sonrisa eterna. La luz que me guía en las noches más oscuras. Te dedico mis logros, pasados y futuros, por insignificantes que sean. Gracias de todo corazón de tu hermano Jorge que te quiere más que a nada en este universo.

Jorge Mariscal Harana, Julio 2020

Related Publications

Most of the original work presented in Chapters 4 to 6 has been included in a manuscript submitted to the *American Journal of Physiology – Heart and Circulatory Physiology* for peer-review:

[1] **Mariscal Harana, J.**, Charlton, P. H., Vennin, S., Aramburu, J., Florkow, M., van Engelen, A., Schneider, T., de Bliek, H., Ruijsink, B., Valverde, I., Beerbaum, P., Grotenhuis, H., Charakida, M., Chowienczyk, P., Sherwin, S., and Alastruey, J. "Estimating central blood pressure from aortic flow: development and assessment of algorithms". [under review].

The work on the 'cohort-specific' *in silico* dataset presented in Chapter 7 is part of a manuscript submitted to the *American Journal of Physiology – Heart and Circulatory Physiology* for peer-review:

[2] Marlevi, D., **Mariscal Harana, J.**, Burris, N. S., Sotelo, J., Ruijsink, B., Hadjicharalambous, M., Asner, L., Sammut, E., Chabiniok, R., Uribe, S., Winter, R., Lamata, P., Alastruey, J. and Nordsletten, D. "Altered aortic hemodynamics and relative pressure in patients with dilated cardiomyopathy". [under review].

I co-authored a journal paper on the development of the one-dimensional dataset of virtual subjects described in Chapter 4:

[3] Charlton, P. H., **Mariscal Harana, J.**, Vennin, S., Li, Y., Chowienczyk, P., and Alastruey, J. (2019). "Modeling arterial pulse waves in healthy aging: a database for in silico evaluation of hemodynamics and pulse wave indexes". *American Journal of Physiology – Heart and Circulatory Physiology*, 317(5), H1062-H1085. **CrossRef**

I co-authored a journal paper on the optimisation of the number of arterial segments in one-dimensional models:

[4] Fossan, F., **Mariscal Harana, J.**, Alastruey, J., and Hellevik, L. (2018). "Optimization of topological complexity for one-dimensional arterial blood flow models". *Journal of the Royal Society Interface*, vol. 15, no. 149, 20180546. **CrossRef**

I co-authored a conference paper on the effect of bifurcations on the pressure amplitude using a one-dimensional computational model:

[5] Abdullateef, S., **Mariscal Harana, J.**, Alastruey, J. and Khir, A. (2018). "A study on the characteristics influencing the pressure at the root of a distributed one-dimensional model of arterial blood flow". *Computing in Cardiology. CinC 2018*, Maastricht, The Netherlands, 23-26 September 2018. **CrossRef**

I also co-authored a conference paper presenting some preliminary work on the central blood pressure estimation algorithms (Chapter 6):

[6] Florkow, M., **Mariscal Harana, J.**, van Engelen, A., Schneider, T., Rafiq, I., de Bliek, H., Alastruey, J., and Botnar, R. (2016). "An integrated software application for non-invasive assessment of local aortic haemodynamic parameters". *Procedia Computer Science* vol. 90, pp. 2-8. MIUA 2016, Loughborough, United Kingdom, 6-8 July 2016. **CrossRef**

Furthermore, I presented part of the work in this thesis at the following conferences:

J. Mariscal Harana, P. H. Charlton, S. Sherwin, and J. Alastruey, "Algorithms for estimating central blood pressure from aortic blood flow," *BioMedEng19*, 5-6 September 2019, Imperial College London, London, United Kingdom.

J. Mariscal Harana, P. H. Charlton, S. Sherwin, and J. Alastruey, "An assessment of algorithms to estimate central blood pressure from non-invasive measurements," *CMBE19*, 10-12 June 2019, Tohoku University, Sendai City, Japan.

J. Mariscal Harana, P. H. Charlton, S. Sherwin, and J. Alastruey, "An assessment of methods to estimate cardiovascular parameters from blood and flow waveforms," *BVBCD2019*, 11-12 April 2019, Imperial College London, London, United Kingdom.

J. Mariscal Harana, P. H. Charlton, S. Vennin, A. van Engelen, T. Schneider, M. Florkow, H. de Bliek, B. Ruijsink, I. Valverde, M. Charakida, K. Pushparajah, S. Sherwin, R. Botnar, and J. Alastruey, "Estimating central blood pressure from MRI data using reduced-order computational models," *ARTERY18*, 18-20 October 2018, Guimaraes, Portugal.

J. Mariscal Harana, P. H. Charlton, S. Sherwin, and J. Alastruey, "Reduced-order computational models for central blood pressure estimation: two clinical scenarios," *BioMedEng18*, 6-7 September 2018, Imperial College London, London, United Kingdom.

J. Mariscal Harana, P. H. Charlton, S. Vennin, A. van Engelen, T. Schneider, M. Florkow, H. de Bliek, B. Ruijsink, I. Valverde, M. Charakida, K. Pushparajah, S. Sherwin, R. Botnar, and J. Alastruey, "A comparison of reduced-order computational models for central blood pressure estimation," *WCB2018*, 8-12 July 2018, Dublin, Ireland.

J. Mariscal Harana, A. van Engelen, T. Schneider, M. Florkow, P. Charlton, B. Ruijsink, H. de Bliek, I. Valverde, M. Charakida, K. Pushparajah, S. Sherwin, R. Botnar, and J. Alastruey, "Non-invasive, MRI-based estimation of patient-specific aortic blood

pressure using one-dimensional blood flow," *ARTERY17*, 12-14 October 2017, Pisa Congressi, Pisa, Italy.

J. Mariscal Harana, A. van Engelen, T. Schneider, M. Florkow, P. Charlton, B. Ruijsink, H. de Bliek, I. Valverde, M. Charakida, K. Pushparajah, S. Sherwin, R. Botnar, and J. Alastruey, "Patient-specific estimation of aortic blood pressure using 1-D blood flow modelling: development and testing using in silico and in vivo data," *MEIBioeng/MPEC 2017*, 13-14 September 2017, Sandown Park, Esher, United Kingdom.

J. Mariscal Harana, P. H. Charlton, S. Sherwin, and J. Alastruey, "Estimation of patient-specific aortic blood pressure using 1-D blood flow modelling: development and testing using a population of virtual subjects," *EUROMECH Colloquium 595: Biomechanics and computer assisted surgery meets medical reality*, 29-31 August 2017, Centrale Lille, Villeneuve d'Ascq, France.

J. Mariscal Harana, F. Cuomo, M. Marcan, C. J. Arthurs, C. A. Figueroa, and J. Alastruey, "CRIMSON: integration of a one-dimensional blood flow solver," *CMBE17*, 10-12 April 2017, Pittsburgh, Pennsylvania, United States.

J. Mariscal Harana, F. Cuomo, M. Marcan, C. J. Arthurs, C. A. Figueroa, and J. Alastruey, "CRIMSON: integration of a one-dimensional blood flow solver," *CMBE17*, 10-12 April 2017, Pittsburgh, Pennsylvania, United States.

J. Mariscal Harana, S. Sherwin, and J. Alastruey, "Central blood pressure estimation: a reduced one-dimensional model of the aortic circulation," *CMBE17*, 10-12 April 2017, Pittsburgh, Pennsylvania, United States.

J. Mariscal Harana, M. Florkow, I. Valverde, A. van Engelen, T. Schneider, and J. Alastruey, "Non-invasive, MRI-based calculation of the aortic blood pressure waveform using computational fluid dynamics," *MEIbioeng 16*, 5-6 September 2016, Oxford, United Kingdom.

Finally, I have collaborated with colleagues in studies which were presented at the following conferences:

S. Vennin, Y. Li, M. Willemet, H. Fok, S. Epstein, **J. Mariscal Harana**, J. Alastruey, and P. Chowienczyk, "Understanding central blood pressure determinants using 1-D modelling," *CMBE17*, 10-12 April 2017, Pittsburgh, Pennsylvania, United States.

F. E. Fossan, **J. Mariscal Harana**, J. Alastruey, and L. R. Hellevik. "A framework for minimizing the number of uncertain parameters in 1D arterial blood flow models," *CMBE17*, 10-12 April 2017, Pittsburgh, Pennsylvania, United States.

J. Alastruey, P. Charlton, P. Chowienczyk, Y. Li, **J. Mariscal Harana**, S. Vennin, and M. Willemet, "Assessment and development of pulse wave indices and algorithms using a database of thousands of virtual subjects," *CMBE17*, 10-12 April 2017, Pittsburgh, Pennsylvania, United States.

Licence

Contents

List of Figures

List of Tables

1 Introduction

1.1 Lay summary

Cardiovascular disease – any medical condition affecting the cardiovascular system – is the most common cause of death worldwide (31% in 2016), with heart attack and stroke accounting for 85% of these deaths [7]. Although there is no specific cause for cardiovascular disease, there are a number of "risk factors" that increase the probability of having it, such as family history, cholesterol, diabetes, obesity, an unhealthy lifestyle, or high blood pressure (hypertension).

Blood pressure is a wave which fluctuates with every heartbeat, in the same way that waves in the sea form peaks and troughs. Clinicians can monitor an individual's cardiovascular health using blood pressure to detect hypertension or to assess arterial abnormalities. Since the invention of the sphygmomanometer (commonly known as brachial cuff) at the end of the XIX century, clinicians have been able to measure maximum (systolic) and minimum (diastolic) blood pressure values non-invasively in the arm. Additionally, recent technology allows the blood pressure wave to be measured non-invasively in peripheral (far from the heart) arteries, such as the carotid or radial arteries. However, blood pressure levels in the heart or in the aorta, which are very useful to assess cardiovascular health, are normally measured via cardiac catheterisation, a highly invasive and expensive procedure which carries a risk for the patient. Although there are non-invasive methods to measure aortic blood pressure, they tend to use a combination of peripheral measurements and empirical data. Therefore, a method which measures aortic blood pressure non-invasively using patient-specific measurements – some of them obtained at the aorta – is highly desirable.

At a fundamental level, the flow of blood pumped by the heart into the arteries can be described similarly to how water flows through a flexible tube, or to how air passes around a Formula One car. These physical phenomena can be studied mathematically using the equations of fluid dynamics. However, solving these equations with pen and paper becomes increasingly difficult as the complexity of the phenomena increases, so a computational model can be used to solve them instead. A computational model is a mathematical representation of a physical phenomenon: it starts from a series of justified assumptions, follows a set of mathematical rules, and can be used to simulate said phenomenon on a computer. In the same way that there are simple phenomena (*e.g.* purely elastic collisions) and more complex ones (*e.g.* n-body problem), there are computational models with different levels of complexity. Zero-dimensional (0-D) models can be used to study the global behaviour of a fluid over time, but are unable to provide information on the direction of flow. One-dimensional (1-D) models can be used to study fluids which move mostly in one direction (*e.g.* blood mainly flows parallel to the wall of the arteries, rather than perpendicular to them). Three-dimensional (3-D) models can represent fluid dynamics in all directions and in all kinds of problems. As complexity increases, so does the computational cost, which indicates the amount of computational resources (e.g. *random access memory* or RAM) required to simulate a given phenomenon. Therefore, the choice of a computational model is normally conditioned by the nature of the phenomenon under study and the availability of computational resources.

Non-invasive measurements remove any risks for the patient compared to cardiac catheterisation, and can be obtained much more quickly using computational models. In this thesis, 0-D and 1-D models have been used to obtain reliable aortic blood pressure measurements from magnetic resonance and ultrasound scans. 0-D models were used because of their relatively low computational cost and because of their ability to measure blood pressure from aortic flow – obtained via magnetic resonance imaging or ultrasound – and a peripheral blood pressure measurement only. When the anatomy of the aorta from magnetic resonance imaging was available, 1-D models were used as they allow the study of the propagation of the blood pressure waves throughout the arteries while keeping the computational cost low enough for a clinical setup. Regardless of the choice of model, patient-specific models are created by extracting a series of cardiovascular parameters, such as the heart rate or the stiffness of the aorta, from a given patient's clinical measurements. Therefore, a part of this thesis is dedicated to finding optimal methods to

extract these parameters from clinical measurements with the ultimate aim of obtaining reliable blood pressure measurements.

The aortic pressure gradient, calculated as the difference in blood pressure before and after a narrowing of the aorta or between either side of the aortic valve, is used to detect and monitor certain cardiovascular diseases. The magnitude of the pressure gradient allows clinicians to plan drug therapy and to decide whether a surgical intervention is necessary. There are both invasive and non-invasive methods to obtain aortic pressure gradient measurements. Using non-invasive measurements of the aortic pressure gradient, a part of this thesis investigates the differences in cardiovascular properties between dilated cardiomyopathy patiens and healthy subjects.

1.2 Thesis objectives

This thesis studies how computational models of arterial blood flow can be used to assess cardiovascular health. The overall aim of this thesis is:

To develop and assess the performance of algorithms to estimate aortic blood pressure from non-invasive clinical measurements using computational models.

The following objectives were identified to achieve the overall aim:

- **To create datasets of thousands of healthy virtual subjects with known cardiovascular parameters and physiological haemodynamic waves.** Three datasets of virtual subjects were created using computational models of arterial blood flow of different complexities. The cardiovascular parameters required by the models were extracted from the clinical literature for healthy adults. Each dataset contained thousands of virtual subjects, whose unique cardiovascular parameters and haemodynamic waves (*i.e.* flow, pressure, area) were known exactly at one or more locations.
- **To identify optimal methods to estimate cardiovascular parameters.** An exhaustive literature review of current methods to estimate cardiovascular parameters was performed. Additionally, novel methods were developed. Using the

datasets of virtual subjects, both current and novel methods were assessed for the first time against a common reference.

- **To develop and assess novel aortic (central) blood pressure estimation algorithms.** Three novel central blood pressure estimation algorithms were developed combining optimal cardiovascular parameter estimation methods and three computational models of arterial blood flow. They were assess assessed on three clinical datasets and one dataset of virtual subjects. Each dataset contained reference central blood pressure and flow waves.

- **To study the influence of individual cardiovascular parameters on the aortic pressure gradient of dilated cardiomyopathy (DCM) patients.** A dataset of virtual subjects was created using the clinical characteristics of a group of DCM patients and healthy controls. Since individual cardiovascular parameters were varied between subjects, whilst all others were held constant, the virtual dataset allowed the influence of cardiovascular parameters on the aortic pressure gradient to be investigated.

1.3 Organisation of the Thesis

This thesis is structured as follows: Chapters 2 and 3 provide the background and motivation of the thesis; Chapters 4 to 7 address each of the four objectives in turn: Chapter 4 describes the datasets and the methodology for creating *in silico* pulse waves; Chapters 5 to 7 report experiments concerning cardiovascular parameter estimation methods, aortic blood pressure estimation algorithms, and the influence of cardiovascular parameters on the aortic pressure gradient, respectively; and Chapter 8 contains the achievements of the thesis and directions for future research. An individual description of each chapter is presented next.

Chapter 2 presents the clinical background, including a brief description of the cardiovascular circulation, the clinical motivation of blood pressure measurements, and an overview of methods for the invasive and non-invasive measurement of blood pressure. In Chapter 3 the use of 0-D and 1-D computational models of the arterial circulation is justified, their main assumptions are presented, and their mathematical formulations are described. In Chapter 4 the different datasets used in this work are presented: the

process of creating datasets of virtual subjects is detailed and the data acquisition and post-processing of the clinical datasets is explained. In Chapter 5 a comprehensive review of current cardiovascular parameter estimation methods is presented, novel methods are developed using three datasets of virtual subjects, and the performance of every method is assessed using the 1-D dataset of virtual subjects. Chapter 6 reports the performance of three central blood pressure estimation algorithms. Their ability to reproduce the central blood pressure wave is assessed using: a clinical dataset containing invasive catheter measurements from patients suffering from coarctation of the aorta; two clinical datasets containing non-invasive reference data for normotensive and hypertensive subjects, respectively; and a dataset of virtual subjects. Chapter 7 presents a study on the influence of individual cardiovascular parameters on the aortic pressure gradient of dilated cardiomyopathy patients and describes the creation of a dataset of virtual subjects tailored to the clinical characteristics of a group of patients and healthy controls. Finally, Chapter 8 summarises the achievements of this thesis, presents its main limitations, and identifies directions for future work.

2 Clinical Background

In this chapter the clinical background to this thesis is presented. Firstly, the anatomy and physiology of the cardiovascular system, focusing on the heart, the systemic arteries, and the blood, is described. Secondly, the clinical motivation of blood pressure measurements to assess cardiovascular health, focusing on non-invasive methods to estimate brachial and central blood pressure, is outlined. Finally, a novel method for central blood pressure estimation, which partly motivated the main aim of this thesis, is presented.

2.1 The cardiovascular circulation

Diffusion is the fundamental transport process at cellular level. However, the rate at which diffusion occurs is inversely proportional to the distance due to the random nature of this transport process. Therefore, for distances greater than $\sim$ 0.1 mm, a faster transport system is required [8]. The main functions of the cardiovascular (CV) system are to provide the rapid transfer of oxygen, nutrients and metabolites to the body and to quickly get rid of metabolic waste products like carbon dioxide, urea and creatinine. The CV system is also part of a control system since it distributes and secretes hormones; plays a vital role in temperature regulation; and is crucial in the defence of the body by the immune system [8]. From an engineering point of view, the cardiovascular system is composed of a fluid (the blood) circulating under the action of a pump (the heart) within a closed network of flexible tubes of varying diameter and thickness (the blood vessels). Hence, the cardiovascular circulation can be analysed according to the physical laws of fluid mechanics, accounting for the fluid-structure interaction between the blood (fluid) and the heart and blood vessels (structure). The anatomy and the role of these

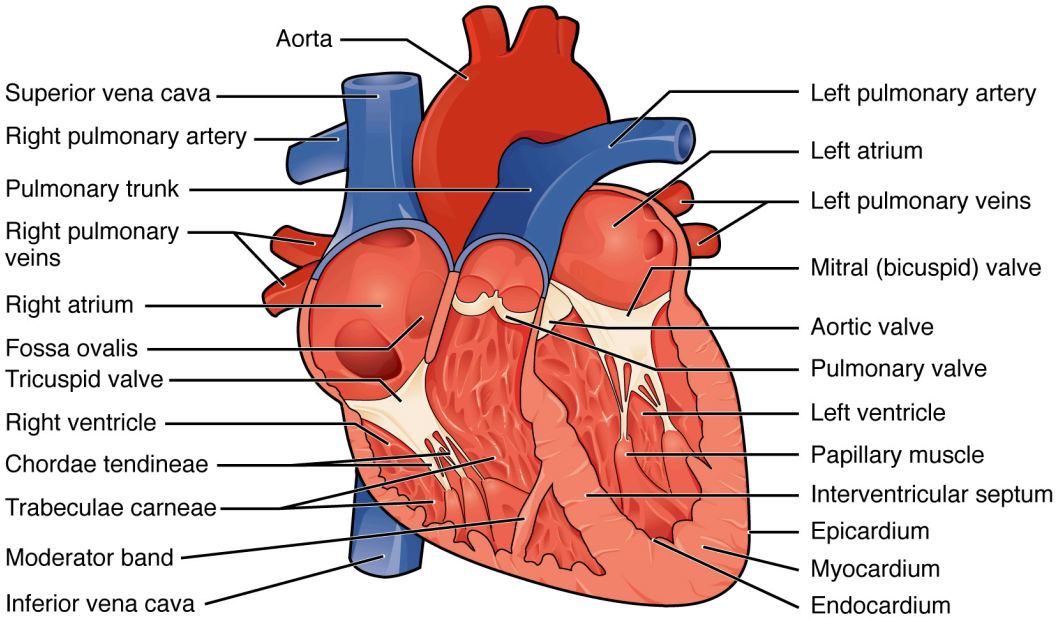

FIGURE 2.1: Anterior view of the heart [9]. This view shows the four chambers (two atria and two ventricles), the major arteries and veins, and the heart valves. The ascending aorta, where central blood pressure is measured, is connected to the left ventricle via the aortic valve.

components within the cardiovascular circulation, together with the propagation of the pulse wave, are described in detail next.

2.1.1 The heart

The heart is an organ divided into four chambers, two on the right side and two on the left side (see Figure 2.1). Each side contains a blood collection chamber (*i.e.* an atrium) and a pump (*i.e.* a ventricle). The right ventricle receives deoxygenated blood from the right atrium and pumps it to the lungs as part of the pulmonary circulation (shown in Figure 2.3). Simultaneously, the left ventricle receives oxygenated blood from the left atrium and pumps it through the aortic valve into the aorta and to the rest of the body as part of the systemic circulation. The blood follows a closed circuit due to the action of one-way valves located in the heart and the veins [8]. The current study focuses on the systemic circulation, particularly on blood flow dynamics involving the left ventricle, the systemic arteries, the arterioles, and the capillaries.

2.1.2 The blood vessels

Blood vessels can distend because their tunica media, a middle layer with important structural and contractile properties, contains two proteins: elastin and collagen (~ 100 times stiffer than elastin) [8]. Arteries branch in a predominantly tree-like structure, called the arterial tree, although there are a number of loops which provide some redundancy (*e.g.* the circle of Willis in the cerebral circulation and the palmar arch in the hand). Elastic arteries, whose diameters range between 1-4 cm, have highly distensible walls because of their high elastin content. In muscular arteries, with diameters between 1-0.1 cm, the tunica media becomes thicker with respect to the diameter, the elastin and collagen content decreases and the smooth muscle content increases. The arterioles, small vessels with diameters < 0.1 cm, branch into even smaller vessels, the capillaries. The flow of blood through these vessels is known as microcirculation, and the exchange of fluids between capillaries and organs or tissues, as perfusion. The capillaries then merge into venules which also merge to form small veins. Veins are thin-walled vessels with valves to prevent backflow. As seen in Figure 2.3, arteries carry blood at a high pressure away from the heart and veins carry blood at a lower pressure towards the heart. Therefore, although arteries and veins present a similar layered structure, arterial walls are thicker due to the much higher blood pressures which they are subjected to (see Figure 2.2).

2.1.3 The blood

Blood is a complex suspension of blood cells in a fluid plasma. Plasma is an aqueous solution containing proteins, mineral ions, hormones, and glucose, and behaves like a Newtonian fluid for *in vivo* conditions. Blood presents high cellular volume concentrations (between 40-45%), with red blood cells (RBCs) being the most common type of cell. RBCs transport oxygen from the lungs to the body's tissues and organs, and carry $\sim 25\%$ of the carbon dioxide waste to the lungs [9]. In blood vessels where the internal diameter is large (*i.e.* > 0.5mm) compared to the size of the RBCs, blood can be assumed to be a homogeneous, incompressible and Newtonian fluid [10, 11]. However, at slow shear rates, blood has a non-Newtonian behaviour due to the aggregation of RBCs [11].

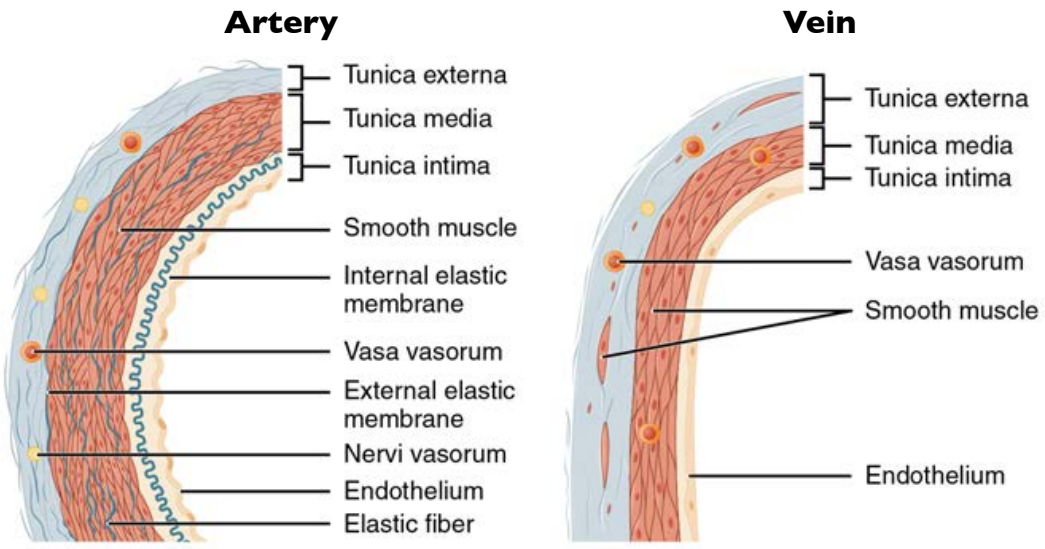

FIGURE 2.2: The structure of blood vessel walls: arteries (left) and veins (right) (adapted from [9]). Arterial walls are thicker and their lumen (*i.e.* the conduct through which blood flows) is smaller. In arteries, the combination of thicker walls and high pressures results in rounded lumens. Due to their thinner walls and lower pressures, venous walls present flatter lumens. Additionally, veins oppose reduced resistance to blood flow due to their larger lumens.

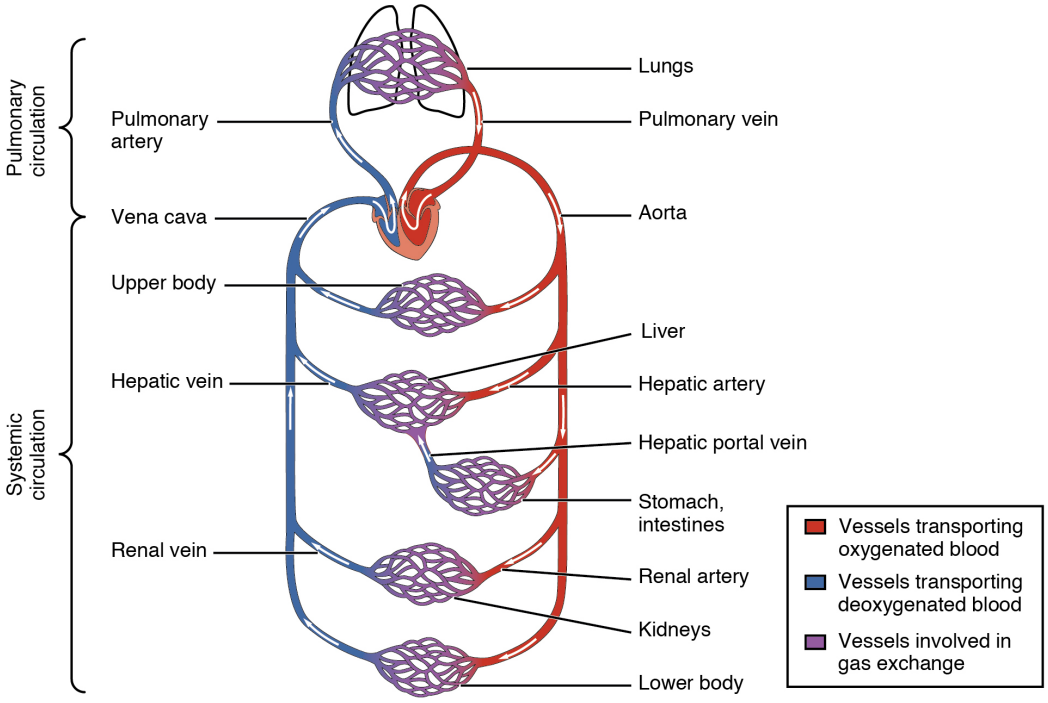

FIGURE 2.3: Diagram of the cardiovascular system (adapted from [9]). The systemic arteries carry oxygenated blood (shown in red) from the left ventricle to the capillaries. The systemic veins return deoxygenated blood (shown in blue) from the capillaries to the right atrium. The pulmonary arteries carry this blood from the right ventricle to the lungs for oxygenation. Finally, the pulmonary veins return this newly oxygenated blood to the left side of the heart, closing the loop.

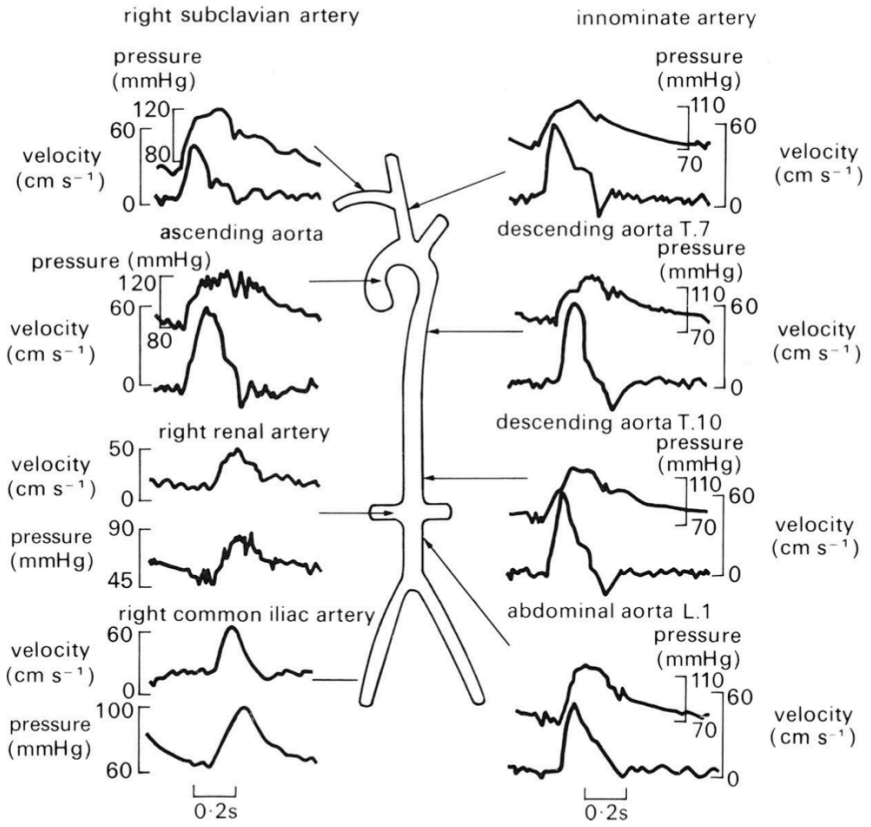

FIGURE 2.4: Pulse wave propagation in the larger systemic arteries (adapted from [12]). The shape of blood pressure and velocity waves changes as the pulse wave propagates from central (ascending aorta) to peripheral (*e.g.* right common iliac artery) locations.

2.1.4 Pulse wave propagation

During systole, the contraction of the left ventricle ejects blood into the aorta through the aortic valve distending the ascending aorta. This distension propagates as a wave, the so-called pulse wave, through the arterial network producing changes in blood flow and pressure with time. The pulse wave reflects multiple times at the aortic valve, arterial bifurcations, and due to arterial wall tapering. This physical phenomenon is known as *pulse wave propagation* and produces a variety of pressure and flow waves throughout the systemic arteries (see Figure 2.4). At the end of systole, the (healthy) aortic valve closes and the flow of blood from the heart stops. During diastole, as blood leaves the larger arteries through the periphery and enters the microcirculation, pressure everywhere in large arteries tends to decrease exponentially [8, 12]. The shape of the pressure wave is determined by the physical properties of the cardiovascular system such as arterial stiffness, arterial resistance, and cardiac ejection patterns. Since these physical properties can be affected by CV disease, this wave carries valuable information for their diagnosis and treatment and plays an important role in conditions such as hypertension.

2.2 Clinical motivation of blood pressure measurements

According to the World Health Organisation, approximately 17.9 million people died from cardiovascular (CV) disease in 2016, representing 31% of all global deaths – 85% of those deaths were due to heart attack and stroke [7]. Although cancer was the largest (29%) cause of death in the United Kingdom in 2014, CV disease followed closely as the second largest (27%) [13]. According to the Office for National Statistics (2015), ischaemic heart disease was the second (12%) leading cause of death in England and Wales [14]. While ischaemic heart disease was the leading (14%) cause of death for males, dementia and Alzheimer disease were the leading (15%) cause of death for females. Furthermore, CV disease also has an important global economic impact. In the USA, the annual cost of CV disease in 2016 was $555 billion; these costs were estimated to exceed $1.1 trillion by 2035 [15]. In England, healthcare costs relating to CV disease are estimated at $7.4 billion per year [16].

High blood pressure (BP), also known as hypertension, is the main risk factor for mortality worldwide. In the year 2010, over 20% (1.4 billion) of the world's adult population had hypertension [17]. It is estimated that by 2025 the global burden of hypertension will exceed 1.6 billion [17, 18]. Hypertension is a high risk factor for CV diseases such as ischemic heart disease, stroke, congestive heart failure, cardiomyopathy, atrial fibrillation, aortic aneurysm, and peripheral vascular disease; and other diseases such as chronic kidney disease, vision loss, and dementia [19–23].

2.2.1 Non-invasive peripheral blood pressure

Recent (2017) clinical guidelines recommend the diagnosis of hypertension for levels of systolic/diastolic BP (SBP/DBP) $\geq$ 130/80 mmHg, measured at the brachial artery at heart level with a validated sphygmomanometer (*i.e.* a pressure cuff) [24]. Brachial BP must be recorded in both arms, with subsequent measurements taken in the arm with the highest BP values. A reliable average BP measurement consists of the average of $\geq$ two measurements obtained on $\geq$ two occasions. A typical brachial pressure wave is shown in Figure 2.5.

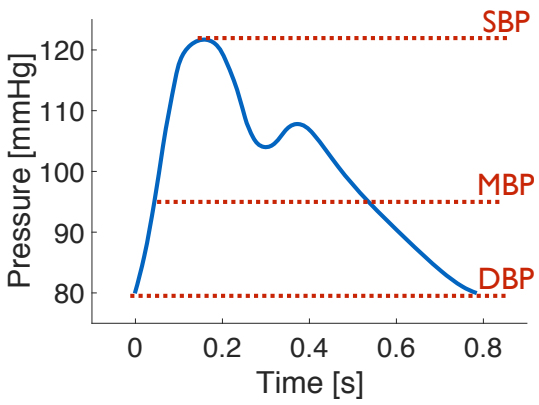

FIGURE 2.5: Brachial blood pressure wave. The blue line respresents the value of blood pressure as a function of time for a cardiac period. From top to bottom, the horizontal red lines indicate the values of systolic (SBP), mean (MBP), and diastolic (DBP) blood pressure measured at the brachial artery.

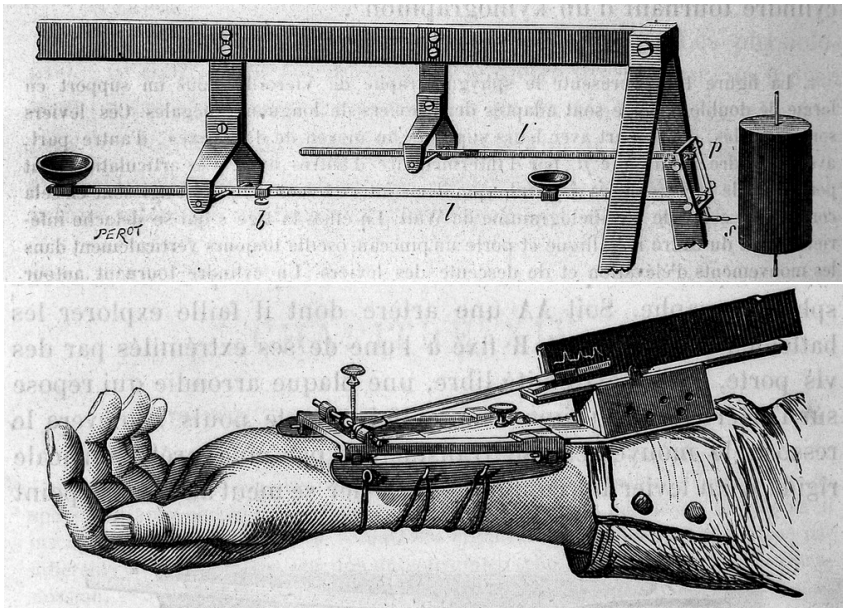

FIGURE 2.6: Diagram of early sphygmographs. Top: Vierordt's original design (adapted from [26]). Bottom: Marey's improved design (adapted from [27]).

2.2.1.1 The sphygmograph and the sphygmomanometer

The first attempt to create a sphygmograph – the predecessor of the sphygmomanometer – to measure peripheral blood pressure non-invasively came from Vierordt (1818-1884) in 1855 [25] (see Figure 2.6, top). This device measured the pressure which was required to collapse the radial artery. In 1880, Marey (1830-1904) substantially improved the design of Vierordt's sphygmograph, but the device was still too cumbersome for routine clinical use (see Figure 2.6, bottom).

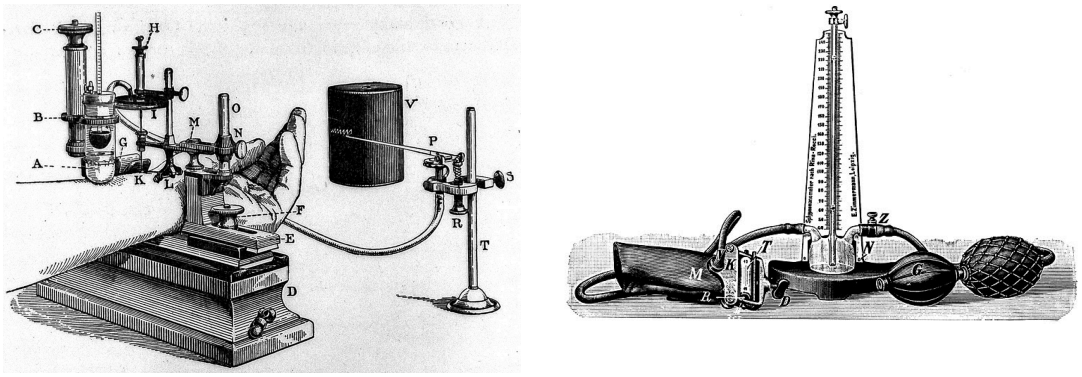

FIGURE 2.7: Diagram of early sphygmomanometers. Left: von Basch's original design (adapted from [29]). Right: Riva-Roci's improved design, used nowadays (adapted from [30]).

The sphygmomanometer, which was a simpler and more accurate device compared to the sphygmograph, was invented by von Basch (1837-1905) in 1881 (see Figure 2.7, left). However, the modern sphygmomanometer was developed by Riva-Rocci (1863-1937) and reported in 1896. This device consisted of an inflatable cuff – connected to a mercury manometer – surrounding the arm's circumference at a radial or brachial location (see Figure 2.7, right). First, the cuff is inflated using a hand pump until the pulse disappears. Then, as the cuff slowly deflates the pulse reappears – detected by palpation – coinciding with brachial SBP. Nevertheless, brachial DBP cannot be determined by palpation alone since the pulse can be felt continuously from the moment it reappears [28].

2.2.1.2 The auscultatory method

Riva-Roci's method became the gold standard for the simple, accurate, non-invasive measurement of brachial SBP. However, it was Korotkoff (1874-1920) who in 1905 proposed the auscultatory method to measure DBP using a sphygmomanometer and a stethoscope. Firstly, the cuff is inflated to stop the flow of blood through the brachial artery. Secondly, the cuff is slowly deflated resulting in a series of sounds – known as Korotkoff's sounds – captured by the stethoscope. Finally, brachial SBP and DBP correspond to the measured cuff pressure values when the first distinct sound appears and when the last (fifth) sound disappears, respectively.

When measuring brachial blood pressure with the auscultatory method, mercury, aneroid, and electronic pressure gauge sphygmomanometers can be used. However, these methods generally present problems with calibration; they depend on the operator's skills; and

rapid inflation or deflation can affect the BP readings, especially in patients with slow heart rates (< 60 bpm). For these reasons, the auscultatory method is being replaced by oscillometric devices [31].

2.2.1.3 Oscillometric methods

Oscillometric methods identify SBP, mean BP (MBP), and DBP from the amplitude of the oscillometric wave (OMW) recorded in the arm as the pressure cuff deflates. The amplitude of the OMW increases between SBP and MBP and decreases below MBP, allowing the direct measurement of MBP [32]. SBP and DBP are then estimated from the OWM using device-specific maximum amplitude (MA) algorithms [33]. However, most oscillometric methods do not provide a direct measurement of SBP and DBP, since they use population-based ratios between SBP/DBP and MBP (SBPR/DBPR) to calculate SBP and DBP for a given subject (see Figure 2.8) [34].

Oscillometric devices intended for out-of-office (home) measurements have been adapted for office use, but present less durability and reliability than more costly, professional oscillometric devices traditionally used in hospitals [31]. More recently, automatic devices with the ability to calculate average BP values from multiple pressure measurements have been developed, allowing automated office BP (AOBP) measurements [31]. An advantage of this device over the auscultatory method is the reduced need for staff presence during BP measurements. In fact, since the presence of an operator can affect the BP measurements (*e.g.* due to the white coat syndrome or to the patient talking), this unattended AOBP measurement is preferred for clinical use [31].

2.2.2 Central blood pressure

Brachial blood pressure (bBP) measurements have been used over the last century for routine clinical assessment. However, as described in the previous section, these measurements suffer from a number of errors due to the patient (*e.g.* recent food consumption, movement, talking); the device (*e.g.* miscalibration, non-validated device); or the procedure (*e.g.* inapropriate cuff size, not levelled with the heart).

Central blood pressure (cBP) is the blood pressure in the ascending aorta and close to the aortic root (see Figure 2.1). Recent clinical studies have shown that cBP is a better

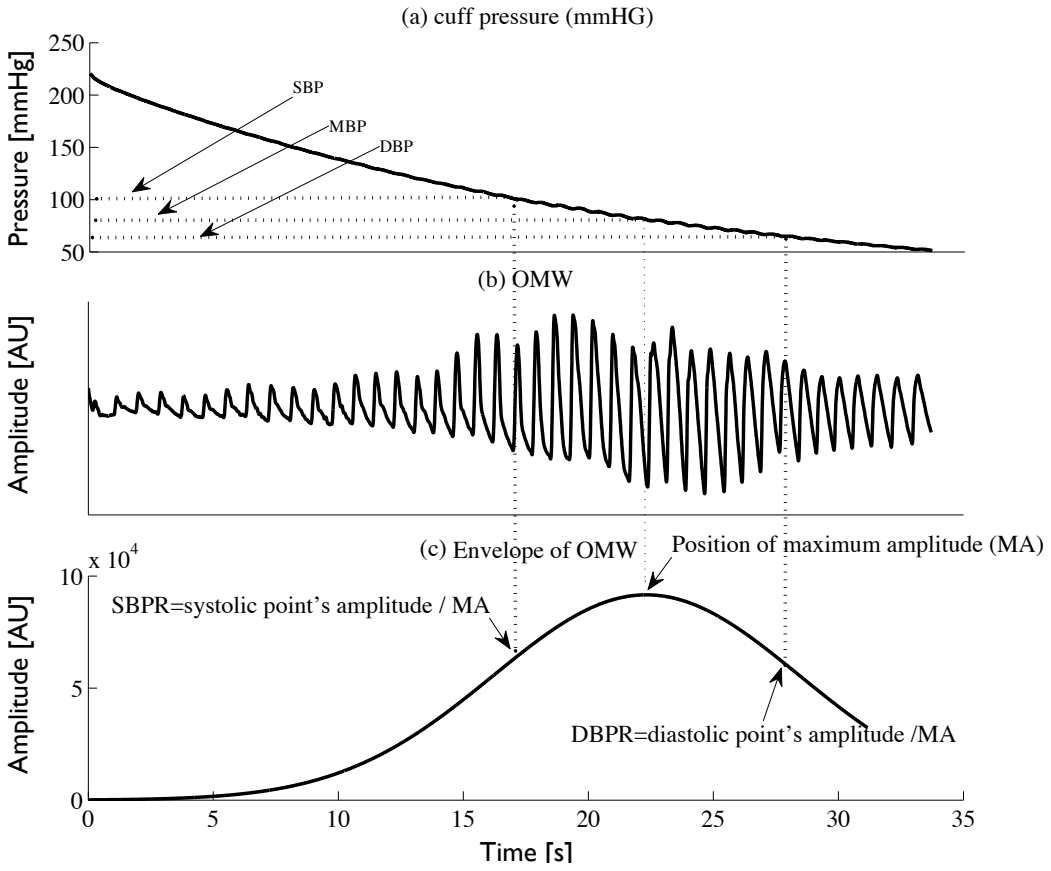

FIGURE 2.8: Blood pressure measurement via oscillometric methods. (a) Cuff pressure as it deflates, showing the values of SBP, MBP, and DBP. (b) Oscillometric wave (OMW). (c) Envelope of the OMW: MBP coincides with the time of maximum amplitude (MA); SBP and DBP are calculated as a function of the MA from empirical ratios. Adapted from [33].

cardiovascular risk indicator than bBP [35–39]. In fact, major organs are exposed to cBP rather than bBP [38, 40]. Regardless of gender or disease, cBPs in subjects with similar brachial SBP may differ by up to 33 mmHg, resulting in "a significant overlap of central SBP scores between brachial SBP risk groups" [41]. Furthermore, bBP can be misleading in healthy young adults due to central-brachial pulse pressure (PP, calculated as SBP minus DBP) amplification of up to 30 mmHg [42]. PP amplification between central and peripheral arteries is illustrated in Figure 2.9.

2.2.2.1 Invasive gold-standard for central blood pressure measurements

The gold standard of cBP measurement is ascending aorta BP via cardiac catheterisation, which carries risks to patients (*e.g.* blood clot formation, embolization, infection) even when performed in specialised centres; is costly; and is not suitable for routine clinical

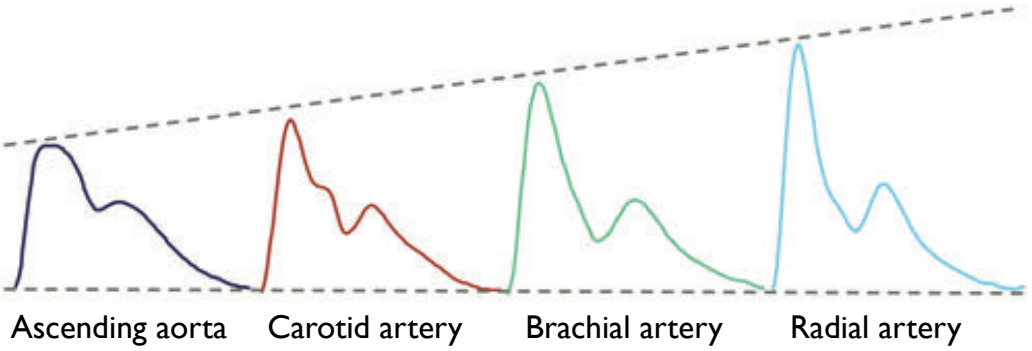

FIGURE 2.9: Blood pressure amplification from central to peripheral arteries (adapted from [37]). Arterial locations from left to right: ascending aorta, carotid artery, brachial artery, and radial artery. While DBP and MBP remain relatively constant within the larger systemic arteries, SBP increases towards the periphery resulting in an amplification of PP.

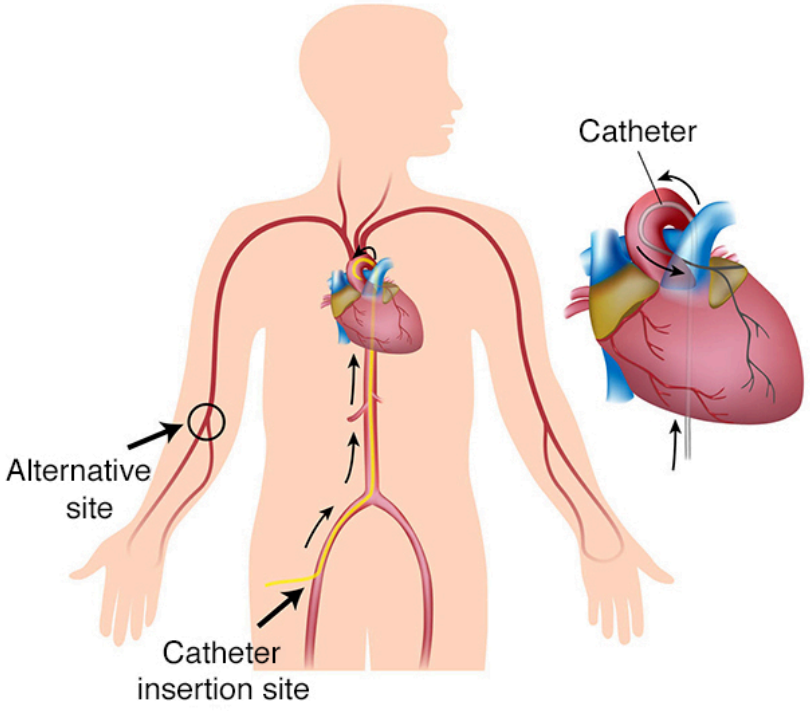

FIGURE 2.10: Central blood pressure measurement via cardiac catheterisation. A catheter is commonly inserted into either the femoral or brachial artery, and threaded up to the aorta where central blood pressure is measured. Adapted from [44].

practice [37, 43] (see Figure 2.10). Consequently, there is great value in developing methods for estimating cBP non-invasively which are less risky and more suitable for frequent use.

TABLE 2.1: Summary of methods, commercial devices, pulse wave measurement methods, and measurement sites for non-invasive central blood pressure estimation. Abbreviations: AT: applanation tonometry; Osc.: oscillometry.

cBP method	**Device**	**Pulse wave measurement**	**Measurement site**
Generalised Transfer Function	SphygmoCor	AT	Radial, Carotid
	GAON 21A	AT	Radial
	Mobil-O-Graph	Osc. (at DBP)	Brachial
	Centron cBP301	Osc. (at 65 mmHg)	Brachial
	Vicorder	Osc. (at 70 mmHg)	Brachial
	PulseCor R7.0	Osc. (30 mmHg above SBP)	Brachial
Surrogate	PulsePen	AT	Superficial arteries
	Complior Analyse	AT	Carotid
Wave analysis	Omron HEM-9000AI	AT	Radial
	Arteriograph	Osc. (35 mmHg above SBP)	Brachial
Moving average filter	BPro (A-Pulse)	AT	Radial
Auscultatory	Novacor Diasys	Osc., electrocardiogram	Brachial

2.2.2.2 Central blood pressure from peripheral blood pressure

A consensus on a specific technique for the non-invasive measurement of cBP does not currently exist. In 2016, Papaioannou *et al.* [45] performed a systematic review and meta-analysis of recent invasive validation studies (2003-2014) assessing commercial devices for the non-invasive measurement of central SBP. Table 2.1 shows a summary of different methods, commercial devices, pulse wave measurement methods, and the corresponding measurement sites.

All these methods estimate cBP from non-invasive measurements recorded either via oscillometric methods or applanation tonometry. Applanation tonometry consists of a pressure sensor which partially flattens (applanates) a superficial artery, such as the carotid or radial arteries, and records a pressure wave which must be calibrated from an invasive or non-invasive BP measurement. This method was popularised by the development of the high-fidelity Millar micromanometer [46]. However, applanation tonometry must be calibrated from brachial BP; and it requires an experienced operator, since the applanation pressure depends on the thickness of the tissues (*e.g.* skin, muscle, arterial wall), and the position and angulation of the tip of the probe.

As seen in Table 2.1, most tonometry-based cBP estimation methods use radial tonometry measurements. Although carotid tonometry is recommended for the measurement of carotid-femoral pulse wave velocity ($PWV_{\mathrm{c-f}}$) [47], it is not currently advisable for routine clinical measurement of cBP waves required in hypertension [43, 45, 46]. Carotid

tonometry suffers from artifacts from patient movement and respiration, and can be uncomfortable for the patient. Furthermore, although this method does not cause clinically significant baroreceptor activation when performed by an experienced operator [48], inadequate applanation pressure does increase the possibility of baroreceptor activation in the carotid artery [46]. Baroreceptors are neurons which are excited when the vessel wall is stretched. This mechanism allows them to sense blood pressure changes and to transmit this information to the brain to ensure that adecuate blood pressure levels are maintained. Therefore, the activation of carotid baroreceptors during carotid tonometry could affect blood pressure levels, thus making the measurement unreliable.

The different methods for the non-invasive estimation of cBP presented in Table 2.1 are described next.

- **Generalised transfer function**: techniques based on the use of a generalised transfer function (GTF), which estimate cBP from peripheral BP waves, have been widely validated [49–51]. The SphygmoCor® system (AtCor Medical, Sydney, New South Wales, Australia) is the most commonly used of such devices [38, 52]. However, since GTFs are designed using data from clinical populations, they do not account for inter-subject or intra-subject variability [53] and rely entirely on peripheral BP, ignoring both patient-specific and central characteristics of the cardiovascular system. GTFs have been developed to estimate cBP from carotid, brachial and radial BP [54, 55].

- **Surrogate measurements**: the PulsePen® (DiaTecne S.R.L. Milan, Italia) [56] and Complior Analyse® (Alam Medical, Saint-Quentin-Fallavier, France) [57, 58] devices assume that the carotid BP wave calibrated by a brachial cuff BP measurement is a surrogate of the cBP wave [45].

- **Wave analysis methods**: the HEM-9000AI® device (Omron Healthcare, Kyoto, Japan) [59] uses a radial BP wave obtained via tonometry to estimate cBP using a regression equation applied to the second systolic peak [60]; the Arteriograph® device (TensioMed, Budapest, Hungary) estimates cBP from the analysis of the waves arriving at the occluded brachial artery (35 mmHg over SBP) [61].

- **Moving average filter**: the BPro® [62] device with the A-Pulse® software (HealthSTATS, New Century, Singapore) measures radial pressure waves at the

wrist using radial applanation tonometry and computes cBP using a mathematical low-pass filter known as the n-point moving average filter [63]. A more recent study showed that this method also works for brachial pressure waves measured via oscillometry [64].

- **Auscultatory methods**: The Diasys® devices (Novacor, Rueil-Malmaison, France) measure brachial BP via an auscultatory method and the QKD interval via an electrocardiogram [65]. The QKD interval is the time between the QRS complex on the electrocardiogram and the detection of the last Korotkoff sound [66]. Central SBP is estimated via the regression equation $SBP = 105 + 1.29 \cdot MBP - 0.39 \cdot HR - 0.30 \cdot H - 0.11 \cdot QKD$, where SBP and MBP are given in mmHg, MBP is calculated from brachial BP as $0.6 \cdot DBP + 0.4 \cdot SBP$, HR is given in bpm, H is height given in cm, and QKD is given in ms.

2.2.2.3 Central blood pressure from aortic flow

As described in the previous section, methods which estimate cBP from a non-invasive peripheral pressure wave based on a generalised transfer function have been widely adopted. Additional cBP estimation methods based on surrogate measurements, wave analysis, mathematical filters, auscultation, and electrocardiograms have also been validated and resulted in a range of commercial devices. However, most of these methods provide limited subject-specificity, given that they depend on clinical population studies and empirical coefficients. Furthermore, they focus on peripheral information such as the radial, brachial, or carotid pressure waves, and disregard the influence of more central information such as the aortic flow velocity.

In a proof-of-concept study, Vennin *et al.* showed that the cBP wave can be accurately estimated combining the aortic flow velocity wave, U, and a peripheral pressure wave [67]. From these waves, ascending aorta pulse wave velocity (PWV), DBP, MBP, and the time constant (τ) of the exponential decay in diastole are extracted. Using *in silico* and *in vivo* data, they developed an algorithm to estimate cBP which combines the water-hammer equation, a second order polynomial, and an exponential fit. This algorithm is divided in four parts (I-IV) if U presents reverse flow, or in three parts (I, II, and IV) if it does not, and estimates cBP:

I in *early systole* (between the start of the cycle and the time of peak aortic flow velocity, t_{peak}) using the water-hammer equation $P_{\text{wh}} = DBP + U\rho PWV$, where ρ is the blood density;

II in *mid-systole* (between t_{peak} and the start of diastole, t_{d}) using a second order polynomial (i) which must result in MBP and (ii) whose start and end values must equal the pressure values estimated from I and III/IV at t_{peak} and t_{d}, respectively;

III between the time where flow velocity first becomes negative and t_{d} using P_{wh};

IV during the *diastolic decay* (between t_{d} and the end of the cycle), using a linear spline interpolation and a least-squares fitting.

However, the original study used simultaneous, invasive measurements of pressure and flow to estimate PWV, DBP, MBP, and τ.

The aim of this thesis, the non-invasive estimation of the cBP wave from aortic flow and peripheral pressure using computational models of the cardiovascular system, was partly motivated by the findings of this study.

2.3 Final remarks

This chapter has described the cardiovascular circulation, focusing on the heart, the blood vessels, and the blood, and has presented the physical phenomenon of pulse wave propagation, which is fundamental to the one-dimensional mathematical formulation presented in Chapter 3. The worldwide impact of cardiovascular disease, and the relevance of hypertension as a cardiovascular risk factor has been highlighted. A review on the different techniques and devices to measure brachial and central blood pressure has been performed. Additionally, a proof-of-concept study which estimates central blood pressure non-invasively from aortic flow and peripheral pressure has been described. Overall, this chapter motivates the development of safe, non-invasive, and non-expensive methods to accurately estimate central blood pressure. This thesis explores the use of computational methods (Chapter 3) to create *in silico* datasets (Chapter 4), to estimate cardiovascular parameters (Chapter 5) and central blood pressure (Chapter 6) from clinical data obtained non-invasively, and to improve the understanding of haemodynamics in disease (Chapter 7).

3 Mathematical Background

This chapter presents the mathematical background of the thesis. Firstly, a justification of the use of zero-dimensional (0-D) and one-dimensional (1-D) computational models of cardiovascular mechanics is provided. These models are used in this thesis to create datasets of virtual subjects to test, develop, and assess cardiovascular parameter estimation methods, and to estimate central blood pressure non-invasively from aortic flow. Secondly, the two-element and three-element Windkessel (0-D) models are derived, and some of their clinical applications are described. Finally, the 1-D mathematical formulation is described, including some examples of clinically relevant applications of different 1-D models.

3.1 Justification for the use of 0-D and 1-D models

Three-dimensional (3-D) computational models of fluid mechanics can be used to study complex physical phenomena (*e.g.* wall shear stress, turbulence, circulation patterns) in complicated arterial geometries, such as those seen in severe aortic coarctation, brain aneurysms, and transposition of the great arteries [68–70]. However, due to their high computational cost, 3-D simulations of pulse wave propagation in the systemic circulation are not feasible in the current clinical setup. Furthermore, the amount of clinical data required to create a personalised computational model is proportional to its complexity. Instead, 0-D or 1-D simulations of the arterial circulation provide an acceptable trade-off between computational cost, required clinical data, and accuracy (Figure 3.1).

Also known as lumped parameter models, 0-D models can capture the global characteristics of the arterial circulation during the cardiac cycle. They have a relatively low

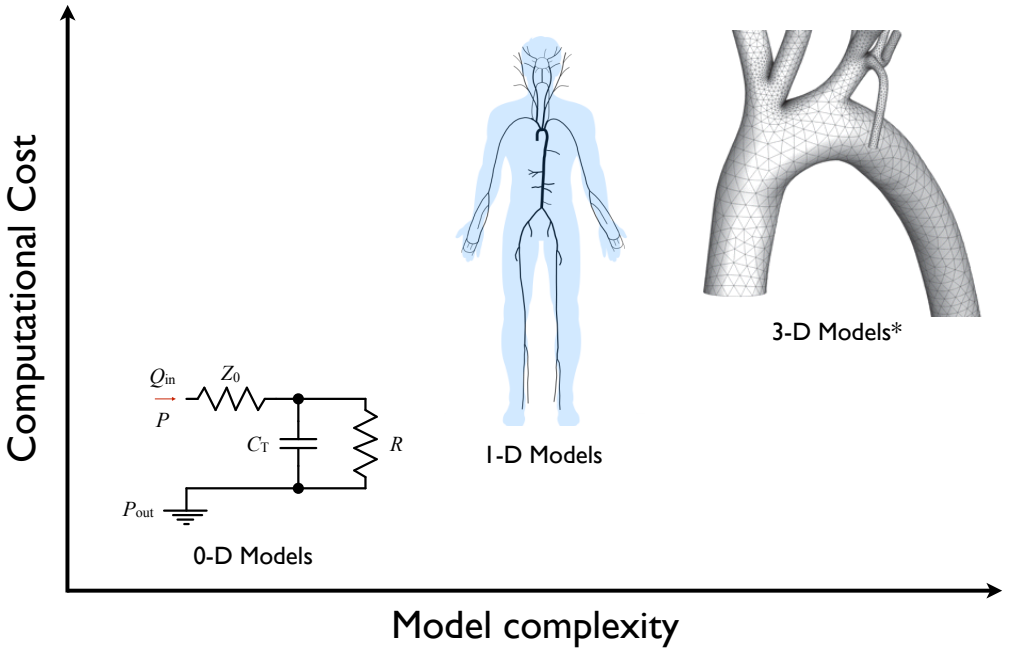

FIGURE 3.1: Computational cost vs model complexity for 0-D, 1-D, and 3-D models. *Adapted from [71].

computational cost compared to other models, with a runtime of a few seconds on a PC. Westerhof *et al.* showed that the 0-D three-element Windkessel model is able to describe the pressure-flow relation for the systemic arterial system [72]. However, 0-D models are space-independent and cannot be used to study pulse wave propagation or local changes in the properties of the arterial system.

1-D models have a higher computational cost than 0-D models, with runtimes ranging from a few seconds to a few minutes on a PC. However, they allow the study of pulse wave propagation phenomena through the arterial system in the axial direction and during the cardiac cycle. Several *in vivo* [73–75], *in vitro* [76–78], and *in silico* [3, 75, 79–82] studies have shown that 1-D modelling can accurately reproduce the clinically relevant features of the pressure, flow and area waveforms. Additionally, 'reduced' 1-D models containing a small number of arteries have been shown to yield similar results to more 'complete' 1-D models containing a large number of arteries at a fraction of the computational cost [4, 83]. The clinical data required to create these 'reduced' 1-D models can be readily obtained in the clinic.

Since this thesis focuses on the application of personalised computational models in a clinical setup, where measurements must be available within a short time, 0-D and 1-D models were chosen over 3-D models. As part of this study, the performance of 0-D and

1-D models at estimating central blood pressure (cBP) in different clinical scenarios will be compared.

3.2 0-D Windkessel models

3.2.1 The two-element Windkessel model

Also known as Frank's Windkessel model in honour to Otto Frank, this model idealises the arterial system as a time-varying reservoir of compliance C_{T} [84]. Blood flows into the reservoir from the heart, $Q_{\mathrm{in}}(t)$, at a pressure $P(t)$, encounters a resistance to flow, R_{T}, and flows out into the vascular beds at a pressure P_{out} (Figure 3.2). The governing ordinary differential equation (ODE) is

$$\frac{dP}{dt} + \frac{P - P_{\mathrm{out}}}{R_{\mathrm{T}} C_{\mathrm{T}}} = \frac{Q_{\mathrm{in}}}{C_{\mathrm{T}}}, \tag{3.1}$$

which can be solved for $P(t)$ using the integrating factor method,

$$P(t) = P_{\mathrm{out}} + (P_0 - P_{\mathrm{out}}) e^{-\frac{t-t_0}{R_{\mathrm{T}} C_{\mathrm{T}}}} + \frac{e^{-\frac{t}{R_{\mathrm{T}} C_{\mathrm{T}}}}}{C_{\mathrm{T}}} \int_{t_0}^{t} Q_{\mathrm{in}}(t') e^{\frac{t'}{R_{\mathrm{T}} C_{\mathrm{T}}}} \, dt', \quad t \geq t_0, \tag{3.2}$$

where t_0 is the initial time and $P_0 = P(t_0)$.

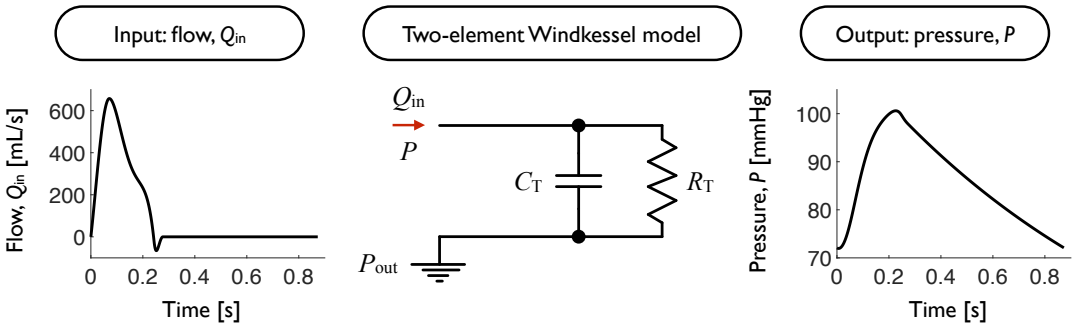

FIGURE 3.2: Two-element Windkessel model (middle). Left: inflow wave corresponding to the baseline virtual subject from the datasets of virtual subjects described in Section 4.1.1.1. Right: corresponding pressure wave simulated using the two-element Windkessel model.

3.2.2 The three-element Windkessel model

This model results from adding a resistor, Z_0, in series to the two-element Windkessel model where $R_\mathrm{T} = Z_0 + R$ (Figure 3.3). Z_0 is commonly known as the characteristic impedance and was initially introduced to represent the impedance of the aorta [72]. The governing ODE is

$$\frac{dP}{dt} + \frac{P - P_\mathrm{out}}{RC_\mathrm{T}} = Z_0 \frac{dQ_\mathrm{in}}{dt} + \frac{(Z_0 + R)Q_\mathrm{in}}{RC_\mathrm{T}}, \tag{3.3}$$

which can be solved analytically for $P(t)$ using the integrating factor method,

$$P(t) = P_\mathrm{out} + (P_0 - P_\mathrm{out} - Z_0 Q_0)e^{-\frac{t-t_0}{RC_\mathrm{T}}} + Z_0 Q_\mathrm{in}(t) + \frac{e^{-\frac{t}{RC_\mathrm{T}}}}{C_\mathrm{T}} \int_{t_0}^{t} Q_\mathrm{in}(t')e^{\frac{t'}{RC_\mathrm{T}}}\,dt', \quad t \geq t_0 \tag{3.4}$$

where $Q_0 = Q_\mathrm{in}(t_0)$.

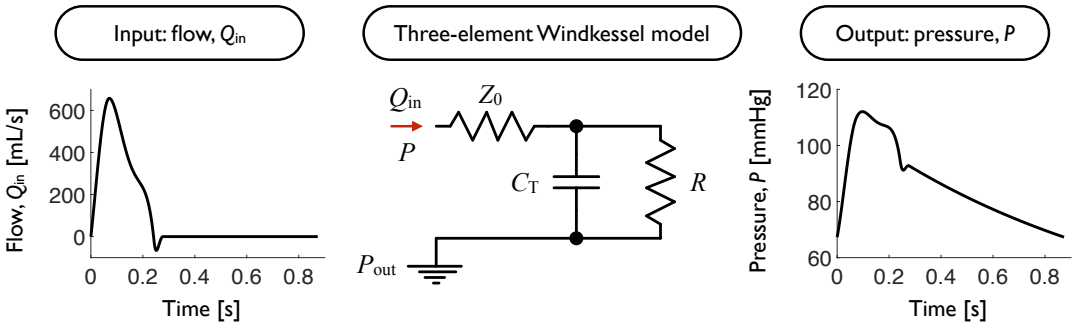

FIGURE 3.3: Three-element Windkessel model (middle). Left: inflow wave corresponding to the baseline virtual subject from the datasets of virtual subjects described in Section 4.1.1.1. Right: corresponding pressure wave simulated using the three-element Windkessel model.

3.2.3 Clinical applications of 0-D models

0-D models are commonly used as boundary conditions for 1-D and 3-D models [75]. They have also been used independently to estimate relevant haemodynamic quantities, such as arterial compliance [72], aortic impedance [85], or cardiac output [86]. Additionally, the parameters derived when performing the reservoir-wave analysis – which uses the two-element Windkessel model – have been shown to have clinical significance for the

assessment of left ventricular diastolic function, hypertension, as a therapeutic target, and as an independent predictor of cardiovascular events [87, 88].

3.3 1-D mathematical formulation

3.3.1 Model assumptions

The arterial network of 1-D models is decomposed into arterial segments connected to each other at nodes. Each segment is modelled as a thin-walled, deformable, impermeable, axisymmetric tube with uniform properties around the circumference whose curvature is small everywhere and can thus be described by the axial (x) coordinate alone. These segments can be divided into non-overlapping spatial elements. Pulse waves propagate in the x-direction with time t, modifying the luminal cross-sectional area, $A(x,t)$, and the cross-sectional averages of blood velocity, $U(x,t)$, flow, $Q(x,t)$, and pressure, $P(x,t)$. A plug flow velocity profile is assumed for the larger arteries [8]. Blood is assumed to be a homogeneous, incompressible and Newtonian fluid, which is reasonable for *in vivo* ranges [12]. Therefore, blood viscosity, μ, and density, ρ, are assumed to be constant. Finally, blood flow is assumed to be laminar (i.e. Reynolds number ≤ 2000), which is reasonable provided that the changes in arterial geometry are smooth.

3.3.2 Governing equations

The equations of mass and momentum conservation in terms of A, Q and P are derived in [89] as

$$\begin{cases} \dfrac{\partial A}{\partial t} + \dfrac{\partial Q}{\partial x} = 0 \\ \\ \dfrac{\partial Q}{\partial t} + \dfrac{\partial}{\partial x}\left(\alpha \dfrac{Q^2}{A}\right) + \dfrac{A}{\rho}\dfrac{\partial P}{\partial x} = \dfrac{f}{\rho} \end{cases}, \tag{3.5}$$

where ρ represents blood density and α is a velocity profile shape factor that affects the frictional term $f = f(\alpha, U)$. An explicit algebraic expression relating P and A, known

as the *tube law*, is used to close the system of equations:

$$P(A,x) = P_0 + \frac{\beta(x)}{A_0(x)}\left(\sqrt{A(x)} - \sqrt{A_0(x)}\right), \tag{3.6}$$

where $\beta(x)$ is related to wall mechanical properties and P_0 and $A_0(x)$ are the reference pressure and area values, which are normally taken as the pressure and area at the end of diastole, respectively. If pulse wave velocity (PWV) is assumed to be constant for the whole 1-D model, $\beta(x)$ only depends on vessel cross-sectional area values $A(x)$ and $A_0(x)$, as seen in Equation (3.7).

3.3.3 Characteristic analysis

The 1-D governing equations (Equation (3.5)) and the tube law (Equation (3.6)), written in non-conservative form, form a system of non-linear hyperbolic partial differential equations which can be analysed using Riemann's method of characteristics [90]. The characteristic variables W_f and W_b are defined as $W_{f,b} = U - U_0 \pm 4(PWV - PWV_0)$, where

$$PWV = \sqrt{\frac{A}{\rho}\frac{\partial P}{\partial A}} = \sqrt{\frac{\beta}{2\rho A_0}}A^{1/4}, \tag{3.7}$$

and PWV_0 is equal to PWV when A is equal to the reference area A_0, which is normally taken as the area at diastolic blood pressure.

In the clinical setup, PWV can be estimated from two pressure or flow waveforms separated by a certain distance using the foot-to-foot method [91]. The characteristic analysis shows that W_f propagates changes in pressure, flow, and cross-sectional area in the positive x-direction of each arterial segment (i.e. from the aortic root towards the peripheral arteries); and W_b propagates these changes in the negative x-direction (i.e. backwards from the periphery towards the aortic root).

The independent contributions of forward and backward waves in the arterial system can be studied using wave separation analysis (WSA) [92] or wave intensity analysis (WIA) [93], and can provide a better understanding of arterial haemodynamics in any of the segments of the 1-D model.

3.3.4 Numerical scheme

In this work, the non-linear system of 1-D equations (Equation (3.5) and Equation (3.6)) was solved using a discontinuous Galerkin finite element scheme, with a high-order 1-D spectral/*hp* element spatial discretisation, as described in [90]. An explicit second-order Adams-Bashforth time-integration scheme, with zero pressures and velocities as initial conditions in each arterial segment, was used.

In this work, the relevant numerical parameters were: time step, polynomial and quadrature order. In the discontinuous Galerkin scheme, each arterial segment is discretised into e non-overlapping spatial elements, Ω_e. The characteristic information moving away from both sides of the boundary between two spatial elements must not affect the solution, which imposes the following restriction on the time step, Δt:

$$\Delta t \leq \frac{\Delta x}{2 \max(|U \pm PWV|)}, \tag{3.8}$$

where Δx is the distance between quadrature points, as explained in [94]. Similarly to Alastruey *et al.* [90], arterial segments were discretised into 2 cm long spatial elements with polynomial and quadrature orders of 3. Segments or elements shorter than 1.1 cm were given polynomial and quadrature orders of 2.

3.3.5 Boundary conditions

Boundary conditions (BCs) are prescribed at the inlet and outlet of every segment. The BCs used in this work, classified as *inflow*, *junction* and *terminal*, are now described:

- An *inflow* BC condition based on a cardiac flow profile, $Q_{\text{in}}(t)$, is imposed at the inlet of the ascending aorta (*e.g.* Figure 3.2, left).
- *Junction* BCs are prescribed at arterial segment connections and bifurcations.
- *Terminal* BCs are represented as three-element Windkessel models coupled to the outlet of terminal arterial segments (Figure 3.3, middle). As suggested by Alastruey *et al.* [90], these 0-D models represent the resistance to flow ($R_T = Z_0 + R$) and the compliance (C_T) of downstream arteries while minimising reflections when Z_0 is equal to the terminal characteristic impedance.

3.3.6 Clinical applications of 1-D models

1-D models of the cardiovascular system allow the study of (i) blood pressure and flow waves in the circulation and (ii) global interactions between the heart and the arteries under normal and pathological conditions [81].

1-D models of the systemic circulation can be used to create datasets of virtual subjects for algorithm testing and development. Willemet *et al.* created 3,325 virtual healthy adult subjects using a 1-D model of the 55 larger arteries of the systemic circulation to assess theoretically the accuracy of foot-to-foot pulse wave velocities as an estimate of aortic stiffness [82]. Charlton *et al.* created 4,374 virtual healthy adult subjects using a 1-D model with 116 arterial segments making up the larger arteries of the thorax, limbs and head to assess theoretically: (i) the determinants of changes in pulse pressure amplification with age, (ii) photoplethysmogram-derived pulse wave indices of aortic stiffness, and (iii) the performance of two algorithms for cardiac output monitoring [3].

'Reduced' 1-D models allow the study of pulse wave propagation in controlled conditions. Abdullateef *et al.* studied the effect of arterial bifurcations on arterial reflections after imposing a Gaussian-shaped pulse at the aortic root [5]. Fossan *et al.* studied the instantaneous wave-free ratio and the fractional flow reserve in a patient-specific coronary network obtaining similar prediction accuracy to that of clinical measurements [4].

In this thesis, 0-D and 1-D models were used to (i) create datasets of virtual subjects to test existing methods for cardiovascular parameter estimation and to develop new ones, and (ii) to develop three algorithms for the non-invasive estimation of cBP from aortic flow. Additionally, a "cohort-specific" dataset of virtual subjects was created using a 1-D model of the 55 larger arteries to study the influence of cardiovascular properties on the aortic pressure gradient in dilated cardiomyopathy patients.

3.4 Final remarks

This chapter has described the mathematical formulation of 0-D and 1-D models and has presented some of their applications. These models will be used in Chapter 4 to generate three datasets of virtual subjects; in Chapter 5 to test and develop methods for cardiovascular parameter estimation; in Chapter 6 to assess algorithms for cBP estimation and to validate them by comparison against datasets of aortic coarctation patients, hypertensive patients, and normotensive volunteers; and in Chapter 7 to investigate ventricular-arterial interactions in a dataset of dilated cardiomyopathy patients and healthy volunteers.

4 Datasets

This chapter describes all clinical and computer-generated datasets used in this thesis to assess the aortic pressure wave. The cardiovascular (CV) parameter estimation methods in Chapter 5 and central blood pressure (cBP) algorithms in Chapter 6 were initially developed and tested using three datasets of virtual subjects (Section 4.1). For each dataset, CV parameters and central blood flow and pressure waves were known exactly for thousands of virtual subjects. The cBP algorithms were then assessed using three clinical datasets (Section 4.2). A "cohort-specific" dataset of virtual subjects (Section 4.1.2.2) was created for the aortic pressure gradient study in Chapter 7. The characteristics of each dataset are shown in Table 4.1.

4.1 Datasets of virtual subjects

Datasets containing pressure and flow waves measured in virtual subjects were created by simulating arterial haemodynamics using 0-D and 1-D computational models respectively. Each virtual subject was created from a unique set of CV parameter values which were extracted from the clinical literature or from the clinical datasets described below. To create a virtual subject, the computational model was parametrised using a set of CV parameters, and an aortic flow wave was simulated as a function of heart rate (HR), stroke volume (SV), and left ventricular ejection time ($LVET$). The cBP wave was simulated by imposing the flow wave as an inflow boundary condition at the aortic root.

TABLE 4.1: Dataset characteristics (presented as mean ± standard deviation). †Age ranges from 25 to 75 years, with 10 year intervals. *Brachial oscillometric measurement. **Radial tonometry measurement. ***Carotid tonometry measurement.

	Clinical datasets			Datasets of virtual subjects			
	Aortic Co.	Normotensive	Hypertensive	Wk2 (0-D)	Wk3 (0-D)	Healthy (1-D)	DCM (1-D)
Subjects (males)	10 (9)	13 (10)	158 (80)	3125 (N/A)	15625 (N/A)	4064 (N/A)	29 (16)
Age [years]	21.1 ± 9.5	48.4 ± 9.4	46.2 ± 16.7	N/A	N/A	51.1 ± 16.9†	45.2 ± 11.7
DBP [mmHg]	51.8 ± 8.0	68.4 ± 10.4*	81.8 ± 12.8*	72.0 ± 11.7	67.0 ± 10.9	75.1 ± 7.4	72.1 ± 6.1
MBP [mmHg]	68.1 ± 9.4	85.6 ± 12.1**	102.0 ± 15.8**	85.9 ± 12.5	85.9 ± 12.5	94.8 ± 6.4	82.5 ± 6.5
pSBP [mmHg]	80.9 ± 13.6	111.4 ± 17.3***	129.6 ± 22.6***	100.8 ± 13.0	114.8 ± 17.0	113.6 ± 11.3	119.4 ± 9.4
cSBP [mmHg]	93.1 ± 12.4	107.2 ± 17.3	126.4 ± 22.2			111.6 ± 11.9	
pPP [mmHg]	30.8 ± 11.6	43.2 ± 12.2	48.2 ± 16.0	28.8 ± 3.7	47.8 ± 12.8	39.3 ± 14.4	N/A
cPP [mmHg]	41.4 ± 13.0	38.8 ± 11.0	44.6 ± 15.4			36.5 ± 14.9	
SV [mL]	78.1 ± 48.6	100.6 ± 35.3	83.3 ± 32.8	88.4 ± 12.2	88.4 ± 12.2	61.0 ± 12.4	90.7 ± 19.6
HR [bpm]	65.5 ± 14.3	62.2 ± 11.2	65.5 ± 10.4	68.8 ± 11.3	68.8 ± 11.3	75.8 ± 9.3	69.1 ± 10.3
CO [L/min]	4.9 ± 2.8	6.2 ± 2.5	5.3 ± 1.9	6.1 ± 1.3	6.1 ± 1.3	4.6 ± 1.1	6.1 ± 1.0

Abbreviations: Aortic Co.: Aortic Coarctation; Wk2 and Wk3: two- and three-element Windkessel; DCM: dilated cardiomyopathy; DBP and MBP: diastolic and mean BP (central values, which are similar to peripheral ones, are used here); pSBP and cSBP: peripheral and central SBP, respectively; pPP and cPP: peripheral and central PP, respectively; SV: stroke volume; HR: heart rate; CO: cardiac output.

New 0-D datasets, whose reference CV parameter values were known precisely, were used to test existing CV parameter estimation methods and to develop new ones (Section 4.1.1). An existing 1-D dataset was used to further test and refine these methods and the cBP estimation algorithms, as this dataset was based on a more complex and physiological model of the arterial circulation of healthy adults (Section 4.1.2.1) [3]. Finally, a different existing 1-D dataset was adapted to study the aortic pressure gradient in dilated cardiomyopathy patients (Section 4.1.2.2) [82].

4.1.1 0-D model datasets of virtual subjects

The 0-D datasets of virtual subjects had the advantage that every CV parameter was imposed when creating the dataset and, hence, reference values were known exactly for each virtual subject. This was not the case for the 1-D model dataset, where some of these reference values needed to be extracted from the simulated pressure and flow waves. Additionally, the computational cost of simulating 0-D virtual subjects is low compared to that of 1-D virtual subjects: thousands of 0-D virtual subjects' cBP waves can be simulated within seconds on a PC, whereas it takes days to simulate the same number of 1-D virtual subjects' cBP waves. Since CV parameter reference values were known exactly for each subject, and given their low computational cost, these datasets were used as the initial step to testing existing CV parameter estimation methods and to developing new ones.

4.1.1.1 Creating 0-D model datasets

Two 0-D datasets were created by using two-element [84] and three-element [95] Windkessel models (Figure 4.1). Each virtual subject's cBP wave was simulated using an aortic flow wave calculated by the *AorticFlowWave* script in [96] (based on prescribed values of HR, SV, and $LVET$, as shown in Figure 4.2) in combination with prescribed values of total arterial resistance (R_{T}) and compliance (C_{T}), characteristic impedance (Z_0), and outflow vascular pressure (P_{out}). Two steps were required to obtain CV parameter values: (i) mean (μ) and standard deviation (σ) values of each cardiovascular parameter in healthy adults were identified from the clinical literature; and (ii) five values for each parameter were calculated as μ, $\mu \pm 0.5\ \sigma$, and $\mu \pm \sigma$ (Table 4.2). A different virtual subject was created for each combination of CV parameters, with a total of 3,125

and 15,625 virtual subjects for the two-element and three-element Windkessel datasets, respectively.

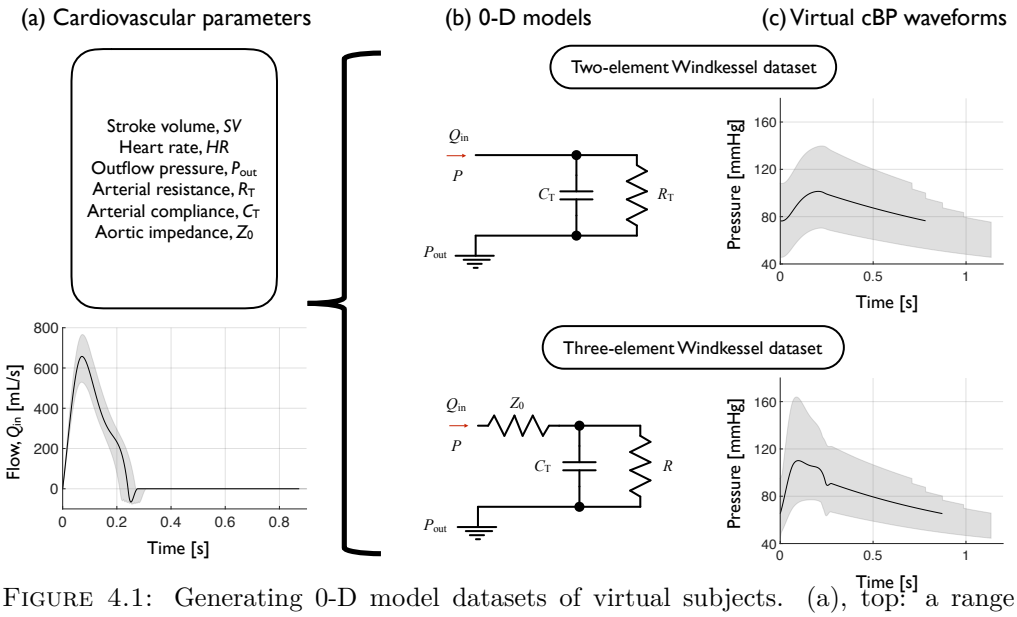

FIGURE 4.1: Generating 0-D model datasets of virtual subjects. (a), top: a range of values for each CV parameter was obtained from the clinical literature for healthy individuals (see Table 4.2). (a), bottom: the thick line illustrates the flow wave corresponding to the baseline values of SV and HR, and the shaded region represents the range of flow waves corresponding to all SV and HR variations. (b) The two-element and three-element Windkessel models were used to generate cBP waves. (c) cBP waves generated by each model: black lines illustrate the cBP wave corresponding to the baseline set of parameter variations, and shaded regions represent the range of cBP waves within each dataset.

The five observed 'steps' in the virtual cBP waves correspond to the five variations in HR. For the 0-D datasets, when all other CV parameters are fixed, as HR increases, cardiac period (T) decreases and $\overline{Q} = 1/T \int_0^T Q(t)dt$ increases. According to Equation (5.2) with $P = MBP - P_{\text{out}}$ and $Q = \overline{Q}$, since R_{T} and P_{out} are fixed, as $\overline{Q}$ increases MBP must increase, too. Finally, since C_{T} is fixed, as MBP increases so does DBP.

4.1.1.2 Cardiovascular parameter variations for healthy adults

Mean and standard deviation values for each CV parameter were extracted from the clinical literature to create two datasets of cBP waves representative of a sample of healthy adults (Table 4.2). SV and HR values were extracted from 17 healthy subjects in supine position [97]. Left ventricular ejection time ($LVET$) values were calculated from SV and HR using the regression equation [97]:

$$LVET = 242 + 1.1SV - 0.9HR, \tag{4.1}$$

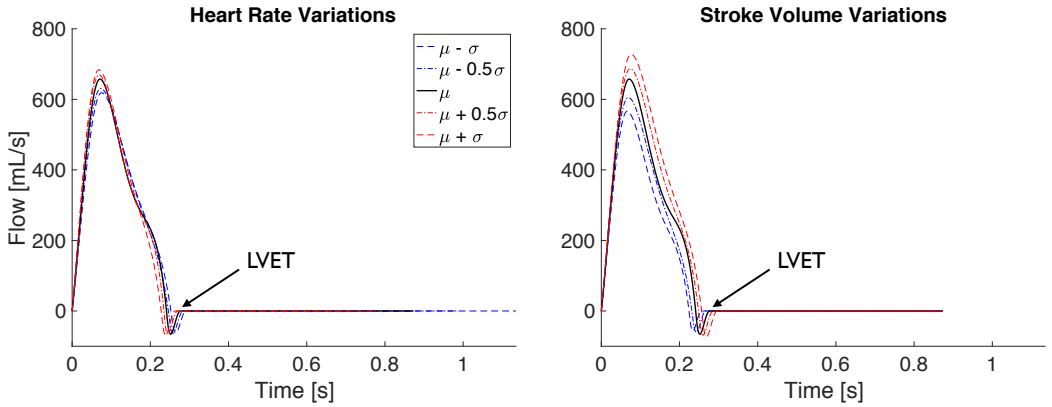

FIGURE 4.2: Aortic flow waves for the 0-D model datasets of virtual subjects. Left: flow waves as a function of heart rate (HR); right: flow waves as a function of stroke volume (SV). Mean (μ) and standard deviation (σ) values for both cardiac parameters were identified from the clinical literature. The baseline case corresponds to the mean values of HR and SV and is represented as a black line. The negative and positive variations are represented as blue and red dashed lines, respectively. In both cases, $LVET$ was calculated as a function of HR and SV using Equation (4.1) and is indicated with an arrow.

with SV in mL and HR in bpm. P_{out} values were extracted from capillary blood pressure measurements in the human lip from 13 healthy subjects seated upright [98]. R_{T} and C_{T} values were extracted from 12 healthy subjects in supine position [99]. Since they were originally normalised by body surface area (A_{body}), μ and σ values for each parameter were multiplied by the mean body surface area to correct for this. Besides, R_{T} values were originally calculated as

$$R_{\text{T,original}} = \frac{\overline{P}}{\overline{Q}}, \tag{4.2}$$

where P and Q were the measured pressure and flow waves, respectively. Thus, to account for non-zero P_{out} values in the calculation of R_{T}, the following correction was required:

$$R_{\text{T,corrected}} = R_{\text{T,original}} - \frac{P_{\text{out}}}{\overline{Q}}, \tag{4.3}$$

where $\overline{Q}$ (mL/s) was calculated from the cardiac index (CI, mL/(min m^2)) as $CI/A_{\text{body}} * 60$. Z_0 values were calculated from pulse wave velocity (PWV), aortic cross-sectional area (A_{Ao}), and blood density (ρ) values using the equation

$$Z_0 = \frac{\rho PWV}{A_{\text{Ao}}}. \tag{4.4}$$

Aortic arch PWV and A_{Ao} values were extracted from 162 healthy subjects using cine phase contrast MRI [100].

TABLE 4.2: CV parameter variations for the 0-D datasets. These variations were used to create the two-element and three-element Windkessel (0-D) datasets. Each CV parameter value is based on observations in healthy humans from the clinical literature.

	Variations					
	Negative		Baseline	Positive		
CV parameter [units]	$\mu - \sigma$	$\mu - 0.5\ \sigma$	μ	$\mu + 0.5\ \sigma$	$\mu + \sigma$	References
SV [mL]	71.2	79.8	88.4	97.0	105.7	[97]
HR [bpm]	52.9	60.8	68.8	76.7	84.7	[97]
P_{out} [mmHg]	27.8	30.5	33.2	35.9	38.6	[98]
R_{T} [mmHg·s/mL]	0.470	0.495	0.520	0.545	0.570	[99]
C_{T} [mL/mmHg]	2.20	2.23	2.27	2.30	2.34	[101]
Z_0 [mmHg·s/mL]	0.0256	0.0358	0.0485	0.0644	0.0847	[100, 102]

Abbreviations: μ and σ: mean and standard deviation values, respectively, for each CV parameter from the clinical literature; SV: stroke volume; HR: heart rate; P_{out}: outflow vascular pressure; R_{T}: total arterial resistance; C_{T}: total arterial compliance; and Z_0: aortic characteristic impedance.

4.1.2 1-D model datasets of virtual subjects

The cBP waves from the 0-D datasets contain some useful clinical features, such as SBP, DBP, the incisura, and the diastolic decay (see Figure 4.1, c). However, since 0-D models cannot simulate pulse wave propagation, these cBP waves do not contain space-dependent features observed in the clinical literature, such as the early systolic inflection point. 1-D models can simulate pulse wave propagation phenomena and thus reproduce a cBP wave whose shape is more detailed and similar to that of physiological cBP waves.

The creation of a 1-D model dataset containing > 4000 virtual healthy adult subjects is described in Section 4.1.2.1 [3]. Each virtual subject contained simulated blood pressure, flow, and area waves at multiple arterial locations and free of measurement errors. For this reason, this dataset was used in this work to test, develop, and assess a number of methods for CV parameter estimation in Chapter 5, and to assess the performance of three cBP estimation algorithms in Chapter 6. In Section 4.1.2.2, the characteristics of the cohort of healthy controls and DCM patients used in Chapter 7 to create a "cohort-specific" 1-D model datset are presented. The creation of both 1-D datasets, including

imposed CV parameters and flow waves, the topology of both 1-D models, and simulated BP waves, is shown in Figure 4.3.

4.1.2.1 Creating a 1-D model dataset

As described in Chapter 4, Charlton *et al.* used a 1-D model of the 116 arterial segments making up the larger arteries of the thorax, limbs and head to create a dataset of 4,374 healthy adult subjects containing pressure, flow velocity, cross-sectional area, and photoplethysmographic (PPG) waves at common measurement locations [3]. The CV parameters of 25-75 years old healthy subjects were identified through a comprehensive literature review. In a similar way to 0-D model datasets (Table 4.2), five values for each CV parameter were calculated as μ, $\mu \pm 0.5\ \sigma$, and $\mu \pm \sigma$, and a different 1-D virtual subject was created for each combination of CV parameters. This 1-D dataset was verified via qualitative comparison between simulated waves and derived indices with corresponding clinical data. A more detailed description of the creation of the 1-D dataset is available in [3].

This thesis contributed to the development of the 1-D dataset by identifying a relationship between HR, SV and $LVET$. As described in Section 4.1.1.2, a regression equation (Equation (4.1)) relating HR and SV to $LVET$ for healthy subjects was found in the clinical literature [97]. This relationship was implemented in the *AorticFlowWave* script in [96] to determine the value of $LVET$ for each simulated aortic flow wave in the 1-D dataset.

4.1.2.2 Creating a "cohort-specific" 1-D model dataset

A "cohort-specific" 1-D model dataset of virtual subjects was created using a 1-D model of the 55 larger systemic arteries [82]. Unlike the previous datasets of virtual subjects, the input CV parameters were extracted from the characteristics of a clinical cohort containing dilated cardiomyopathy (DCM) patients and controls (healthy volunteers). This 1-D dataset provided new insights into arterial-ventricular interactions in DCM as part of the study by Marlevi & Mariscal-Harana[1] *et al.* [2]. This thesis' main contributions towards the manuscript, together with extended sections on the creation, analysis, and discussion

[1] Equal contributions

of the "cohort-specific" dataset are presented in Chapter 7. The original manuscript and supplementary material are reproduced in Appendices A.3 and A.4, respectively.

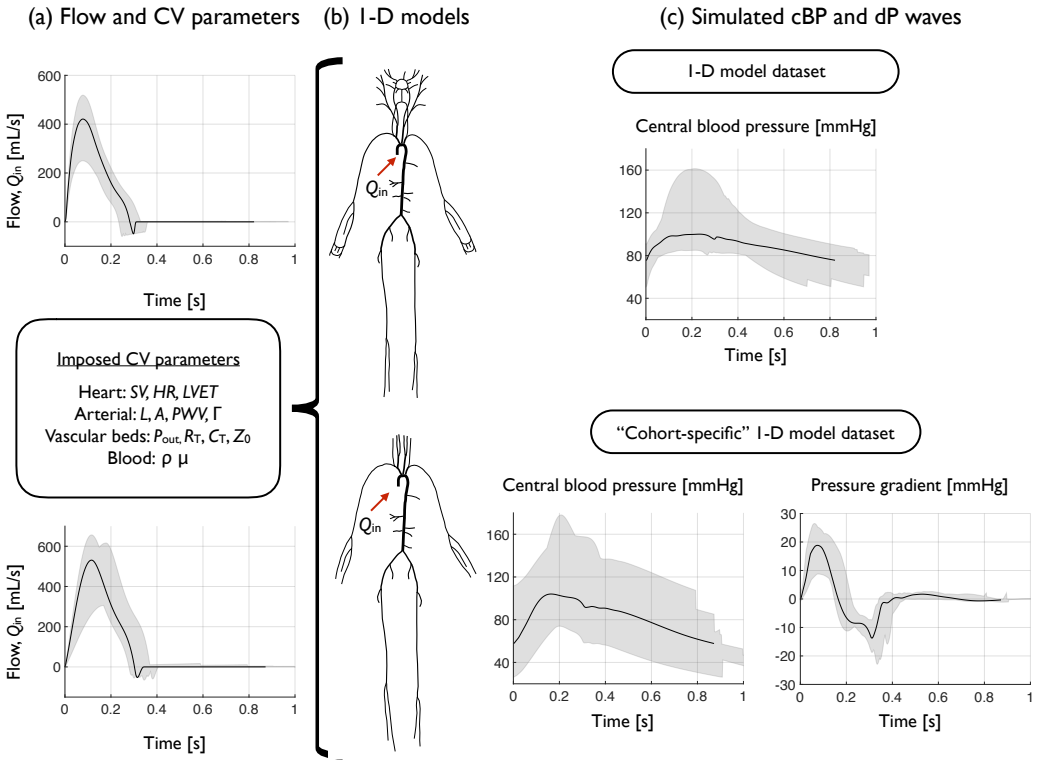

FIGURE 4.3: Creating 1-D model datasets of virtual subjects. (a), top and bottom; inflow waves for the 1-D model dataset and the "cohort-specific" 1-D model dataset, respectively. The thick line illustrates the flow wave corresponding to the baseline values of SV and HR, and the shaded region represents the range of flow waves corresponding to all SV and HR variations. (a), middle; a range of CV parameter values was obtained either from the clinical literature for healthy individuals (see [3]) or from the characteristics of the DCM cohort (see Table 4.1). (b) two 1-D models containing 116 (top) and 55 (bottom) arterial segments were used to generate BP waves. (c) Central blood pressure (top) and pressure gradient (bottom) waves: the thick line illustrates the waves corresponding to the baseline set of parameter variations, and the shaded regions represent the range of waves within each dataset.

Similarly to the 0-D datasets, the 1-D datasets present a series of 'steps' in the virtual cBP waves which correspond to a discrete distribution of HR variations.

4.1.3 Physiological cBP filters from clinical datasets

To ensure that the simulated cBP waves in the previous datasets of virtual subjects were within physiological ranges, filters based on BP values from the 'Hypertensive' and 'Normotensive' datasets (Table 4.1) were applied. Maximum values of central systolic BP (cSBP) and central pulse pressure (cPP) were obtained from the 'Hypertensive' dataset. Minimum values of central diastolic BP (cDBP) and cPP were obtained from

the 'Normotensive' dataset. Consequently, subjects with cSBP > 220 mmHg, cDBP < 44 mmHg, and cPP < 18 mmHg or > 109 mmHg were excluded. No subjects were excluded from the two-element Windkessel dataset; 43 subjects were excluded from the three-element Windkessel dataset; and 310 subjects were excluded from the 1-D model dataset. These filters were not applied to the "cohort-specific" 1-D dataset, since studying CV parameters and BP values in both healthy controls and in DCM patients was of interest.

4.2 Clinical datasets

Three clinical datasets were used for the validation of the cBP estimation algorithms. The 'Aortic Coarctation' dataset contained invasive cBP measurements from aortic coarctation patients obtained via cardiac catheterisation. The 'Normotensive' and 'Hypertensive' datasets contained non-invasive cBP estimates from the widely used SphygmoCor® (AtCor, West Ryde, Australia) device. cBP and aortic flow waves for each dataset are shown in Figure 4.4.

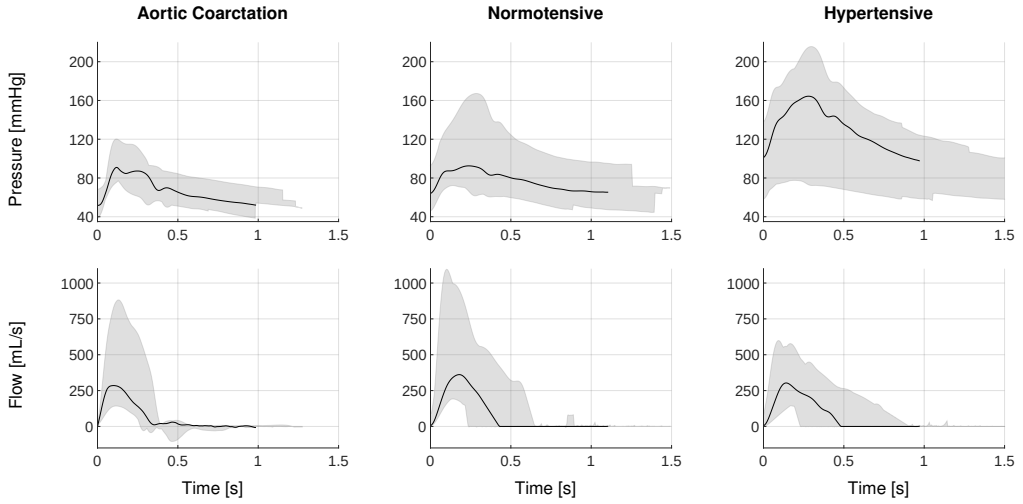

FIGURE 4.4: Blood pressure (top) and flow (bottom) waves for the clinical datasets. cBP waves were obtained invasively for the Aortic Coarctation dataset (left), and non-invasively for the Normotensive and Hypertensive datasets (middle and right, respectively). Aortic flow waves were obtained via 2-D phase contrast MRI for the Aortic Coarctation dataset, and via continuous wave Doppler ultrasound for the Normotensive and Hypertensive datasets. Black lines illustrate a random patient's cBP or aortic flow wave. Shaded regions represent the range of cBP or aortic flow waves within each dataset.

4.2.1 Aortic Coarctation

The 'Aortic Coarctation' dataset contains data acquired from 10 patients with aortic coarctation. Inclusion criteria comprised native (5) or repaired (5) aortic coarctation. According to the coarctation index (CI), calculated as the ratio of the coarctation minimum diameter to the descending aorta maximum diameter, four of these patients presented risk of recurrent coarctation (CI < 0.7 [103, 104]). These coarctations may present local differences in aortic wall properties due to the aortic narrowing or to the surgical procedure. However, these differences were not deemed significant enough for modelling purposes to motivate exclusion. Exclusion criteria were the presence of stented aortic coarctation or aortic dissection. These two clinical scenarios were expected to introduce more significant differences in aortic wall properties: stents create discontinuities in wall properties and dissections present complex geometries (*i.e.* two parallel vessels with different flows and wall properties) which the 1-D model used in this work does not currently account for.

The 'Aortic Coarctation' dataset has been used in several studies to assess methods for the estimation of the pressure gradient, artery wall stiffness, and pulse wave velocity. Brown *et al.* used the data from one patient to compare the accuracy and computational cost of three 3-D computational fluid methodologies to estimate blood pressure and flow waves [105]. Barber *et al.* used the data from six patients to estimate aortic distensibility and pulse wave velocity [106]. Bertoglio *et al.* used the data from another patient to estimate artery wall stiffness combining a data assimilation method and a 3-D computational model [107]. Sotelo *et al.* used data from seven patients to assess the accuracy of non-invasive aortic pressure gradient estimates using 3-D computational models [108]. Urbina *et al.* used data from 10 healthy volunteers and from two patients to design MRI-compatible aortic phantoms simulating normal and aortic coarctation conditions, and to compare their haemodynamics to those of volunteers and patients [109]. Finally, Shi *et al.* used data from 14 patients to validate a non-invasive aortic pressure gradient estimation method with a lower computational cost than previous methods [110].

4.2.1.1 Data acquisition

The clinical data acquisition was performed in a hybrid magnetic resonance/X-ray suite guidance system. MRI data was obtained from a 1.5-T cylindrical bore MR scanner

(Philips Intera, Philips, Best, The Netherlands). MRI data acquisition consisted of a breath-hold 3-D contrast-enhanced angiography of the upper-thoracic aorta (used to obtain aortic geometry measurements); and time-resolved, free-breathing 2-D phase contrast MRI flow velocity through-plane scans at the ascending aorta and at the descending aorta (used to obtain flow waves at both locations).

Invasive BP data were obtained using X-ray cardiac catheterisation (Philips BV Pulsera). Measurements were obtained simultaneously at the aortic root and at the abdominal aorta, right after flow acquisition, using multi-purpose catheters (angiographic catheter 4F with carbon dioxide-filled balloon). A breath-hold was performed to register the catheter pressures with a 1 kHz sampling rate over 20-50 heart cycles. A detailed description of the data acquisition process can be found in [110].

4.2.1.2 Data post-processing

The geometry of the aorta and supra-aortic arteries was segmented from the angiography data using an in-house prototype software being developed by Philips Healthcare (a detailed description can be found in [6]). User input was required to select the aortic inlet and outlet, and the outlet of each supra-aortic artery. Automatic centreline tracking was performed using a vesselness filter [111] to detect each artery, followed by a bi-directional fast marching algorithm to find the minimal path [112]. The centreline was then centred and smoothed using an active contour – an energy minimizing, deformable spline – and resampled at equidistant locations. Arterial lumen contours were calculated at each location based on the maximum intensity gradient [113]. Aortic and supra-aortic centrelines were merged, and intersecting contours were removed to avoid arterial volume duplication. In some cases, manual adjustment was required to correct for data inaccuracies, such as the variation of lumen voxel intensity or poor intensity gradients at the arterial wall. The segmentation process is shown for an Aortic Coarctation patient in Figure 4.5.

Through-plane blood velocity and luminal area were extracted from 2-D phase contrast MRI data for each time frame at the user-defined locations in the ascending and descending aorta using the in-house software, too. Velocity and area were extracted by propagating the segmentation of the arterial lumen throughout the cardiac cycle. Time-resolved volumetric blood flow waves were then calculated at each arterial location via

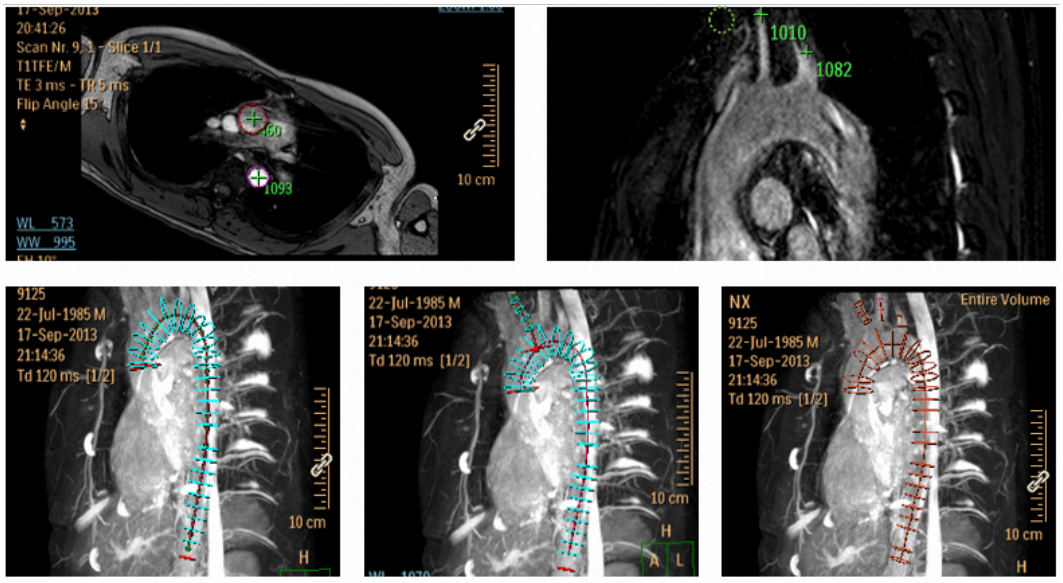

FIGURE 4.5: Segmentation of the upper-thoracic aorta using an in-house software. Top, left: two seed points are placed on different 2-D phase contrast images to indicate the location of the start and end points of the aortic centreline; top, right: multiplanar reconstruction is used to indicate the location of the end point of the supra-aortic centrelines; bottom, left: the aortic centreline is generated; bottom, middle: the supra-aortic centrelines are connected to the aortic centreline; bottom, right: the segmentation is complete.

integration of the velocity over the area for each time frame. The flow waves were filtered as follows:

- the wave was upsampled via spline interpolation to ensure a cycle length ≥ 100 datapoints;
- a Savitzky-Golay polynomial smoothing filter (polynomial order = 4, window length = 21 points) was applied to eliminate signal noise (*i.e.* high frequencies);
- and the resulting wave was analysed to identify the start of systole and shifted accordingly if required.

The post-processing of the flow data from a patient is shown in Figure 4.6, top.

Raw pressure data obtained via cardiac catheterisation was sampled at 1 kHz over 20-50 cardiac cycles. The ensemble average pressure wave was calculated for each patient and aortic location following these steps:

- a Savitzky-Golay polynomial smoothing filter (polynomial order = 2, window length = 83 points) was applied to the raw data to eliminate signal noise;

- periodic waves were identified using a feet detection algorithm [91];
- waves whose cardiac period was 25% shorter or longer than the median period were removed;
- remaining waves were truncated to the shortest period;
- and the ensemble average of these waves was calculated.

The post-processing of the pressure data from a patient is shown in Figure 4.6, bottom.

Since pressure and flow waves were measured at different times and using different techniques, the period of the post-processed waves does not coincide. Thus, the cardiac period was extracted from the corresponding aortic root flow wave for each patient. A visual check was performed for each flow and pressure wave, but no manual correction was required.

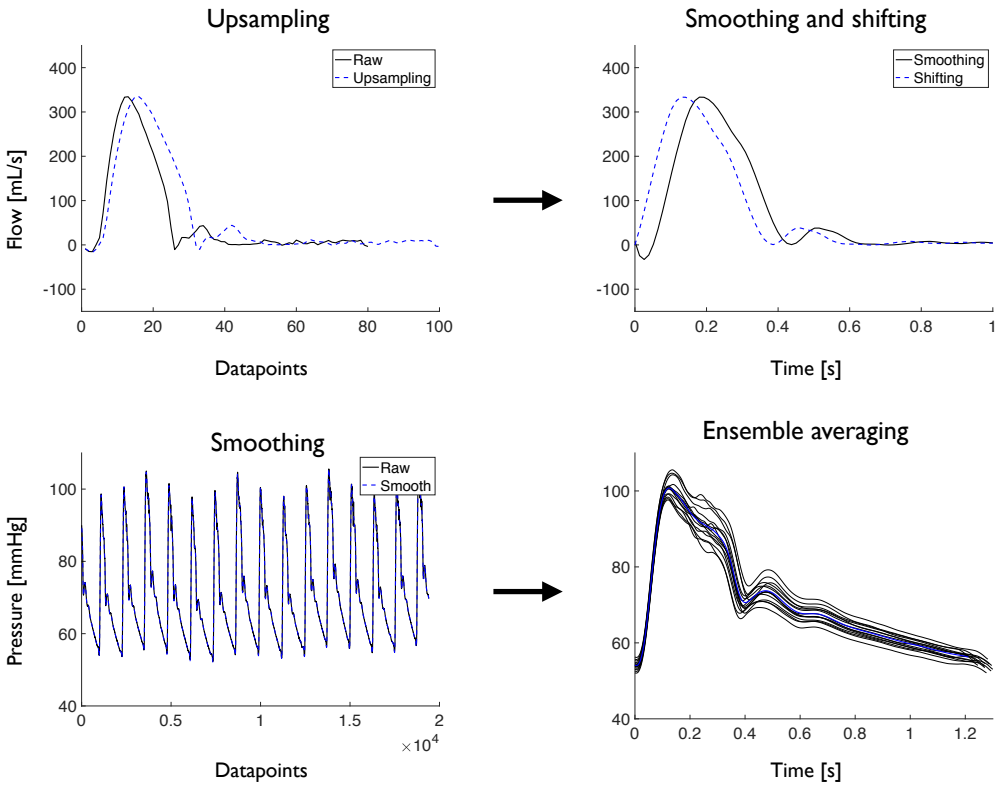

FIGURE 4.6: Post-processing flow (top) and pressure (bottom) data for the Aortic Coarctation dataset for a random patient. Top, left: upsampling using a spline interpolation to ensure a minimum cycle length of 100 datapoints; top, right: smoothing via the Savitzky-Golay filter and shifting the start of systole; bottom, left: smoothing multiple cycles via the Savitzky-Golay filter; bottom, right: ensemble averaging of similar cycles.

4.2.2 Normotensive and Hypertensive

The 'Normotensive' and 'Hypertensive' datasets were obtained from [114]: (i) 13 normotensive healthy volunteers at baseline and after the administration of different doses of four drugs with different inotropic and vasoactive properties (dobutamine, norepinephrine, phentolamine, and nitroglycerin); and (ii) 158 subjects assessed for hypertension (those found to be normotensive are included, too). Inotropic drugs increase or decrease the force of cardiac contractions; vasoactive drugs increase (vasodilation) or decrease (vasoconstriction) the arterial lumen diameter. The 'Normotensive' and 'Hypertensive' datasets have been used in several studies to identify the main cardiovascular determinants of increased central pulse pressure in hypertension. Fok *et al.* showed that increased central pulse pressure during inotropic and vasopressor stimulation, and in essential hypertension is mainly due to the forward component of the pressure wave [114]. Li *et al.* showed that the backward component of the pressure wave has little effect on the increased central pulse pressure during inotropic and vasomotor stimulation, and in essential hypertension [115]. Finally, Vennin *et al.* found that arterial stiffness and ventricular ejection (flow and volume) are the most important determinants of increased central pulse pressure in hypertension [116].

Although half of the subjects in the 'Hypertensive' dataset were on treatment, subjects found to be normotensive were not necessarily on treatment, as this information was not available. In fact, this dataset is made up of "those [subjects] evaluated for hypertension". From the modelling perspective, given that the estimates from the 0-D algorithms are independent of health or disease, and given that clinical data acquisition was similar for those subjects from the 'Hypertensive' and 'Normotensive' datasets, it would have been possible to group subjects in other ways. Depending on the clinical question, different groupings are possible: hypertensives vs normotensives, young vs old, males vs females, or a single group containing all subjects. In this case, the decision of grouping patients into the 'Normotensive' and 'Hypertensive' datasets was taken for consistency with previous studies using the same datasets.

4.2.2.1 Data acquisition

Aortic root velocity time integral (VTI) was acquired using continuous wave Doppler obtained in the apical 5-chamber view using the Vivid-7® ultrasound platform (General

Electric Healthcare, Pollards Wood, United Kingdom). The cross-sectional area of the aortic valve was obtained in the parasternal long-axis view.

Carotid and radial pressure waves were acquired non-invasively by applanation tonometry using the SphygmoCor device, which uses a transfer function to calculate cBP from the carotid pressure waves. The ensemble average of approximately 10 cardiac cycles for each carotid pressure wave was used as input to the SphygmoCor device to obtain cBP. A detailed description of the data acquisition process can be found in [114].

4.2.2.2 Data post-processing

VTI data was acquired during at least three cardiac cycles for all subjects. The original data files contained three columns: time, raw VTI waves, and filtered VTI waves. Filtered VTI waves were generated from raw VTI waves by setting any VTI values under a certain threshold to 0 in order to eliminate noise during diastole. The filtered VTI waves were further post-processed as follows:

- the start of each cardiac cycle was detected;
- the ensemble average was calculated for $\geq$ three cycles;
- the diastolic portion of the ensemble was set to zero;
- the resulting VTI wave was analysed to identify the start of systole, shifted accordingly if required, and multiplied by the cross-sectional area of the aortic valve to obtain aortic flow.

The post-processing of the flow data from a volunteer is shown in Figure 4.7.

Carotid pressure data obtained via the SphygmoCor device was acquired at 128 Hz over approximately 10 cardiac cycles. For each subject, the ensemble average carotid pressure wave was calculated automatically and used as input to the SphygmoCor transfer function to obtain an estimate of cBP, as shown in Figure 4.8. The pressure waves did not require further modifications.

Since pressure and flow waves were measured at different times and using different techniques, the period of the post-processed waves does not coincide. Thus, the cardiac period was extracted from the corresponding aortic root flow wave for each patient. A

visual check was performed for each flow and pressure wave, but no manual correction was required.

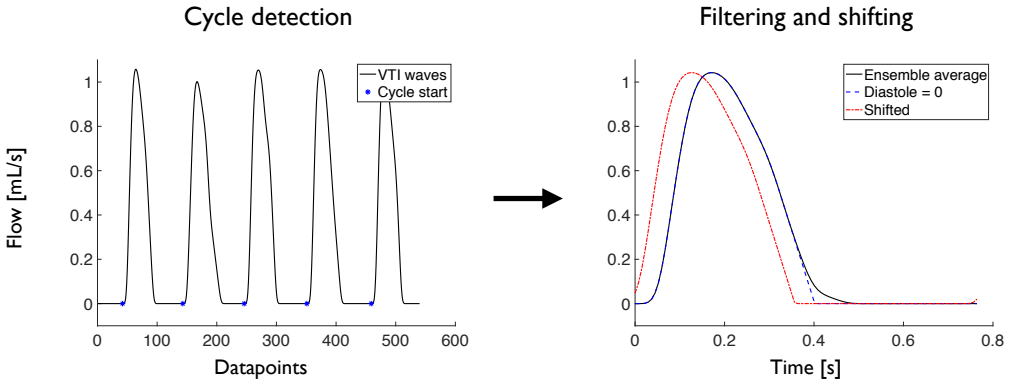

FIGURE 4.7: Post-processing flow data for the Normotensive and Hypertensive datasets. Left: the start of each cycle is identified to calculate an ensemble average VTI wave; right: the value of the VTI wave during diastole is set to zero and the resulting wave is shifted so that the first datapoint coincides with the start of systole.

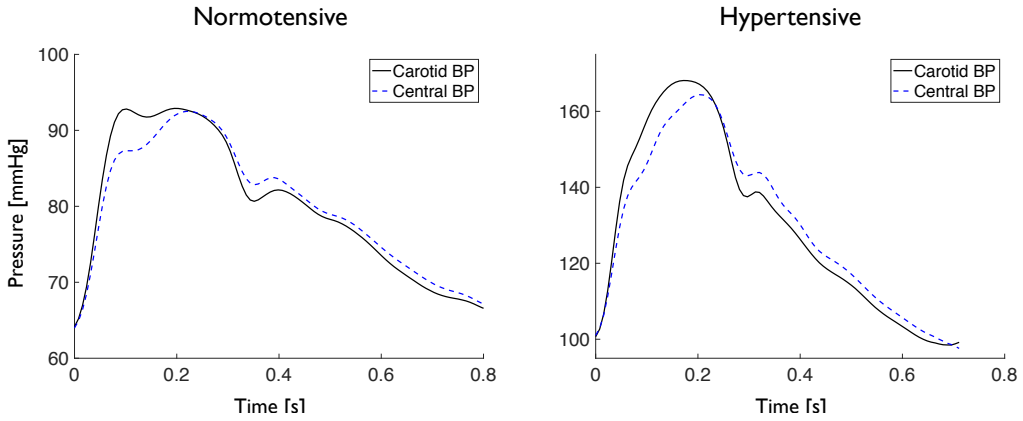

FIGURE 4.8: Estimation of central blood pressure (dashed blue line) from carotid blood pressure (black line) using the SphygmoCor device. Left: pressure data for a random patient from the Normotensive dataset; right: pressure data for a random patient from the Hypertensive dataset.

4.3 Justification for the choice of clinical scenarios

The choice of clinical scenarios presented in this chapter (i.e. aortic coarctation, hypertension, dilated cardiomyopathy, and disease-free) was partly driven by data availability. However, from the modelling and clinial perspectives, this choice can be justified by several reasons which will be discussed in turn.

Firstly, the 'Aortic Coarctation' dataset allowed both the 0-D and 1-D algorithms to be tested since it contained MRI data of aortic geometry and flow (required to run

the 1-D algorithm). This dataset included invasive measurements of cBP, which were necessary to validate all algorithms *in vivo*, and it allowed algorithm testing in patients with tortuous aortic geometries. The heart of aortic coarctation patients must pump harder as a consequence of an increased afterload, so a regular assessment of cBP would be beneficial.

Secondly, the 'Normotensive' and 'Hypertensive' datasets allowed the 0-D algorithms to be tested since they contained ultrasound aortic flow data. Since these datasets contained cBP data from a large number of volunteers and patients, a wide range of non-invasive cBP wave morphologies (representative of both health and disease) was available. Similarly to aortic coarctation patients, hypertensives would benefit from a central rather than brachial assessment of blood pressure.

Finally, the 'Dilated Cardiomyopathy' dataset allowed the use of the 1-D algorithm since it contained sufficient MRI data of aortic geometry and flow. Instead of cBP measurements, this dataset contained non-invasive measurements of the aortic pressure gradient between the aortic root and the diaphragm. This dataset allowed the study of how the aortic pressure gradient can help to differentiate between healthy and unhealthy subjects with normal aortic geometries. Furthermore, patients suffering from DCM or other cardiac diseases would also benefit from a non-invasive assessment of cBP, which is related to relevant cardiac metrics such as left-ventricular pressure, afterload, and myocardial stress.

4.4 Final remarks

This has described the datasets of virtual and clinical subjects which will be used in the following chapters. The 0-D and 1-D datasets will be used in Chapter 5 to test and develop methods for cardiovascular parameter estimation. The 1-D dataset will also be used in Chapter 6 to assess algorithms for cBP estimation *in silico*. The "cohort-specific" 1-D dataset will be used in Chapter 7 to investigate ventricular-arterial haemodynamics in a dataset of dilated cardiomyopathy patients. Finally, the three clinical datasets will be used in Chapter 6 to assess and validate algorithms for cBP estimation *in vivo*.

5 Cardiovascular Parameter Estimation

In this chapter, (i) a comprehensive literature review of current cardiovascular parameter estimation methods is presented; (ii) the development of new methods is described; (iii) and the performance of every method is assessed using three datasets of virtual subjects (described in Chapter 4) to identify optimal methods to estimate each cardiovascular parameter.

5.1 Introduction

Cardiovascular (CV) parameters can be used to assess CV function from non-invasive data available in the clinic. The clinical relevance of the CV parameters used in this work is described next.

Left ventricular ejection time ($LVET$) is the period during which blood is ejected from the left ventricle across the aortic valve and into the aorta, and coincides with the duration of systole. $LVET$ is influenced by CV parameters such as heart rate, stroke volume, preload or afterload, and by inotropic drugs, and is a valuable metric of left ventricular performance both in health and disease [117].

The asymptotic pressure (P_{out}) is sometimes defined as the asymptotic value of the blood pressure wave if the heart stopped beating [118], or as the pressure at which flow to the microcirculation ceases [75]. Regardless of its definition, the physiological meaning and range of values of P_{out} are still not fully understood [119]. According to some studies, P_{out} is related to capillary and venous pressure [120], though others argue this pressure is larger than the venous pressure due to the waterfall effect [121–123].

Arterial resistance (R_{T}) is the resistance to flow which the heart needs to overcome to transport blood through the systemic arteries into the capillaries. In his book entitled *Haemastaticks* (1733), the Reverend Stephen Hales (1677-1761) was the first to show experimentally that most of this resistance is offered by the smallest blood vessels (arterioles and capillaries) [124]. In 1846, Poiseuille (1799-1869) was the first to obtain accurate experimental results which indicated that there is a relationship between the pressure gradient (ΔP), flow (Q), tube length (L), and the fourth power of the tube's internal radius (r). This was later derived from first principles independently by Wiedemann (1856) and Hagenbach (1860) into the mathematical expression known as the Hagen-Poiseuille equation:

$$Q = \frac{\pi r^4 \Delta P}{8\mu L}, \tag{5.1}$$

where μ is the dynamic viscosity of the fluid. It can be shown from first principles that R_{T} for any arterial segment is given as:

$$R_{\mathrm{T}} = \frac{\Delta P}{Q} = \frac{8\mu L}{\pi r^4}. \tag{5.2}$$

However, the right-hand side of Equation (5.2) requires the dimensions of every vessel down to the capillaries, which is unfeasible. Instead, R_{T} can be approximated using the middle term of Equation (5.2), with $\Delta P = MBP - P_{\mathrm{out}}$ and $Q = \overline{Q}$, where MBP and $\overline{Q}$ represent the mean pressure and flow, respectively, measured at the aortic root. Due to this relationship between arterial resistance and radius, small vessels exposed to high blood pressure can constrict to increase R_{T} to deliver steady flow to the capillary beds in the terminal organs [125, 126].

Arterial compliance (C_{T}) is the property of arteries which allows them to store blood by distending during systole and to release it during diastole to maintain diastolic flow [127]. Additionally, compliance is the inverse of arterial stiffness [124], which is also related to pulse wave velocity. Therefore, changes in C_{T} can have important effects on the pulse wave, left ventricular dynamics, cardiac output, and the ratio of systolic to diastolic flow into the capillary beds [128].

Pulse wave velocity (PWV) is the velocity of travel of pulse waves originating from the left ventricle. It is regarded as the 'gold standard' for the assessment of arterial

compliance, which is directly related to arterial stiffness, and has recently been proposed as a marker of cardiovascular risk [124].

Input impedance (Z) is defined as the ratio between P and Q measured simultaneously at the same arterial site [124], which is calculated for a given harmonic as

$$Z = \frac{|P|e^{\theta}}{|Q|}, \tag{5.3}$$

where $|Z| = |P|/|Q|$ and θ are the modulus and the phase, respectively. Characteristic impedance (Z_0) is a measurement of input impedance assuming that P and Q are not affected by wave reflections. However, since there are no physiological conditions where this is the case, this measurement will always be influenced by wave reflections arriving at the measurement site. Furthermore, Z_0 is directly and linearly related to PWV as [129]:

$$Z_0 = \frac{PWV\rho}{A}, \tag{5.4}$$

where ρ is the blood density and A is the arterial cross-sectional area. Thus, aortic PWV and aortic Z_0 are directly related to aortic stiffness, and are independent predictors of CV risk [102, 116, 130, 131].

The main objective of this study was to identify optimal methods to estimate CV parameters using three datasets of virtual subjects whose reference CV parameter values could be obtained free of measurement errors (see Chapter 4). These optimal methods were then used as inputs to computational models of the circulation to estimate cBP (see Chapter 6). The rationale behind this study was that using the most accurate CV parameter estimation methods should lead to the most accurate cBP estimates.

5.2 Methods

The following CV parameters were required as inputs to at least one of the cBP estimation algorithms: left ventricular ejection time ($LVET$), outflow vascular pressure (P_{out}), total arterial resistance (R_{T}) and compliance (C_{T}), aortic pulse wave velocity (PWV), and aortic characteristic impedance (Z_0).

A comprehensive literature review of CV parameter estimation methods was performed. Although the Preferred Reporting Items for Systematic Reviews and Meta-Analyses (PRISMA) [132, 133] approach is considered the model of best practice, this literature review belongs to this thesis' earliest work and did not follow strict search criteria. Articles were primarily found using Google Scholar, KCL's Library Search, and Google (UK), but articles from other sources were also included (often identified from the references of articles, and through discussions with colleagues). The main search terms included different combinations of the terms "cardiovascular", "parameters/properties" and "estimation/measurement" with the names of the cardiovascular parameters under study (e.g. "left ventricular ejection time", "outflow vascular pressure"). The methods listed in Table 5.1 were implemented and assessed in this study. To be included, they had to satisfy at least one of the following inclusion criteria: they were reported as the optimal method [72, 134–138]; their performance was similar to that of the optimal method [72, 134, 138–140]; they were the only reported method [84, 85, 91, 99, 129, 130, 141–154]; or their performance had not been sufficiently assessed due to their novelty [91, 147, 148]. Furthermore, each time a gap was identified upon implementing and assessing the previous methods, new, improved methods were developed. All CV parameter estimation methods used in this study are described next. Novel methods are marked with an asterisk in the title.

5.2.1 LV - Left ventricular ejection time, LVET

LV1 - dP/dt analysis, 1*

A peripheral pressure wave, P, is analysed from the time of peak pressure to 80% of the duration of the cardiac cycle, T (Figure 5.1). The points at which dP/dt is equal to zero are identified. If such intersection points exist, $LVET$ corresponds to the last of these points. Otherwise, a tangent to P at the point of maximum negative dP/dt is projected. $LVET$ corresponds to the first point where the value of the tangent is $\leq DBP$.

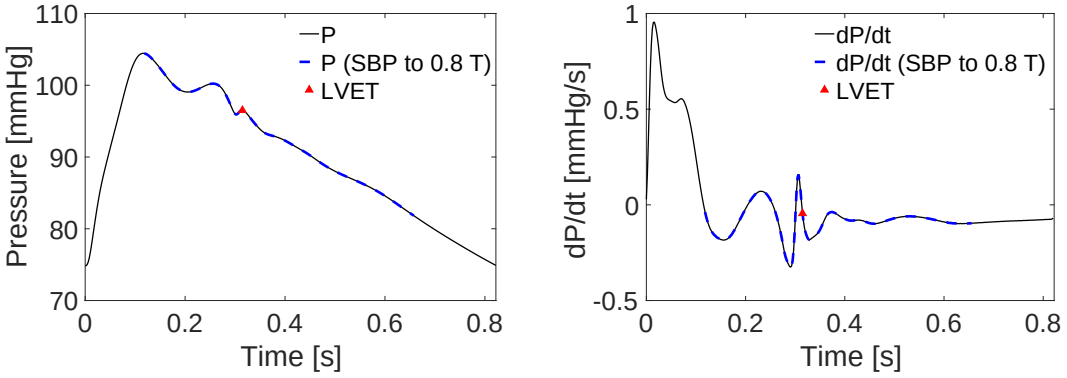

FIGURE 5.1: Novel method to estimate $LVET$ from a peripheral pressure wave, P. P (left) and dP/dt (right) with time. Values from peak pressure to $0.8T$ are highlighted in dashed lines. $LVET$ corresponds to the time of the last intersection point between dP/dt and the x-axis (red triangle).

LV2 - dP/dt analysis, 2

This method is described in [148]. $LVET$ coincides with the minimum of

$$\frac{dP}{dt}\left(0.5 - \left|0.5 - \frac{HR \cdot t}{60}\right|\right)^2, \tag{5.5}$$

where P is a peripheral pressure wave and HR represents the heart rate in bpm.

LV3 - $0.37\sqrt{T}$

$LVET$ is calculated using the empirical relationship described in [149]: $0.37\sqrt{T}$, where T is the duration of the cardiac cycle in seconds.

LV4 - Q analysis*

Q is analysed from the global minimum after peak flow to 50% of T (Figure 5.2). If all Q values are smaller than 1% of maximum Q, $LVET$ corresponds to the time of the global minimum. Otherwise, starting from the time of the global minimum, all sign changes (from negative to positive), all maxima, and all zero values are found. $LVET$ corresponds to either the first sign change, the first local maximum, or the first zero value (whichever one occurs first). If all else fails, method LV3 is used.

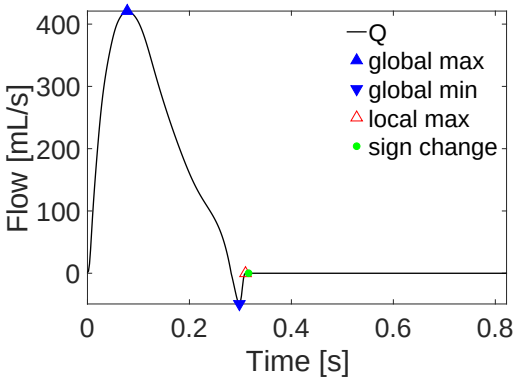

FIGURE 5.2: Novel method to estimate $LVET$ from the aortic flow wave, Q. $LVET$ corresponds to the time of the first sign change (green circle), which occurs earlier than the local maximum (red triangle).

5.2.2 OP - Outflow pressure

OP1 - Diastolic decay fit, 1

The concept of a diastolic decay fit was first described in [84]. P is analysed between $LVET$ and the end of diastole (P_d). The multidimensional unconstrained nonlinear minimisation (Nelder-Mead) MATLAB® function *fminsearch* is used to find the best fit between P_d and an exponential decay curve of the form: $P_\mathrm{exp} = P_\mathrm{out} + (P_\mathrm{exp}(t_0) - P_\mathrm{out})e^{-(t-t_0)/\tau}$, where $t_0 = LVET$. To avoid non-physiological values of P_out, the following filters are applied: if $\tau < 0$ or $P_\mathrm{out} < 0$, P_out is set to 0; and if $P_\mathrm{out} \geq 0.75DBP$, P_out is set to $0.5DBP$.

OP2 - Diastolic decay fit, 2

Similarly to OP1, but using $t_0 = \frac{2}{3}LVET + \frac{1}{3}T$ instead, as described in [99].

OP3 - 50% of DBP*

P_out is estimated as 50% of DBP.

OP4 - 70% of DBP

As suggested by Parragh *et al.* P_out is estimated as 70% of DBP [119].

5.2.3 AR - Arterial resistance

AR1 - Peripheral pressure waveform

R_{T} is calculated using Equation (5.12) and MBP is calculated as the mean of P.

AR2 - Peripheral DBP and SBP values

Similarly to AR1, but using $MBP = DBP + 0.4PP$ instead, as described in [137].

5.2.4 AC - Arterial compliance

AC1 - 2-point diastolic decay

The concept of a diastolic decay fit was first described in [84]. Using only the first and last points of the diastolic part of P, C_{T} is calculated as:

$$\frac{T - LVET}{\ln(\frac{P(LVET) - P_{\mathrm{out}}}{DBP - P_{\mathrm{out}}})R_{\mathrm{T}}}. \tag{5.6}$$

AC2 - Diastolic decay fit, 1

Given that $\tau = (R_{\mathrm{T}} - Z_0)C_{\mathrm{T}}$ (for the three-element Windkessel model), OP1 can be used to calculate τ, and rearranging:

$$C_{\mathrm{T}} = \frac{\tau}{R_{\mathrm{T}} - Z_0}. \tag{5.7}$$

If τ is negative then P_{out} is set to 0 and τ is recalculated.

AC3 - Diastolic decay fit, 2

Similarly to AC2, but using $t_0 = \frac{2}{3}LVET + \frac{1}{3}T$ instead, as described in [99].

AC4 - Area method

This method is described in [150]. C_{T} is calculated as:

$$\frac{\int_{t_1}^{t_2}(P - P_{\mathrm{out}})dt}{R_{\mathrm{T}}(P(t_1) - P(t_2))}, \tag{5.8}$$

where t_1 and t_2 are equal to $\frac{2}{3}LVET + \frac{1}{3}T$ and 90% of T, respectively.

AC5 - Two-area method

This method is described in [151]. C_{T} is calculated by solving two simultaneous equations of the form:

$$\int_{t_1}^{t_2} Qdt - \frac{1}{R_{\mathrm{T}}}\int_{t_1}^{t_2}(P - P_{\mathrm{out}})dt = C_{\mathrm{T}}(P(t_1) - P(t_2)), \tag{5.9}$$

from the start of the cycle to $LVET$, and from $LVET$ to T.

AC6 - Diastolic blood pressure method*

C_{T} is calculated by minimising the relative error, $DBP_{\mathrm{err}} = (DBP_{\mathrm{est}} - DBP_{\mathrm{ref}})/DBP_{\mathrm{ref}}$, between the estimated (DBP_{est}) and reference (DBP_{ref}) values of DBP, as seen in Figure 5.3. For each iteration, j, DBP_{est} is calculated as the minimum of the estimated pressure, P_{est}, using the three-element Windkessel model (Equation (3.4)). The initial conditions are $C_{\mathrm{T},0} = SV/PP$ and $P_0 = DBP_{\mathrm{ref}}$. While $DBP_{\mathrm{err}} > 1\%$, $C_{\mathrm{T,j}} = C_{\mathrm{T,j-1}}/(1 + DBP_{\mathrm{err}})^2$. C_{T} corresponds to the value of $C_{\mathrm{T,j}}$ when $DBP_{\mathrm{err}} < 1\%$.

AC7 - Pulse pressure method

This method is described in [135]. Similarly to AC6, but minimising the relative PP error, PP_{err}, instead.

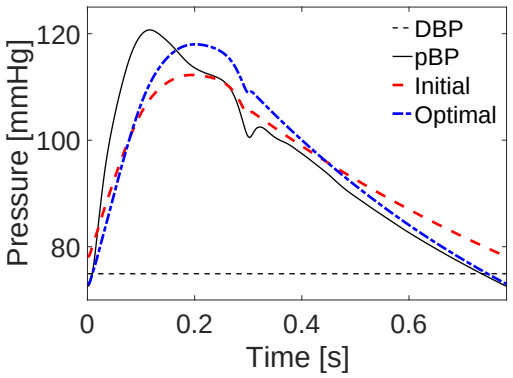

FIGURE 5.3: Novel iterative method to estimate C_{T} from the aortic flow and peripheral pressure (pBP) waves. C_{T} estimates are calculated by minimising the relative error between the estimated and reference values of DBP. The latter is obtained from the pBP wave (black line). The pressure waves corresponding to the initial and optimal estimates of C_{T} are shown in red and blue lines, respectively. The black dashed line indicates the value of DBP extracted from the cBP wave.

AC8 - Stroke volume over pulse pressure

This method is described in [140]. C_{T} corresponds to SV/PP.

AC9 - Three-element Windkessel optimisation*

This method is described in A.1. The initial value of C_{T} is calculated using AC8.

5.2.5 PV - Pulse wave velocity

The foot-to-foot (PV1 and PV2) and least-squares (PV3 and PV4) methods used here are described in [91]. Both methods require the measurement of two pulse waves at both ends of a given arterial path of length L. The foot-to-foot method focuses on detecting the 'feet' (*i.e.* minimum value) of both pulse waves to calculate the transit time (TT) between them. For each pulse wave, the 'foot' is detected as the intersection between a horizontal projection of the minimum value and a projection of the maximum slope of the systolic upstroke.

The least-squares method calculates the sum of the squared differences between the systolic upstroke of both waveforms multiple times, by fixing one wave and shifting the other one by one datapoint at a time. The temporal shift which minimises the squared

differences is used to estimate TT. For both methods, PWV is then calculated as $PWV = L/TT$.

PV1 - Foot-to-foot: aortic flow

The inputs are two non-invasive flow waveforms at the ascending and descending aorta.

PV2 - Foot-to-foot: carotid-femoral pressures

The inputs are two non-invasive pressure waveforms at the carotid and femoral arteries.

PV3 - Least-squares: aortic flow

The inputs are two non-invasive flow waveforms at the ascending and descending aorta.

PV4 - Least-squares: carotid-femoral pressures

The inputs are two non-invasive pressure waveforms at the carotid and femoral arteries.

PV5 - Sum of squares

This method has been adapted from the original one described in [153]. PWV is calculated from the peripheral pressure, P, and aortic flow, Q waves using

$$PWV = \frac{1}{\rho A}\sqrt{\frac{\sum dP^2}{\sum dQ^2}}, \tag{5.10}$$

where ρ is the blood density, A is the cross-sectional area at the aortic root, dP and dQ are differences in P and Q, respectively, between two adjacent time points, and the sums extend over a cardiac cycle. P and Q do not need to be aligned in time.

5.2.6 Z - Aortic characteristic impedance

Methods Z1 and Z2 are sensitive to temporal mis-alignments between P and Q, so the following restrictions were applied to account for waves which were not recorded simultaneously and/or at the same site: (i) P is shifted so that its value at the start of the cycle coincides with DBP, and (ii) Q is shifted so that its value at the start of the cycle is as close as possible to the intersection between the x-axis and the tangent of Q at the time of maximum dQ/dt in early systole.

Z1 - Frequency methods

Frequency domain methods to estimate characteristic impedance (Z_0) are based on the Fourier analysis of P and Q extracted simultaneously at the ascending aorta. Z_0 is usually estimated as the average impedance modulus over a range of frequencies where fluctuations – due to wave reflections – above and below the characteristic impedance value are expected to cancel each other out. The following harmonic ranges, extracted from the literature, have been assessed in this study: 2-12th [130], 6-10th [145], 1-8th [143], 1-9th [134], 2-10th [144], 3-10th [146], 4-10th [141], 6-8th [142], and 4-8th harmonics [138]. These methods, in their original form, require P and Q measured simultaneously at the ascending aorta. However, for the proposed algorithms, a peripheral P measurement is used instead.

Z2 - P-Q loop methods

P-Q loop methods analyse the relationship between aortic P and Q during early systole, assuming that during this interval the effects of wave reflections are minimal [134, 139], and hence

$$Z_0 \simeq \frac{P(t) - DBP}{Q(t) - Q(0)}, \tag{5.11}$$

where $Q(0)$ is the value of Q at the start of the cycle (normally zero). In this study, four P-Q loop methods were assessed where Z_0 was estimated as:

I the mean value of Equation (5.11) between the start of the cycle and the time of maximum Q;

II the slope of the linear least squares fit to the ratio between P and Q between the start of the cycle and the time of maximum flow;

III the value of Equation (5.11) at the time of maximum dQ/dt in early systole; and

IV the mean value of Equation (5.11) between the start of the cycle and the time of maximum dQ/dt in early systole.

The best performing P-Q loop method, IV, was used to calculate the errors in Table 5.1.

These methods, in their original form, require P and Q measured simultaneously at the ascending aorta. However, for the proposed algorithms, a peripheral P measurement is used instead.

Z3 - 5% of R_{T}

As suggested by Murgo *et al.* Z_0 is estimated as 5% of R_{T} [154].

Z4 - Approximated aortic characteristics*

During early systole, wave reflections reaching the aortic root are assumed to be absent, and characteristic impedance can be estimated as $Z_0 = \Delta P/\Delta Q$, where ΔP and ΔQ are the changes in blood pressure and flow rate, respectively [146]. Peak flow, Q_{peak}, and the first systolic shoulder/peak, $P1$, occur at a similar time, so $\Delta Q = Q_{\mathrm{peak}}$ and $\Delta P = P1$, and therefore $Z_0 \simeq P1/Q_{\mathrm{peak}}$, as seen in Figure 5.4. Assuming that DBP and MBP remain constant within the large arteries, $P1$ is approximated as $MBP - DBP$ extracted from a peripheral P measurement. Hence, $Z_0 \simeq (MBP - DBP)/Q_{\mathrm{peak}}$.

Z5 - Aortic characteristics

This method is described in [129]. Assuming that the aortic radius is much larger than the aortic wall thickness, Z_0 corresponds to $\rho PWV/A$, where ρ is the blood density, PWV is the aortic pulse wave velocity, and A is the aortic-root cross-sectional area.

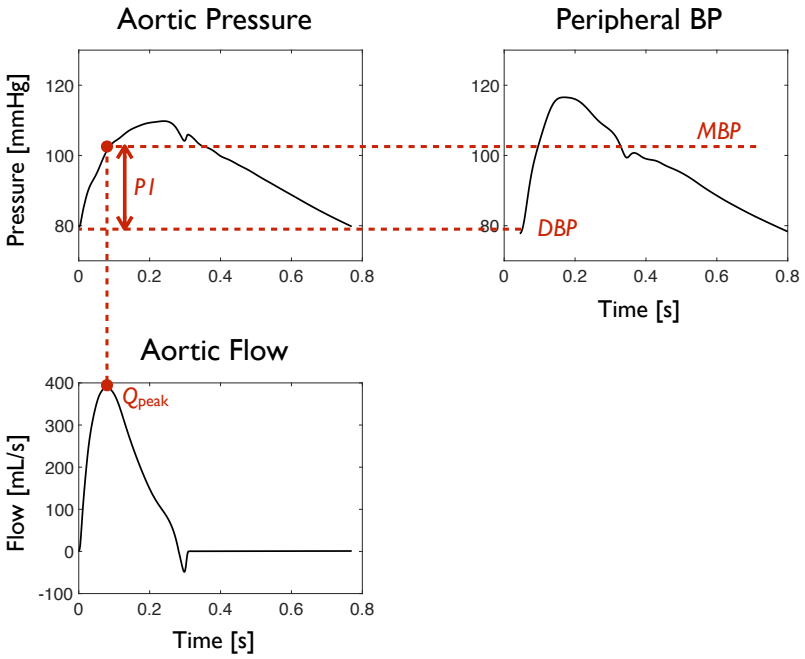

FIGURE 5.4: Novel method to estimate aortic characteristic impedance from the aortic flow and peripheral pressure waves. Pressure (top) and flow (bottom) waves at central (left) and peripheral (right) arterial locations for a subject from the 1-D dataset. The time of Q_{peak} and $P1$ is indicated by the vertical, red, dashed line. The value of $P1$ is approximated as $MBP - DBP$ calculated from the peripheral pressure wave.

Z6 - Three-element Windkessel optimisation*

This method is described in Appendix A.1. The initial values of C_{T} and Z_0 are calculated using the AC8 and Z3 methods, respectively.

5.2.7 Performance assessment of cardiovascular parameter estimation methods

The performance of the CV parameter estimation methods was assessed using the mean percentage error (MPE) and standard deviation (SD) between estimated and reference CV parameter values for the three datasets of virtual subjects (described in Chapter 4). Additionally, Bland-Altman plots [155] were created to show the bias (MPE) and limits of agreement ($\pm$ 1.96 SD from the bias) between the estimated and reference CV parameter values. For the 0-D datasets, reference values were obtained from the prescribed values used to create each virtual subject (Table 4.2). For the 1-D dataset, reference values for $LVET$ and P_{out} were obtained from the prescribed values. R_{T} was calculated from the

aortic root pressure and flow waveforms using [84]

$$R_{\mathrm{T}} = \frac{MBP - P_{\mathrm{out}}}{\overline{Q_{\mathrm{in}}}}, \tag{5.12}$$

where MBP is the mean blood pressure and $\overline{Q_{\mathrm{in}}}$ is the mean blood flow. C_{T} and Z_0 were extracted from aortic root pressure and flow waveforms using the optimised three-element Windkessel model described in A.1. Aortic root PWV was extracted using

$$PWV = \sqrt{\frac{2}{3\rho}\left[k_1 e^{(k_2 r)} + k_3\right]}, \tag{5.13}$$

where r is the aortic root radius at MBP, and k_1, k_2, and k_3 are empirical constants [81].

Two common clinical scenarios were considered when assessing CV parameter estimation: 'Scenario 1', where the carotid pressure waveform was available; and 'Scenario 2', where only brachial DBP and SBP values were available (Figure 6.1a). The three-element Windkessel and 1-D datasets of virtual subjects were used to determine, for each scenario and CV parameter, the optimal (*i.e.* smallest MPE and SD) CV parameter estimation methods to be used by the cBP algorithms described in Chapter 6. The two-element Windkessel dataset contained a smaller range of cBP values and wave shapes than the three-element Windkessel dataset. For this reason, and given that their mathematical formulations are very similar, the two-element Windkessel dataset was only used for a preliminary analysis, and was excluded from the final assessment. MPE and SD values for the three datasets are presented in Table 5.1.

5.3 Results

The last three columns of Table 5.1 show mean percentage errors (MPE) and standard deviation (SD) for all CV parameter estimation methods assessed using the three datasets of virtual subjects. Table 5.2 shows the methods that led to the smallest MPE for each scenario and dataset. For the 1-D dataset, MPE were reduced by at least 40% when using the carotid pressure waveform (Scenario 1) instead of brachial DBP and SBP values (Scenario 2). By using these optimal methods, all parameters from the 1-D dataset but Z_0 were estimated with MPE $< 6\%$ and $< 10\%$ for Scenario 1 and 2, respectively. Much larger errors were obtained for Z_0, especially in Scenario 2 (82%). All parameters from the three-element Windkessel dataset were estimated with MPE $< 2\%$ in both scenarios.

For the two-element Windkessel dataset, all parameters but C_{T} were estimated with MPE $< 0.2\%$ and $< 10\%$ for Scenario 1 and 2, respectively. Although MPE for C_{T} for Scenario 1 were $< 0.1\%$, they were much larger for Scenario 2 (36%).

Figures 5.5 and 5.6 show Bland-Altman plots for all CV parameters estimated using the optimal methods obtained from the two-element and three-element Windkessel datasets, respectively. Figure 5.7 shows Bland-Altman plots for all CV parameters estimated using the optimal methods obtained from the 1-D dataset.

Firstly, for the two-element Windkessel dataset, all parameters were estimated without any considerable bias in Scenario 1. In Scenario 2, only R_{T} and C_{T} showed a considerable bias, with a 5% underestimation and a 36% overestimation, respectively. The bias as a function of each CV parameter reference value remained approximately unchanged, with the exception of P_{out} in Scenario 2, whose bias decreased with increasing reference values.

Secondly, for the three-element Windkessel dataset, all parameters were estimated without any considerable bias in both scenarios. The bias as a function of the reference values of each CV parameter remained approximately unchanged, with the exception of P_{out} and Z_0 in Scenario 2, whose bias decreased with increasing reference values.

Finally, for the 1-D dataset, $LVET$, P_{out}, R_{T}, C_{T}, and PWV were estimated without any considerable bias of their corresponding reference mean values ($< 6\%$ for Scenario 1 and $< 10\%$ for Scenario 2), whereas Z_0 was overestimated with a much greater bias of its corresponding reference mean value (16% for Scenario 1 and 82% for Scenario 2). The bias as a function of the reference values of each CV parameter remained approximately unchanged, with the exceptions of P_{out} (which had a unique reference value), $LVET$ in Scenario 2 (whose bias increased with increasing reference values), and C_{T} in Scenario 2 (whose bias decreased with increasing reference values). The same optimal methods were identified for PWV in Scenario 1 and 2. These optimal methods were then used in the cBP estimation algorithms.

For each subject in the 0-D and 1-D datasets, all CV parameters were calculated in less than 1 second using a standard PC (less than 1 hour for the entire 0-D or 1-D datasets).

TABLE 5.1: Assessed CV parameter estimation methods. They were trialled using the 0-D and 1-D datasets in two clinical scenarios (Figure 6.1a). Scenario 1: carotid BP waveform available. Scenario 2: only brachial DBP and SBP values available. Errors are presented as the mean ± standard deviation of the percentage error between estimated and reference CV parameter values. †New methods. *Pressure at the carotid and femoral arteries required.

Param	**Sc**	**Ref**	**Abb**	**Percentage error** [%]		
				2-Wk dataset	**3-Wk dataset**	**1-D dataset**
$LVET$	1	†	LV1	108.7 ± 12.9	-1.2 ± 0.6	11.6 ± 8.7
	1	[148]	LV2	61.5 ± 22.7	-12.4 ± 0.1	3.0 ± 4.4
	1,2	[149]	LV3	26.2 ± 8.6	26.2 ± 8.6	16.9 ± 8.9
	1,2	†	LV4	0.1 ± 0.2	0.1 ± 0.2	9.7 ± 0.7
P_{out}	1	[72, 84]	OP1	0.0 ± 0.0	0.0 ± 0.0	-5.1 ± 8.0
	1	[84, 99]	OP2	0.0 ± 0.0	0.0 ± 0.0	-10.5 ± 7.5
	1,2	†	OP3	9.2 ± 18.4	1.6 ± 16.9	9.1 ± 11.0
	1,2	[119]	OP4	52.9 ± 25.7	42.3 ± 23.6	52.7 ± 15.4
R_{T}	1	[84]	AR1	0.0 ± 0.0	0.0 ± 0.0	0.0 ± 0.1
	2	[84, 136, 137]	AR2	-4.6 ± 0.3	0.7 ± 5.7	-4.9 ± 2.9
C_{T}	1	[84]	AC1	9.6 ± 0.8	-0.1 ± 0.0	-6.5 ± 4.9
	1	[84]	AC2	10.3 ± 0.8	0.0 ± 0.0	-6.6 ± 3.3
	1	[84, 99]	AC3	10.3 ± 0.8	0.0 ± 0.0	-10.2 ± 5.0
	1	[72, 140, 150]	AC4	0.0 ± 0.0	-10.0 ± 4.1	-11.4 ± 4.6
	1	[72, 151]	AC5	0.0 ± 0.0	-10.0 ± 4.1	-7.1 ± 7.1
	1,2	†	AC6	45.7 ± 10.7	-1.5 ± 4.1	-17.3 ± 7.5
	1,2	[72, 135]	AC7	-	-0.1 ± 0.2	-27.6 ± 11.6
	1,2	[140]	AC8	35.6 ± 5.8	-13.8 ± 20.3	4.9 ± 18.4
	1	†	AC9	0.2 ± 0.3	0.0 ± 0.3	-0.8 ± 4.2
PWV	1,2	[91]	PV1	-	-	8.2 ± 6.0
	1*	[91]	PV2	-	-	27.8 ± 10.8
	1,2	[91]	PV3	-	-	-12.7 ± 8.3
	1*	[91]	PV4	-	-	43.0 ± 36.0
	1	[153]	PV5	-	-	33.2 ± 17.2
Z_0	1	[130, 134, 138, 142–146]	Z1	-	2.5 ± 2.1	64.6 ± 44.3
	1	[134, 139, 141]	Z2	-	0.2 ± 1.4	13.4 ± 56.6
	1,2	[85, 154]	Z3	-	-1.5 ± 40.8	133.8 ± 66.7
	1,2	†	Z4	-	-38.7 ± 12.4	82.3 ± 32.6
	1,2	[129]	Z5	-	-	90.4 ± 18.1
	1	†	Z6	-	-0.1 ± 0.7	37.1 ± 20.0

Abbreviations: **Param**: cardiovascular parameters; **Sc**: clinical scenarios; **Ref**: references; **Abb**: coded abbreviations used to refer to each method; $LVET$: left-ventricular ejection time; P_{out}: outflow pressure; R_{T}: arterial resistance; C_{T}: arterial compliance; PWV: pulse wave velocity; Z_0: characteristic impedance; 2-Wk and 3-Wk: two-element and three-element Windkessel, respectively.

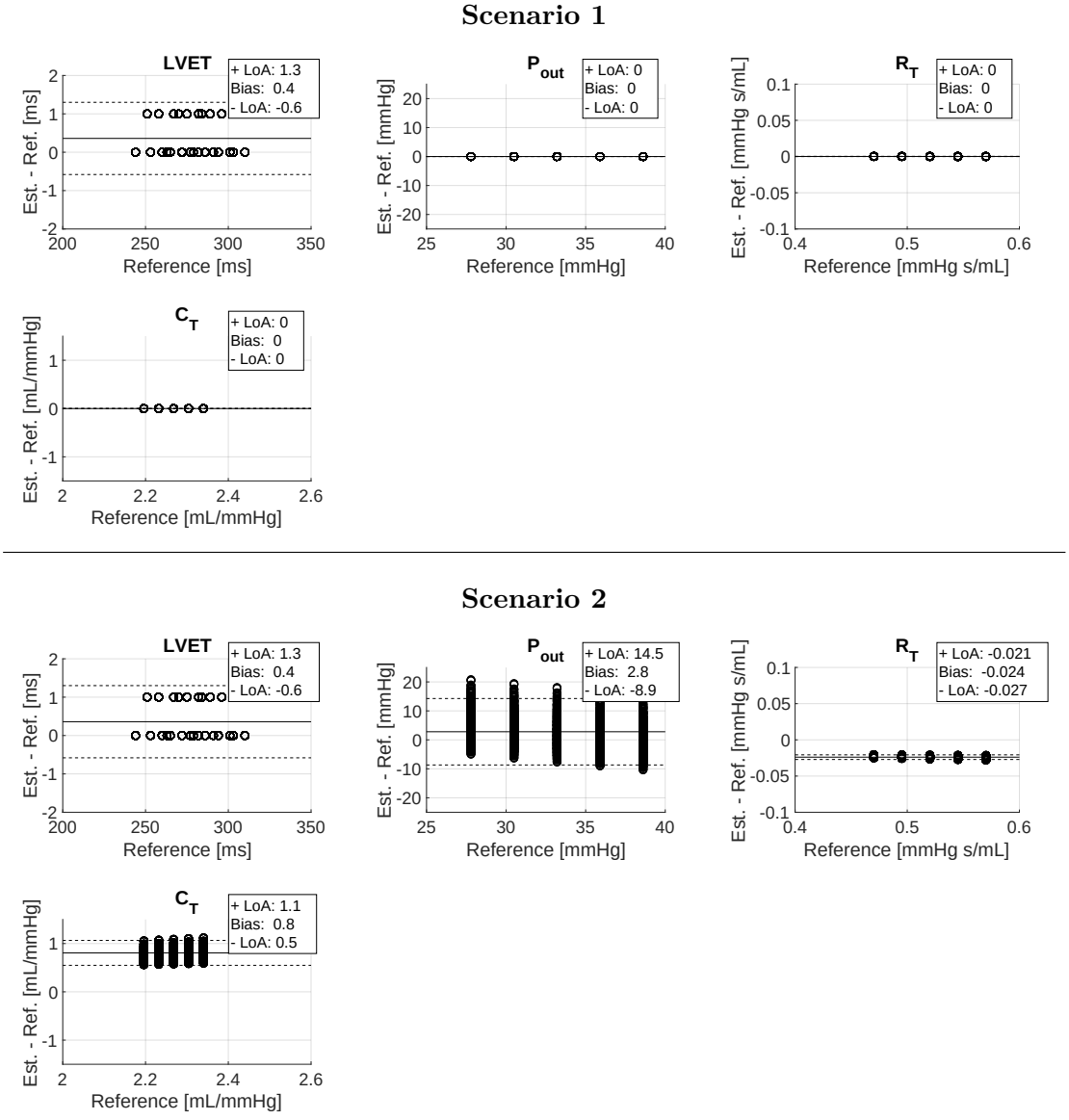

FIGURE 5.5: Bland-Altman plots: optimal CV parameter estimation methods using the two-element Windkessel dataset. Estimates were obtained from the aortic flow and pressure waves using Scenario 1 (top) and 2 (bottom).

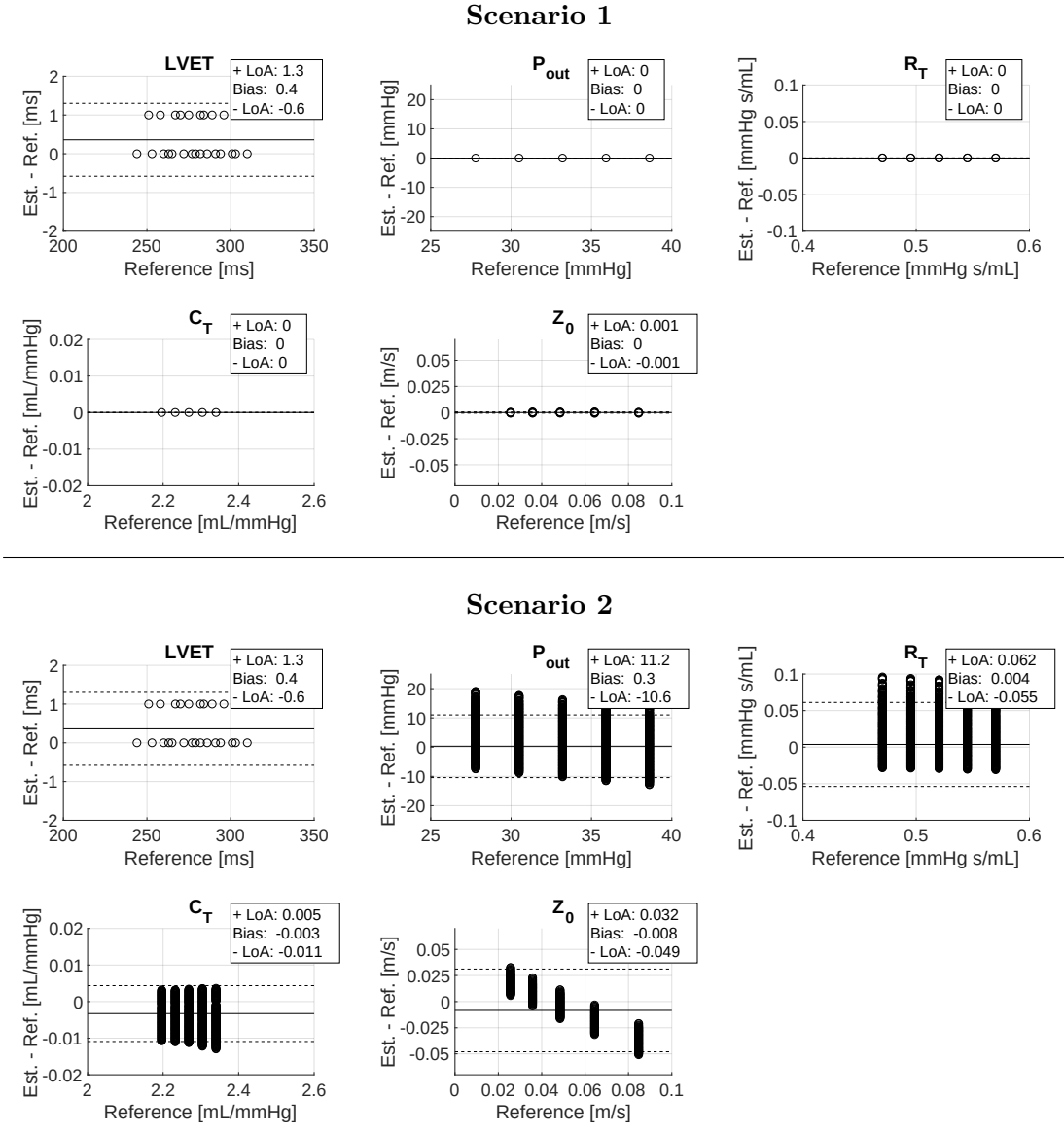

FIGURE 5.6: Bland-Altman plots: optimal CV parameter estimation methods using the three-element Windkessel dataset. Estimates were obtained from the aortic flow and pressure waves using Scenario 1 (top) and 2 (bottom).

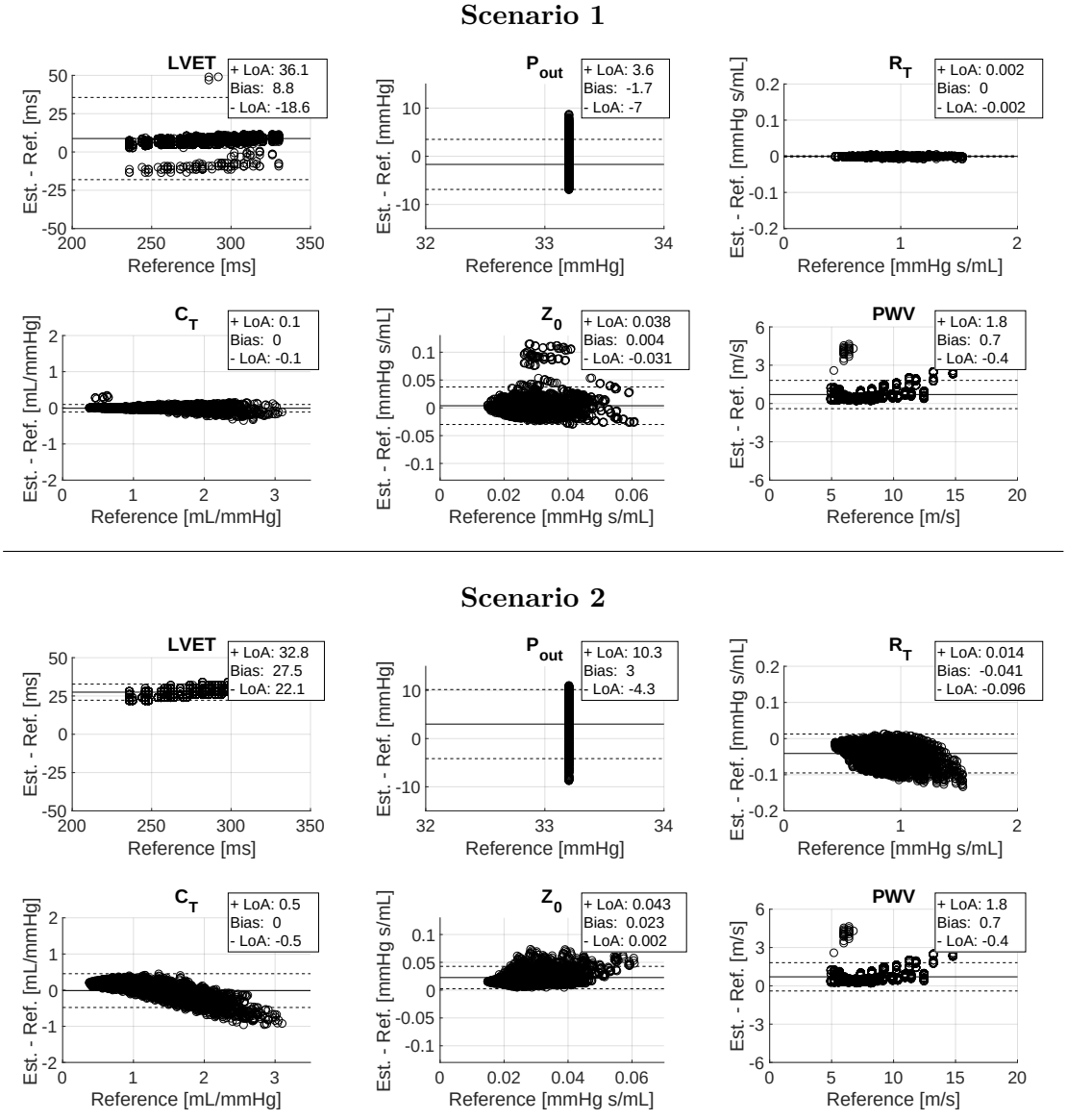

FIGURE 5.7: Bland-Altman plots: optimal CV parameter estimation methods using the 1-D dataset. Estimates were obtained from the aortic flow and pressure waves using Scenario 1 (top) and 2 (bottom).

TABLE 5.2: Optimal CV parameter estimation methods. Performance was assessed for both clinical scenarios using the 0-D and 1-D virtual datasets.

		Independent CV parameter estimation (mean percentage error [%])					
Dataset	**Sc**	$LVET$	P_{out}	R_{T}	C_{T}	PWV	Z_0
2-Wk	1	LV4 (0.1)	OP1/2 (0.0)	AR1 (0.0)	AC4/5 (0.0)	N/A	N/A
	2		OP3 (9.2)	AR2 (-4.7)	AC8 (35.6)		
3-Wk	1	LV4 (0.1)	OP1/2 (0.0)	AR1 (0.0)	AC2/3 (0.0)	N/A	Z6 (-0.1)
	2		OP3 (1.6)	AR2 (0.7)	AC7 (-0.1)		Z3 (-1.5)
1-D	1	LV2 (3.0)	OP1 (-5.1)	AR1 (0.0)	AC9 (-0.8)	PV1 (8.2)	Z2 (15.8)
	2	LV4 (9.7)	OP3 (9.1)	AR2 (-4.9)	AC8 (4.9)		Z4 (82.3)

Abbreviations: **Sc**: scenario; $LVET$: left-ventricular ejection time; P_{out}: outflow pressure; R_{T}: arterial resistance; C_{T}: arterial compliance; PWV: pulse wave velocity; Z_0: characteristic impedance; 2-Wk and 3-Wk: two-element and three-element Windkessel, respectively.

5.4 Discussion

Obtaining reliable *in vivo* reference values for the CV parameters studied here is challenging. Therefore the accuracy of several CV parameter estimation methods was assessed using three datasets of virtual subjects for which theoretical reference values were known exactly, without measurement errors. This approach provided the optimal combination of methods for the cBP algorithms and identified accurate methods for estimating CV parameters that, by themselves, can be used to assess cardiovascular function from non-invasive data available in the clinic. The optimal methods according to the results from the assessment using the 1-D dataset of virtual subjects are discussed next.

5.4.1 $LVET$ estimation methods

Left ventricular ejection time ($LVET$) is a relevant metric of cardiac performance [117]. According to the results for Scenario 1 (MPE $\pm$ SD: $3 \pm 4\%$), $LVET$ can be estimated accurately from the peripheral pressure wave using an existing method for dicrotic notch detection [148]. However, the incisura, which is a high frequency feature of the pressure wave caused by aortic valve closure, provides a more accurate value of $LVET$ [10]. The dicrotic notch is actually a feature of the pressure wave caused by the reflection of waves produced by the resistance of peripheral vessels (see Figure 5.8). In fact, as seen in

O'Rourke [156] and in Figure 5.8, as the pulse wave travels from the aortic root towards the periphery, the dicrotic notch moves away from the pulse wave onset. This explains the observed $LVET$ overestimation, since both dP/dt methods focus on the detection of the dicrotic notch rather than the incisura. Future studies could look at ways of improving this estimate by applying a variable correction factor (based on clinical data) to account for the location of the peripheral pressure wave.

When a peripheral pressure measurement is not available (Scenario 2), analysis of the aortic flow wave can also lead to reasonable estimates ($10 \pm 1\%$). Estimating $LVET$ as a fixed proportion of the cardiac period led to larger errors in this assessment. This is explained by the fact that $LVET$ depends both on T and SV, as it was prescribed using Equation (4.1) [97] when creating the *in silico* flow waves.

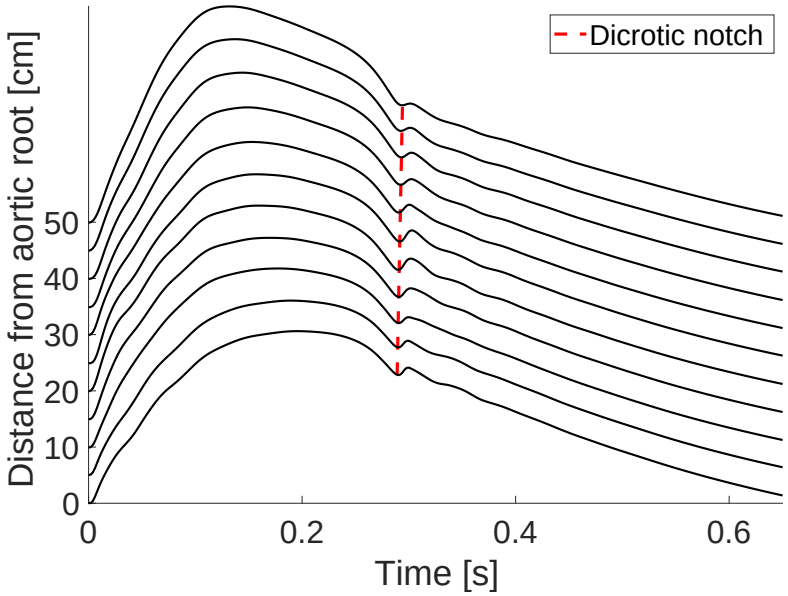

FIGURE 5.8: Evolution of the pressure wave along the aorta at 5 cm intervals for a subject from the 1-D dataset. As indicated by the dashed line, the dicrotic notch moves away from the pressure wave onset as the pressure wave travels towards the periphery. The delay between the dicrotic notch measured at the aortic root and at a 50 cm distance along the aorta is in this case approximately 50 ms. All pressure waves are plotted starting at the time of pressure wave onset for comparison. Only the onset of the aortic root pressure wave coincides with the start of the cardiac cycle.

The poor performance ($> 100\%$ MPE) of the novel LV1 method on the two-element Windkessel dataset is a consequence of the shape of the pressure waves created by the two-element Windkessel model. These pressure waves lack a pair of local minimum/-maximum points, and therefore the method proceeds to estimate $LVET$ as described

in Section 5.2.1. This issue disappears in the more physiological three-element Windkessel and 1-D datasets, where at least one pair of local minimum/maximum points is present for each subject's pressure waveform. Consequently, MPE are smaller for these two datasets (1% and 15%, respectively).

5.4.2 P_{out} estimation methods

The asymptotic pressure P_{out} is currently not fully understood [119]. It was found that estimation methods based on an exponential fit to the diastolic part of the pressure wave outperformed those using a percentage of DBP ($-5 \pm 8\%$ vs $9 \pm 11\%$).

5.4.3 R_{T} estimation methods

The arterial resistance (R_{T}) estimated at the aortic root represents the resistance opposed by peripheral vessels to the flow of blood into the microcirculation. According to the results of this study, accurate estimates could be obtained when using the whole peripheral pressure wave (Scenario 1) to estimate MBP (MPE and SD $< 1\%$). Estimation of R_{T} using an empirical relation [136, 137] requiring peripheral DBP and SBP values (Scenario 2) to estimate MBP underestimated reference R_{T} values by 5% on average. Although the second method assumes that MBP remains constant in the large arteries, MBP at the brachial artery is on average 0.2% lower than that at the aortic root. This difference contributes towards the underestimation of R_{T} in Scenario 2.

5.4.4 C_{T} estimation methods

Arterial compliance (C_{T}) affects the pulse wave, left ventricular dynamics, and flow delivery to the capillaries [128]. The proposed optimised three-element Windkessel method (Scenario 1), performed much better than existing methods ($-1 \pm 4\%$). In Scenario 2, the 'stroke volume over pulse pressure' method had a lower MPE than the 'diastolic blood pressure' and 'pulse pressure' methods (5% vs 18 and 28%, respectively), but a higher SD (18% vs 8 and 12%, respectively). Similarly to [157], this study found MPE $< 12\%$ for the 'diastolic decay', 'area' and 'two-area' methods. However, the MPE for the 'pulse pressure' method were higher (-28%) than those reported in [157] (17%).

5.4.5 PWV estimation methods

Aortic pulse wave velocity (PWV) is a proxy for aortic stiffness and an independent cardiovascular risk indicator [102, 131]. Methods for estimating PWV which used the ascending and descending aorta flows were found to outperform those using the carotid and femoral pressure waves (8% and 13% vs 28 and 43%). In both cases, the foot-to-foot (f-f) method was preferred over the least-squares method. This superiority of methods based on the aortic flow is explained by the fact that the reference value of PWV for the 1-D dataset was calculated using Equation (5.13) at the aortic root. According to this equation, PWV will be minimum at the aortic root, where the arterial radius, r, is largest, and will increase towards the periphery as r decreases. The average r along the carotid-femoral arterial path is smaller than that along the ascending-descending aorta path, which results in a larger overestimation of PWV for the former path. Similarly, Obeid *et al.* [158] also generated aortic pressure waveforms using a 1-D model containing 143 arterial segments and found that aortic PWV is better captured by the f-f method when using waveform pairs located closer to the aorta. Although the carotid-femoral pulse wave velocity ($PWV_{\mathrm{c-f}}$) is considered as the 'gold-standard' method for the measurement of arterial stiffness [159], the current expert consensus does not specify a preferred measurement site along the femoral artery [159–161]. In any case, it has been suggested that the shorter the distance between two recording sites, the greater the relative error in the measurement of arterial length and transit time, and hence the greater the $PWV_{\mathrm{c-f}}$ estimation error [159].

5.4.6 Z_0 estimation methods

Similarly to aortic PWV, aortic characteristic impedance (Z_0) is directly related to aortic stiffness [116, 130]. Existing methods involving P and Q waves normally require these waves to be measured simultaneously at the same location, but in this study, P was taken from the periphery (Scenario 1) and combined with the aortic flow wave, which resulted in the large MPE seen in Table 5.1. The PQ-loop method was the exception since it led to reasonable MPE, though with a large SD ($13 \pm 57\%$). The PQ-loop method assumes a linear proportionality between aortic P and Q in early systole which, according to current results, is largely maintained between peripheral P and aortic Q, most likely because P and Q morphology in early systole is mainly determined by the propagation

of the forward wave travelling from the heart to the periphery, with the backward wave having little influence [93]. This observation led to the derivation of the novel method Z4 which provided the smallest MPE for Scenario 2 (82%). The proposed optimised three-element Windkessel method led to a higher MPE than the PQ-loop method (37% vs 13%), but to a considerably lower SD (20% vs 57%).

Comparative studies for the estimation of $LVET$, P_{out} or R_{T} could not be found in the literature.

5.5 Final remarks

Using the datasets of virtual subjects, methods from the literature were tested and some new methods were designed to address the limitations of the existing ones. Since theoretical reference values were know exactly, without any measurement error, it was expected that this testing approach should provide lower bounds for mean percentage errors. As seen when comparing the results for the 0-D and 1-D datasets, the performance of CV parameter estimation methods depends on the dataset. However, since the reference values of most CV parameters cannot be obtained in the clinic, CV parameter estimation methods can only be assessed using virtual datasets. The optimal combination of methods was chosen based on the results from the 1-D dataset since it displayed more physiological features than the 0-D datasets.

In Scenario 1, when a peripheral pressure wave (P) was available, optimal CV parameter estimation methods used: the derivative of P to estimate $LVET$; an exponential fit applied to the diastolic portion of P to estimate P_{out}; P and the ascending aorta flow (Q) to estimate R_{T}; an optimisation based on the three-element Windkessel model using P and Q to estimate C_T; and a PQ-loop method applied to the early systolic portion of P and Q to estimate Z_0. In Scenario 2, when only peripheral DBP and SBP were available, the optimal methods used instead: and analysis of Q to estimate $LVET$; half of DBP to estimate P_{out}; DBP, SBP, and Q to estimate R_{T}; SV and PP to estimate C_T; and DBP, SBP, and Q to estimate Z_0. The foot-to-foot method applied to the ascending and descending aorta flows was used to estimate PWV in both scenarios. These optimal methods will be used in Chapter 6 to assess cBP estimation algorithms in both scenarios.

6 Central Blood Pressure Estimation

In this chapter, (i) the clinical motivation of and current gold standards for central (aortic) blood pressure (cBP) measurements are presented; (ii) a novel patient specific, non-invasive approach for the measurement of cBP using aortic flow, peripheral pressure, and computational models is proposed; (iii) the calculation of the model parameters from clinical data is described; (iv) the approach is assessed using a combination of *in silico* and *in vivo* data.

6.1 Introduction

As seen in Chapter 2, recent clinical evidence suggets that cBP is a better marker of cardiovascular risk than brachial blood pressure (bBP), which highlights the importance of obtaining accurate, non-invasive cBP measurements.

A potential approach is to use a computational model of the circulation to estimate cBP from non-invasive measurements of aortic flow and peripheral BP [162]. Aortic flow can be measured using magnetic resonance imaging (MRI) or ultrasound. Peripheral systolic and diastolic BP can be easily measured using a brachial cuff, whilst a peripheral pressure waveform can be measured using applanation tonometry. MRI can also measure vascular geometry which can be used to further refine the model. Consequently, computational models could be personalised to estimate cBP in cardiac MRI and ultrasound settings. Although previous studies have used reduced-order models to estimate cBP non-invasively, they did not validate their cBP estimates against invasive cBP measurements or compare the performance of several algorithms [75, 162–165].

The aim of this study was to develop and assess three novel algorithms of increasing complexity for estimating cBP from aortic flow, using non-invasive, patient-specific data and physical phenomena occurring in the upper-thoracic aorta (Figure 6.1). Each algorithm used a different blood flow model: the two-element [84] and three-element [95] zero-dimensional (0-D) Windkessel models, and a one-dimensional (1-D) model of the upper-thoracic aorta [75]. The first step in each algorithm was to estimate cardiovascular (CV) parameters from non-invasive haemodynamic data measured in the upper-thoracic aorta coupled with a peripheral blood pressure measurement, using the optimal methods described in Chapter 5. The second step was to use these parameters as inputs to one of the three blood flow models to estimate a patient-specific cBP waveform. Finally, the performance of the cBP algorithms against reference clinical data, including invasive cBP measurements, was assessed.

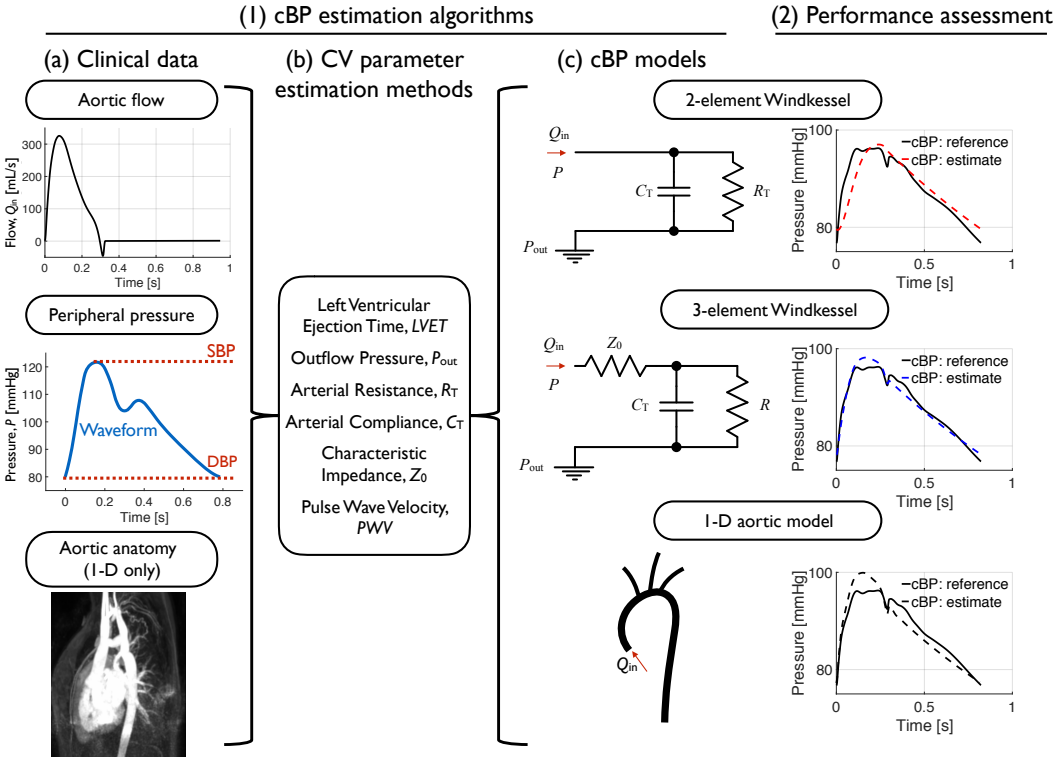

FIGURE 6.1: Methodology for the study of cBP estimation algorithms. (1) cBP estimation algorithms consisted of three steps. (a) Clinical data acquisition and pre-processing: blood flow measured at the ascending and descending (1-D algorithm only) aorta; peripheral pressure measurement; and aortic anatomy (1-D algorithm only). (b) Cardiovascular (CV) parameters estimated from clinical data. (c) These parameters, along with the non-invasive clinical data, were used as inputs to one of three cBP models. (2) Algorithm performance was assessed by comparing cBP estimates provided by each model to reference values.

6.2 Methods

The three algorithms used to estimate cBP each consisted of two stages (see Figure 6.1). Firstly, CV parameters were estimated using the optimal CV parameter estimation methods described in Chapter 5. Secondly, a cBP waveform was simulated using a computational model of arterial blood flow. Two 0-D models were considered: the two-element and three-element Windkessel models; and a 1-D model of the upper-thoracic aorta, referred to as the '1-D aortic' model hereafter [75]. The mathematical formulation of and the inputs to the two-element and three-element Windkessel models are described in Chapter 4 (Sections 3.2.1 and 3.2.2, respectively). The 1-D mathematical formulation is described in Chapter 4 (Section 3.3). The inputs to the '1-D aortic' model are presented in Section 6.2.1.

6.2.1 1-D aortic model

This model uses the 1-D equations of blood flow in the network of compliant vessels shown in Figure 6.1c (bottom) to compute cBP [75]. The inputs to the model are: (i) the geometry (*i.e.* lengths and cross-sectional areas) of the upper-thoracic aorta, including the supra-aortic arteries; (ii) flow waves at the ascending and descending aorta and, when available, each supra-aortic artery; and (iii) a peripheral BP measurement. This model was used to estimate cBP in the two datasets described in Chapter 4 which contained the required geometry, flow, and pressure data: the 1-D model dataset and the 'Aortic Coarctation' dataset.

For the 1-D model dataset, the arterial geometry (*i.e.* arterial length, and cross-sectional area at diastolic BP) and haemodynamic data were extracted at the following arterial locations (Figure 6.2):

- (1) Ascending aorta (geometry, flow wave at the aortic root)
- (2) Aortic arch (geometry)
- (3) Descending aorta (geometry, flow wave at the outlet)
- (4) Brachiocephalic artery (geometry)

- (5) Left common carotid artery (geometry, pressure wave at 50% length; Scenario 1 only)
- (6) Left subclavian artery (geometry)
- (7) Brachial artery (SBP and DBP at 75% length; Scenario 2 only)

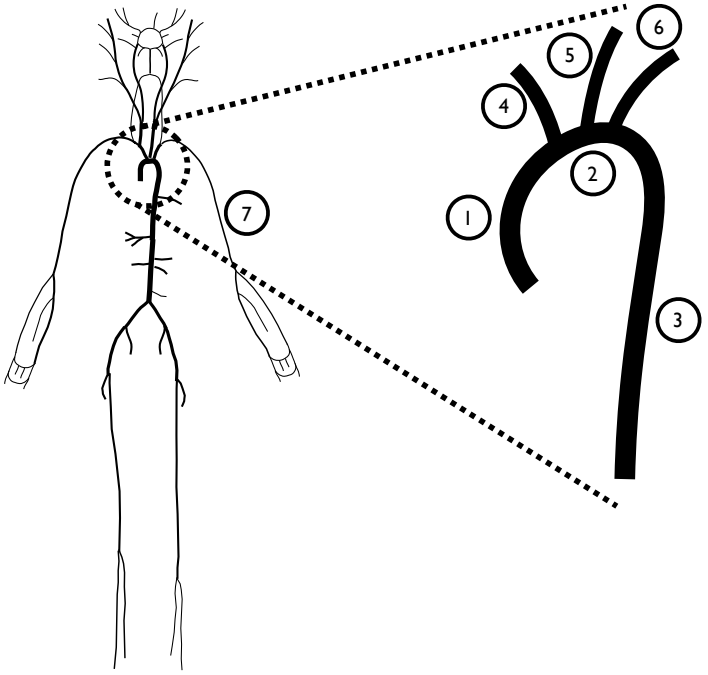

FIGURE 6.2: Arterial locations in the 1-D dataset. Arterial geometry and flow and pressure waves were extracted at these locations to create a corresponding 'reduced' 1-D model for each virtual subject in the 1-D dataset.

For the 'Aortic Coarctation' dataset, the geometry of the upper-thoracic aorta was extracted from MRI data using an in-house prototype software being developed by Philips Healthcare (a detailed description can be found in [6]), as shown in Figure 4.5.

For both datasets, volumetric blood flow waves were obtained at the ascending (Q_{in}, acquired as close to the aortic root as possible) and descending thoracic (Q_{out}) aorta. Q_{in} and Q_{out} were used to calculate the pulse wave velocity, PWV, as described in Table 5.1. Q_{in} was imposed as an inflow boundary condition at the aortic root. Outflow boundary conditions were calculated as 3-element Windkessel models coupled to the outlet of each terminal 1-D model segment. The parameters of each outflow model j are $Z^j_{0,\text{Wk}}$, $C^j_{\text{T,Wk}}$ and R^j_{Wk}, were calculated using Q_{in}, Q_{out}, and the outflow distribution (OD) in the supra-aortic arteries, $OD^j_{\text{flow}} = \overline{Q}^j_{\text{out}}/\overline{Q}_{\text{in}}$, under the assumption that DBP, MBP, and

P_{out} remain constant within large arteries [38]. The following equations were used [75]:

$$Z^j_{0,\text{Wk}} = \frac{\rho PWV}{A^j_{\text{out}}}, \tag{6.1}$$

$$R^j_{\text{Wk}} = \frac{R_{\text{T}}}{OD^j} - Z^j_{0,\text{Wk}}, \tag{6.2}$$

$$C^j_{\text{T,Wk}} = (C_{\text{T}} - C_{\text{T,art}})\,\frac{R_{\text{T}}}{R^j_{\text{Wk}}}, \tag{6.3}$$

where $C_{\text{T,art}}$ is the total compliance of the 1-D model arterial segments calculated as the sum of each segment's compliance,

$$C^k_{\text{T,art}} = \frac{\overline{A}^k L^k}{\rho PWV^2}, \tag{6.4}$$

with $\overline{A}^k$ the average area and L^k the length of the arterial segment k. When $\overline{Q}^j_{\text{out}}$ were unavailable at each outflow j, the difference between the mean values of Q_{in} and Q_{out} was distributed among the supra-aortic arteries proportionally to their outlet areas, A^j_{out}, as $OD^j_{\text{area}} = (\overline{Q}_{\text{in}} - \overline{Q}_{\text{out}})A^j_{\text{out}} / \sum^j A^j_{\text{out}}$.

6.2.2 Assessing central blood pressure estimation algorithms

The performance of each cBP estimation algorithm was assessed by comparing estimated cBP values to corresponding reference cBP values in the three clinical datasets, and in the 1-D dataset of virtual subjects. The 0-D datasets of virtual subjects were excluded since the 1-D dataset was based on a more complex and physiological model of the arterial circulation and hence presented a broader range of pulse waves. Performance was quantified using the mean absolute error and standard deviation for central diastolic ($cDBP$), mean ($cMBP$), and systolic ($cSBP$) blood pressure, and pulse pressure (cPP). Additionally, Bland-Altman plots [155] were used to show the bias and limits of agreement between the estimated and reference BP values. Finally, the root mean square error (RMSE) between estimated and reference cBP waves was computed.

6.3 Results

Table 6.1 shows the estimation errors for all three cBP estimation algorithms, with each algorithm evaluated in four datasets for both clinical scenarios. In the 1-D dataset,

RMSEs in Scenario 1 (mean ± SD: $< 3.4 \pm < 1.7$ mmHg) were lower than those in Scenario 2 ($< 5.1 \pm < 2.5$ mmHg). In the clinical datasets, RMSEs were similar for both scenarios and larger than those obtained in the 1-D dataset. The 1-D aortic algorithm led to the smallest RMSEs in the 1-D dataset (2.0 ± 1.0 mmHg) and 'Aortic Coarctation' (6.4 ± 2.8 mmHg) dataset. The 3-element Windkessel algorithm led to the smallest RMSEs in the 'Normotensive' (5.9 ± 2.4 mmHg) and 'Hypertensive' (5.7 ± 2.4 mmHg) datasets, where the 1-D aortic algorithm could not be applied.

Overall, estimation errors for $cDBP$, $cMBP$, $cSBP$ and cPP were smaller in the 1-D dataset compared to the clinical datasets, for all cBP algorithms and scenarios. Furthermore, $cDBP$ and $cMBP$ errors were smaller than $cSBP$ and cPP errors in all datasets and for all algorithms and scenarios. In each dataset and scenario, all three cBP algorithms led to similar $cMBP$ errors. However, $cDBP$, $cSBP$ and cPP errors changed considerably with the type of cBP algorithm used.

The 1-D and 'Aortic Coarctation' datasets contain the vascular geometry and PWV information required to run the 1-D aortic algorithm. In both datasets and scenarios, the 1-D aortic algorithm led to $cSBP$ and cPP errors that were smaller or similar compared to the 0-D models ($< 2.2 \pm < 6.3$ mmHg vs $< 5.3 \pm < 7.2$ mmHg for the 1-D dataset; $< 4.1 \pm < 10.7$ mmHg vs $< 16.4 \pm < 9.2$ mmHg for the 'Aortic Coarctation' dataset). Both 0-D algorithms performed similarly in both datasets and led to smaller $cDBP$ errors than the 1-D aortic algorithm.

In the 'Normotensive' and 'Hypertensive' datasets, both 0-D models estimated $cDBP$, $cMBP$, $cSBP$, and cPP values with errors $< 6.0 \pm 4.9$ mmHg, though the 3-element Windkessel algorithm led to smaller RMSEs ($< 5.9 \pm 2.4$ mmHg vs $< 10.6 \pm 4.1$ mmHg). All errors were considerably smaller in Scenario 2.

TABLE 6.1: Performance of cBP estimation algorithms. They are denoted as 2-Wk (2-element Windkessel), 3-Wk (3-element Windkessel) and 1-D aortic. Results are presented as mean (μ) and standard deviation (SD) errors between estimated and reference values of cDBP, cMBP, cSBP, and cPP. The RMSEs between estimated and reference cBP waves is shown in the last column. Each cBP algorithm was assessed in four datasets and two clinical scenarios: Scenario 1 (peripheral BP waveform available) and Scenario 2 (only peripheral SBP and DBP available). Abbreviations: **Sc**: clinical scenario; **cBP algo**: cBP algorithm.

			Estimation error ($\mu \pm$ SD) [mmHg]				
Datasets	**Sc**	**cBP algo**	cDBP	cMBP	cSBP	cPP	RMSE
1-D dataset	1	2-Wk	1.2 ± 0.7	0.1 ± 0.1	1.0 ± 0.8	-0.2 ± 1.3	3.4 ± 1.1
		3-Wk	0.1 ± 1.0	0.1 ± 0.1	1.8 ± 1.9	1.7 ± 2.8	2.0 ± 1.7
		1-D aortic	0.1 ± 1.1	0.2 ± 0.6	2.2 ± 1.8	2.1 ± 2.3	2.0 ± 1.0
	2	2-Wk	0.8 ± 1.5	-3.0 ± 1.9	-4.5 ± 5.9	-5.3 ± 7.2	5.0 ± 2.5
		3-Wk	-2.6 ± 0.8	-2.9 ± 1.9	-0.2 ± 4.7	2.4 ± 5.2	5.1 ± 2.0
		1-D aortic	-1.5 ± 1.2	-2.9 ± 1.9	-1.7 ± 5.3	-0.2 ± 6.3	4.2 ± 2.1
Aortic Coarctation	1	2-Wk	0.8 ± 3.1	-3.4 ± 2.8	-15.7 ± 7.2	-16.4 ± 8.5	10.1 ± 3.9
		3-Wk	0.2 ± 2.8	-3.5 ± 2.8	-15.4 ± 7.4	-15.6 ± 8.6	8.0 ± 3.2
		1-D aortic	-3.4 ± 4.8	-2.5 ± 2.6	-0.0 ± 9.7	3.4 ± 10.7	6.4 ± 2.8
	2	2-Wk	-1.5 ± 2.4	-5.5 ± 2.8	-17.3 ± 7.9	-15.8 ± 9.2	10.9 ± 4.3
		3-Wk	-1.8 ± 2.5	-5.7 ± 2.9	-17.2 ± 7.9	-15.4 ± 9.1	8.4 ± 3.6
		1-D aortic	-6.1 ± 2.8	-5.3 ± 3.0	-2.1 ± 9.2	4.1 ± 10.6	7.8 ± 3.3
Normotensive	1	2-Wk	4.7 ± 1.9	0.3 ± 0.1	-8.6 ± 5.0	-13.3 ± 6.2	10.3 ± 3.0
		3-Wk	-4.4 ± 3.5	-0.9 ± 0.7	13.4 ± 13.4	17.9 ± 16.5	8.6 ± 5.5
	2	2-Wk	-0.1 ± 0.5	0.2 ± 2.2	-3.3 ± 3.5	-3.2 ± 3.4	11.0 ± 3.5
		3-Wk	0.2 ± 0.5	-0.2 ± 2.1	-3.7 ± 4.0	-3.9 ± 4.1	5.9 ± 2.4
Hypertensive	1	2-Wk	5.0 ± 3.2	0.3 ± 0.1	-8.3 ± 6.3	-13.3 ± 9.0	10.6 ± 4.1
		3-Wk	-2.9 ± 3.6	-0.9 ± 1.0	8.0 ± 10.6	11.0 ± 13.4	7.1 ± 4.2
	2	2-Wk	-0.3 ± 0.8	-1.1 ± 2.0	-5.5 ± 4.0	-5.2 ± 4.1	11.1 ± 4.2
		3-Wk	0.0 ± 0.6	-1.5 ± 2.0	-6.0 ± 4.7	-6.0 ± 4.9	5.7 ± 2.4

Bland-Altman plots of $cDBP$ (Figures 6.3 and 6.4), $cMBP$ (Figures 6.5 and 6.6), $cSBP$ (Figures 6.7 and 6.8), and cPP (Figures 6.9 and 6.10) show increases in the absolute bias for $cMBP$, $cSBP$, and cPP with increasing reference BP values in the 1-D dataset in Scenario 2. Furthermore, in the 'Normotensive' and 'Hypertensive' datasets, the absolute bias for cPP increased with increasing reference BP values when using the 2-element Windkessel algorithm in Scenario 1, and $cSBP$ followed the same trend when using both 0-D algorithms in Scenario 2. Remaining estimates were less affected by varying reference BP values.

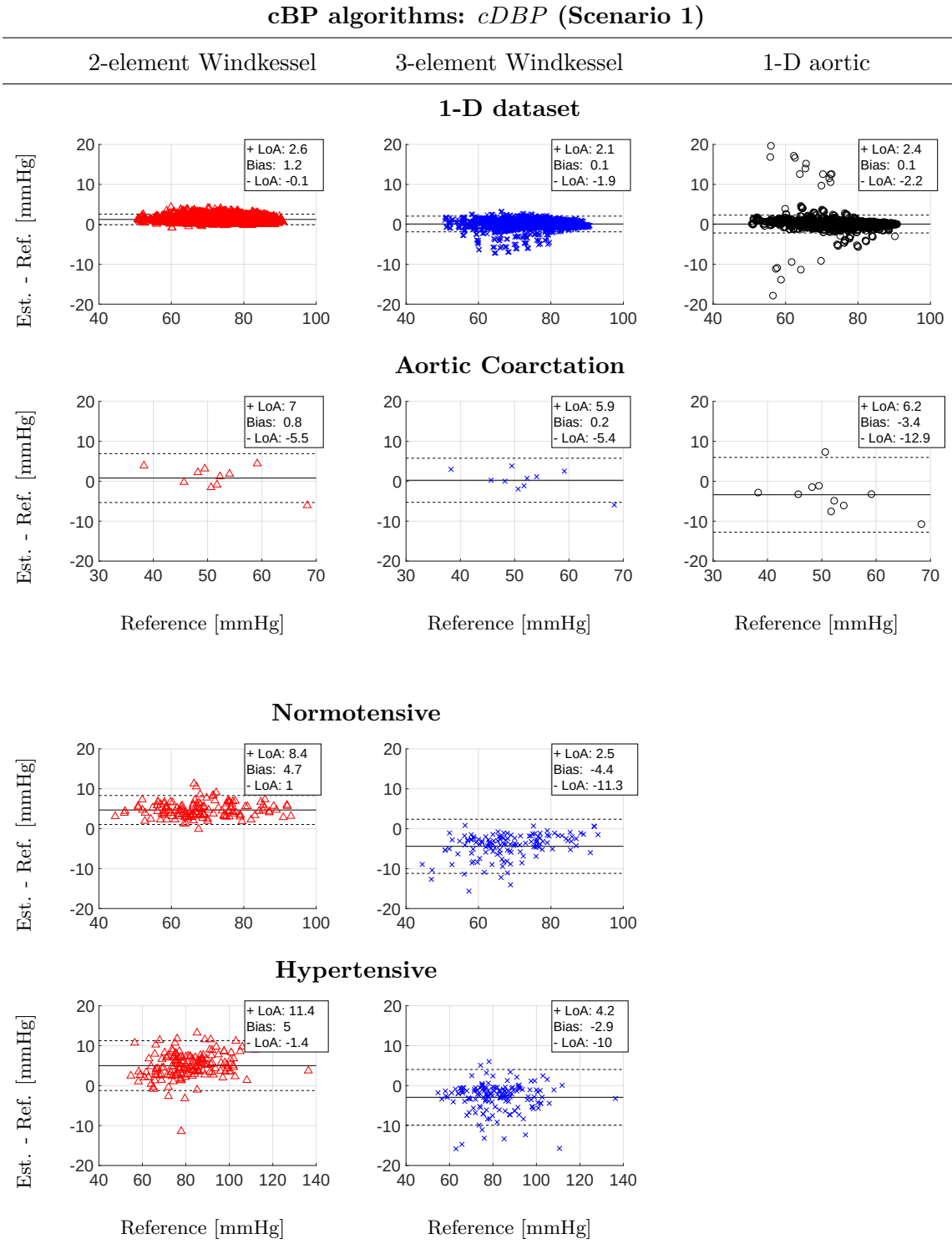

FIGURE 6.3: Bland-Altman plots for cDBP estimation for Scenario 1. The 2-element Windkessel (△), 3-element Windkessel (×) and 1-D aortic (◯) algorithms were assessed in the 1-D (top), 'Aortic Coarctation' (second row), 'Normotensive' (third row), and 'Hypertensive' (bottom) datasets. y-axes are estimated minus reference cDBP values.

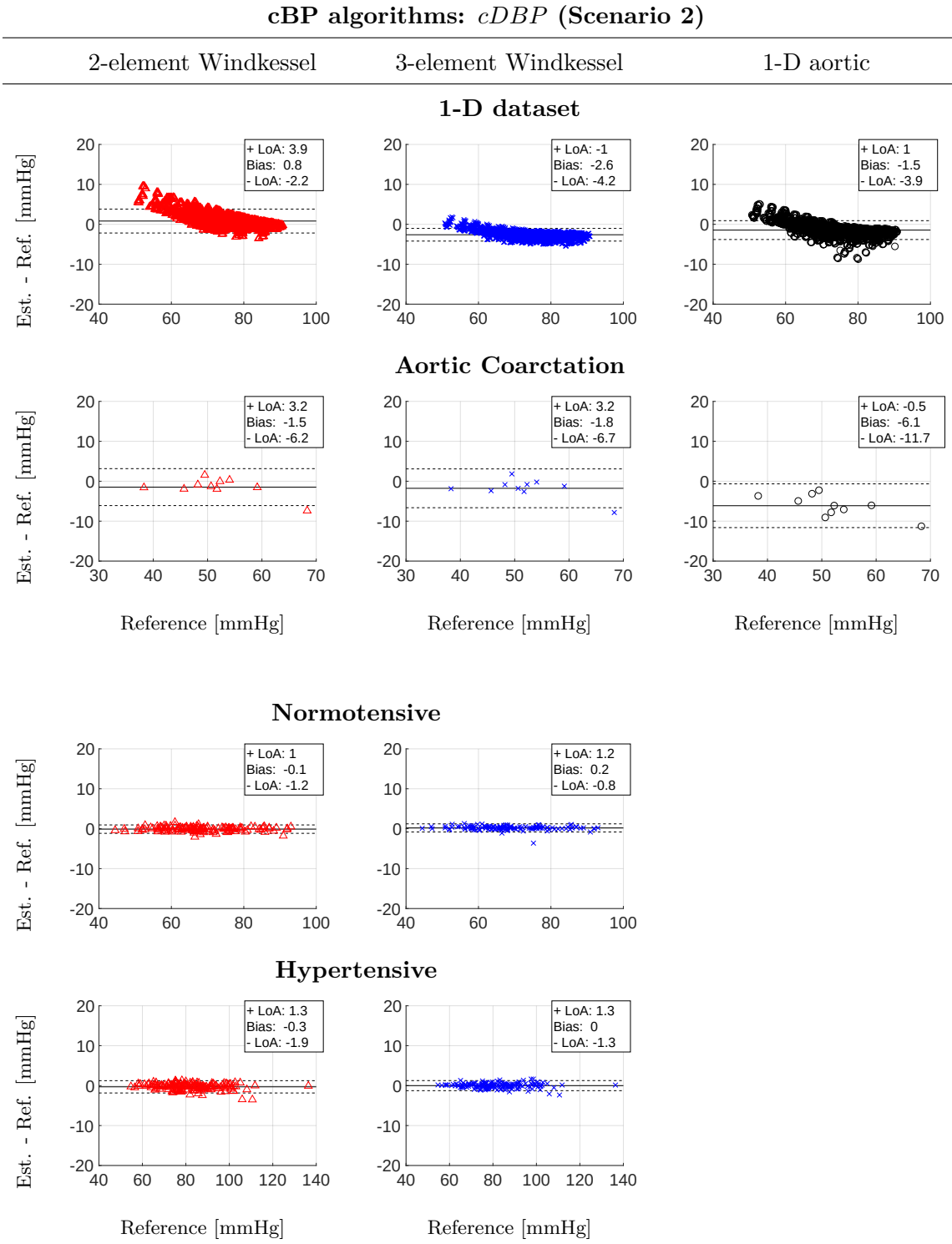

FIGURE 6.4: Bland-Altman plots for cDBP estimation for Scenario 2. The 2-element Windkessel (△), 3-element Windkessel (×) and 1-D aortic (◯) algorithms were assessed in the 1-D (top), 'Aortic Coarctation' (second row), 'Normotensive' (third row), and 'Hypertensive' (bottom) datasets. y-axes are estimated minus reference cDBP values.

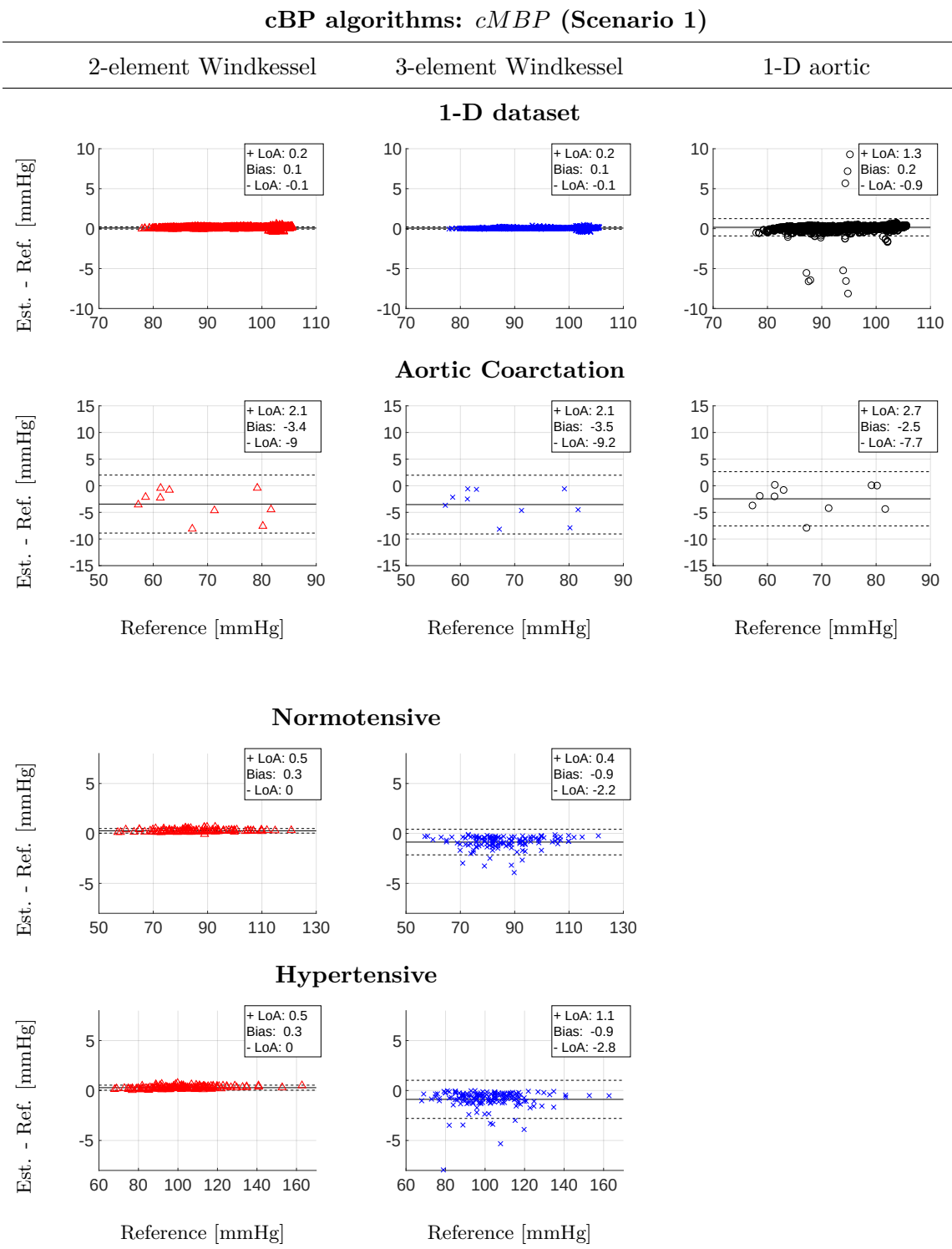

FIGURE 6.5: Bland-Altman plots for cMBP estimation for Scenario 1. The 2-element Windkessel (△), 3-element Windkessel (×) and 1-D aortic (◯) algorithms were assessed in the 1-D (top), 'Aortic Coarctation' (second row), 'Normotensive' (third row), and 'Hypertensive' (bottom) datasets. y-axes are estimated minus reference cDBP values.

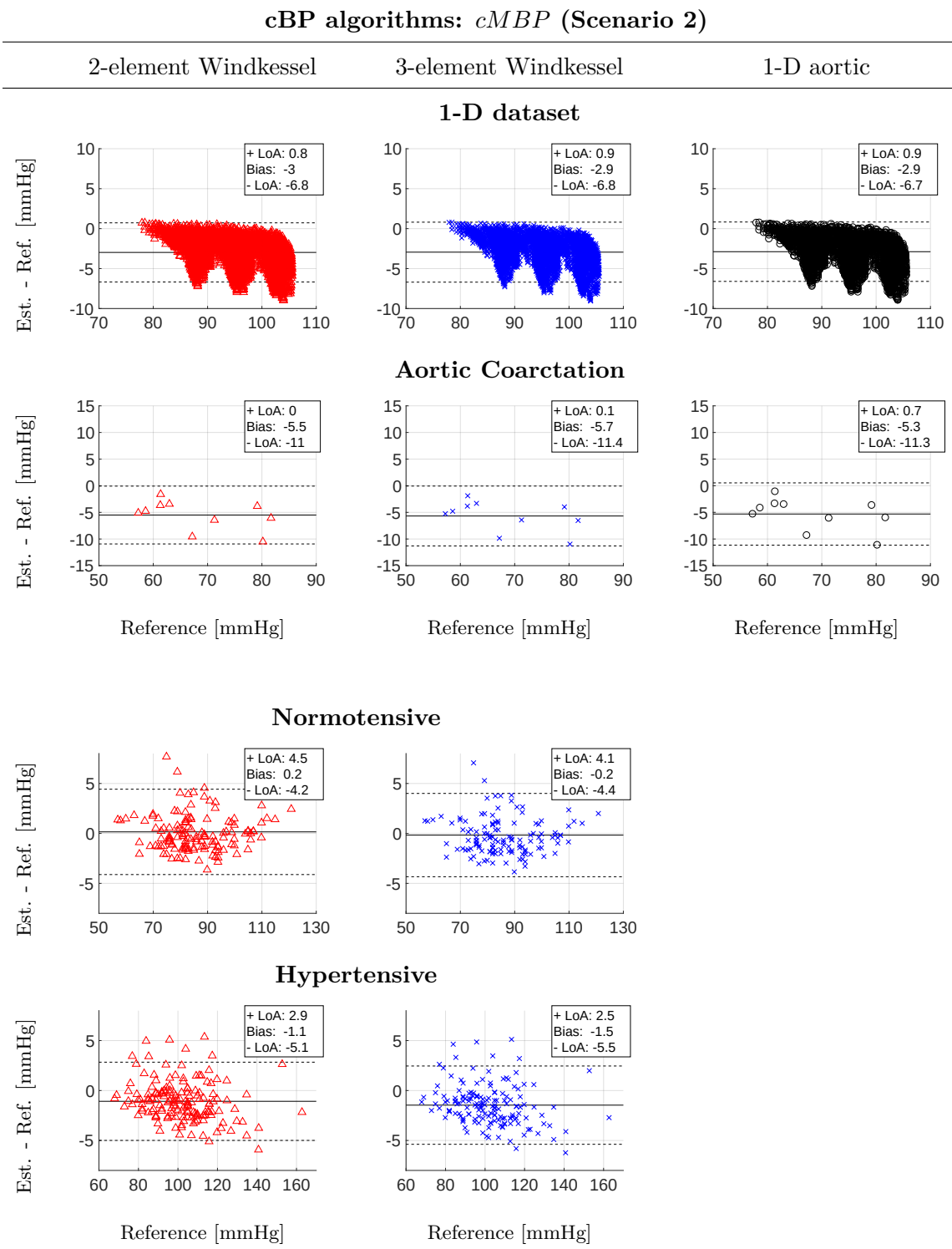

FIGURE 6.6: Bland-Altman plots for cMBP estimation for Scenario 2. The 2-element Windkessel (△), 3-element Windkessel (×) and 1-D aortic (◯) algorithms were assessed in the 1-D (top), 'Aortic Coarctation' (second row), 'Normotensive' (third row), and 'Hypertensive' (bottom) datasets. y-axes are estimated minus reference cDBP values.

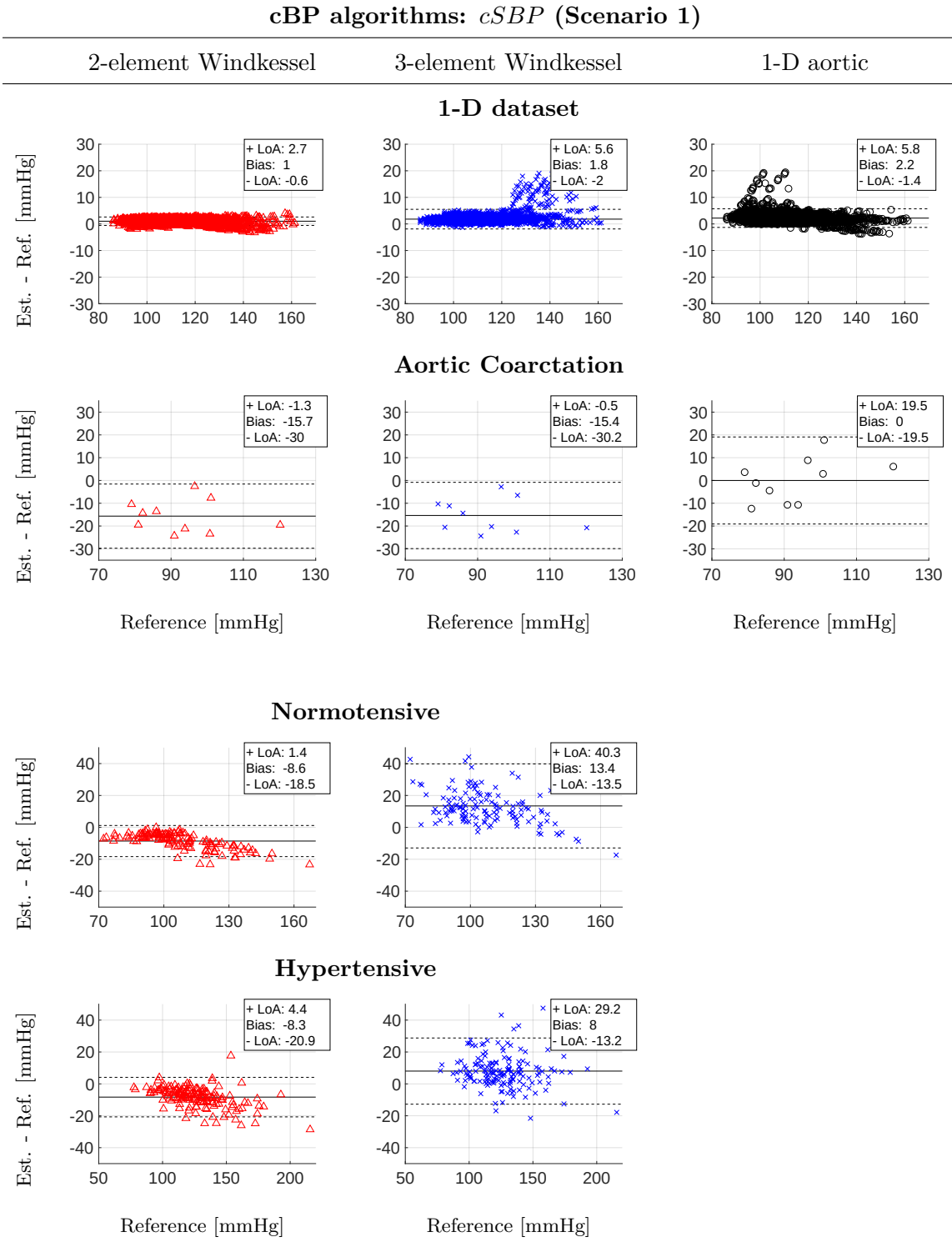

FIGURE 6.7: Bland-Altman plots for cSBP estimation for Scenario 1. The 2-element Windkessel (△), 3-element Windkessel (×) and 1-D aortic (◯) algorithms were assessed in the 1-D (top), 'Aortic Coarctation' (second row), 'Normotensive' (third row), and 'Hypertensive' (bottom) datasets. y-axes are estimated minus reference cDBP values.

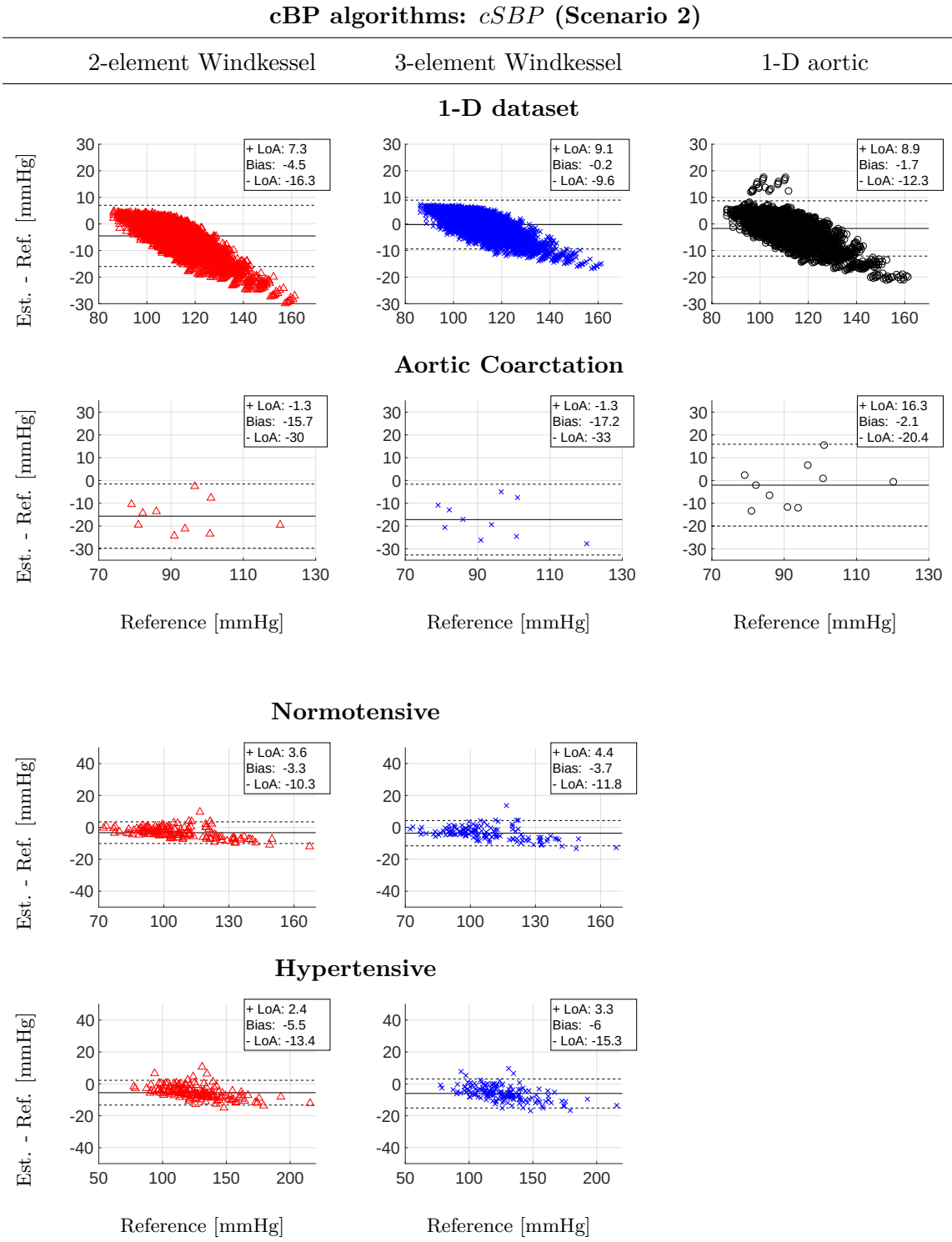

FIGURE 6.8: Bland-Altman plots for cSBP estimation for Scenario 2. The 2-element Windkessel (△), 3-element Windkessel (×) and 1-D aortic (◯) algorithms were assessed in the 1-D (top), 'Aortic Coarctation' (second row), 'Normotensive' (third row), and 'Hypertensive' (bottom) datasets. y-axes are estimated minus reference cDBP values.

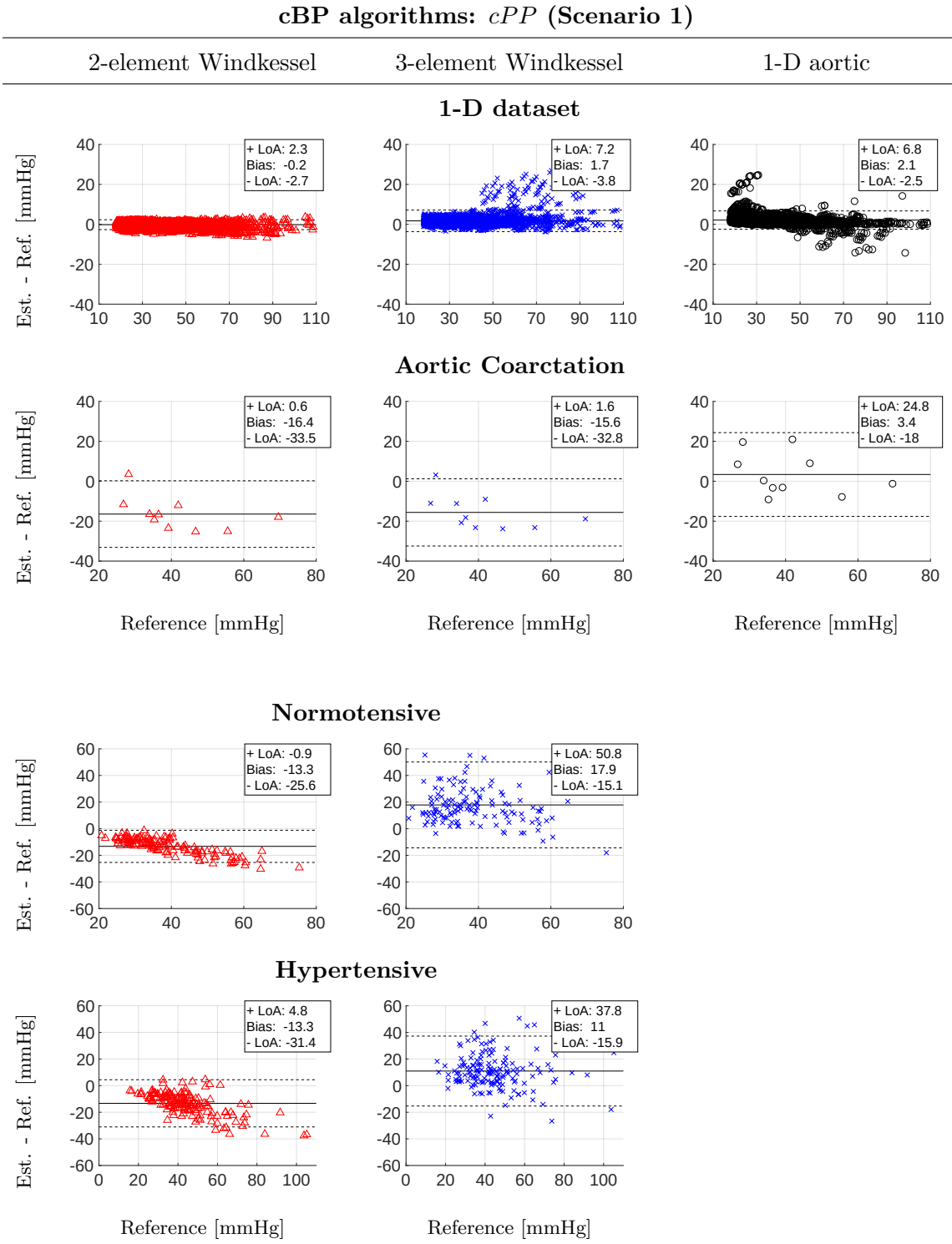

FIGURE 6.9: Bland-Altman plots for cPP estimation for Scenario 1. The 2-element Windkessel (△), 3-element Windkessel (×) and 1-D aortic (◯) algorithms were assessed in the 1-D (top), 'Aortic Coarctation' (second row), 'Normotensive' (third row), and 'Hypertensive' (bottom) datasets. y-axes are estimated minus reference cPP values.

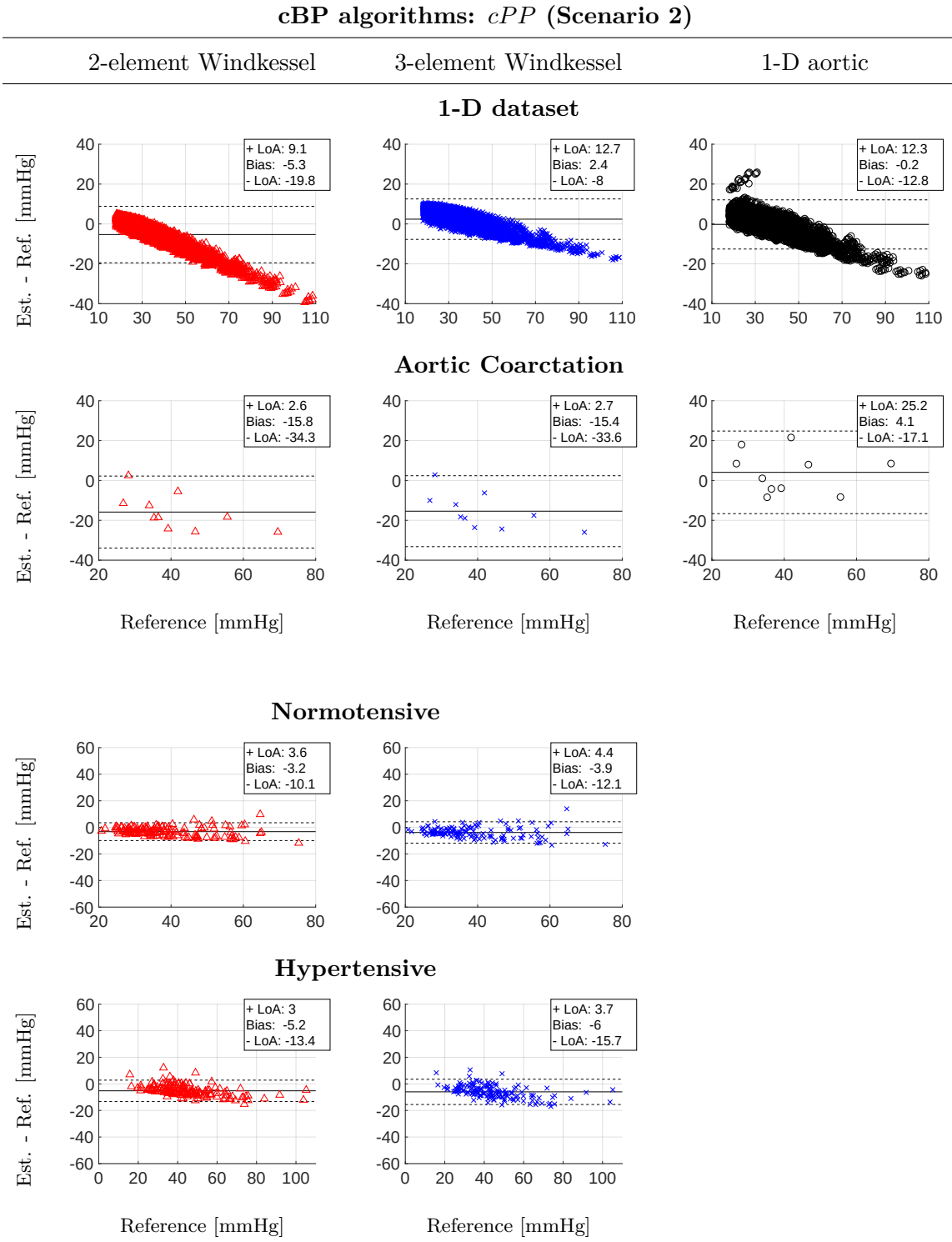

FIGURE 6.10: Bland-Altman plots for cPP estimation for Scenario 2. The 2-element Windkessel (△), 3-element Windkessel (×) and 1-D aortic (◯) algorithms were assessed in the 1-D (top), 'Aortic Coarctation' (second row), 'Normotensive' (third row), and 'Hypertensive' (bottom) datasets. y-axes are estimated minus reference cPP values.

Figures in Appendix A.2 show individual cBP waveform estimations by each cBP algorithm for a set of randomly chosen subjects in the 1-D dataset and for all subjects in the

'Aortic Coarctation', 'Normotensive' and 'Hypertensive' datasets, in both clinical scenarios. The 0-D algorithms spent less than 1 second per patient to compute the cBP wave using a standard PC, whereas the 1-D aortic algorithm took less than 1 minute (both times account for the time required to calculate all patient-specific CV parameters).

6.4 Discussion

Algorithms for reconstructing the cBP waveform from non-invasive data have been developed. These algorithms are based on physical phenomena occurring in the upper-thoracic aorta and are patient-specific – all physical parameters except for blood density and viscosity can be calculated from non-invasive data obtained by tonometry and ultrasound or magnetic resonance imaging. Results showed that the 1-D aortic algorithm outperformed the 0-D algorithms at estimating cBP wave morphology (RMSE $< 6.4 \pm 2.8$ mmHg for the clinical data), as well as $cSBP$ and cPP values (errors $< 3.4 \pm 10.7$ mmHg), when the aortic vascular geometry was available. When only the aortic flow and peripheral pressure waves were available, both 0-D models estimated $cDBP$, $cMBP$, $cSBP$, and cPP values with similar errors ($<6.0 \pm 4.9$ mmHg), though the 3-element Windkessel algorithm produced smaller RMSEs.

6.4.1 Proportional bias and outlier clusters

Proportional bias was observed in the 1-D model dataset for all cBP algorithms in Scenario 2. Given that Bland-Altman error values and trends were similar across all three algorithms, this proportional bias is most likely a consequence of a sub-optimal cardiovascular parameter estimation. Focusing on the results for the 1-D aortic algorithm, Figure 5.7 shows two parameters which were estimated with proportional bias and relatively poorly in Scenario 2 compared to Scenario 1: R_{T} and C_{T}. Firstly, consistent $cMBP$ underestimation in Figure 6.6 may be explained by a corresponding R_{T} underestimation in Figure 5.7. Secondly, negative proportional bias in cPP estimation may be explained by a corresponding negative proportional bias in C_{T} estimation. Due to the inverse relationship between C_{T} and cPP, C_{T} overestimates should result in cPP underestimates. In Figure 5.7, C_{T} overestimates correspond to small C_{T} reference values, which in turn correspond to large cPP reference values. Figure 6.10 shows that large cPP reference values do correspond to cPP underestimates. Furthermore, Figure 6.11 confirms that

cPP overestimates/underestimates correspond to C_{T} underestimates/overestimates for the 1-D aortic algorithm. Finally, given that $cDBP$ errors are small compared to $cSBP$ ones, the latter may be better explained by cPP results, which present both a similar negative proportional bias and error values.

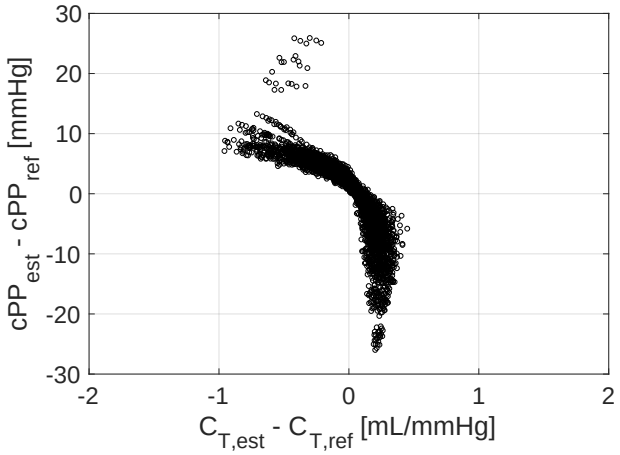

FIGURE 6.11: Inverse relationship between cPP and C_{T} estimation errors in the 1-D dataset using the 1-D algorithm in Scenario 2.

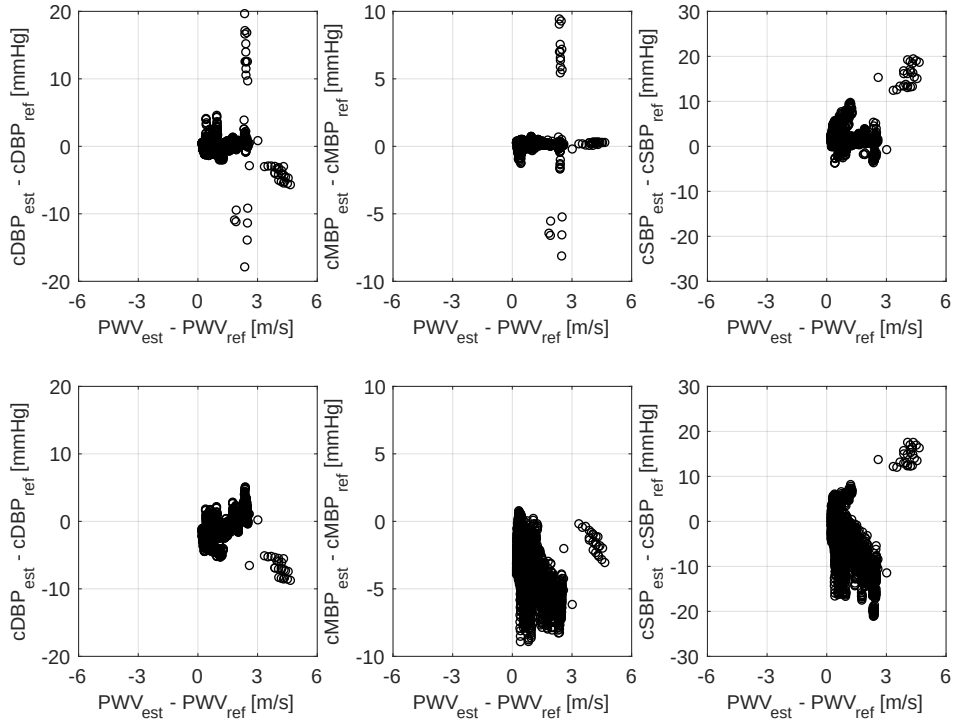

FIGURE 6.12: $cDBP$ (left), $cMBP$ (middle) and $cSBP$ (right) errors against PWV errors in the 1-D model dataset for the 1-D algorithm in Scenario 1 (top) and Scenario 2 (bottom).

Clusters of outliers were observed in the 1-D model dataset for the 1-D algorithm in both scenarios. These clusters correspond to those observed for PWV estimates in Figure 5.7 for both scenarios, as confirmed by Figure 6.12.

6.4.2 Central blood pressure algorithms

When choosing the computational models for the cBP estimation algorithms, 0-D models were chosen for their simplicity and low number of required CV parameters, and the 1-D aortic model was chosen because it captures pulse wave propagation phenomena, though at the expense of a much larger number of parameter estimations. The rationale behind the chosen arterial segments of the 1-D aortic model is twofold. Firstly, cardiac MRI generally provides arterial geometry and flow of the thoracic aorta only. Secondly, previous work showed that it is possible to reduce 1-D models containing a large number of arterial segments to a 1-D model containing fewer segments, decreasing the topological complexity of the arterial network and the number of parameters to be estimated, while sufficiently capturing relevant blood pressure values such as cSBP and cPP [4, 83].

Although the CV parameter estimation methods for the cBP algorithms were chosen according to the results from the 1-D dataset (Table 5.2, bottom), all possible combinations of optimal methods according to the 0-D datasets were also trialled. However, since cBP estimation errors were always similar or higher, and given that the 1-D dataset presents more 'physiological' pressure waves than the 0-D dataset, these results are not presented here.

In the 1-D aortic model, pulse wave velocity (PWV) is used to prescribe wall properties through an elastic tube law which relates pressure (P) and area (A):

$$P(A,x) = P_0 + \frac{\beta(x)}{A_0(x)}\left(\sqrt{A} - \sqrt{A_0(x)}\right), \tag{6.5}$$

where β is related to the wall elasticity, P_0 is the reference pressure (normally DBP), and A_0 is the reference area when $P = P_0$ [90]. Although PWV (and hence wall properties) increases along the aorta [74], clinical PWV can only be obtained locally (*e.g.* using the sum of squares method [153]) or as an average value over an arterial path (*e.g.* using the foot-to-foot method [91]). This limitation means that wall properties were not accurately prescribed in the 1-D aortic model. Furthermore, although nonlinear viscoelastic 1-D

models are more representative of arterial wall properties, current clinical data only allows the characterisation of an elastic model.

Bayesian optimization (a machine learning method) has been applied to a 1-D model of the arterial circulation to calculate outflow boundary conditions [166]. The ability to numerically generate datasets containing thousands of physiological virtual subjects opens up the possibility of testing machine learning methods, such as long short-term memory (LSTM) recurrent neural networks, to estimate cBP values from readily available non-invasive data [167–169].

6.5 Final remarks

In this chapter, fast algorithms for reconstructing the cBP waveform from non-invasive data have been developed. These algorithms use 0-D and 1-D computational models based on physical phenomena occurring in the upper-thoracic aorta and are patient-specific; *i.e.* all physical parameters except for blood density and viscosity can be calculated from non-invasive data obtained by tonometry or brachial cuffing, and ultrasound or magnetic resonance imaging. 0-D models were chosen for their simplicity and low number of CV parameters. The 1-D aortic model was chosen because it captures pulse wave propagation phenomena, though at the expense of a much larger number of parameter estimations. Only the upper-thoracic aorta was simulated using 1-D model segments, since cardiac MRI can generally provide arterial geometry and flow in the thoracic aorta only. Results showed that, when the aortic vascular geometry was available, the 1-D aortic algorithm outperformed the 0-D algorithms at estimating cBP wave morphology as well as $cSBP$ and cPP values, leading to RMSE $<2.0 \pm 1.0$ when all input data and reference cBP waves are free of measurement errors and $<6.4 \pm 2.8$ mmHg when considering clinical data with invasive reference cBP waves. When only the aortic flow and peripheral pressure waves were available, both 0-D models estimated $cDBP$, $cMBP$, $cSBP$, and cPP values with similar errors though the 3-element Windkessel algorithm produced the smallest RMSEs.

7 Haemodynamics in Dilated Cardiomyopathy

Some of the contents of this chapter are part of a manuscript submitted, as a joint-first author, to the *American Journal of Phisiology – Heart and Circulatory Phisiology* [2]. The aim of this study was to evaluate aortic structure and haemodynamics in dilated cardiomyopathy (DCM) using 4-D flow magnetic resonance imaging (MRI) and a "cohort-specific" 1-D model dataset – referred to as a "virtual cohort" in the manuscript and in this chapter, for consistency. A novel methodology to create a virtual cohort representative of three clinical groups – two groups of DCM patients, and one group of controls – was developed as an extension to the methodology described in Chapter 4. My main contributions towards the original manuscript, which included the creation of the 'cohort-specific' dataset and the analysis and discussion of the results, are presented and expanded on in this chapter. Additionally, a summary of each original section (*i.e.* Introduction, Methods, Results, Discussion and Conclusion), which I contributed towards through discussion and draft revisions, is provided for context. The manuscript and supplementary material are provided in Appendices A.3 and A.4 for reference[1].

7.1 Introduction

Although remodelling mechanisms and haemodynamics in the heart and arteries are closely related, cardiomyopathy patients are commonly assessed using cardiac metrics. However, aortic stiffness [170] and hypertension [171] have been related to dilated cardiomyopathy (DCM), and prognosis after cardiac resynchronization [172] and ventricular reverse remodelling [173] have been related to arterial behaviour. Medical imaging, and

[1]Note that, although this thesis follows British English spelling rules, the manuscript followed American English spelling rules.

particularly cardiac magnetic resonance imaging (MRI), is increasingly used for the clinical assessment of cardiovascular function. Recently, 4-D flow MRI has been shown to provide valuable clinical information about diastolic ventricular flow in DCM [174], aortic relative pressure [175–177], ventricular-vascular interaction in chronic heart failure [178], and right-ventricular-pulmonary coupling [179]. The aim of this study was to investigate ventricular-arterial interactions in DCM using aortic relative pressure (*i.e.* blood pressure difference between two aortic locations) derived from 4-D flow MRI. Additionally, a "virtual cohort" based on DCM patients and healthy volunteers was developed to study isolated effects of such interactions.

7.2 Methods

Figure 7.1 shows an overview of data sources and analysed cardiovascular (CV) parameters.

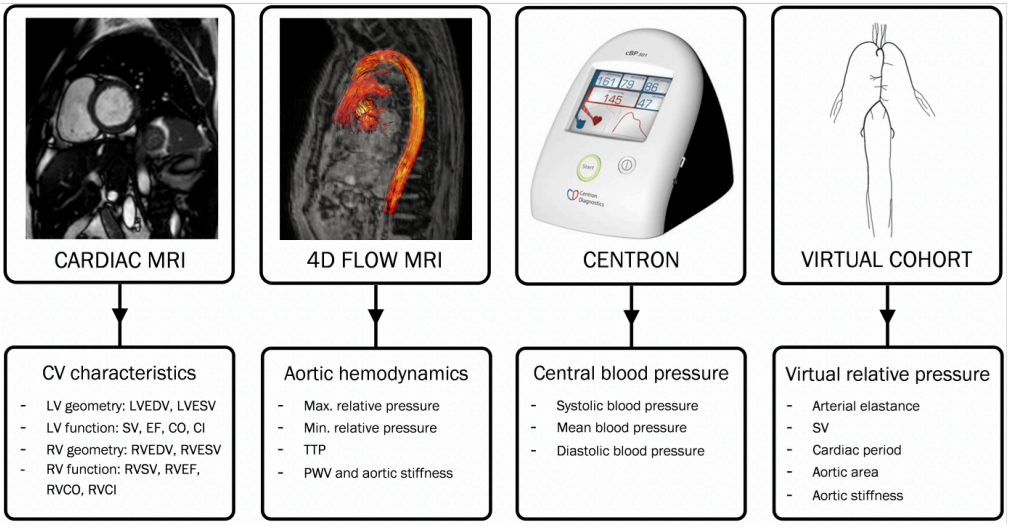

FIGURE 7.1: Overview of assessed study metrics. Cardiovascular (CV) characteristics were given by cardiac MRI, aortic haemodynamics were obtained from 4-D flow MRI, and central blood pressure from sphygmomanometer measurements. The isolated influence of listed CV parameters on aortic relative pressure is determined using a computational virtual cohort. LV: left ventricular; RV: right ventricular; EDV: end-diastolic volume; ESV: end-systolic volume; SV: stroke volume; EF: ejection fraction; CO: cardiac output; CI: cardiac index, PWV: pulse wave velocity; TTP: time-to-peak relative pressure.

7.2.1 Study population

The dataset included 14 patients treated for moderate DCM-related heart failure and 16 healthy controls. At the time of scanning, several DCM patients presented improved left ventricular (LV) function. As a result, DCM patients were divided into two groups: subjects with reduced LV function (DCM_{red}, EF $< 50\%$, n = 9) and subjects with preserved LV function (DCM_{pres}, EF $\geq 50\%$, n = 5). Prior to data collection, DCM patients had their beta blocker treatment discontinued for 48 hours to examine their native CV function. All subjects participated under informed consent, with data collection approved by the Regional Ethics Committee, South East London, UK (REC, 12/LO/1456). Subject characteristics are shown in Table 7.2.

7.2.2 Imaging, data collection, and post-processing

Full-field tissue structure and blood flow was quantified using structural and 4-D flow MRI (1.5 T, Philips ACHIEVA, Philips, Best, The Netherlands). Relevant cardiac indices were calculated for all subjects from the short-axis images using cvi42® (Circle Cardiovascular Imaging Inc, Alberta, Canada). The thoracic aorta was segmented for all subjects using an in-house algorithm implemented in MATLAB® R2016a (MathWorks, Natick, MA, USA). Aortic relative pressure was computed using a validated virtual work-energy approach (shown in Figure 7.2) [177]. The mathematical details of this computation are provided in Appendix A.4. Additionally, time-to-peak aortic relative pressure was computed as the time from acquisition onset (triggered by the ECG R-wave) to maximum relative pressure. Aortic pulse wave velocity was estimated from the ascending and descending aorta flow waves using a validated cross-correlation method [91]. Aortic stiffness was subsequently calculated using the Moens-Korteweg equation (Equation (7.1)). Finally, cBP was estimated using a validated transfer function device applied to the brachial cuff pressure wave (Centron cBP301®, SunTech Medical Inc., Morrisville, NC, USA).

7.2.3 Virtual cohort

Structural and functional CV characteristics can be studied by means of non-invasive imaging. However, the intertwined nature of ventricular-vascular interaction makes it

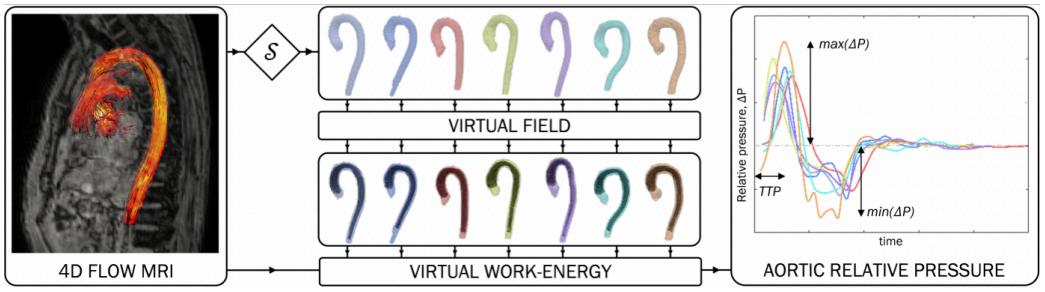

FIGURE 7.2: Overview of the virtual work-energy principle. This principle was used to derive aortic relative pressure (ΔP) from 4-D flow MRI (left). Aortic segmentations (S, upper mid-portion) are shown together with corresponding virtual work-energy fields (lower mid-portion), used to isolate aortic relative pressure. Maximum relative pressure, minimum relative pressure, and time-to-peak relative pressure (TTP) are derived (right). Each case is processed individually, with the colour coding of the segmentations corresponding to the ones of the relative pressure traces.

difficult to isolate independent factors that impact CV function. Computational modelling, however, allows for the study of the CV system while also enabling controlled variation of isolated factors (*e.g.* stroke volume, aortic pulse wave velocity). To understand aortic relative pressures, the methodology presented by Willemet *et al.* [82] was used to create a novel virtual cohort, where blood pressure (BP), blood flow, and arterial area waveforms were simulated using a validated one-dimensional (1-D) computational model of arterial haemodynamics consisting of the 55 larger arteries of the human systemic circulation [90]. Importantly, such models have been extensively validated and verified to accurately represent 1D arterial hemodynamic behavior through the larger arterial system [73, 74].

The methods used to create the virtual cohort were adapted to match the clinical characteristics for arterial resistance (R_{T}), stroke volume (SV), cardiac period (T), aortic area (A), and aortic pulse wave velocity (PWV). A virtual group was created for each clinical group: virtual DCM patients with reduced and preserved LV function (DCM_{red} and DCM_{pres}, respectively) and virtual controls. For each virtual group, a baseline virtual subject was first created to match the mean of the clinical characteristics shown in Table 7.1. For each parameter under study, two virtual subjects were then created by varying said parameter whilst keeping the remaining parameters at baseline level. Parameter variations corresponded to the 'min' and 'max' values shown in Table 7.1, respectively. Thus, 11 (1 baseline $+2 * 5$ variations) virtual subjects were created for each virtual group, and the isolated influence on aortic relative pressure from R_{T}, SV,

T, aortic A, and aortic PWV could be evaluated. Input CV parameter values for each virtual group (all originating from the clinical acquisitions) are presented in Table 7.1.

TABLE 7.1: Cardiovascular (CV) parameter variations for each virtual group with all data derived from *in vivo* imaging. For each group, the baseline virtual subject corresponded to the mean CV parameter value. Each additional virtual subject within that group corresponded to the variation of a single, isolated CV parameter (varied from minimum to maximum, one at a time). [1] [mmHg s/mL]

	Virtual DCM$_{red}$			Virtual DCM$_{pres}$			Virtual controls		
CV parameters	min	mean	max	min	mean	max	min	mean	max
Arterial resistance, [1]	0.69	0.77	0.84	0.64	0.89	1.2	0.61	0.78	1.04
Stroke volume, [mL]	55	95.5	132	53	86	100	66.3	91.7	122.9
Cardiac period, [s]	0.75	0.91	1.13	0.59	0.8	1	0.7	0.88	1.03
Aortic area, [cm^2]	1.86	2.96	3.87	1.21	1.96	2.72	1.72	2.49	3.66
Aortic PWV, [m/s]	6.1	11	19.4	5.2	7.7	10	4.5	7.5	13.9

Similarly, flow profiles were generated based on through-plane left ventricular outflow tract ($LVOT$) flows from the 4-D flow MRI of each group, respectively. For each virtual subject, aortic relative pressure was calculated from the $LVOT$ to the end of the thoracic aorta, with relative pressure normalized by aortic length to match the derived clinical data.

General cardiovascular parameter values, which were kept constant over all virtual subjects, were taken from Willemet *et al.* [82] and modified when appropriate. The parameters (and their corresponding values) were: blood density (1050 kg/m^3), blood viscosity (0.0025 Pa s), velocity profile coefficient (1.33, corresponding to Poiseuille flow), and outflow pressure, P_{out} (0 Pa). 1-D simulations were run for a total of 20 s, with a 0.1 ms time step to ensure numerical convergence according to Equation (3.8). Remaining numerical parameters were chosen as described in Section 3.3.4. Additionally, a visual check of all simulated pressure waveforms at the aortic root and the end of the thoracic aorta was employed to confirm convergence.

For each virtual group, left ventricular ejection time ($LVET$) and time-to-peak flow (TTP) were extracted from the corresponding clinical flow data. Firstly, flow waveforms containing less than 100 datapoints were filtered using a 100-point spline interpolation to ensure sufficient smoothness. Secondly, the filtered wave was modulated to enforce zero flow during diastole by: (i) contructing a tangent to the point of maximum negative

slope during the systolic downslope, (ii) finding the intercept between this tangent and the x-axis, and (iii) making the flow equal to zero from this point until the end of the cycle. Finally, $LVET$ was extracted as the first zero flow value during diastole using the novel $LV4$ method proposed in Section 5.2.1, and TTP was extracted as the time of maximum flow. For each group, the average values of $LVET$ and TTP were used to generate the virtual flow profiles.

R_{T} values were calculated from mean pressure (MBP, in mmHg) and mean flow ($\overline{Q}$, in mL/s) values from each clinical group using Equation (5.2), with P_{out} equal to zero in this study.

The clinical aortic lengths ranged from 21 to 38 cm. These values were extracted by collaborators from the centrelines obtained using the approach presented in [177]. However, this data did not include all the aortic sections of interest (*i.e.* from the aortic root to the end of the thoracic aorta), so all the aortic segment lengths for the virtual cohort were taken from [82]. Therefore, relative pressure was calculated between the start and end points of the arterial path along the following aortic segments (see indices in Figure 7.3): ascending aorta (1), aortic arch (2 and 14), and thoracic aorta (18 and 27). The combined length of these virtual segments was 30.6 cm, a value which falls within the extracted clinical values (21-38 cm). Virtual aortic segment areas (at DBP) were initially extracted from [82]. Then, the areas corresponding to the aortic segments noted as 1, 2, 14, 18, 27, 28, 35, 37, 39, and 41 in Figure 7.3 were scaled according to the ratio between clinical and virtual average aortic areas calculated as follows:

- a weight was given to each segment based on the ratio between segment length and total aortic length (*i.e.* 30.6 cm);
- each weight was multiplied by its corresponding virtual segment average area (calculated as the average of the inlet and outlet areas, which is correct for linearly-tapered arterial segments);
- the virtual average aortic area was calculated as the sum of these weighted average areas;
- the clinical average aortic area was calculated as the average area of the MRI aortic geometry;

- the "area scaling factor" was calculated as the ratio between clinical and virtual average aortic areas.

Remaining virtual segment areas (*i.e.* those not corresponding to the aorta) were taken from the original reference.

Aortic stiffness was calculated using the Moens-Korteweg equation [124]:

$$E = \frac{2PWV^2 r\rho}{h}, \tag{7.1}$$

where 'h' is the arterial wall thickness and was set to 1.6 mm [180], and ensuring that PWV in the virtual groups was equal to the PWV values extracted from each clinical group. PWV was imposed in the 1-D model using the empirical tube law described in Equation (5.13). The following iterative method was used to calculate the value of k_3 which minimised the absolute difference between the desired (clinical) and the theoretical average aortic PWVs [3]:

- an initial set of constants was provided: inlet and outlet segment radii, segment lengths, desired average aortic PWV, blood density, and three empirical constants, k_1, k_2, and k_3;
- the theoretical average PWV for each segment was calculated using Equation (5.13), with r calculated as the average of the inlet and outlet radii;
- the theoretical wave transit time (TT) for each segment was calculated by dividing the segment length by its theoretical average PWV;
- the theoretical average aortic PWV was calculated by dividing the total aortic length by the sum of all TTs;
- *fminsearch.m*, a MATLAB® minimisation function, is used to find the value of k_3 – while keeping k_1 and k_2 constant – which minimises the absolute difference between desired and theoretical average aortic PWVs.

Although the subdivision into two groups of DCM patients is not ideal from the modelling perspective and given the small number of patients, it was imposed by the main clinical analysis. Ideally, DCM patients should be grouped to work with a more representative sample of the disease.

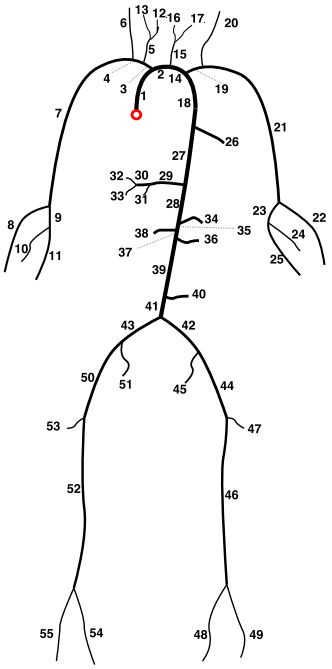

FIGURE 7.3: Arterial network of the 1-D model used to create the virtual cohort. It contains the 55 larger arteries of the human systemic circulation. Aortic relative pressure was calculated between the aortic root (inlet of segment 1) and the thoracic aorta (outlet of segment 27). The "area scaling factor" was applied to the segments along the aortic path starting at segment 1 and ending at segment 41.

7.2.4 Statistical analysis

Statistical differences in subject characteristics, cardiac metrics, and aortic outputs were evaluated to assess potential correlations between subject characteristics and output metrics. All evaluations were performed using MATLAB® R2016a (MathWorks, Natick, MA, USA).

7.3 Results

7.3.1 Clinical data and subject characteristics

Clinical data and subject characteristics are provided in Table 7.2. The DCM_{red} group showed significantly higher body mass index, LV volumes and systolic and mean BP; and significantly lower EF, LV cardiac index (CI) and right ventricular CI than the controls. In comparison, the DCM_{pres} group only differed from the controls in EF (56.6% versus 63.9%).

7.3.2 Aortic relative pressure in dilated cardiomyopathy patients

Aortic relative pressure characteristics are provided in Table 7.2, with Figure 7.4 showing the flow-derived markers where significant differences were inferred.

TABLE 7.2: Data and subject characteristics for the reduced LV function (DCM_{red}), preserved LV function (DCM_{pres}), and control groups, respectively. Intragroup p-values are reported with significant differences indicated by * ($p<0.05$), ** ($p<0.01$), or *** ($p<0.001$). Volumes are normalized by body surface area (BSA). [1][mL/m^2], [2][mmHg/m], [3][ms].

				p-value		
	DCM_{red} (n = 8)	DCM_{pres} (n = 5)	Controls (n = 16)	DCM_{red} Controls	DCM_{pres} Controls	DCM_{red} DCM_{pres}
Characteristics						
Age [years]	50.9 ± 5.5	42.8 ± 15.5	42.4 ± 12.4	0.08	0.97	0.52
Height [cm]	169.8 ± 5.8	165.6 ± 10.4	173.0 ± 8.7	0.35	0.17	0.45
Weight [kg]	87.8 ± 15.7	73.8 ± 24.1	72.3 ± 14.9	0.02*	0.8	0.33
BSA [m^2]	2.05 ± 0.22	1.83 ± 0.35	1.85 ± 0.23	0.05	0.97	0.28
Male / Female [n]	4 / 4	3 / 2	9 / 7	0.77	0.88	0.72
HR [beats/min]	66 ± 10.5	75.2 ± 15.8	68.3 ± 8.0	0.4	0.38	0.33
Cine SSFP MRI						
LVEDV/BSA [1]	109.6 ± 38.9	86.7 ± 21.5	78.5 ± 9.4	0.03*	0.69	0.44
LVESV/BSA [1]	69.2 ± 33.1	37.2 ± 11.9	28.8 ± 6.6	0.0003***	0.18	0.04*
SV/BSA [1]	46.1 ± 10.9	47.0 ± 6.2	49.6 ± 5.5	0.56	0.5	0.94
EF [%]	41.6 ± 5.7	56.6 ± 6.1	63.9 ± 5.9	0.0001***	0.04*	0.002**
CO [L/min]	6.1 ± 1.1	6.3 ± 1.1	6.2 ± 1.0	0.67	0.97	0.83
CI [$L/(min/m^2)$]	2.9 ± 0.4	3.5 ± 0.4	3.4 ± 0.5	0.03*	0.62	0.04*
RVEDV/BSA [mL]	86.0 ± 28.5	76.9 ± 13.1	84.7 ± 8.6	0.97	0.3	0.83
RVESV/BSA [mL]	44.3 ± 9.4	29.6 ± 7.7	36.0 ± 5.3	0.81	0.07	0.52
RVSV/BSA [mL]	44.3 ± 9.4	47.1 ± 6.1	49.5 ± 5.5	0.21	0.56	0.52
RVEF [%]	53.3 ± 8.2	61.8 ± 4.7	58.3 ± 4.1	0.26	0.2	0.12
RVCO [L/min]	5.9 ± 1.1	6.3 ± 1.1	6.2 ± 1.0	0.46	1	0.5
RVCI [$L/(min/m^2)$]	2.9 ± 0.4	3.5 ± 0.4	3.4 ± 0.5	0.02*	0.69	0.02*
Aortic curvature [-]	0.5 ± 0.1	0.5 ± 0.0	0.5 ± 0.1	0.93	0.97	0.52
Aortic length [cm]	27.8 ± 4.8	26.9 ± 3.1	25.5 ± 2.1	0.43	0.71	0.83
Aortic radius [cm]	0.8 ± 0.1	0.6 ± 0.1	0.7 ± 0.1	0.15	0.08	0.03*
cBP						
SBP [mmHg]	125.3 ± 8.8	116 ± 10.2	116.9 ± 8.8	0.02*	0.99	0.17
DBP [mmHg]	75.5 ± 5.6	69.6 ± 7.3	71.4 ± 5.8	0.12	0.43	0.11
MBP [mmHg]	86.8 ± 4.9	79.6 ± 7.8	81.3 ± 6.3	0.03*	0.51	0.06
4-D flow MRI						
Maximum $\Delta P/L$ [2]	61.6 ± 10.0	79.4 ± 13.8	78.9 ± 18.0	0.02*	0.65	0.02*
Minimum $\Delta P/L$ [2]	-41.3 ± 5.6	-58.3 ± 25.9	-39.4 ± 12.3	0.23	0.06	0.17
Time-to-peak ΔP [3]	109 ± 22	108 ± 38	55 ± 22	0.0002***	0.01*	0.91
PWV [m/s]	11.0 ± 4.6	7.5 ± 2.5	7.5 ± 2.6	0.03*	0.97	0.13
Aortic stiffness [kPa]	14.5 ± 12.0	5.5 ± 3.6	6.3 ± 5.1	0.03*	0.84	0.13

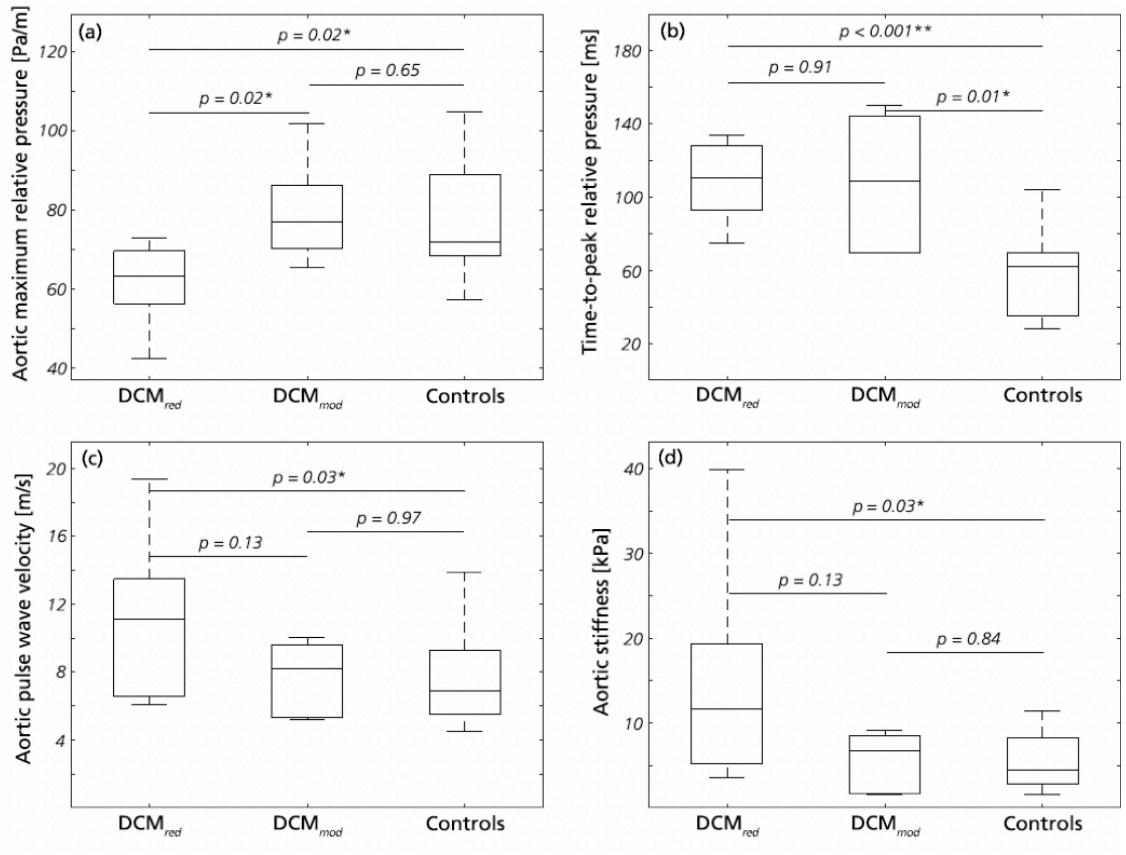

FIGURE 7.4: A comparison of aortic parameters between dilated cardiomyopathy subjects (with reduced and preserved LV function) and controls. (a) Maximum relative pressure, (b) TTP, (c) PWV, and (d) aortic stiffness for DCM$_{red}$, DCM$_{pres}$, and the control groups, respectively. p-values are reported throughout with significance indicated by * ($p<0.05$) or ** ($p<0.01$).

7.3.3 Correlation of aortic relative pressure with clinical, structural, and central blood pressure metrics

Complete correlation results are provided in Supplementary Table 2 (Appendix A.4). For the DCM$_{red}$ and DCM$_{pres}$ groups, no correlations could be inferred between any clinical parameter and the derived aortic metrics, including central blood pressures. For the control group, similar behavior was observed, with only body surface area and body mass index correlated to minimum relative pressure and aortic stiffness, respectively.

7.3.4 Influence of isolated cardiovascular parameters on aortic relative pressure

The isolated influence of CV parameters on aortic relative pressure was analysed using the virtual cohort. Aortic relative pressure for each virtual group, together with the

corresponding clinical traces, are shown in Figure 7.5.

For the virtual cohort, aortic maximum relative pressure varied within a range of 23.9 – 56.5, 28.3 – 62.5, and 30.4 – 72.1 Pa/m for the reduced LV function (DCM_{red}), preserved LV function (DCM_{pres}), and control groups, respectively. For reference, the clinical cohort showed variations of 61.2 ± 10.0, 79.6 ± 14.2, and 78.9 ± 18.0 Pa/m within the same three groups, respectively.

Aortic stiffness and aortic area were the two dominant CV parameters influencing maximum relative pressure. Specifically, variations in aortic stiffness accounted for 47% of the possible variations in maximum relative pressure in the DCM_{red} group, 63% in the DCM_{pres} group, and 100% in the control group. Similarly, variations in aortic area accounted for 87, 91, and 73% of the possible variations in maximum relative pressure in the same three groups, respectively. Cardiac parameters had an inferior influence, with variations in SV accounting for 67, 46 and 46% of the possible variations in the DCM_{red}, DCM_{pres}, and control groups, respectively. Aortic maximum relative pressure values as a function of individual CV parameter variations are given in Table 7.3.

For minimum relative pressure, similar behaviour could be observed where aortic stiffness and aortic area were the two major contributors to the observed variations, with aortic stiffness equalling 70, 63, and 94% of the total variations, and aortic area equalling 95, 100, and 92% (again reported for the DCM_{red}, DCM_{pres}, and control groups, respectively). Aortic minimum relative pressure values as a function of individual CV parameter variations are given in Table 7.4.

TABLE 7.3: Virtual cohort analysis: aortic maximum relative pressure per unit length. Variations in relative pressure are shown as a function of isolated variations of arterial resistance, stroke volume, cardiac period, aortic area, and aortic stiffness, respectively. Data provided for mean (baseline), minimum and maximum range, with all values reported in mmHg/m. The bottom row shows the complete range of aortic maximum relative pressure over all variations.

	Virtual DCM_{red}			Virtual DCM_{pres}			Virtual controls		
CV parameters	min	mean	max	min	mean	max	min	mean	max
Arterial resistance	36.3	36.5	36.7	39.8	42.0	43.8	49.4	51.3	52.5
Stroke Volume	23.9	36.5	45.6	30.1	42.0	46.0	41.5	51.3	60.8
Cardiac period	35.9	36.5	37.2	42.7	42 .0	42.9	50.2	51.3	51.3
Aortic area	28.1	36.5	56.5	31.5	42.0	62.5	38.1	51.3	68.5
Aortic stiffness	26.5	36.5	41.9	28.3	42.0	49.7	30.4	51.3	72.1
All CV parameters	23.9	36.5	56.5	28.3	42.0	62.5	30.4	51.3	72.1

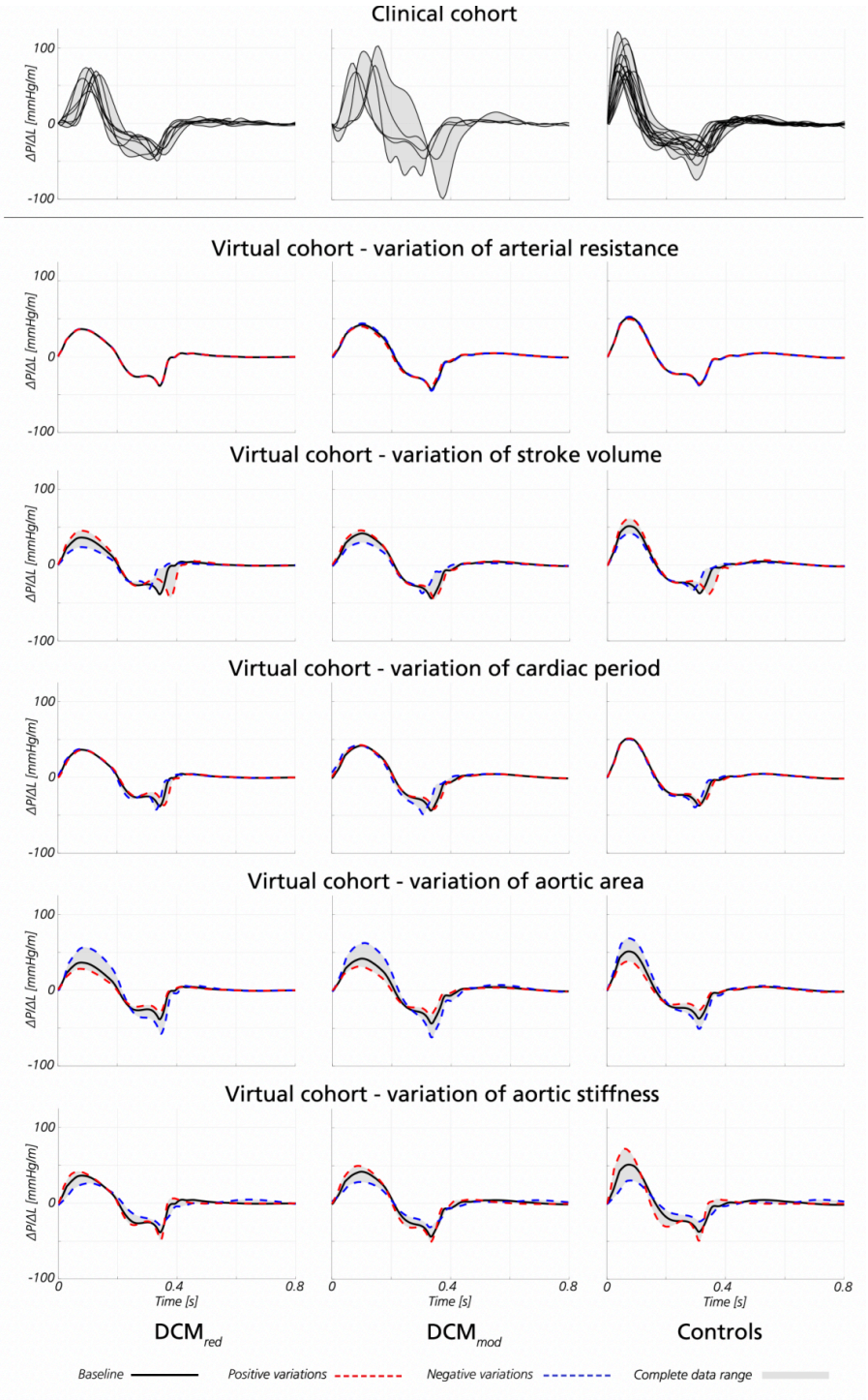

FIGURE 7.5: Aortic relative pressure traces from clinical and virtual analysis. Aortic relative pressure traces from the clinical (top row) and virtual cohort (remaining rows), presented as a function of isolated variations of arterial resistance, stroke volume, cardiac period, aortic area, and aortic stiffness, respectively. Relative pressure is shown for DCM_{red} (left), DCM_{pres} (middle), and controls (right). For the clinical data, each individual subject is given in black. For the virtual data, isolated variations around baseline (black) are given as positive variations (red) and negative variations (blue), respectively, superimposed on the data range (grey).

TABLE 7.4: Virtual cohort analysis: aortic minimum relative pressure per unit length. Variations in relative pressure are shown as a function of isolated variations of arterial resistance, stroke volume, cardiac period, aortic area, and aortic stiffness, respectively. Data provided for mean (baseline), minimum and maximum range, with all values reported in mmHg/m. The bottom row shows the complete range of aortic maximum relative pressure over all variations.

	Virtual DCM_{red}			Virtual DCM_{pres}			Virtual controls		
CV parameters	min	mean	max	min	mean	max	min	mean	max
Arterial resistance	-38.4	-38.5	-38.7	-45.2	-43.8	-41.9	-38.5	-37.5	-36.1
Stroke Volume	-42.8	-38.5	-32.2	-45.0	-43.8	-37.2	-38.9	-37.5	-34.1
Cardiac period	-43.0	-38.5	-37.1	-49.0	-43.8	-42.0	-39.8	-37.5	-36.4
Aortic area	-57.8	-38.5	-30.2	-62.2	-43.8	-33.2	-51.1	-37.5	-26.5
Aortic stiffness	-49.0	-38.5	-28.9	-50.7	-43.8	-31.4	-49.2	-37.5	-23.9
All CV parameters	-57.8	-38.5	-28.9	-62.2	-43.8	-31.4	-51.1	-37.5	-23.9

7.4 Discussion

Aortic relative pressure in DCM has been assessed using 4-D flow MRI in this study, uncovering a set of significant hemodynamic alterations. At inclusion, all patients reported DCM-related heart failure, however, the imaging session was not performed until after treatment had been initiated. During this period, patients had the chance to respond to therapy, and the DCM group was consequently split in two: a responding DCM_{pres} group, and a non-responding DCM_{red} group. Thus, indicated hemodynamic changes could be examined in conjunction to patient treatment response.

7.4.1 Changes in aortic relative pressure – relation to cardiac and aortic physiology

The DCM_{red} group showed a significantly reduced maximum aortic relative pressure. The corresponding differences in aortic relative pressure between the DCM_{red} and DCM_{pres} groups indicate that differences in cardiac function are reflected on the vascular side. In previous studies, DCM has been associated with a reduction in peak aortic outflow acceleration [181]; deteriorating cardiovascular status in DCM has been correlated to a decrease in $LVOT$ outflow gradients [182]; and aortic relative pressure has been directly correlated to LV remodelling [175]; highlighting how ventricular dilation affects vascular

hemodynamics. Together with this study's findings, this indicates how vascular response could be used as a potential surrogate measure for intrinsic cardiac behaviour.

In contrast, no significant differences could be inferred for minimum aortic relative pressure. Minimum aortic relative pressure, which is related to the deceleration of blood during late systole, has been linked to aortic reservoir function [183] rather than cardiac disease. However, with apparent differences in aortic stiffness suggesting reservoir differences between DCM_{red} and DCM_{pres} groups, this indicates an intertwined relationship between cardiac status, aortic function, and relative pressure. In other diseases, aortic relative pressure has been related to both cardiac and aortic physiology [184], supporting the notion of coupled cardiac and vascular hemodynamic behaviour.

In comparison to the above, TTP is a metric directly coupled to the contractile pumping efficiency of the left ventricle: the shorter the TTP the faster the ventricular contraction. In this study, a significant delay in TTP was observed in DCM patients regardless of LV function, with an almost doubling of the time required to reach peak driving acceleration, indicating that an underlying electrocardiac pathophysiology seems to persist. In DCM, ventricular conduction delay is commonly reported [185] and it has been shown to be a powerful prognosis predictor [186]. Current findings on TTP seem to indicate the presence a conductive abnormality masked by the pharmaceutically improved cardiac output.

A significant increase in PWV and aortic stiffness was reported in the DCM_{red} group. Arterial stiffening in DCM patients has been described previously [170] and reduced maximum relative pressure was recently reported in an elderly cohort [175], connecting reduced aortic acceleration to increased arterial stiffness in a similar way to how findings from this study connect reduced relative pressure with increased aortic stiffness. In general, arterial stiffening is a commonly ascribed vascular response mechanism following cardiovascular disease development where – in the case of impaired ventricular efficiency – increased arterial stiffening may arise to help maintain a timely forward-flow of blood into the peripheral circulation.

Lastly, the DCM_{red} group showed significantly increased systolic blood pressure compared to the control group. This increase in afterload is however not coupled to any variations in SV, signalling that an increase in ejection force is required to maintain systemic circulation. Besides, an increase in mean blood pressure indicates elevated systemic

resistance in the same group. However, this is slightly opposed by unaltered diastolic blood pressure. In general, the development of hypertension is common in DCM [187]. It highlights a persistent detrimental remodeling feedback loop, in which long-term congestion leads to increased afterload due to sympathetic activation. The chronic overload of the ventricle thus in turn leads to worsening contractile properties.

7.4.2 Correlation to aortic relative pressure – independent role of aortic hemodynamics

The correlation analysis revealed a general lack of defined relationships between aortic hemodynamics and standard metrics for the DCM patients. However, aortic metrics derived in this study provided a clear differentiation for the DCM_{red} group, separating responding from non-responding DCM patients. Furthermore, the independent association between aortic relative pressure and LV remodelling [175] has been indicated, highlighting relative pressure as a complementary and independent biomarker for refined cardiac diagnosis.

7.4.3 The role of isolated cardiac and aortic parameters on relative pressure – virtual cohort study

Out of the evaluated metrics in the virtual cohort analysis, aortic stiffness and area were the main determinants of aortic relative pressure. While positive variations in stiffness increased relative pressure magnitudes, positive variations in area decreased them (see Figure 7.5, two last rows). The combination of these two phenomena could explain the similar minimum relative pressures observed in DCM patients and controls (see Figure 7.5, first row). However, this does not explain the observed decrease in maximum relative pressure with decreased LV function. This reduction could instead be attributed to cardiac changes such as modified contractility [188] or a lack of contractile coordination [185], but could also be influenced by coupled reservoir behaviour. Nevertheless, the combination of clinical and computational results indicate adapted reservoir function and altered cardiac conductivity, both present in DCM.

7.4.4 Aortic change in DCM – clinical implications of image-based findings

A number of aortic hemodynamic changes have been inferred for DCM. Non-responding DCM_{red} patients showed depressed relative pressure, delayed TTP, increased aortic stiffness and increased systolic blood pressure, whereas responding DCM_{pres} patients showed a comparable normalisation of aortic metrics. Considering the fact that all DCM patients followed the same treatment protocol, this separation is particularly noteworthy, and could in fact indicate that cardiac treatment efficacy is coupled to vascular adaption abilities.

Antihypertensive medications have been shown to reduce arterial stiffness [189], being part of a general strategy to hinder continuous dilation through ventricular unloading. Poor vascular adaption in non-responders could keep the ventricle in a state which requires excessive work to maintain systemic perfusion due to increased BP and aortic stiffness. Furthermore, with sustained hypertension correlated to aortic dilation [190], and with aortic area decreasing relative pressure, these patients will experience decreased acceleration of the ejected blood, potentially affecting long-term stable systemic circulation. If additional medication could decrease stiffness or BP, a continuous unfavourable depression of relative pressure could follow. Thus, through poor vascular adaption, the general treatment potentially fails in unloading the heart, instead pushing it further down a pathological remodelling spiral. Using arterial function as a measure of drug effectiveness is not a new concept [191], but this study indicates that unloading the heart requires a unified look at cardiac, aortic, and systemic function.

7.4.5 Clinical outlook – non-invasive imaging for the assessment of ventricular-vascular function

4-D flow MRI permits detailed hemodynamic analysis and improves the assessment of cardiovascular disease[175–177, 192]. This study has shown that aortic hemodynamics are altered in cardiac disease, and that aortic relative pressure can be directly connected to cardiac and vascular function, as well as potential treatment efficacy, highlighting clinical impact of refined flow imaging. The proposed biomarkers can thus be added as a complement to the traditional diagnostic procedure. Further studies are required to

uncover the initiation and sequential order of the remodelling response, however, imaging has the potential to play a key role in studying such behaviour in a non-invasive setting.

7.4.6 Limitations

A fairly small sample size was used, and the generalisation of these findings to a global DCM population is potentially limited. However, since the statistical methods incorporated sample size effects, the observed behaviour might still be representative of aortic change in DCM.

For the virtual cohort, the analysis was limited to a selection of conventional CV parameters (*i.e.* R_{T}, SV, T, A and PWV). Additional parameters (*e.g.* varying $LVET$, $LVOT$ outflow gradient) could be included in order to disentangle cardiac and aortic influence. The virtual cohort also showed slightly lower relative pressure compared to the retrieved clinical data in all three subgroups. While some characteristics (*e.g.* SV, T) were tailored to reflect DCM behaviour, other (*e.g.* aortic lengths) were retrieved from published literature values on healthy subjects. Consequently, these underlying baseline characteristics might not be entirely reflective of the assessed clinical cohort and might cause the observed bias. Nonetheless, with virtual and clinical cohorts showing similar trends with respect to aortic relative pressure (*i.e.* decreasing relative pressure with increasing LV impairment), this may indicate that the influence of evaluated cardiovascular parameters on the virtual cohort is reflective of similar behaviour on the clinical side.

7.5 Conclusion

In this study, 4-D flow MRI and computational modelling were used to study aortic relative pressure in DCM. Significant aortic hemodynamic changes were observed, relating to specific physiological aspects of the disease: decreased maximum relative pressure indicating affected ventricular ejection, prolonged time-to-peak relative pressure indicating remaining latent conduction delay, and increased aortic stiffness and systolic blood pressure indicating pathological arterial remodelling. With the aortic response separating responders from non-responders, vascular adaption could be a novel marker in assessing treatment efficacy in DCM. Similarly, with the assessed hemodynamic metrics uncorrelated to conventional diagnostic metrics, complementary diagnostic value could

be achieved through aortic assessment. Overall, the study highlights the clinical value of vascular adaption in DCM and shows how ventricular-vascular interactions can be effectively studied using 4-D flow MRI and computational models of the systemic circulation.

8 Conclusions

This chapter contains a summary of the achievements of this thesis (Section 8.1) and directions for future work (Section 8.2).

8.1 Summary of Achievements

This thesis has successfully achieved the aim and objectives outlined in Section 1.2. The aim and main achievement of this thesis was the development and assessment of algorithms to estimate central blood pressure (cBP) from clinical data obtained non-invasively. This was achieved using 0-D and 1-D computational models of fluid dynamics, which augment the clinical data obtained from ultrasound and magnetic resonance imaging by providing an accurate, patient-specific, non-invasive estimate of cBP.

Chapters 4 to 7 present the research done to address the individual objectives. Additionally, Chapter 7 presents a clinical cohort study where some of the methods developed in the previous chapters were applied and extended. The individual achievements of this thesis are summarised below for each chapter.

Chapter 4: Datasets

The main achievement of Chapter 4 was the creation of three *in silico* datasets, each containing thousands of healthy virtual subjects with unique cardiovascular (CV) parameters and haemodynamic waves. The cardiovascular parameters were extracted from the clinical literature for healthy adults. For all virtual patients in each dataset, the haemodynamic waves (*i.e.* flow, pressure, and area) were simulated using a different

computational model of arterial blood flow. These waves were available at the aortic root for all three datasets, and at additional locations (*e.g.* carotid and brachial arteries) for a dataset created using a 1-D model. The unique cardiovascular parameters and haemodynamic waves from each virtual patient – free of experimental error due to their *in silico* nature – were used as reference data for the development and assessment of algorithms for the estimation of cardiovascular parameters (Chapter 5) and cBP (Chapter 6). These datasets are also a valuable tool for developing and assessing future methods for cardiovascular parameter or cBP estimation. This chapter also presented the creation of a "cohort-specific" *in silico* dataset based on the characteristics of dilated cardiomyopathy patients and healthy controls.

This chapter also described three *in vivo* datasets containing reference cardiovascular data. Several post-processing operations were performed to make the *in vivo* datasets ready to be used in the next chapters. Invasive aortic blood pressure waves – obtained via cardiac catheterisation – and aortic geometry and blood flow measurements – acquired from cardiac magnetic resonance scans – were available for a dataset of "Aortic Coarctation" patients. The other two datasets corresponded to a "Normotensive" and a "Hypertensive" dataset, respectively. Both datasets contained aortic flow measured using ultrasound, non-invasive peripheral blood pressure waves from carotid applanation tonometry, and non-invasive cBP waves calculated using the SphygmoCor® device. Similarly to the 1-D model *in silico* datasets, the *in vivo* datasets were used as reference data for the assessment of algorithms for the estimation of cBP (Chapter 6).

Chapter 5: Cardiovascular Parameter Estimation

The main achievement of Chapter 5 was to identify optimal methods to estimate cardiovascular parameters from non-invasive clinical data. To achieve this, a comprehensive literature review was performed to find current methods to estimate cardiovascular parameters was performed. Additionally, novel methods were developed for some cardivoascular parameters. Current and novel methods were assessed using the three datasets of virtual subjects presented in this chapter as reference data. The six cardiovascular parameters of interest were: left-ventricular ejection time, asymptotic pressure, arterial resistance, arterial compliance, pulse wave velocity, and characteristic impedance (Z_0).

For each dataset, all parameters but Z_0 were estimated with mean absolute errors smaller $< 10\%$. Z_0 was the most challenging parameter, with 16% errors when using the carotid blood pressure wave, and 82% errors when only using brachial diastolic and systolic blood pressure values. For any virtual subject, estimating all six cardiovascular parameters using the optimal methods took less than one second on a standard PC. These methods were combined with three different computational models of arterial blood flow to develop the algorithms to estimate cBP presented in (Chapter 6).

Chapter 6: Central Blood Pressure Estimation

The main achievement of Chapter 6 was the development of three novel cBP estimation algorithms using optimal cardiovascular parameter estimation methods and three computational models of arterial blood flow. These algorithms were then tested on three clinical datasets and one dataset of virtual subjects. Each dataset contained reference central blood pressure and flow waves.

Each algorithm used one of three computational models of arterial blood flow – the two-element or three-element Windkessel models, or a 1-D model of the larger systemic arteries – in combination with the optimal cardiovascular parameter estimation methods identified in Chapter 5. These algorithms were developed using reference haemodynamic waves from the 1-D model dataset of virtual subjects, and tested *in vivo* using three clinical datasets.

In the "Aortic Coarctation" dataset – the only *in vivo* dataset containing aortic geometry and invasive aortic pressure measurements – the 1-D model algorithm led to smaller systolic blood pressure and pulse pressure mean absolute errors ($< 4.1 \pm < 10.7$ mmHg) than the 0-D model algorithms ($< 17.3 \pm < 9.2$ mmHg). In the "Normotensive" and "Hypertensive" datasets, both 0-D model algorithms estimated blood pressure values similarly with errors $< 6.0 \pm 4.9$ mmHg, although according to the root mean square error, the three-element Windkessel outperformed the two-element Windkessel ($< 5.9 \pm 2.4$ mmHg vs $< 10.6 \pm 4.1$ mmHg). Interestingly, errors for the 0-D models were considerably smaller when using brachial DBP and MBP instead of the entire carotid pressure wave. This study has shown that, in a clinical setup where the aortic geometry can be acquired, a 1-D model of the upper-thoracic aorta can simulate aortic haemodynamics more accurately than 0-D models. These findings will be useful to augment the clinical

data from cardiac magnetic resonance and ultrasound scans, providing a patient-specific, non-invasive estimate of cBP.

Chapter 7: Haemodynamics in Dilated Cardiomyopathy

The main achievement of Chapter 7 was the development and analysis of the first cohort-specific dataset of virtual subjects. This chapter was part of an *in vivo* and *in silico* study investigating the influence of individual cardiovascular parameters on the aortic pressure gradient of dilated cardiomyopathy (DCM) patients. While previous datasets were created using the characteristics of healthy subjects found in the clinical literature only, this cohort-specific dataset contained virtual patients created from the characteristics of DCM patients. Subjects from this dataset were divided into three groups: healthy controls, DCM patients with moderate cardiac function, and DCM patients with reduced cardiac function.

Significant differences in aortic hemodynamics, relating to specific aspects of the disease, were observed in DCM patients: decreased maximum relative pressure; prolonged time-to-peak relative pressure; and increased aortic stiffness and systolic blood pressure. These findings suggest that, in DCM patients, arterial remodelling could be a novel marker in assessing treatment efficacy, and that these four hemodynamic metrics could provide additional diagnostic value. Furthermore, the added value of a cohort-specific *in silico* analysis for the study of the independent physical mechanisms behind a cardiovascular disease has been shown.

"Disease-specific" datasets of virtual patients can be helpful in pre-clinical studies to better understand the role played by haemodynamics in a given disease. However, the virtual patients contained in these datasets represent a range of average population CV parameters rather than those of a given patient. Instead, the results from computational models parametrised using "patient-specific" clinical data, such as the ones studied in this thesis, should be used to guide clinical decisions. These physics-based models rely heavily on fluid mechanics rather than statistics, and hence provide clinical measurements which are tailored to the cardiovascular properties and function of individual patients.

8.2 Future Work

This thesis has identified a number of challenges which will need to be addressed so that these novel algorithms for the non-invasive estimation of central blood pressure (cBP) and cardiovascular parameters can be translated into the clinic. These challenges and their potential solutions are listed below, together with a number of ideas for future research, based on the experience gained throughout this work.

8.2.1 Central Blood Pressure Algorithms

The main clinical assessment for the current work was performed using the "Aortic Coarctation" dataset, which contained invasive cBP data for 10 patients only. Although two larger datasets – containing reference cBP values acquired using the current non-invasive gold-standard device for non-invasive cBP estimation – were used as well, invasive reference cBP values are preferred. Therefore, larger clinical populations of patients with a range of cardiovascular diseases containing invasive cBP, aortic geometry and flow, and non-invasive peripheral pressures are required to fully assess the cBP algorithms. Cardiovascular diseases which do not significantly alter the aortic geometry would be preferred, given that current 1-D models do not account for energy losses due to the appearance of turbulent blood flow or recirculation (phenomena which occur, respectively, in aortic coarctation or aortic aneurysm patients). In fact, the *in silico* or *in vitro* development and assessment of 1-D models with the ability to account for tortuous aortic geometries could increase the accuracy of current cBP estimation algorithms for such patients.

8.2.2 Cardiovascular Parameter Estimation

Optimal cardiovascular parameter estimation methods were identified using *in silico* reference data representative of healthy populations only. Ideally, an assessment of both current and novel methods should be performed using *in vivo* reference data obtained from healthy and unhealthy subjects, although this may not be feasible for some cardiovascular parameters. Among the parameters under study, arterial resistance, characteristic impedance, and pulse wave velocity at the aortic root, and left ventricular ejection time, can all be measured directly and accurately *in vivo*. In fact, in a recent study, Asai *et al.* [193] compared a number of cardiovascular parameter estimation methods using

swine data. However, asymptotic pressure (whose physiological meaning is not clear yet) and arterial compliance (which mainly accounts for the compliance of the larger systemic arteries) are parameters whose measurement *in vivo* are technically challenging. On the one hand, asymptotic pressure should be measured simultaneously at multiple capillary locations to better understand it and to extract reference values in humans. On the other hand, reference arterial compliance should be measured from full body dynamic arterial volume measurements. Methods for the reliable direct measurement of these cardiovascular parameters *in vivo* must be developed to validate the proposed non-invasive estimation methods.

As seen in Chapter 5, the estimation of aortic characteristic impedance from aortic flow and peripheral pressure requires substantial further work. However, since this parameter is determined only by local arterial properties, it may be difficult to improve estimates using a peripheral pressure wave. Furthermore, the cBP estimation algorithm which uses a three-element Windkessel model would significantly benefit from an accurate estimate of aortic characteristic impedance.

8.2.3 Machine Learning, Wearables and the Digital Twin

The availability of larger numbers of *in silico* (*e.g.* virtual subjects presented in this thesis) and *in vivo* (*e.g.* UK Biobank) datasets motivates the development and assessment of machine learning methods to estimate blood pressure and cardiovascular parameters not only centrally but also at other arterial locations of clinical relevance. The potential utility of such methods for estimating relevant cardiovascular metrics is increasing with the widespread use of wearables, which could potentially facilitate continuous cardiovascular monitoring.

Several examples of algorithms for monitoring physiological parameters have been proposed in the literature. For instance, Charlton's PhD thesis (2017) "developed and assessed the performance of techniques for continuous respiratory rate monitoring using electrocardiogram (ECG) and photoplethysmogram (PPG) signals for use in wearable sensors to detect deteriorations" [194]. In 2018, Mathieu *et al.* demonstrated the feasibility of assessing left ventricular ejection time using wrist PPG signals, such as those acquired by smart watches [195]. More recently, Tanveer *et al.* proposed a "Long Short Term Memory" Artificial Neural Network model for the continuous estimation of blood

pressure using data from ECG and PPG wearable sensors [168]. Furthermore, Apple is currently conducting a very large study on "the ability of the Apple Watch algorithm to identify pulse irregularity and variability which may reflect previously unknown atrial fibrillation (AF)" [196]. Preliminary results show that this smart watch accurately detects AF [197].

These methods and sources of continuous physiological data could be combined with current algorithms based on computational models of fluid dynamics to create a digital twin. A digital twin, in this context, is a digital replica of a human which updates using data from multiple sources such as machine learning models, wearables, clinical populations, biophysical models, or even other digital twins. Digital twins, using such statistical and physical models, would ideally be able to benefit from vast amounts of data and use it to predict negative health outcomes for its corresponding human and advise accordingly. Finally, the efficacy of the digital twin would improve with time as it "learns" from mistakes and from the vast amounts of data provided by the Internet of things, which allows the any kind of smart device to connect to others and constantly send and receive data.

Bibliography

[1] J. Mariscal-Harana, P. H. Charlton, S. Vennin *et al.*, "Estimating central blood pressure from aortic flow: development and assessment of algorithms," *[under review]*, 2020.

[2] D. Marlevi, J. Mariscal-Harana, N. S. Burris *et al.*, "Altered aortic hemodynamics and relative pressure in patients with dilated cardiomyopathy," *[under review]*, 2020.

[3] P. H. Charlton, J. Mariscal-Harana, S. Vennin *et al.*, "Modeling arterial pulse waves in healthy aging: a database for in silico evaluation of hemodynamics and pulse wave indexes," *American Journal of Physiology - Heart and Circulatory Physiology*, vol. 317, no. 5, pp. H1062–H1085, 2019.

[4] F. E. Fossan, J. Mariscal-Harana, J. Alastruey *et al.*, "Optimization of topological complexity for one-dimensional arterial blood flow models," *Journal of The Royal Society Interface*, vol. 15, no. 149, p. 20180546, 2018.

[5] S. Abdullateef, J. Mariscal-Harana, J. Alastruey *et al.*, "A study on the characteristics influencing the pressure at the root of a distributed one-dimensional model of arterial blood flow," in *2018 Computing in Cardiology Conference (CinC)*, vol. 45, 2018, pp. 1–4.

[6] M. Florkow, J. Mariscal-Harana, A. van Engelen *et al.*, "An integrated software application for non-invasive assessment of local aortic haemodynamic parameters," in *Procedia Computer Science*, vol. 90, no. July, 2016, pp. 2–8.

[7] World Health Organisation, "Cardiovascular diseases (CVDs)," 2017.

[8] R. J. Levick, *An Introduction to Cardiovascular Physiology*, 1991.

[9] J. G. Betts, K. A. Young, J. A. Wise *et al.*, *Anatomy and Physiology.* OpenStax, 2013.

[10] W. W. Nichols, M. F. O'Rourke, C. Vlachopoulos *et al.*, *McDonald's Blood Flow in Arteries: Theoretical, Experimental and Clinical Principles.* Hodder Arnold, 2011.

[11] G. Cokelet, "Hemorheology and Hemodynamics," *Colloquium Series on Integrated Systems Physiology: From Molecule to Function*, vol. 3, no. 5, pp. 1–140, jul 2011.

[12] C. G. Caro, T. J. Pedley, R. C. Schroter *et al.*, *The Mechanics of the Circulation.* Cambridge: Cambridge University Press, 2011.

[13] N. Townsend, P. Bhatnagar, E. Wilkins *et al.*, *Cardiovascular Disease Statistics 2015*, 2015.

[14] Office for National Statistics, "Deaths Registered in England and Wales (Series DR), 2015 (Statistical Bulletin)," pp. 1–15, 2016.

[15] R. International, "Cardiovascular disease costs will exceed $1 trillion by 2035: Nearly half of Americans will develop pre-existing cardiovascular disease conditions, analysis shows," 2016.

[16] GOV.UK, "Health matters," 2019.

[17] B. M. Egan, S. E. Kjeldsen, G. Grassi *et al.*, "The global burden of hypertension exceeds 1.4 billion people: should a systolic blood pressure target below 130 become the universal standard?" *Journal of hypertension*, vol. 37, no. 6, pp. 1148–1153, 2019.

[18] Patricia M Kearney, Megan Whelton, Kristi Reynolds *et al.*, "Global burden of hypertension–analysis of worldwide data," *Lancet*, vol. 365, pp. 217–223, 2005.

[19] G. M. Singh, G. Danaei, F. Farzadfar *et al.*, "The age-specific quantitative effects of metabolic risk factors on cardiovascular diseases and diabetes: A pooled analysis," *PLoS ONE*, vol. 8, no. 7, 2013.

[20] D. T. Lackland and M. A. Weber, "Global burden of cardiovascular disease and stroke: Hypertension at the core," *Canadian Journal of Cardiology*, vol. 31, no. 5, pp. 569–571, 2015.

[21] I. Hernandorena, E. Duron, J. S. Vidal *et al.*, "Treatment options and considerations for hypertensive patients to prevent dementia," *Expert Opinion on Pharmacotherapy*, vol. 18, no. 10, pp. 989–1000, 2017.

[22] D. H. Lau, S. Nattel, J. M. Kalman *et al.*, "Modifiable Risk Factors and Atrial Fibrillation," *Circulation*, vol. 136, no. 6, pp. 583–596, 2017.

[23] M. H. Forouzanfar, P. Liu, G. A. Roth *et al.*, "Global Burden of Hypertension and Systolic Blood Pressure of at Least 110 to 115 mm Hg, 1990-2015," *JAMA*, vol. 317, no. 2, p. 165, jan 2017.

[24] P. K. Whelton, R. M. Carey, W. S. Aronow *et al.*, *2017 ACC/AHA/AAPA/ABC/ACPM/AGS/APhA/ASH/ASPC/NMA/PCNA Guideline for the Prevention, Detection, Evaluation, and Management of High Blood Pressure in Adults*, 2017.

[25] J. Booth, "A Short History of Blood Pressure Measurement," *Proceedings of the Royal Society of Medicine*, vol. 70, no. 11, pp. 793–799, nov 1977.

[26] "Wood engraving: Vierordt's sphygmograph. Wellcome Collection. CC BY 4.0."

[27] "Engraving: direct sphymograph; E.J. Marey. Wellcome Collection. CC BY 4.0."

[28] A. P. Avolio, M. Butlin, and A. Walsh, "Arterial blood pressure measurement and pulse wave analysis-âĂŞtheir role in enhancing cardiovascular assessment," *Physiological Measurement*, vol. 31, no. 1, pp. R1–R47, jan 2010.

[29] "Engraving: sphygmomanometer devised by S.S. von Basch, circa 1881. Wellcome Collection. CC BY 4.0."

[30] "Sphygmomanometer according to Riva-Rocci for the measurement of the arterial blood pressure," Max Planck Institute for the History of Science, Berlin.

[31] P. Muntner, D. Shimbo, R. M. Carey *et al.*, "Measurement of Blood Pressure in Humans: A Scientific Statement From the American Heart Association," *Hypertension*, vol. 73, no. 5, pp. e35–e66, 2019.

[32] C. F. Babbs, "Oscillometric measurement of systolic and diastolic blood pressures validated in a physiologic mathematical model," *BioMedical Engineering Online*, vol. 11, no. 1, p. 1, 2012.

[33] S. Lee, G. Jeon, and G. Lee, "On using maximum a Posteriori probability based on a Bayesian model for oscillometric blood pressure estimation," *Sensors (Switzerland)*, vol. 13, no. 10, pp. 13 609–13 623, 2013.

[34] J. Liu, H.-M. Cheng, C.-H. Chen *et al.*, "Patient-specific oscillometric blood pressure measurement: validation for accuracy and repeatability," *IEEE Journal of Translational Engineering in Health and Medicine*, vol. 5, no. 1, pp. 1–10, 2017.

[35] E. Agabiti-Rosei, G. Mancia, M. F. O'Rourke *et al.*, "Central blood pressure measurements and antihypertensive therapy: A consensus document," *Hypertension*, vol. 50, no. 1, pp. 154–160, 2007.

[36] J. E. Sharman, T. H. Marwick, D. Gilroy *et al.*, "Randomized trial of guiding hypertension management using central aortic blood pressure compared with best-practice care," *Hypertension*, vol. 62, no. 6, pp. 1138–1145, dec 2013.

[37] C. M. McEniery, J. R. Cockcroft, M. J. Roman *et al.*, "Central blood pressure: Current evidence and clinical importance," *European Heart Journal*, vol. 35, no. 26, pp. 1719–1725, 2014.

[38] E. Agabiti-Rosei, K. Fox, and R. Ferrari, "Understanding and treating central blood pressure," *Dialogues in Cardiovascular Medicine*, vol. 20, no. 3, pp. 169–184, 2015.

[39] B. Williams, P. Brunel, P. S. Lacy *et al.*, "Application of non-invasive central aortic pressure assessment in clinical trials: Clinical experience and value," *Artery Research*, vol. 17, pp. 1–15, 2017.

[40] A. Herbert, J. K. Cruickshank, S. Laurent *et al.*, "Establishing reference values for central blood pressure and its amplification in a general healthy population and according to cardiovascular risk factors," *European Heart Journal*, vol. 35, no. 44, pp. 3122–3133, 2014.

[41] J. E. Sharman, M. Stowasser, R. G. Fassett *et al.*, "Central blood pressure measurement may improve risk stratification," *Journal of Human Hypertension*, vol. 22, no. 12, pp. 838–844, 2008.

[42] C. M. McEniery, Yasmin, I. R. Hall *et al.*, "Normal vascular aging: Differential effects on wave reflection and aortic pulse wave velocity - The Anglo-Cardiff Collaborative Trial (ACCT)," *Journal of the American College of Cardiology*, vol. 46, no. 9, pp. 1753–1760, 2005.

[43] H. M. Cheng, D. Lang, C. Tufanaru *et al.*, "Measurement accuracy of non-invasively obtained central blood pressure by applanation tonometry: A systematic review and meta-analysis," *International Journal of Cardiology*, vol. 167, no. 5, pp. 1867–1876, 2013.

[44] Health Direct, "Cardiac catheterisation," 2019.

[45] T. G. Papaioannou, T. D. Karageorgopoulou, T. N. Sergentanis *et al.*, "Accuracy of commercial devices and methods for noninvasive estimation of aortic systolic blood pressure a systematic review and meta-analysis of invasive validation studies," *Journal of Hypertension*, vol. 34, no. 7, pp. 1237–1248, jul 2016.

[46] M. F. O'Rourke, "Carotid Artery Tonometry: Pros and Cons," *American Journal of Hypertension*, vol. 29, no. 3, pp. 296–298, 2016.

[47] R. R. Townsend, I. B. Wilkinson, E. L. Schiffrin *et al.*, "Recommendations for Improving and Standardizing Vascular Research on Arterial Stiffness," *Hypertension*, vol. 66, no. 3, pp. 698–722, sep 2015.

[48] B. Spronck, T. Delhaas, J. Op'T Roodt *et al.*, "Carotid Artery Applanation Tonometry Does Not Cause Significant Baroreceptor Activation," *American Journal of Hypertension*, vol. 29, no. 3, pp. 299–302, 2016.

[49] Y. T. Shih, H. M. Cheng, S. H. Sung *et al.*, "Quantification of the calibration error in the transfer function-derived central aortic blood pressures," *American Journal of Hypertension*, vol. 24, no. 12, pp. 1312–1317, 2011.

[50] J. E. Sharman, R. Lim, A. M. Qasem *et al.*, "Validation of a generalized transfer function to noninvasively derive central blood pressure during exercise," *Hypertension*, vol. 47, no. 6, pp. 1203–1208, 2006.

[51] D. Gallagher, A. Adji, and M. O'Rourke, "Validation of the transfer function technique for generating central from peripheral upper limb pressure waveform," *American Journal of Hypertension*, vol. 17, no. 11, pp. 1059–1067, 2004.

[52] J. E. Sharman, A. P. Avolio, J. Baulmann *et al.*, "Validation of non-invasive central blood pressure devices: Artery society task force consensus statement on protocol standardization," *Artery Research*, vol. 20, pp. 35–43, 2017.

[53] Y. Yao, L. Xu, Y. Sun *et al.*, "Validation of an Adaptive Transfer Function Method to Estimate the Aortic Pressure Waveform," *IEEE Journal of Biomedical and Health Informatics*, vol. 2194, no. c, pp. 1–1, 2016.

[54] M. Karamanoglu, M. F. O'Rourke, A. P. Avolio *et al.*, "An analysis of the relationship between central aortic and peripheral upper limb pressure waves in man." *European Heart Journal*, vol. 14, no. 2, pp. 160–7, 1993.

[55] M. Karamanoglu and M. P. Feneley, "Derivation of the ascending aortic-carotid pressure transfer function with an arterial model," *American Journal of Physiology-Heart and Circulatory Physiology*, vol. 271, no. 6, pp. H2399–H2404, dec 1996.

[56] P. Salvi, G. Lio, C. Labat *et al.*, "Validation of a new non-invasive portable tonometer for determining arterial pressure wave and pulse wave velocity: The PulsePen device," *Journal of Hypertension*, vol. 22, no. 12, pp. 2285–2293, 2004.

[57] T. Pereira, J. Maldonado, R. Coutinho *et al.*, "Invasive validation of the Complior Analyse in the assessment of central artery pressure curves: A methodological study," *Blood Pressure Monitoring*, vol. 19, no. 5, pp. 280–287, 2014.

[58] F. Stea, E. Bozec, S. Millasseau *et al.*, "Comparison of the Complior Analyse device with Sphygmocor and Complior SP for pulse wave velocity and central pressure assessment," *Journal of Hypertension*, vol. 32, no. 4, pp. 873–880, 2014.

[59] F. H. Ding, W. X. Fan, R. Y. Zhang *et al.*, "Validation of the noninvasive assessment of central blood pressure by the sphygmocor and omron devices against the invasive catheter measurement," *American Journal of Hypertension*, vol. 24, no. 12, pp. 1306–1311, 2011.

[60] K. Takazawa, H. Kobayashi, I. Kojima *et al.*, "Estimation of central aortic systolic pressure using late systolic inflection of radial artery pulse and its application to vasodilator therapy," *Journal of Hypertension*, vol. 30, no. 5, pp. 908–916, 2012.

[61] I. G. Horváth, Á. Németh, Z. Lenkey *et al.*, "Invasive validation of a new oscillometric device (Arteriograph) for measuring augmentation index, central blood pressure and aortic pulse wave velocity," *Journal of Hypertension*, vol. 28, no. 10, pp. 2068–2075, oct 2010.

[62] C. Ott, S. Haetinger, M. P. Schneider *et al.*, "Comparison of two noninvasive devices for measurement of central systolic blood pressure with invasive measurement during cardiac catheterization," *Journal of Clinical Hypertension*, vol. 14, no. 9, pp. 575–579, 2012.

[63] B. Williams, P. S. Lacy, P. Yan *et al.*, "Development and validation of a novel method to derive central aortic systolic pressure from the radial pressure waveform using an n-point moving average method," *Journal of the American College of Cardiology*, vol. 57, no. 8, pp. 951–961, 2011.

[64] Y. T. Shih, H. M. Cheng, S. H. Sung *et al.*, "Application of the N-point moving average method for brachial pressure waveform-derived estimation of central aortic systolic pressure," *Hypertension*, vol. 63, no. 4, pp. 865–870, 2014.

[65] A. Cremer, M. Butlin, L. Codjo *et al.*, "Determination of central blood pressure by a noninvasive method (brachial BP and QKD interval)," *Journal of Hypertension*, vol. 30, no. 8, pp. 1533–1539, 2012.

[66] P. Gosse, R. Lasserre, C. Minifié *et al.*, "Arterial stiffness evaluated by measurement of the QKD interval is an independent predictor of cardiovascular events," *American Journal of Hypertension*, vol. 18, no. 4, pp. 470–476, 2005.

[67] S. Vennin, A. Mayer, Y. Li *et al.*, "Noninvasive calculation of the aortic blood pressure waveform from the flow velocity waveform: a proof of concept." *American Journal of Physiology - Heart and Circulatory Physiology*, vol. 309, no. 5, pp. H969–76, 2015.

[68] J. F. Ladisa, C. Alberto Figueroa, I. E. Vignon-Clementel *et al.*, "Computational simulations for aortic coarctation: Representative results from a sampling of patients," *Journal of Biomechanical Engineering*, vol. 133, no. 9, 2011.

[69] D. M. Sforza, C. M. Putman, and J. R. Cebral, "Computational fluid dynamics in brain aneurysms," *International Journal for Numerical Methods in Biomedical Engineering*, vol. 28, no. 6-7, pp. 801–808, 2012.

[70] G. Biglino, D. Cosentino, J. A. Steeden *et al.*, "Using 4D Cardiovascular Magnetic Resonance Imaging to Validate Computational Fluid Dynamics: A Case Study," *Frontiers in Pediatrics*, vol. 3, no. December, pp. 1–10, 2015.

[71] P. E. Vincent, A. M. Plata, A. A. E. Hunt *et al.*, "Blood flow in the rabbit aortic arch and descending thoracic aorta," *Journal of The Royal Society Interface*, vol. 8, no. 65, pp. 1708–1719, 2011.

[72] N. Westerhof, J.-W. Lankhaar, and B. E. Westerhof, "The arterial Windkessel," *Medical & Biological Engineering & Computing*, vol. 47, no. 2, pp. 131–141, 2009.

[73] M. S. Olufsen, C. S. Peskin, W. Y. Kim *et al.*, "Numerical simulation and experimental validation of blood flow in arteries with structured-tree outflow conditions," *Annals of Biomedical Engineering*, vol. 28, no. 11, pp. 1281–1299, 2000.

[74] P. Reymond, Y. Bohraus, F. Perren *et al.*, "Validation of a patient-specific one-dimensional model of the systemic arterial tree," *American Journal of Physiology-Heart and Circulatory Physiology*, vol. 301, no. 3, pp. H1173–H1182, 2011.

[75] J. Alastruey, N. Xiao, H. Fok *et al.*, "On the impact of modelling assumptions in multi-scale, subject-specific models of aortic haemodynamics," *Journal of The Royal Society Interface*, vol. 13, no. 119, p. 20160073, 2016.

[76] K. S. Matthys, J. Alastruey, J. Peiró *et al.*, "Pulse wave propagation in a model human arterial network: Assessment of 1-D numerical simulations against in vitro measurements," *Journal of Biomechanics*, vol. 40, no. 15, pp. 3476–3486, 2007.

[77] J. Alastruey, A. W. Khir, K. S. Matthys *et al.*, "Pulse wave propagation in a model human arterial network: Assessment of 1-D visco-elastic simulations against in vitro measurements," *Journal of Biomechanics*, vol. 44, no. 12, pp. 2250–2258, 2011.

[78] W. Huberts, K. Van Canneyt, P. Segers *et al.*, "Experimental validation of a pulse wave propagation model for predicting hemodynamics after vascular access surgery," *Journal of Biomechanics*, vol. 45, no. 9, pp. 1684–1691, 2012.

[79] N. Xiao, J. Alastruey, and C. Alberto Figueroa, "A systematic comparison between 1-D and 3-D hemodynamics in compliant arterial models," *International Journal for Numerical Methods in Biomedical Engineering*, vol. 30, no. 2, pp. 204–231, 2014.

[80] E. Boileau, P. Nithiarasu, P. J. Blanco *et al.*, "A benchmark study of numerical schemes for one-dimensional arterial blood flow modelling," *International Journal for Numerical Methods in Biomedical Engineering*, vol. 31, no. 10, p. e02732, 2015.

[81] J. P. Mynard and J. J. Smolich, "One-dimensional haemodynamic modeling and wave dynamics in the entire adult circulation," *Annals of Biomedical Engineering*, vol. 43, no. 6, pp. 1443–1460, 2015.

[82] M. Willemet, P. Chowienczyk, and J. Alastruey, "A database of virtual healthy subjects to assess the accuracy of foot-to-foot pulse wave velocities for estimation of aortic stiffness," *American Journal of Physiology-Heart and Circulatory Physiology*, vol. 309, no. 4, pp. H663–H675, 2015.

[83] S. Epstein, M. Willemet, P. J. Chowienczyk *et al.*, "Reducing the number of parameters in 1D arterial blood flow modeling: less is more for patient-specific simulations," *American Journal of Physiology - Heart and Circulatory Physiology*, vol. 309, no. 1, pp. H222–H234, 2015.

[84] O. Frank, "The basic shape of the arterial pulse. First treatise: mathematical analysis. 1899." *Journal of Molecular and Cellular Cardiology*, vol. 22, no. 3, pp. 255–77, 1990.

[85] N. Westerhof and G. Elzinga, "Normalized input impedance and arterial decay time over heart period are independent of animal size." *The American Journal of Physiology*, vol. 261, no. 30, pp. R126–R133, 1991.

[86] P. Charlton, J. Smith, L. Camporota *et al.*, "Optimising the Windkessel model for cardiac output monitoring during changes in vascular tone," *Conf Proc Eng Med Biol Soc.*, pp. 3759–3762, 2014.

[87] O. Narayan, J. E. Davies, A. D. Hughes *et al.*, "Central aortic reservoir-wave analysis improves prediction of cardiovascular events in elderly hypertensives," *Hypertension*, vol. 65, no. 3, pp. 629–635, 2015.

[88] R. D. Gray, K. H. Parker, M. A. Quail *et al.*, "A method to implement the reservoir-wave hypothesis using phase-contrast magnetic resonance imaging," *MethodsX*, vol. 3, pp. 508–512, 2016.

[89] S. J. Sherwin, V. Franke, J. Peiró *et al.*, "One-dimensional modelling of a vascular network in space-time variables," *Journal of Engineering Mathematics*, vol. 47, no. 3-4, pp. 217–250, 2003.

[90] J. Alastruey, K. H. Parker, and S. J. Sherwin, "Arterial pulse wave haemodynamics," *11th International Conference on Pressure Surges*, pp. 401 – 443, 2012.

[91] N. R. Gaddum, J. Alastruey, P. Beerbaum *et al.*, "A technical assessment of pulse wave velocity algorithms applied to non-invasive arterial waveforms," *Annals of Biomedical Engineering*, vol. 41, no. 12, pp. 2617–2629, 2013.

[92] K. H. Parker and C. J. H. Jones, "Forward and Backward Running Waves in the Arteries: Analysis Using the Method of Characteristics," *Journal of Biomechanical Engineering*, vol. 112, no. 3, pp. 322–326, 1990.

[93] A. Khir, A. O'Brien, J. Gibbs *et al.*, "Determination of wave speed and wave separation in the arteries," *Journal of Biomechanics*, vol. 34, no. 9, pp. 1145–1155, sep 2001.

[94] J. Alastruey, "Numerical modelling of pulse wave propagation in the cardiovascular system: development, validation and clinical applications," Ph.D. dissertation, 2006.

[95] N. Westerhof, G. Elzinga, and P. Sipkema, "An artificial arterial system for pumping hearts." *Journal of Applied Physiology*, vol. 31, no. 5, pp. 776–81, 1971.

[96] P. Charlton, J. Mariscal Harana, S. Vennin *et al.*, "Pulse Wave Database (PWDB) Algorithms," 2019.

[97] A. M. Weissler, R. G. Peeler, and W. H. Roehll, "Relationships between left ventricular ejection time, stroke volume, and heart rate in normal individuals and patients with cardiovascular disease," *American Heart Journal*, vol. 62, no. 3, pp. 367–378, 1961.

[98] S. E. Parazynski, B. J. Tucker, M. Aratow *et al.*, "Direct measurement of capillary blood pressure in the human lip," *Journal of Applied Physiology*, vol. 74, no. 2, pp. 946–950, 1993.

[99] A. C. Simon, M. E. Safar, J. A. Levenson *et al.*, "An evaluation of large arteries compliance in man," *American Journal of Physiology-Heart and Circulatory Physiology*, vol. 237, no. 5, pp. H550–H554, 1979.

[100] S. S. Hickson, M. Butlin, M. Graves *et al.*, "The relationship of age with regional aortic stiffness and diameter," *JACC: Cardiovascular Imaging*, vol. 3, no. 12, pp. 1247–1255, 2010.

[101] Y.-L. Liang, H. Teede, D. Kotsopoulos *et al.*, "Non-invasive measurements of arterial structure and function: repeatability, interrelationships and trial sample size," *Clinical Science*, vol. 95, no. 6, pp. 669–679, 1998.

[102] M. A. Bailey, J. M. Davies, K. J. Griffin *et al.*, "Carotid-femoral pulse wave velocity is negatively correlated with aortic diameter," *Hypertension Research*, vol. 37, no. 10, pp. 926–932, 2014.

[103] M. S. Lemler, T. M. Zellers, K. A. Harris *et al.*, "Coarctation index: identification of recurrent coarctation in infants with hypoplastic left heart syndrome after the Norwood procedure," *The American Journal of Cardiology*, vol. 86, no. 6, pp. 697–699, sep 2000.

[104] G. Adamson, T. Karamlou, P. Moore *et al.*, "Coarctation Index Predicts Recurrent Aortic Arch Obstruction Following Surgical Repair of Coarctation of the Aorta in Infants," *Pediatric Cardiology*, vol. 38, no. 6, pp. 1241–1246, aug 2017.

[105] A. G. Brown, Y. Shi, A. Marzo *et al.*, "Accuracy vs. computational time: Translating aortic simulations to the clinic," *Journal of Biomechanics*, vol. 45, no. 3, pp. 516–523, 2012.

[106] D. C. Barber, I. Valverde, Y. Shi *et al.*, "Derivation of aortic distensibility and pulse wave velocity by image registration with a physics-based regularisation term." *International journal for numerical methods in biomedical engineering*, vol. 30, no. 1, pp. 55–68, 2014.

[107] C. Bertoglio, D. Barber, N. Gaddum *et al.*, "Identification of artery wall stiffness: In vitro validation and in vivo results of a data assimilation procedure applied to a 3D fluid-structure interaction model," *Journal of Biomechanics*, vol. 47, no. 5, pp. 1027–1034, 2014.

[108] J. A. Sotelo, I. Valverde, P. B. Beerbaum *et al.*, "Pressure gradient prediction in aortic coarctation using a computational-fluid-dynamics model: validation against invasive pressure catheterization at rest and pharmacological stress," *Journal of Cardiovascular Magnetic Resonance*, vol. 17, no. S1, pp. 1–3, 2015.

[109] J. Urbina, J. A. Sotelo, D. Springmüller *et al.*, "Realistic aortic phantom to study hemodynamics using MRI and cardiac catheterization in normal and aortic coarctation conditions," *Journal of Magnetic Resonance Imaging*, vol. 44, no. 3, pp. 683–697, 2016.

[110] Y. Shi, I. Valverde, P. V. Lawford *et al.*, "Patient-specific non-invasive estimation of pressure gradient across aortic coarctation using magnetic resonance imaging," *Journal of Cardiology*, vol. 73, no. 6, pp. 544–552, 2019.

[111] A. F. Frangi, "Three-dimensional model-based analysis of vascular and cardiac images," Ph.D. dissertation, University Medical Center Utrecht, 2001.

[112] O. Wink, "Vessel Axis Determination for Diagnosis and Treatment," Ph.D. dissertation, University Medical Center Utrecht, 2004.

[113] O. Wink, W. Niessen, and M. Viergever, "Fast delineation and visualization of vessels in 3-D angiographic images," *IEEE Transactions on Medical Imaging*, vol. 19, no. 4, pp. 337–346, 2000.

[114] H. Fok, A. Guilcher, S. Brett *et al.*, "Dominance of the forward compression wave in determining pulsatile components of blood pressure: Similarities between inotropic stimulation and essential hypertension," *Hypertension*, vol. 64, no. 5, pp. 1116–1123, 2014.

[115] Y. Li, H. Gu, H. Fok *et al.*, "Forward and backward pressure waveform morphology in hypertension: novelty and significance," *Hypertension*, vol. 69, no. 2, pp. 375–381, feb 2017.

[116] S. Vennin, Y. Li, M. Willemet *et al.*, "Identifying hemodynamic determinants of pulse pressure: A combined numerical and physiological approach," *Hypertension*, vol. 70, no. 6, pp. 1176–1182, 2017.

[117] S. Hassan and P. Turner, "Systolic time intervals: A review of the method in the non-invasive investigation of cardiac function in health, disease and clinical pharmacology," *Postgraduate Medical Journal*, vol. 59, no. 693, pp. 423–434, 1983.

[118] K. H. Parker, "Arterial reservoir pressure, subservient to the McDonald lecture, Artery 13," *Artery Research*, vol. 7, no. 3-4, pp. 171–185, sep 2013.

[119] S. Parragh, B. Hametner, and S. Wassertheurer, "Influence of an asymptotic pressure level on the windkessel models of the arterial system," *IFAC-PapersOnLine*, vol. 28, no. 1, pp. 17–22, 2015.

[120] S. J. Vermeersch, E. R. Rietzschel, M. L. Buyzere *et al.*, "The reservoir pressure concept: The 3-element windkessel model revisited? Application to the Asklepios population study," *Journal of Engineering Mathematics*, vol. 64, no. 4, pp. 417–428, 2009.

[121] P. Caldini, S. Permutt, J. A. Waddell *et al.*, "Effect of epinephrine on pressure, flow, and volume relationships in the systemic circulation of dogs." *Circulation research*, vol. 34, no. 5, pp. 606–623, 1974.

[122] J.-J. Wang, J. A. Flewitt, N. G. Shrive *et al.*, "Systemic venous circulation. Waves propagating on a windkessel: relation of arterial and venous windkessels to systemic vascular resistance," *American Journal of Physiology-Heart and Circulatory Physiology*, vol. 290, no. 1, pp. H154–H162, jan 2006.

[123] J. Aguado-Sierra, J. Alastruey, J.-J. Wang *et al.*, "Separation of the reservoir and wave pressure and velocity from measurements at an arbitrary location in arteries," *Proceedings of the Institution of Mechanical Engineers, Part H: Journal of Engineering in Medicine*, vol. 222, no. 4, pp. 403–416, apr 2008.

[124] W. Nichols, M. O'Rourke, and C. Vlachopoulos, "McDonald's Blood Flow in Arteries," p. 768, 2011.

[125] M. F. O'Rourke, "Arterial aging: Pathophysiological principles," *Vascular Medicine*, vol. 12, no. 4, pp. 329–341, 2007.

[126] Y. Ohno, "Central blood pressure and chronic kidney disease," *World Journal of Nephrology*, vol. 5, no. 1, p. 90, 2016.

[127] G. E. McVeigh, A. J. Bank, and J. N. Cohn, "Arterial Compliance," in *Cardiovascular Medicine*. London: Springer London, 2007, pp. 1811–1831.

[128] O. S. Randall, G. C. Van den Bos, and N. Westerhof, "Systemic compliance: does it play a role in the genesis of essential hypertension?" *Cardiovascular Research*, vol. 18, no. 8, pp. 455–462, aug 1984.

[129] N. Westerhof, F. Bosman, C. J. De Vries *et al.*, "Analog studies of the human systemic arterial tree." *Journal of biomechanics*, vol. 2, no. 2, pp. 121–43, 1969.

[130] W. W. Nichols, C. R. Conti, W. E. Walker *et al.*, "Input impedance of the systemic circulation in man," *Circulation Research*, vol. 40, no. 5, pp. 451–458, 1977.

[131] Reference Values for Arterial Stiffness' Collaboration, "Determinants of pulse wave velocity in healthy people and in the presence of cardiovascular risk factors: 'establishing normal and reference values'." *European heart journal*, vol. 31, no. 19, pp. 2338–50, oct 2010.

[132] L. Shamseer, D. Moher, M. Clarke *et al.*, "Preferred reporting items for systematic review and meta-analysis protocols (PRISMA-P) 2015: elaboration and explanation." *BMJ (Clinical research ed.)*, vol. 350, no. g7647, 2015.

[133] D. Moher, L. Shamseer, M. Clarke *et al.*, "Preferred reporting items for systematic review and meta-analysis protocols (PRISMA-P) 2015 statement," *Systematic Reviews*, vol. 4, no. 1, 2015.

[134] J. P. Dujardin and D. N. Stone, "Characteristic impedance of the proximal aorta determined in the time and frequency domain: a comparison." *Medical & biological engineering & computing*, vol. 19, no. 5, pp. 565–8, 1981.

[135] N. Stergiopulos, J. J. Meister, and N. Westerhof, "Simple and accurate way for estimating total and segmental arterial compliance: the pulse pressure method." *Annals of Biomedical Engineering*, vol. 22, no. 4, pp. 392–7, 1994.

[136] E. Meaney, F. Alva, R. Moguel *et al.*, "Formula and nomogram for the sphygmomanometric calculation of the mean arterial pressure." *Heart (British Cardiac Society)*, vol. 84, no. 1, p. 64, 2000.

[137] W. J. W. Bos, E. Verrij, H. H. Vincent *et al.*, "How to assess mean blood pressure properly at the brachial artery level," *Journal of Hypertension*, vol. 25, no. 4, pp. 751–755, 2007.

[138] M. U. Qureshi, M. J. Colebank, D. A. Schreier *et al.*, "Characteristic impedance: frequency or time domain approach?" *Physiological Measurement*, vol. 39, no. 1, p. 014004, 2018.

[139] C. Lucas, B. Wilcox, B. Ha *et al.*, "Comparison of time domain algorithms for estimating aortic characteristic impedance in humans," *IEEE Transactions on Biomedical Engineering*, vol. 35, no. 1, pp. 62–68, 1988.

[140] D. Chemla, J.-L. Hébert, C. Coirault *et al.*, "Total arterial compliance estimated by stroke volume-to-aortic pulse pressure ratio in humans," *American Journal of Physiology-Heart and Circulatory Physiology*, vol. 274, no. 2, pp. H500–H505, 1998.

[141] D. M. Tabima, A. Roldan-Alzate, Z. Wang *et al.*, "Persistent vascular collagen accumulation alters hemodynamic recovery from chronic hypoxia," *Journal of Biomechanics*, vol. 45, no. 5, pp. 799–804, 2012.

[142] F. L. Abel, "Fourier Analysis of Left Ventricular Performance," *Circulation Research*, vol. 28, no. 2, pp. 119–135, 1971.

[143] T. N. S. Clarke, C. Prys-Roberts, G. Biro *et al.*, "Aortic input impedance and left ventricular energetics in acute isovolumic anaemia," *Cardiovascular Research*, vol. 12, no. 1, pp. 49–55, 1978.

[144] G. F. Mitchell, M. A. Pfeffer, N. Westerhof *et al.*, "Measurement of aortic input impedance in rats," *American Journal of Physiology-Heart and Circulatory Physiology*, vol. 267, no. 5, pp. H1907–H1915, 1994.

[145] P. Segers and P. Verdonck, "Role of tapering in aortic wave reflection: hydraulic and mathematical model study," *Journal of Biomechanics*, vol. 33, no. 3, pp. 299–306, mar 2000.

[146] A. D. Hughes and K. H. Parker, "Forward and backward waves in the arterial system: impedance or wave intensity analysis?" *Medical & Biological Engineering & Computing*, vol. 47, no. 2, pp. 207–210, 2009.

[147] P. H. Charlton, P. Celka, B. Farukh *et al.*, "Assessing mental stress from the photoplethysmogram: a numerical study," *Physiological Measurement*, vol. 39, no. 5, p. 054001, 2018.

[148] S. Kamoi, C. Pretty, J. Balmer *et al.*, "Improved pressure contour analysis for estimating cardiac stroke volume using pulse wave velocity measurement," *BioMedical Engineering OnLine*, vol. 16, no. 1, p. 51, 2017.

[149] H. C. Bazett, "An analysis of the time-relations of electrocardiograms," *Annals of Noninvasive Electrocardiology*, vol. 2, no. 2, pp. 177–194, 1997.

[150] O. S. Randall, M. D. Esler, R. V. Calfee *et al.*, "Arterial compliance in hypertension," *Australian and New Zealand Journal of Medicine*, vol. 6, no. s2, pp. 49–59, 1976.

[151] D. A. Self, D. L. Ewert, R. D. Swope *et al.*, "Beat-to-beat determination of peripheral resistance and arterial compliance during +Gz centrifugation." *Aviation, Space, and Environmental Medicine*, vol. 65, no. 5, pp. 396–403, 1994.

[152] J. Alastruey, K. H. Parker, and J. Peiró, "Lumped parameter outflow models for 1-D blood flow simulations: effect on pulse waves and parameter estimation," *Annals of Biomedical Engineering*, vol. 40, no. 11, pp. 1–19, 2008.

[153] J. E. Davies, "Use of simultaneous pressure and velocity measurements to estimate arterial wave speed at a single site in humans," *AJP: Heart and Circulatory Physiology*, vol. 290, no. 2, pp. H878–H885, 2005.

[154] J. P. Murgo, N. Westerhof, J. P. Giolma *et al.*, "Aortic input impedance in normal man: relationship to pressure wave forms." *Circulation*, vol. 62, no. 1, pp. 105–16, 1980.

[155] J. Bland and D. Altman, "Statistical Methods for Assessing Agreement Between Two Methods of Clinical Measurement," *Lancet*, vol. 327, pp. 307–310, 1986.

[156] M. F. O'Rourke, "Pressure and flow waves in systemic arteries and the anatomical design of the arterial system." *Journal of Applied Physiology*, vol. 23, no. 2, pp. 139–149, aug 1967.

[157] N. Stergiopulos, J. J. Meister, and N. Westerhof, "Evaluation of methods for estimation of total arterial compliance." *The American journal of physiology*, vol. 268, no. 4 Pt 2, pp. H1540–8, 1995.

[158] H. Obeid, G. Soulat, E. Mousseaux *et al.*, "Numerical assessment and comparison of pulse wave velocity methods aiming at measuring aortic stiffness," *Physiological Measurement*, vol. 38, no. 11, pp. 1953–1967, oct 2017.

[159] S. Laurent, J. Cockcroft, L. Van Bortel *et al.*, "Expert consensus document on arterial stiffness: Methodological issues and clinical applications," *European Heart Journal*, vol. 27, no. 21, pp. 2588–2605, 2006.

[160] I. B. Wilkinson, C. M. McEniery, G. Schillaci *et al.*, "ARTERY Society guidelines for validation of non-invasive haemodynamic measurement devices: Part 1, arterial pulse wave velocity," *Artery Research*, vol. 4, no. 2, pp. 34–40, jun 2010.

[161] L. M. Van Bortel, S. Laurent, P. Boutouyrie *et al.*, "Expert consensus document on the measurement of aortic stiffness in daily practice using carotid-femoral pulse wave velocity." *Journal of Hypertension*, vol. 30, no. 3, pp. 445–8, 2012.

[162] L. Itu, D. Neumann, V. Mihalef *et al.*, "Non-invasive assessment of patient-specific aortic haemodynamics from four-dimensional flow MRI data." *Interface focus*, vol. 8, no. 1, p. 20170006, 2018.

[163] M. Delles, F. Rengier, Y.-J. Jeong *et al.*, "Estimation of aortic pressure waveforms from 4D phase-contrast MRI." *Proceedings of the Annual International Conference of the IEEE Engineering in Medicine and Biology Society, EMBS*, pp. 731–734, 2013.

[164] M. Khalifé, A. Decoene, F. Caetano *et al.*, "Estimating absolute aortic pressure using MRI and a one-dimensional model." *Journal of Biomechanics*, vol. 47, no. 13, pp. 3390–9, oct 2014.

[165] E. Bollache, N. Kachenoura, A. Redheuil *et al.*, "Descending aorta subject-specific one-dimensional model validated against in vivo data." *Journal of Biomechanics*, vol. 47, no. 2, pp. 424–31, 2014.

[166] P. Perdikaris and G. E. Karniadakis, "Model inversion via multi-fidelity Bayesian optimization: a new paradigm for parameter estimation in haemodynamics, and beyond," *Journal of The Royal Society Interface*, vol. 13, no. 118, p. 20151107, may 2016.

[167] P. Su, X.-R. Ding, Y.-T. Zhang *et al.*, "Long-term blood pressure prediction with deep recurrent neural networks," in *2018 IEEE EMBS International Conference on Biomedical & Health Informatics (BHI)*, vol. 2018-Janua. IEEE, 2018, pp. 323–328.

[168] M. S. Tanveer and M. K. Hasan, "Cuffless blood pressure estimation from electrocardiogram and photoplethysmogram using waveform based ANN-LSTM network," *Biomedical Signal Processing and Control*, vol. 51, pp. 382–392, 2019.

[169] M. Radha, K. de Groot, N. Rajani *et al.*, "Estimating blood pressure trends and the nocturnal dip from photoplethysmography," *Physiological Measurement*, vol. 40, no. 2, p. 025006, feb 2019.

[170] S. Bonapace, A. Rossi, M. Cicoira *et al.*, "Aortic stiffness correlates with an increased extracellular matrix turnover in patients with dilated cardiomyopathy," *American Heart Journal*, vol. 152, no. 1, pp. 93.e1–93.e6, 2006.

[171] S. V. Abramson, "Pulmonary Hypertension Predicts Mortality and Morbidity in Patients with Dilated Cardiomyopathy," *Annals of Internal Medicine*, vol. 116, no. 11, p. 888, jun 1992.

[172] F. Zanon, S. Aggio, E. Baracca *et al.*, "Ventricular-arterial coupling in patients with heart failure treated with cardiac resynchronization therapy: May we predict the long-term clinical response?" *European Journal of Echocardiography*, vol. 10, no. 1, pp. 106–111, 2009.

[173] M. Merlo, T. Caiffa, M. Gobbo *et al.*, "Reverse remodeling in dilated cardiomyopathy: insights and future perspectives," *IJC Heart and Vasculature*, vol. 18, pp. 52–57, 2018.

[174] J. Eriksson, A. F. Bolger, T. Ebbers *et al.*, "Four-dimensional blood flow-specific markers of LV dysfunction in dilated cardiomyopathy," *European Heart Journal Cardiovascular Imaging*, vol. 14, no. 5, pp. 417–424, 2013.

[175] K. Bouaou, I. Bargiotas, T. Dietenbeck *et al.*, "Analysis of aortic pressure fields from 4D flow MRI in healthy volunteers: Associations with age and left ventricular remodeling," *Journal of Magnetic Resonance Imaging*, 2019.

[176] F. Donati, S. Myerson, M. M. Bissell *et al.*, "Beyond bernoulli: improving the accuracy and precision of noninvasive estimation of peak pressure drops," *Circulation: Cardiovascular Imaging*, vol. 10, no. 1, pp. 1–9, 2017.

[177] D. Marlevi, B. Ruijsink, M. Balmus *et al.*, "Estimation of cardiovascular relative pressure using virtual work-energy," *Scientific Reports*, vol. 9, no. 1, pp. 1–16, 2019.

[178] J. A. Chirinos, "Deciphering Systolic-Diastolic Coupling in the Intact Heart," *Hypertension*, vol. 69, no. 4, pp. 575–577, 2017.

[179] N. Lee, M. D. Taylor, and R. K. Banerjee, "Right ventricle-pulmonary circulation dysfunction: a review of energy-based approach," *Biomedical engineering online*, vol. 14, no. Suppl 1, p. S8, 2015.

[180] B. Mensel, J.-P. Kühn, T. Schneider *et al.*, "Mean Thoracic Aortic Wall Thickness Determination by Cine MRI with Steady-State Free Precession," *Academic Radiology*, vol. 20, no. 8, pp. 1004–1008, aug 2013.

[181] K. Isaaz and A. Pasipoularides, "Noninvasive assessment of intrinsic ventricular load dynamics in dilated cardiomyopathy," *Journal of the American College of Cardiology*, vol. 17, no. 1, pp. 112–121, 1991.

[182] D. Avramides, A. Perakis, V. Voudris *et al.*, "Noninvasive assessment of left ventricular systolic function by stress-shortening relation, rate of change of power, preload-adjusted maximal power, and ejection force in idiopathic dilated cardiomyopathy: prognostic implications." *Journal of the American Society of Echocardiography : official publication of the American Society of Echocardiography*, vol. 13, no. 2, pp. 87–95, feb 2000.

[183] P. Reymond, N. Westerhof, and N. Stergiopulos, "Systolic hypertension mechanisms: Effect of global and local proximal aorta stiffening on pulse pressure," *Annals of Biomedical Engineering*, vol. 40, no. 3, pp. 742–749, 2012.

[184] P. Lamata, A. Pitcher, S. Krittian *et al.*, "Aortic relative pressure components derived from four-dimensional flow cardiovascular magnetic resonance," *Magnetic Resonance in Medicine*, vol. 72, no. 4, pp. 1162–1169, 2014.

[185] W. F. Kerwin, E. H. Botvinick, J. W. O'Connell *et al.*, "Ventricular contraction abnormalities in dilated cardiomyopathy: Effect of biventricular pacing to correct interventricular dyssynchrony," *Journal of the American College of Cardiology*, vol. 35, no. 5, pp. 1221–1227, 2000.

[186] D. V. Unverferth, R. D. Magorien, M. L. Moeschberger *et al.*, "Factors influencing the one-year mortality of dilated cardiomyopathy," *The American Journal of Cardiology*, vol. 54, no. 1, pp. 147–152, 1984.

[187] G. W. Dec and V. Fuster, "Idiopathic dilated cardiomyopathy," *The New England journal of medicine*, vol. 331, no. 23, pp. 1564–75, 1994.

[188] G. Hasenfuss, L. A. Mulieri, B. J. Leavitt *et al.*, "Alteration of contractile function and excitation-contraction coupling in dilated cardiomyopathy," *Circulation Research*, vol. 70, no. 6, pp. 1225–1232, 1990.

[189] T. Dudenbostel and S. P. Glasser, "Effects of Antihypertensive Drugs on Arterial Stiffness," *Cardiology in Review*, vol. 20, no. 5, pp. 259–263, 2012.

[190] M. F. O'Rourke and W. W. Nichols, "Aortic diameter, aortic stiffness, and wave reflection increase with age and isolated systolic hypertension," *Hypertension*, vol. 45, pp. 652–658, 2005.

[191] J. N. Cohn, D. A. Duprez, and G. A. Grandits, "Arterial elasticity as part of a comprehensive assessment of cardiovascular risk and drug treatment," *Hypertension*, vol. 46, no. 1, pp. 217–220, 2005.

[192] V. Stoll, A. Hess, C. Rodgers *et al.*, "Left ventricular flow analysis: novel imaging biomarkers and predictors of exercise capacity in heart failure." vol. 12, no. 5, 2019.

[193] T. Arai, K. Lee, and R. J. Cohen, "Comparison of cardiovascular parameter estimation methods using swine data," *Journal of Clinical Monitoring and Computing*, vol. 34, no. 2, pp. 261–270, 2020.

[194] P. H. Charlton, "Continuous respiratory rate monitoring to detect clinical deteriorations using wearable sensors," no. June, 2017.

[195] A. Mathieu, P. H. Charlton, and J. Alastruey, "Using Smart Wearables to Monitor Cardiac Ejection," *Proceedings*, vol. 4, no. 1, p. 48, 2018.

[196] M. P. Turakhia, M. Desai, H. Hedlin *et al.*, "Rationale and design of a large-scale, app-based study to identify cardiac arrhythmias using a smartwatch: The Apple Heart Study," *American Heart Journal*, vol. 207, pp. 66–75, 2019.

[197] M. Caffrey, "Giant Study Suggests Apple Watch Accurately Catches Atrial Fibrillation," 2019.

A Appendix

A.1 Calculating reference Z_0 and C_T at the aortic root

Reference Z_0 and C_T values for the 1-D dataset were calculated from aortic root pressure, P, and flow, Q_in, waves using an in-house algorithm written in MATLAB® and based on the 3-element Windkessel model (Figure A.1). Assuming that P_out is known and that the total resistance $R_\mathrm{T} = Z_0 + R$ is given by Equation (5.12), a parameter estimation problem can be solved for Z_0 and C_T. The estimated pressure at time t_k can be written as

$$P(t_\mathrm{k}) = f(Z_0', C_\mathrm{T}', Q_\mathrm{in}(t_\mathrm{k})) + e_\mathrm{k}, \tag{A.1}$$

with e_k the residual error between the estimated and reference pressures at each time t_k, $k = 1, \ldots, K$, and Z_0' and C_T' the estimated parameters. The problem can be solved through iterative minimisation of the cost function $\mathbf{e}^\top\mathbf{e}$, where $\mathbf{e}$ is the vector containing the residual errors at each time t_k. The iterative procedure starts from an initial estimate ($Z_{0,0}'$, $C_{\mathrm{T},0}'$). The parameters at iteration i+1 are then calculated using the recursive equation

$$(Z_{0,i+1}', C_{\mathrm{T,i+1}}') = (Z_{0,\mathrm{i}}', C_{\mathrm{T,i}}') - \mathbf{H}_i\mathbf{q}_i, \tag{A.2}$$

where $\mathbf{H}_i$ and $\mathbf{q}_i$ are the Hessian and the gradient, respectively, of the cost function evaluated at iteration i. This equation can be obtained by approaching the cost function by a second-order Taylor expansion and minimising the approached function. The 'mean cBP difference' shown in Figure A.1(b,c) was calculated for each iteration as $\frac{1}{K}\sqrt{\sum_{k=1}^{K} {e_\mathrm{k}}^2}$, with e_k the residual error at time t_k.

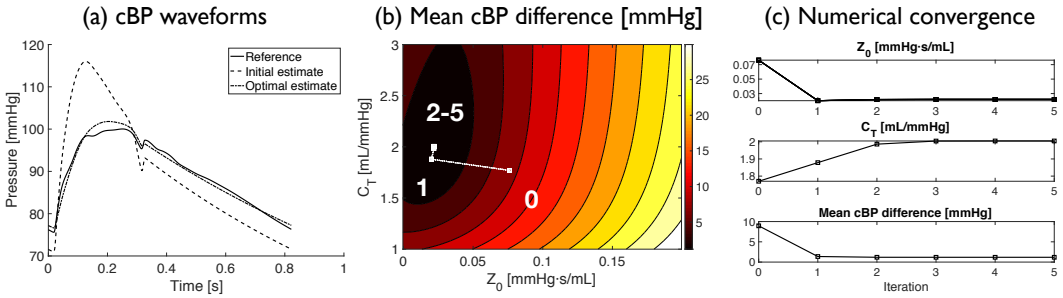

FIGURE A.1: Extracting reference Z_0 and C_T values at the aortic root. (a) Reference cBP waveform for a 1-D model virtual subject, and corresponding initial and optimal estimates. (b) Contour plot (in mmHg) of the mean difference between the estimated and reference cBP waves, with Z_0 in the x-axis and C_T in the y-axis. Each iteration is shown in white squares; iterations 0 and 5 correspond to the initial and optimal cBP estimates, respectively. (c) The values of Z_0, C_T, and the cBP mean difference are shown for the initial estimate and for every iteration until numerical convergence is reached.

A.2 Reference vs estimated cBP waves

A.2.1 cBP estimations in a set of randomly chosen 1-D model subjects

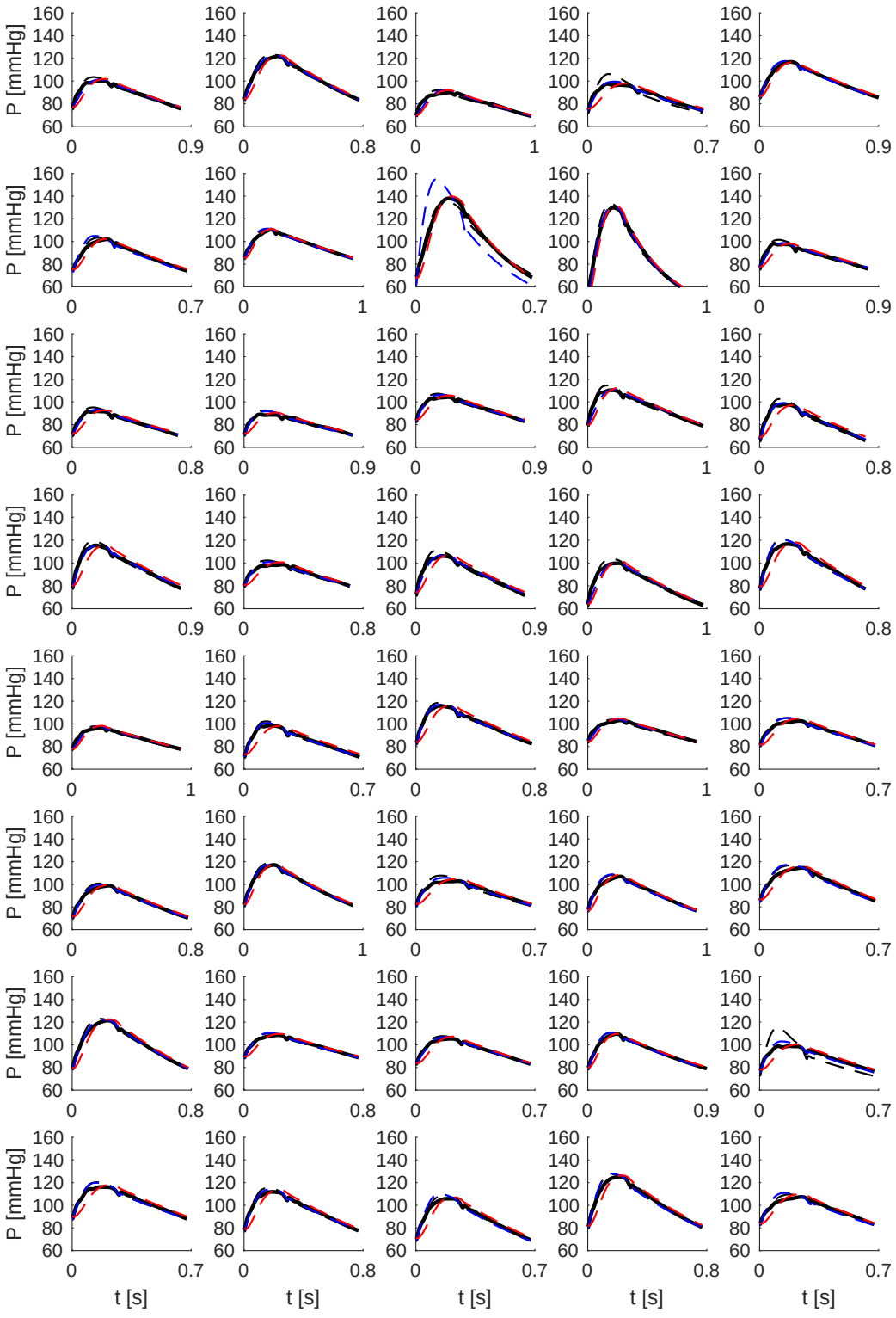

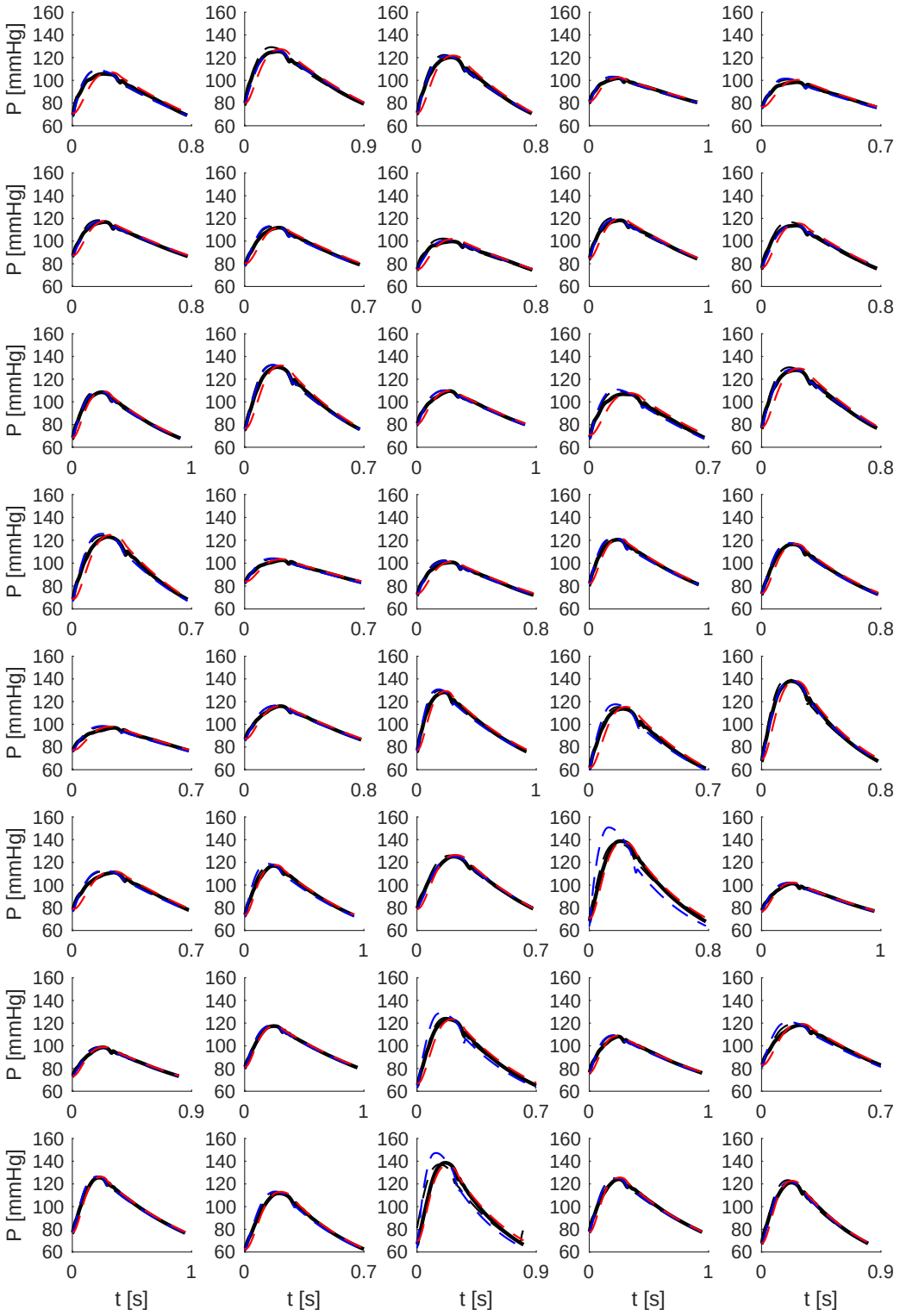

FIGURE A.2: cBP waveform estimations for Scenario 1. cBP waves calculated using the 2-element Windkessel (dashed red lines), 3-element Windkessel (dashed blue lines), and 1-D aortic (dashed black lines) cBP algorithms. They are compared against reference cBP waves from the 1-D model dataset (thick black lines).

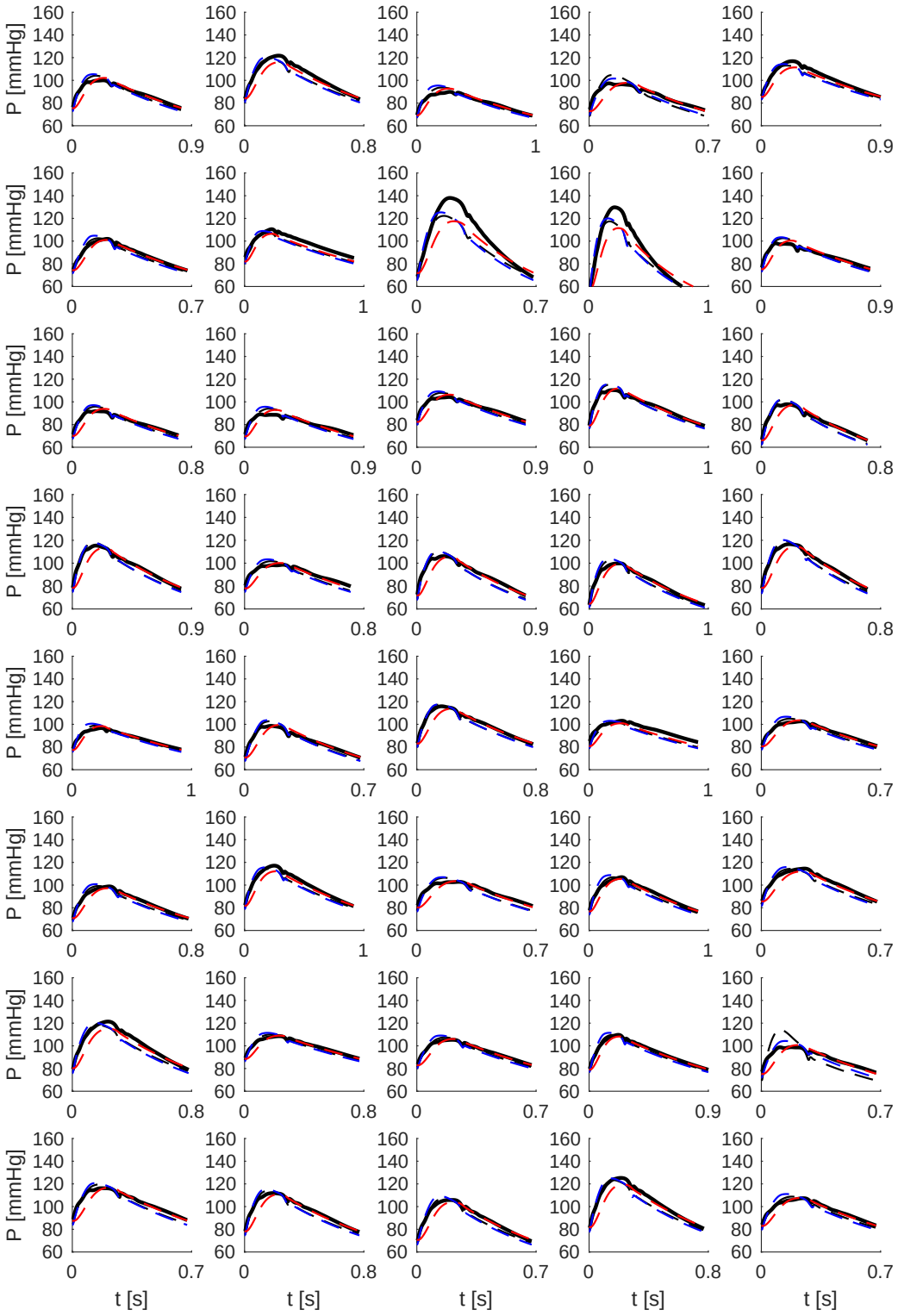
P [mmHg]
t [s]

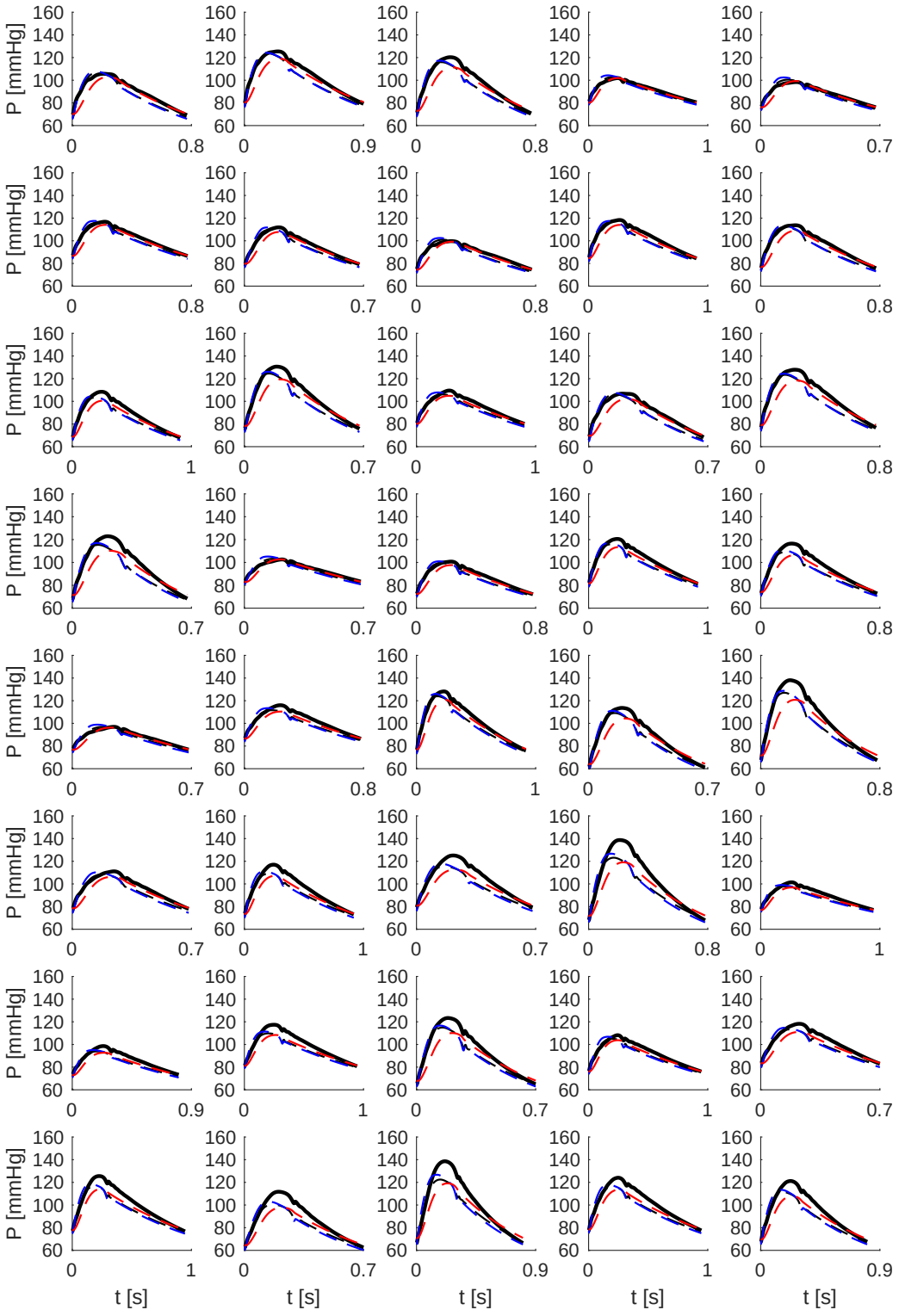

FIGURE A.3: cBP waveform estimations for Scenario 2. cBP waves calculated using the 2-element Windkessel (dashed red lines), 3-element Windkessel (dashed blue lines), and 1-D aortic (dashed black lines) cBP algorithms. They are compared against reference cBP waves from the 1-D model dataset (thick black lines).

A.2.2 cBP estimations in the 'Aortic Coarctation' dataset

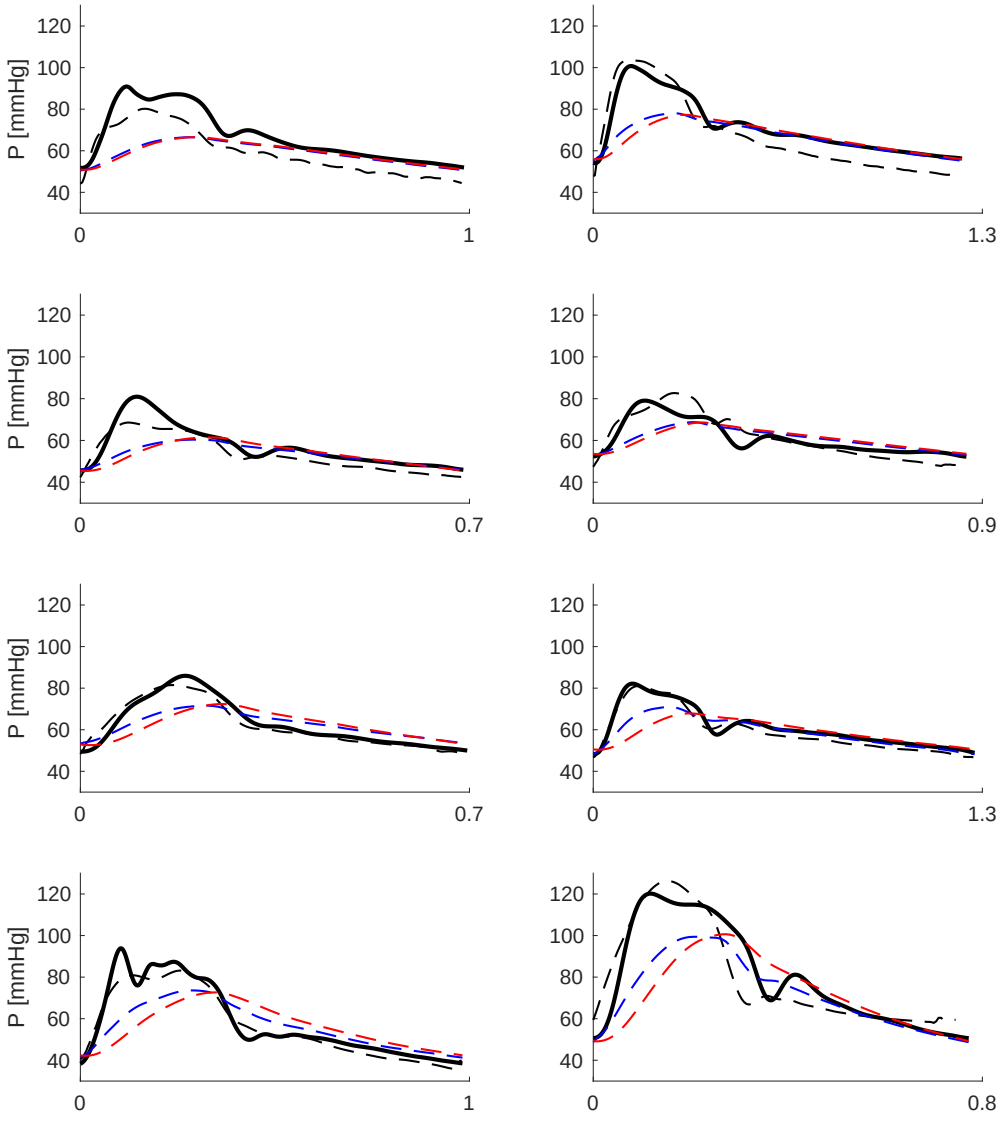

FIGURE A.4: cBP waveform estimations for Scenario 1. cBP waves calculated using the 2-element Windkessel (dashed red lines), 3-element Windkessel (dashed blue lines), and 1-D aortic (dashed black lines) cBP algorithms. They are compared against catheter measurements from the 'Aortic Coarctation' dataset (thick black lines).

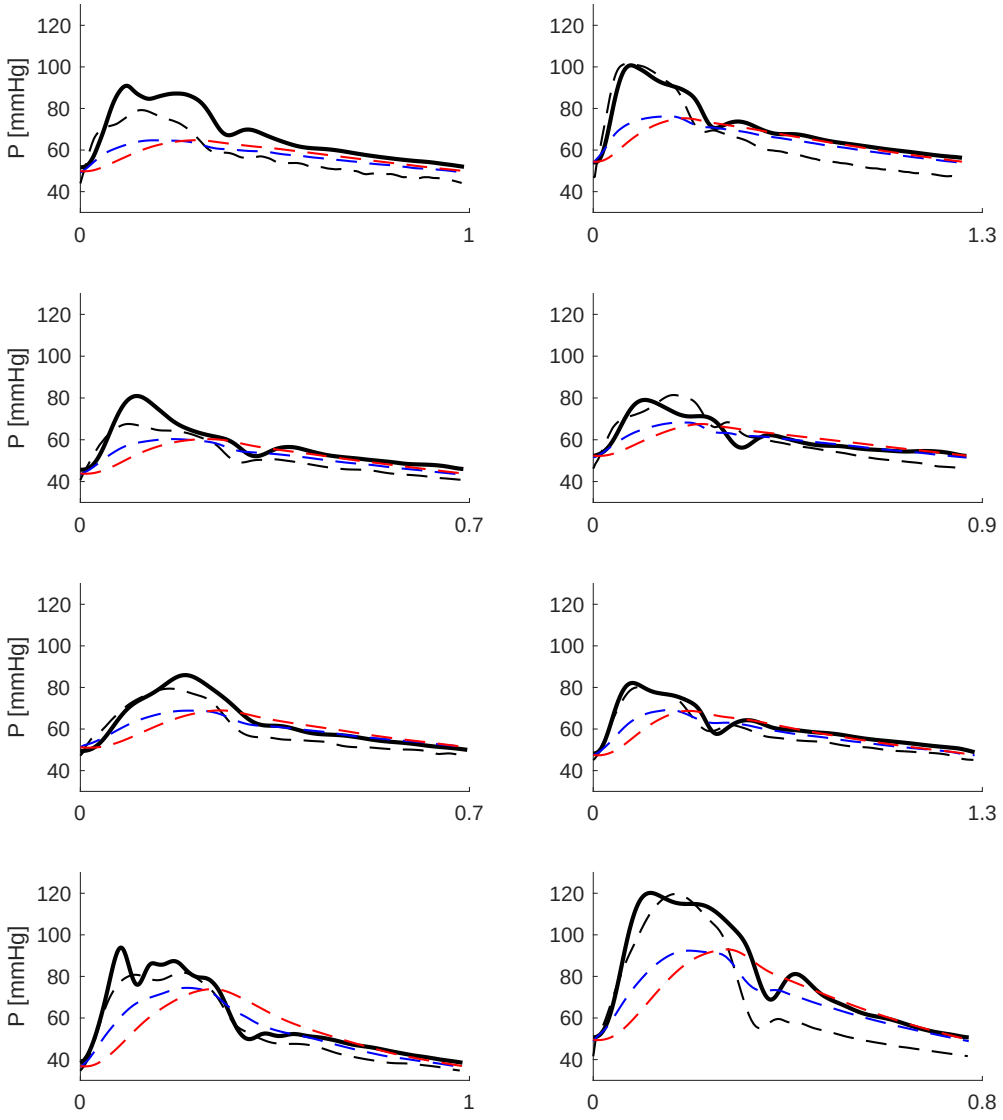

FIGURE A.5: cBP waveform estimations for Scenario 2. cBP waves calculated using the 2-element Windkessel (dashed red lines), 3-element Windkessel (dashed blue lines), and 1-D aortic (dashed black lines) cBP algorithms. They are compared against catheter measurements from the 'Aortic Coarctation' dataset (thick black lines).

A.2.3 cBP estimations in the 'Normotensive' dataset

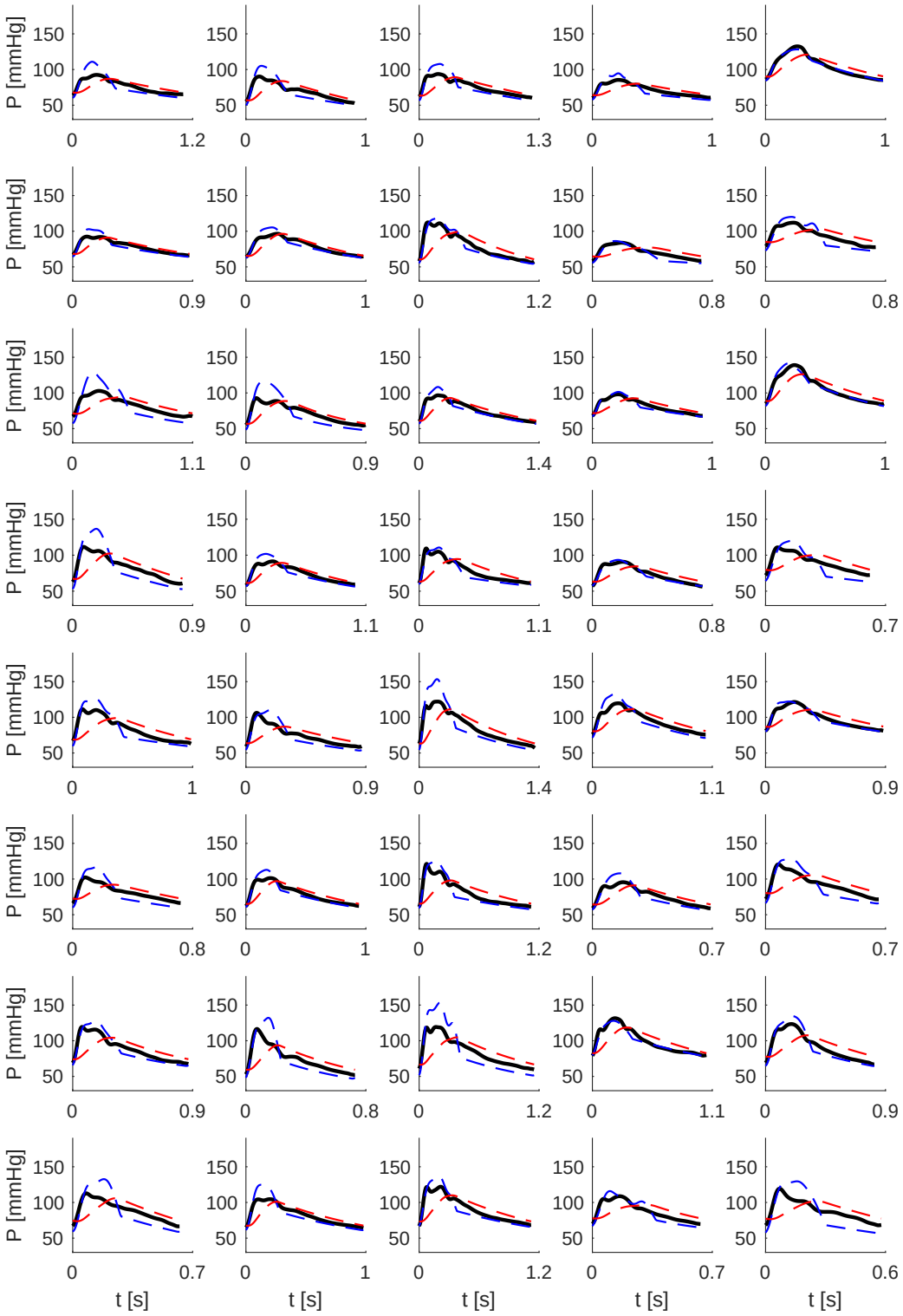

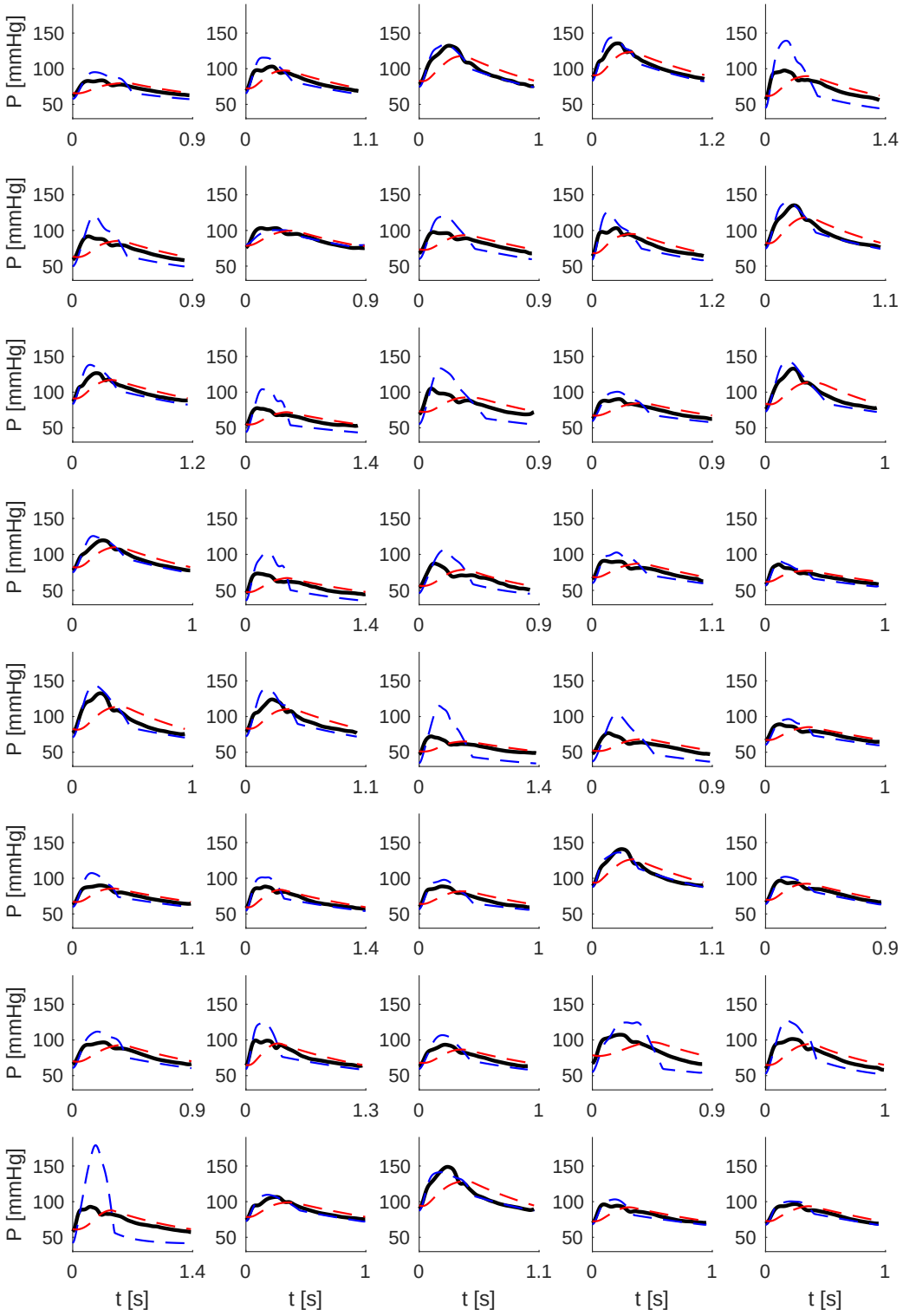
P [mmHg]
150
100
50
0
0.9
1.1
1
1.2
1.4
1.3
t [s]

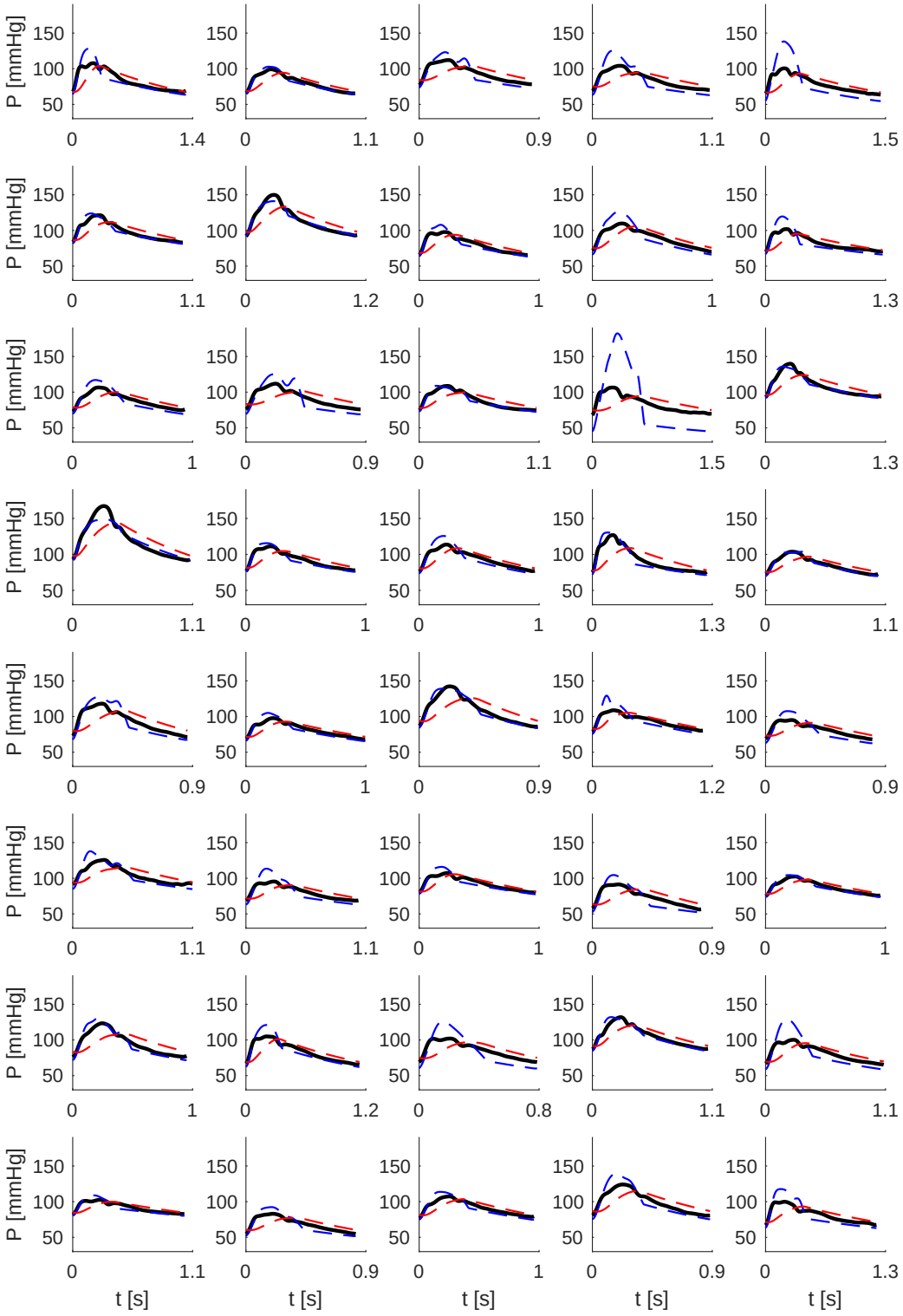
P [mmHg]
150
100
50
0
1.4
1.1
0.9
1.1
1.5
1.2
1
1.3
1.5
1.3
1.1
1.3
1.1
0.9
1.2
0.9
1.1
1
0.9
1
1.2
1.1
0.8
1.1
1.1
1.1
0.9
1.3
t [s]

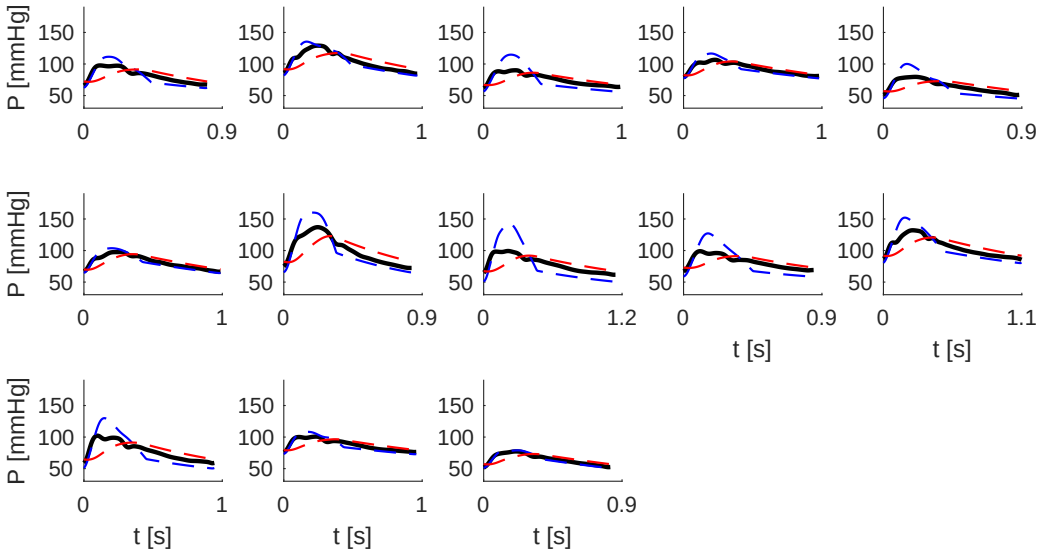

FIGURE A.6: cBP waveform estimations for Scenario 1. cBP waves calculated using the 2-element Windkessel (dashed red lines), 3-element Windkessel (dashed blue lines), and 1-D aortic (dashed black lines) cBP algorithms. They are compared against reference cBP waves from the 'Normotensive' dataset (thick black lines).

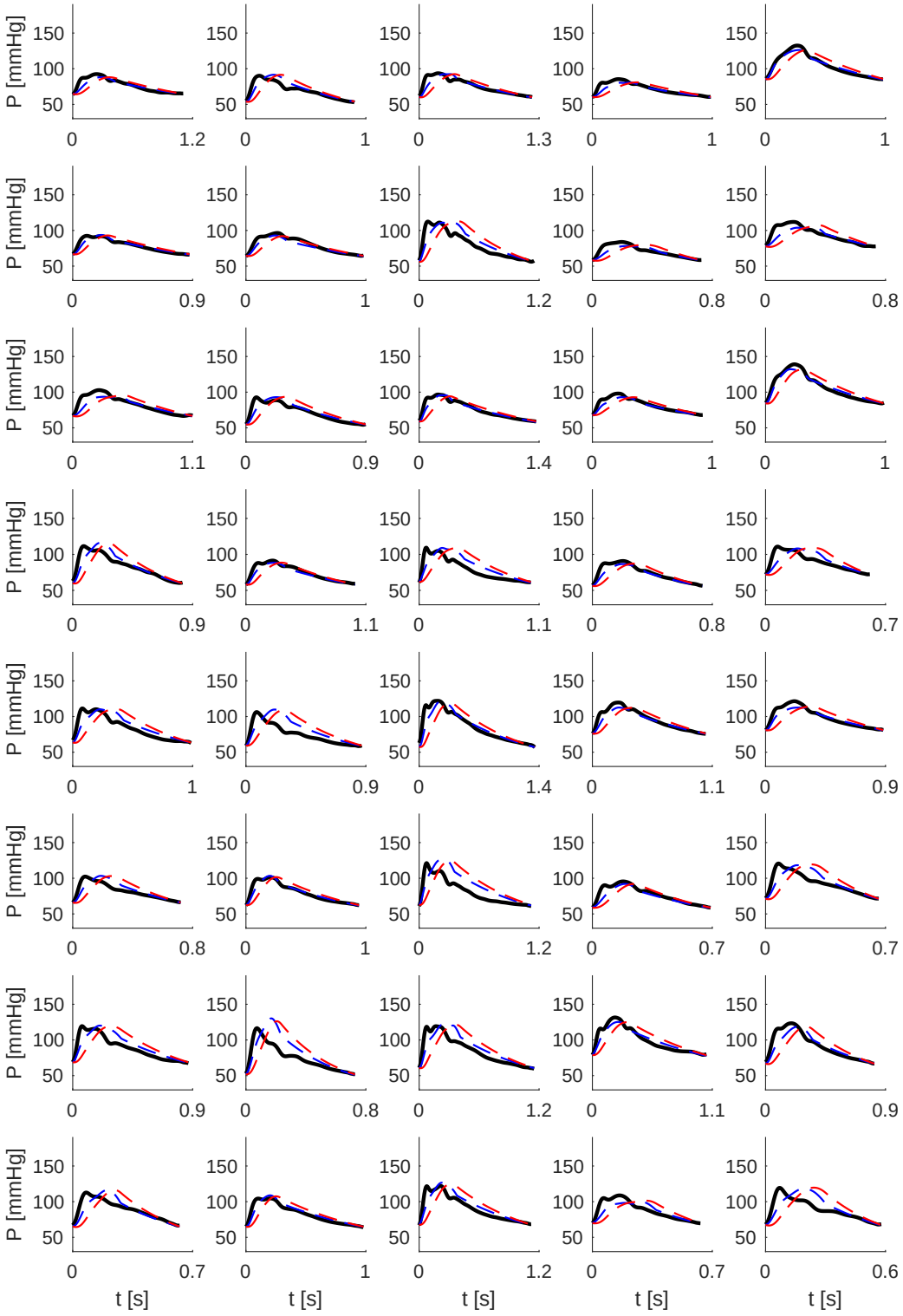
P [mmHg]
150
100
50
0
1.2
1
1.3
1
1
0.9
1
1.2
0.8
0.8
1.1
0.9
1.4
1
1
0.9
1.1
1.1
0.8
0.7
1
0.9
1.4
1.1
0.9
0.8
1
1.2
0.7
0.7
0.9
0.8
1.2
1.1
0.9
0.7
1
1.2
0.7
0.6
t [s]

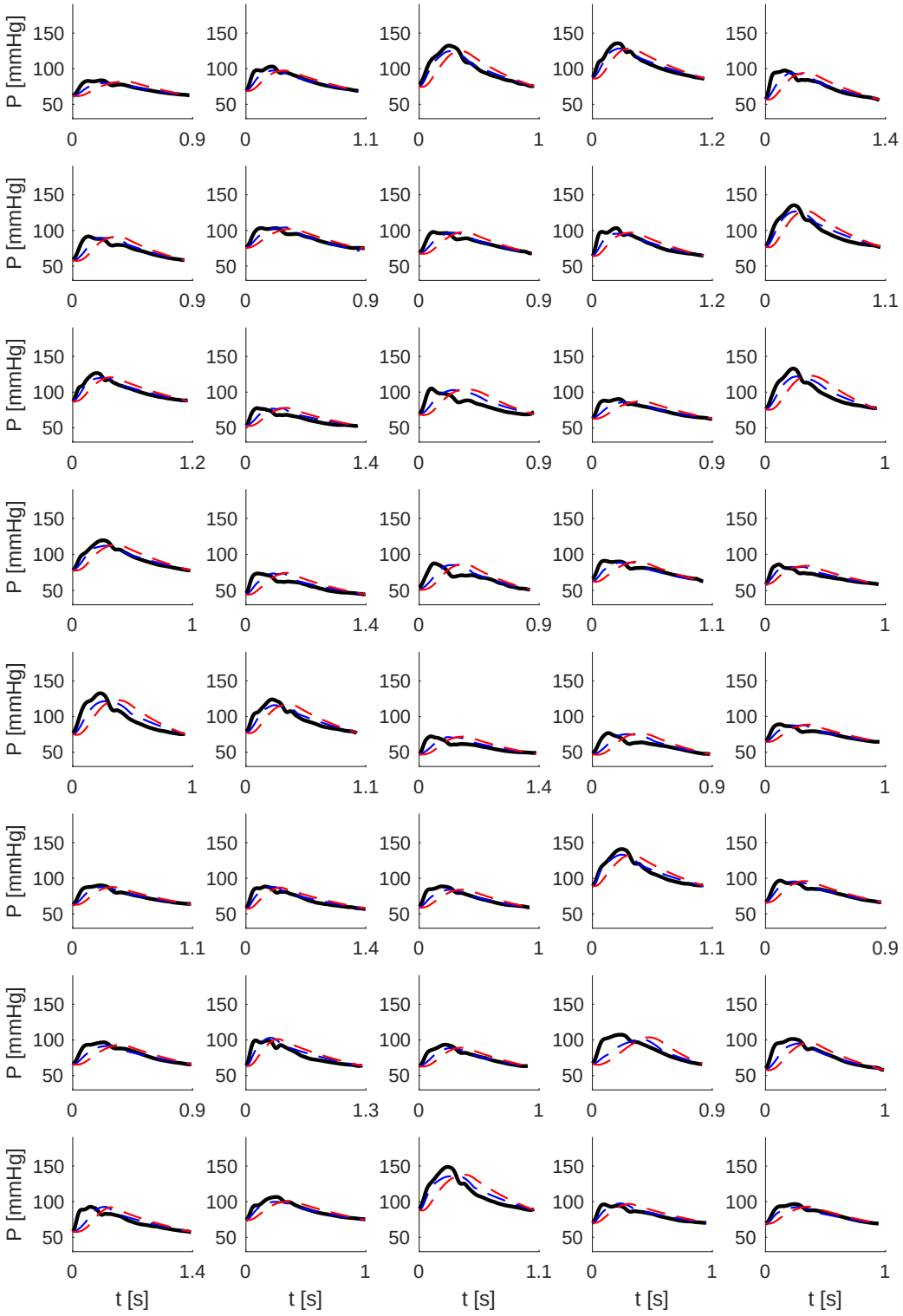
P [mmHg]
150
100
50
0
0.9
1.1
1
1.2
1.4
1.3
t [s]

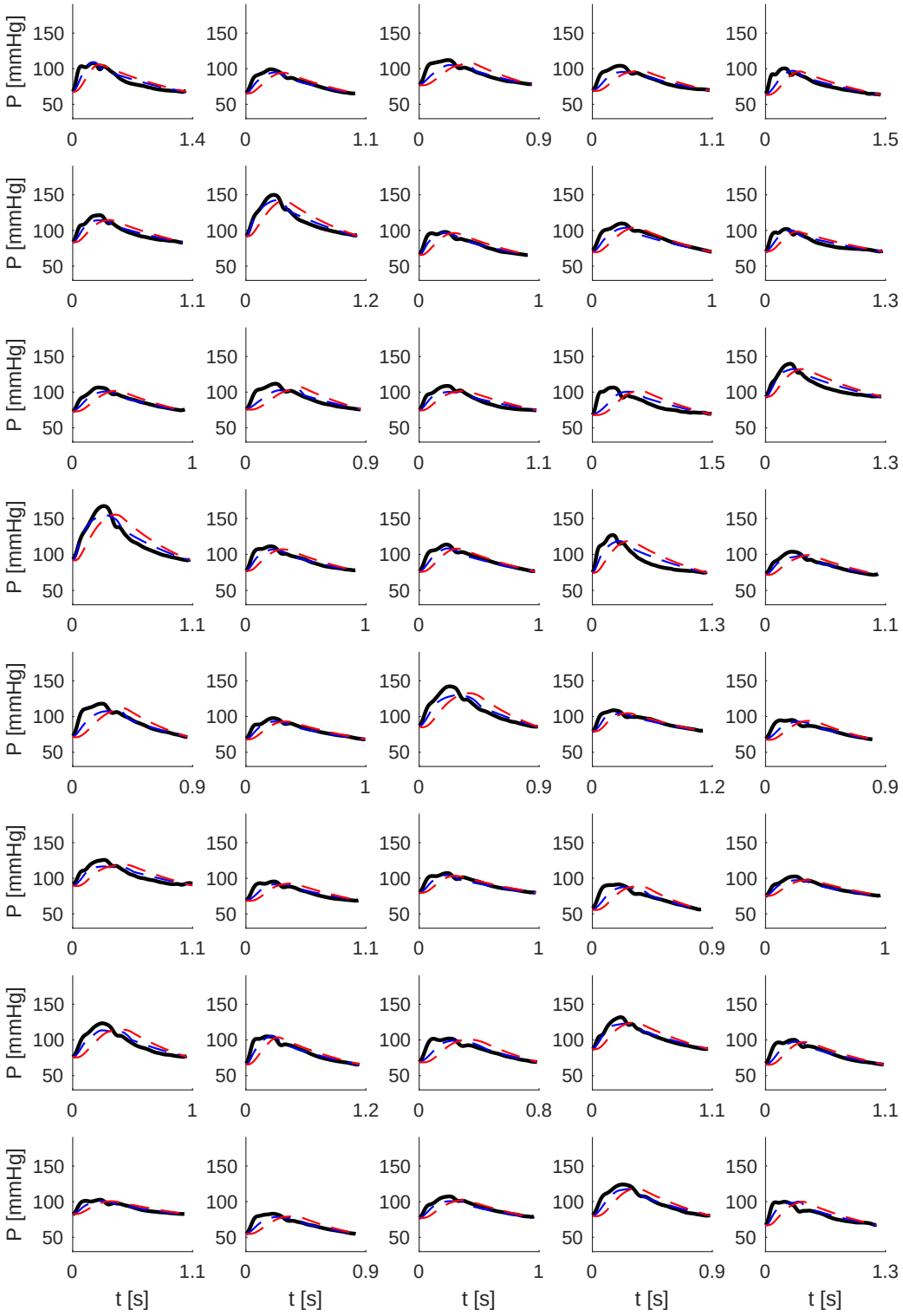
P [mmHg]
150
100
50
0
1.4
1.1
0.9
1.1
1.5
1.1
1.2
1
1
1.3
1
0.9
1.1
1.5
1.3
1.1
1
1
1.3
1.1
0.9
1
0.9
1.2
0.9
1.1
1.1
1
0.9
1
1.2
1
0.8
1.1
1.1
1.1
0.9
1
1.3
t [s]

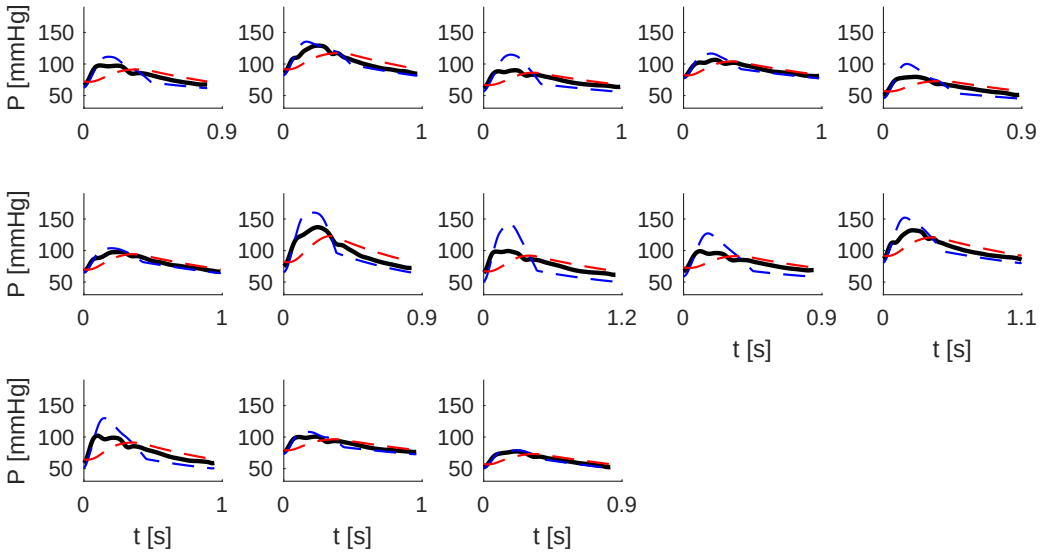

FIGURE A.7: cBP waveform estimations for Scenario 2. cBP waves calculated using the 2-element Windkessel (dashed red lines), 3-element Windkessel (dashed blue lines), and 1-D aortic (dashed black lines) cBP algorithms. They are compared against reference cBP waves from the 'Normotensive' dataset (thick black lines).

A.2.4 cBP estimations in the 'Hypertensive' dataset

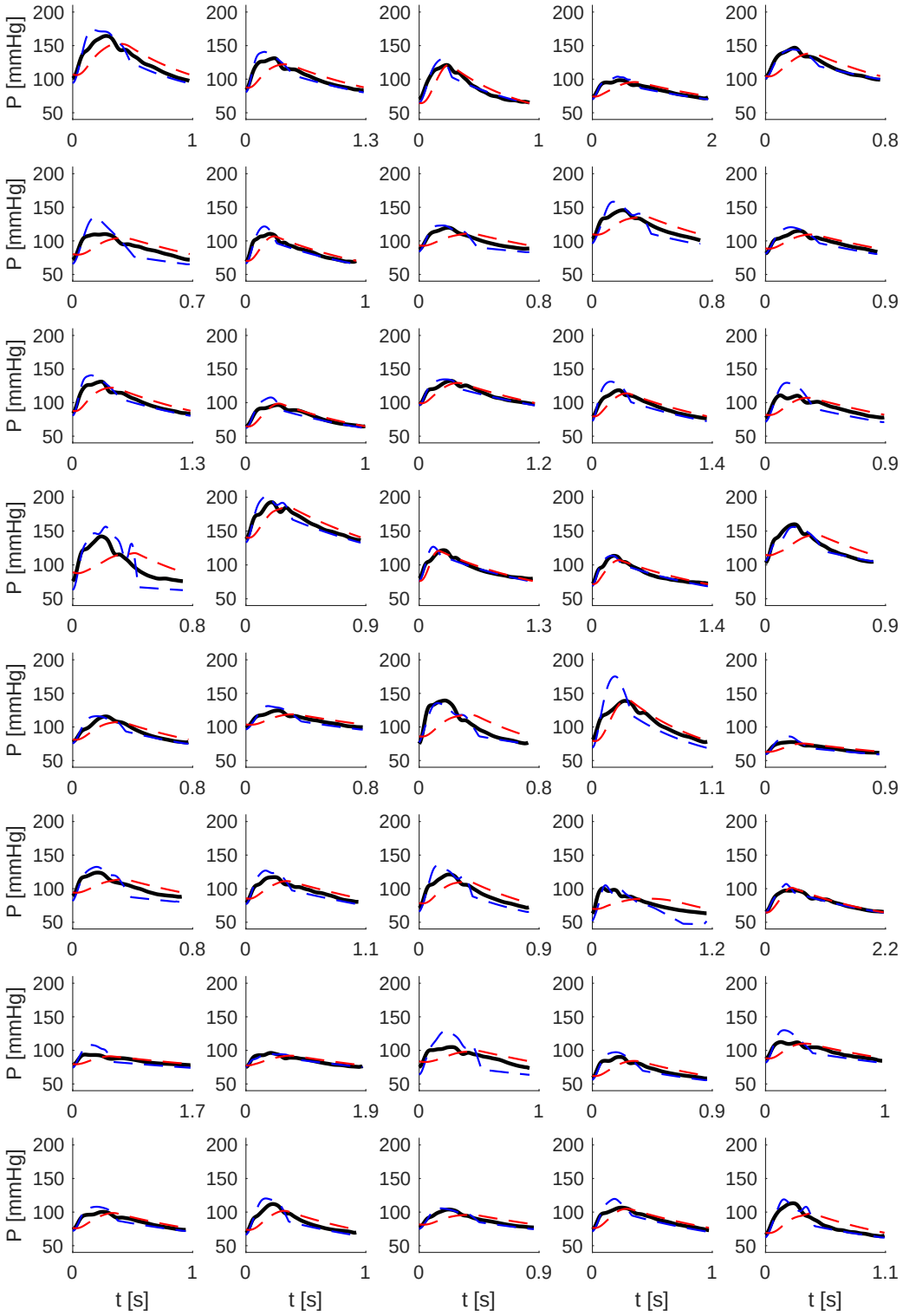

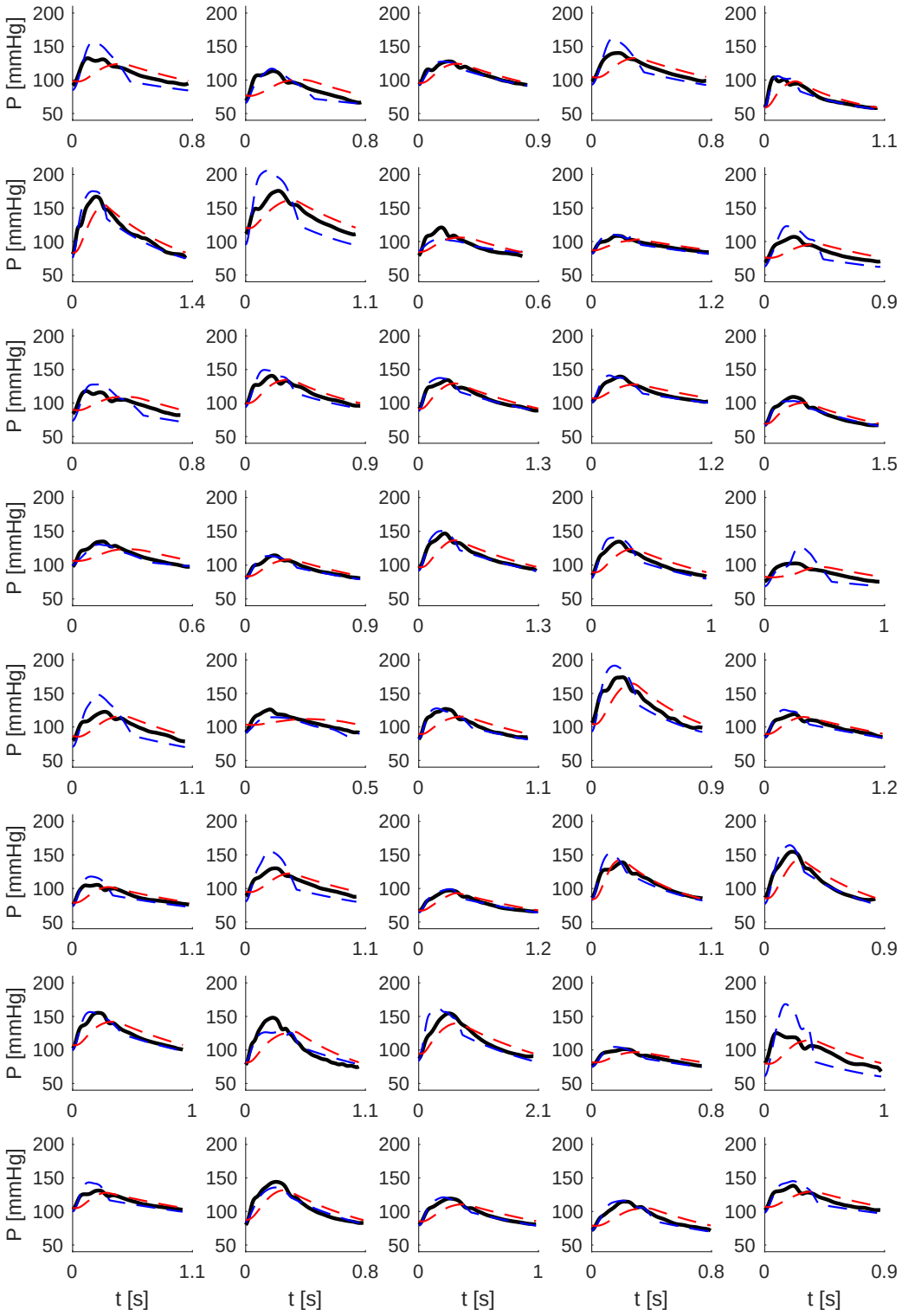
P [mmHg]
200
150
100
50
0
0.8
0.8
0.9
0.8
1.1
1.4
1.1
0.6
1.2
0.9
0.8
0.9
1.3
1.2
1.5
0.6
0.9
1.3
1
1
1.1
0.5
1.1
0.9
1.2
1.1
1.1
1.2
1.1
0.9
1
1.1
2.1
0.8
1
1.1
0.8
1
0.8
0.9
t [s]

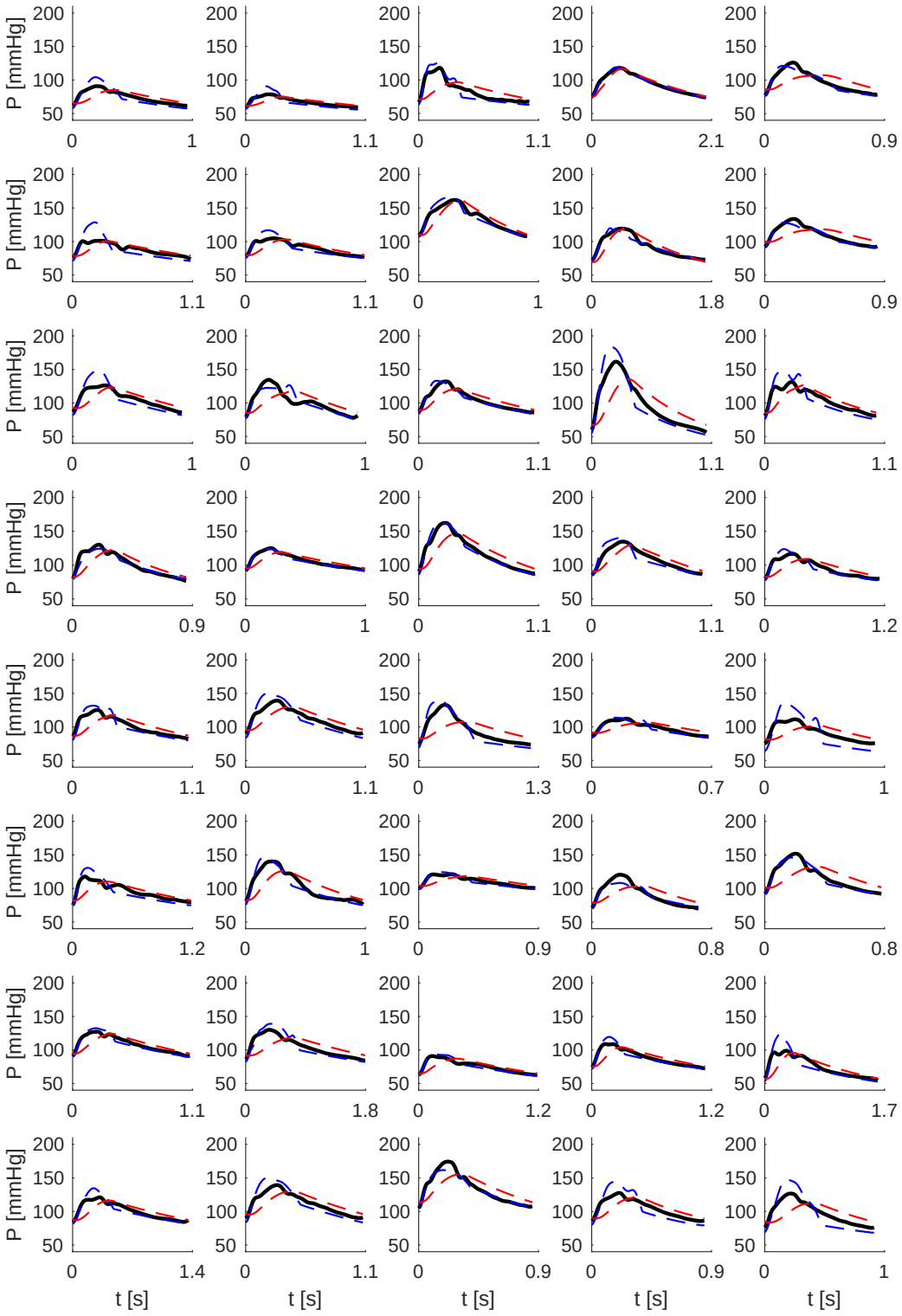
P [mmHg]
200
150
100
50
0
1
1.1
2.1
0.9
1.8
1.2
0.7
1.3
0.8
1.7
1.4
t [s]

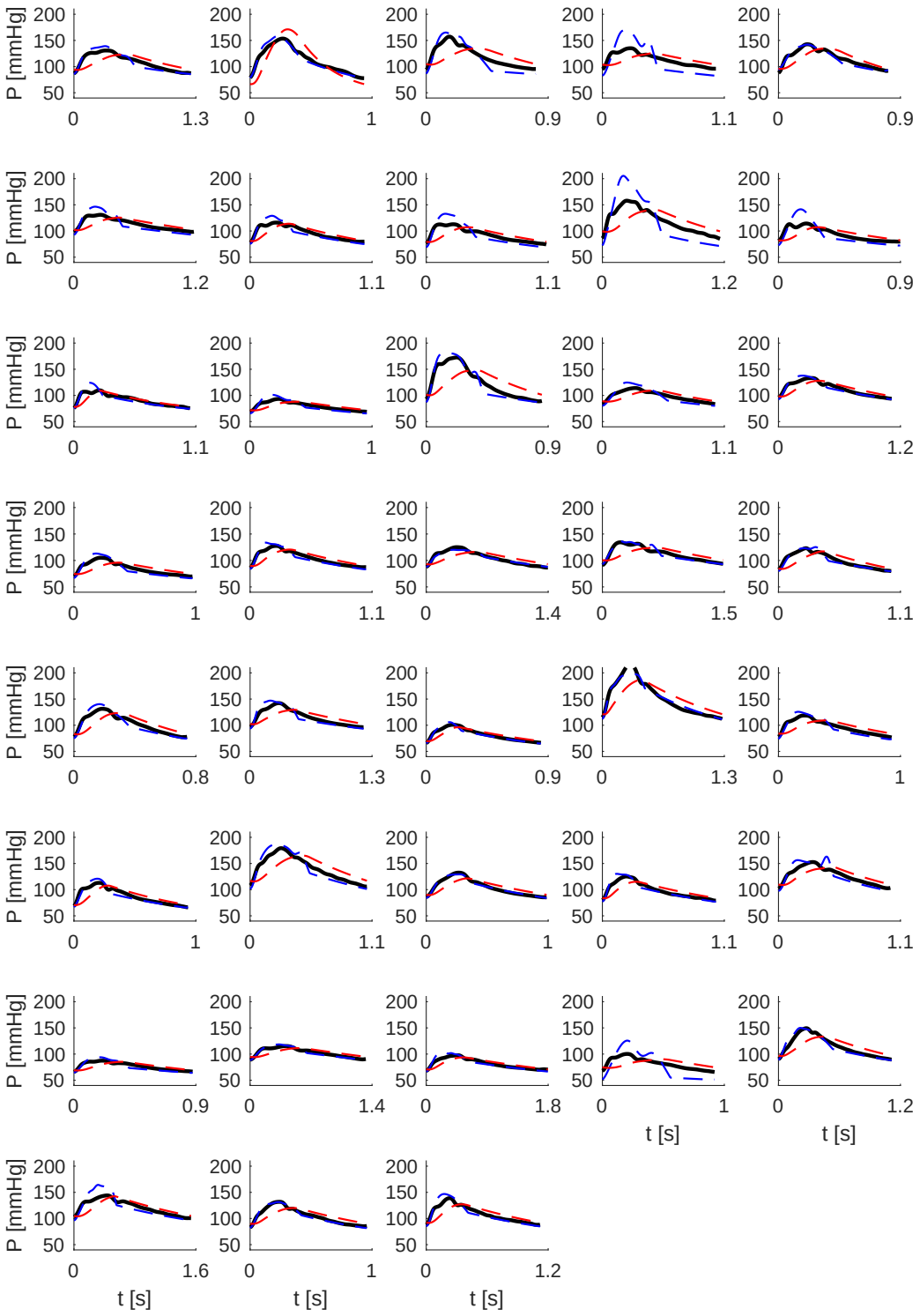

FIGURE A.8: cBP waveform estimations for Scenario 1. cBP waves calculated using the 2-element Windkessel (dashed red lines), 3-element Windkessel (dashed blue lines), and 1-D aortic (dashed black lines) cBP algorithms. They are compared against reference cBP waves from the 'Hypertensive' dataset (thick black lines).

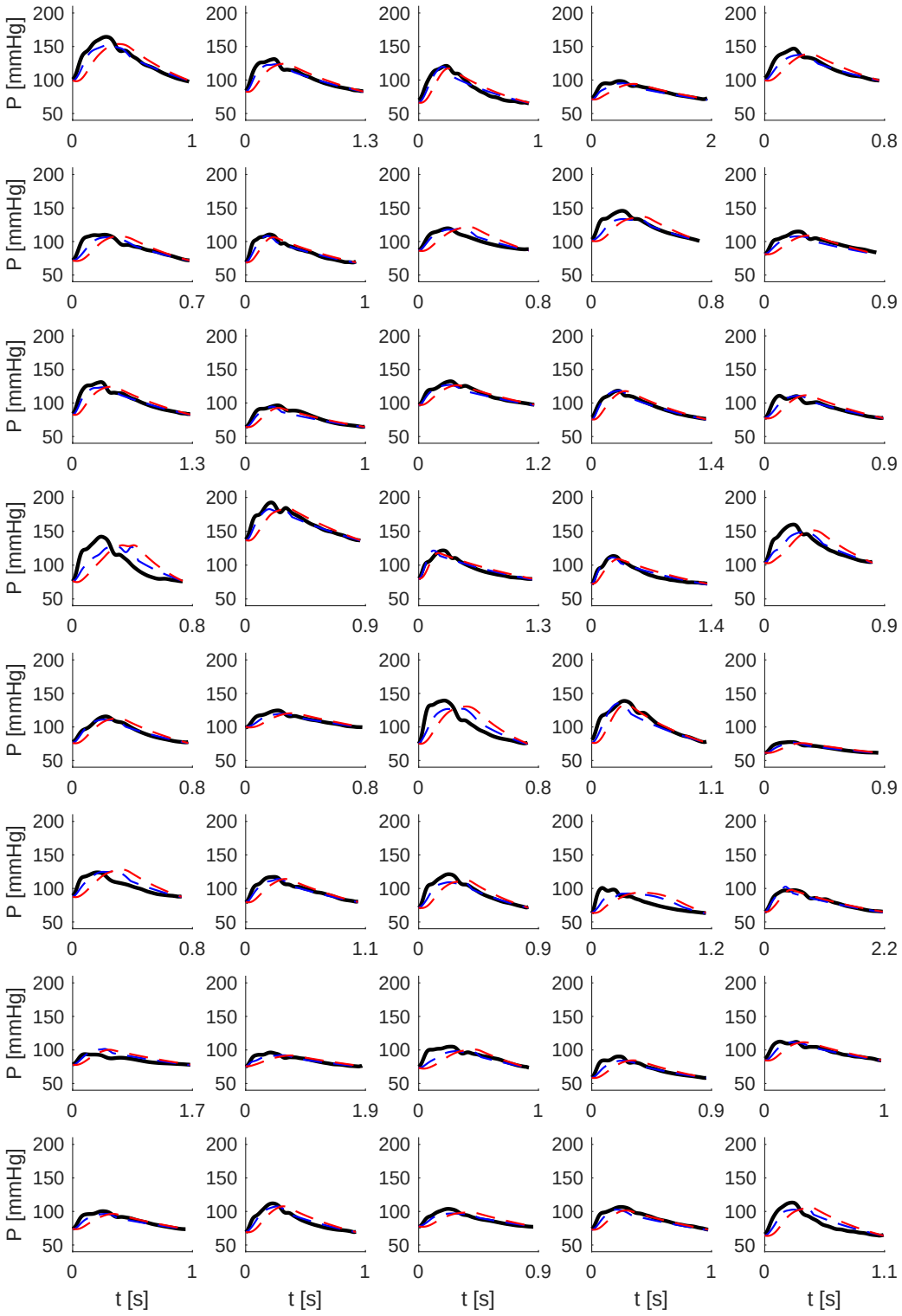
P [mmHg]
200
150
100
50
0
1
1.3
0.8
2
0.7
0.9
1.2
1.4
1.1
1.7
1.9
t [s]

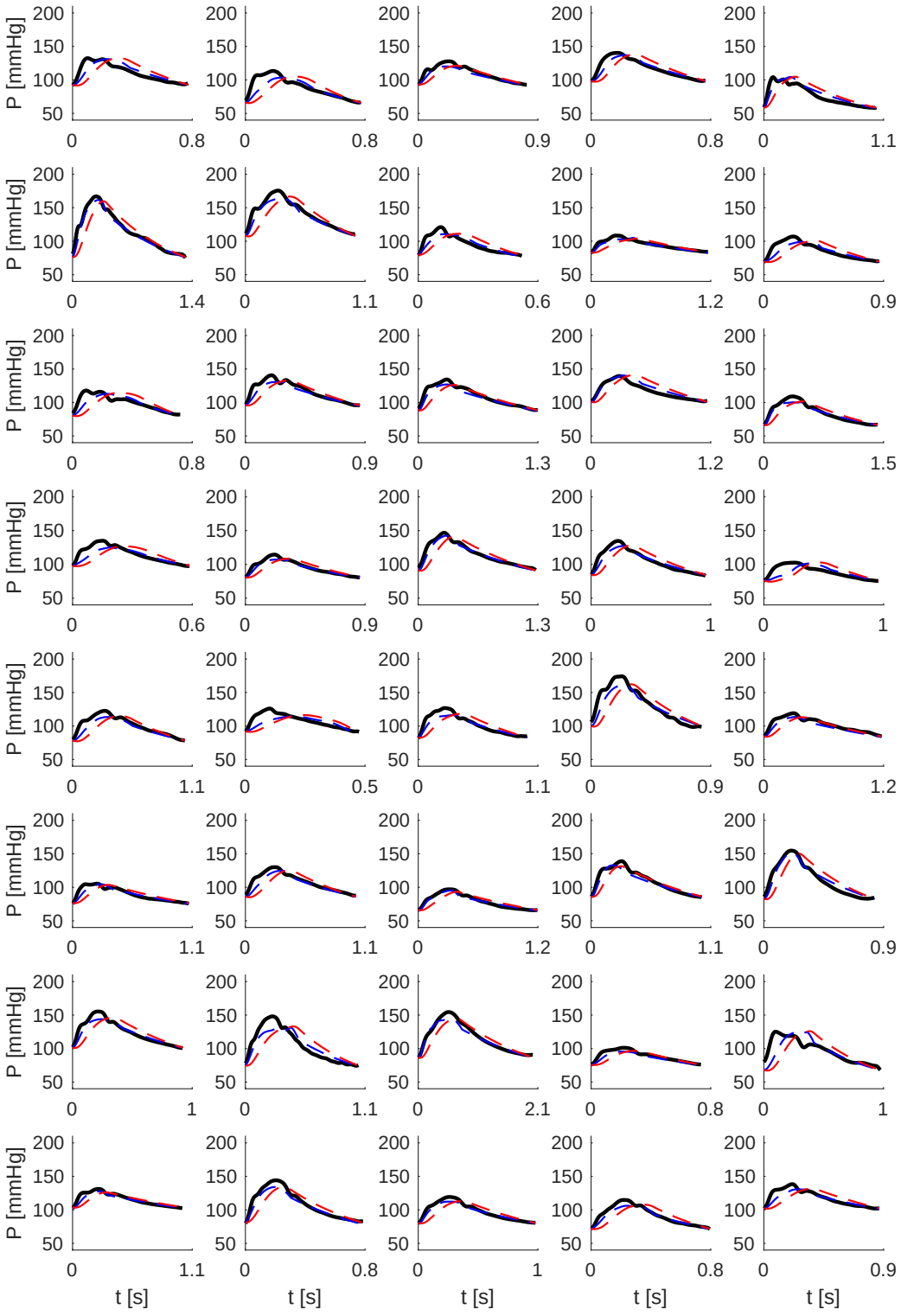
P [mmHg]
200
150
100
50
0
0.8
0.8
0.9
0.8
1.1
1.4
1.1
0.6
1.2
0.9
0.8
0.9
1.3
1.2
1.5
0.6
0.9
1.3
1
1
1.1
0.5
1.1
0.9
1.2
1.1
1.1
1.2
1.1
0.9
1
1.1
2.1
0.8
1
1.1
0.8
1
0.8
0.9
t [s]

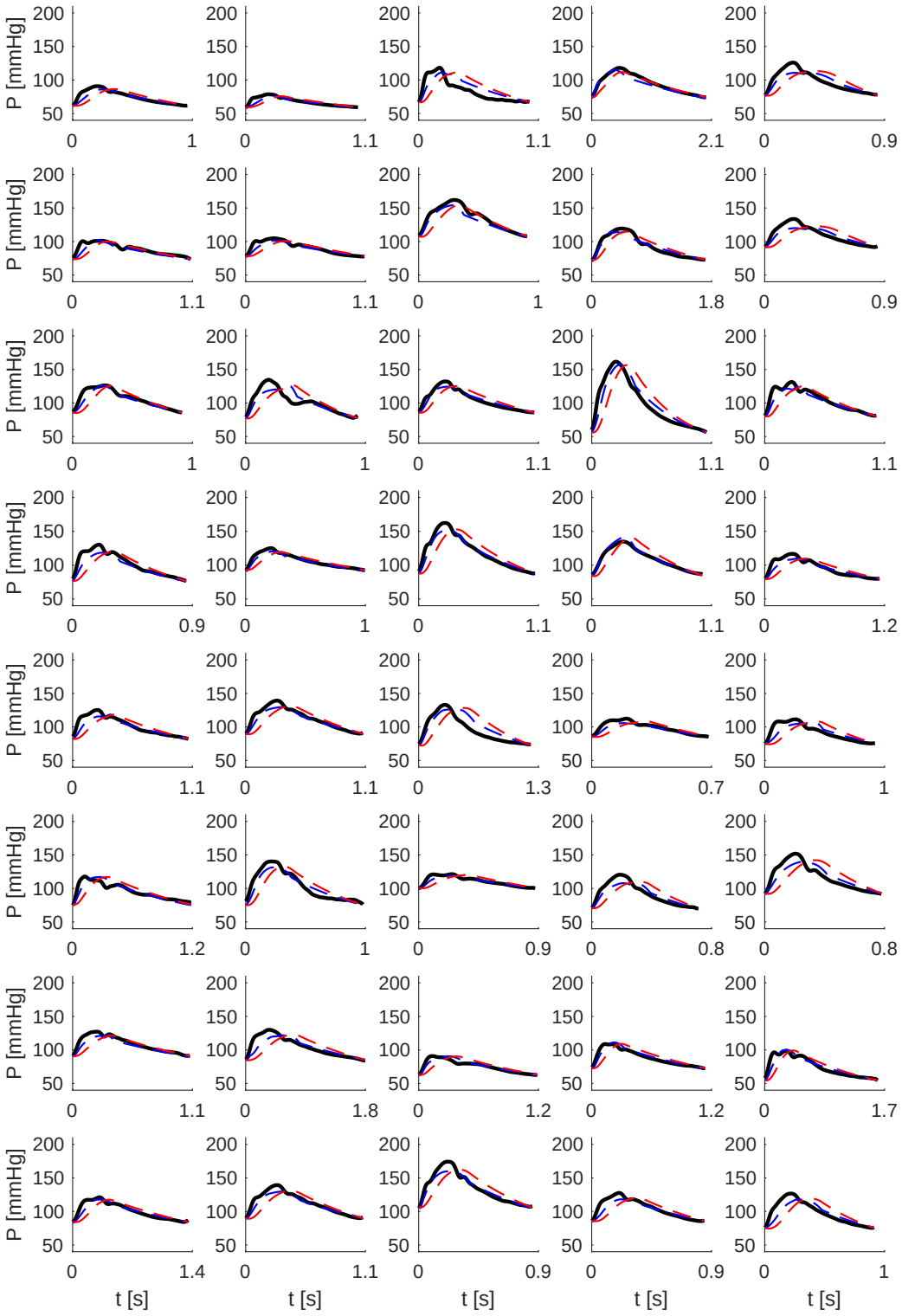
P [mmHg]
200
150
100
50
0
1
1.1
2.1
0.9
1.8
1.3
0.7
1.2
0.8
1.4
t [s]

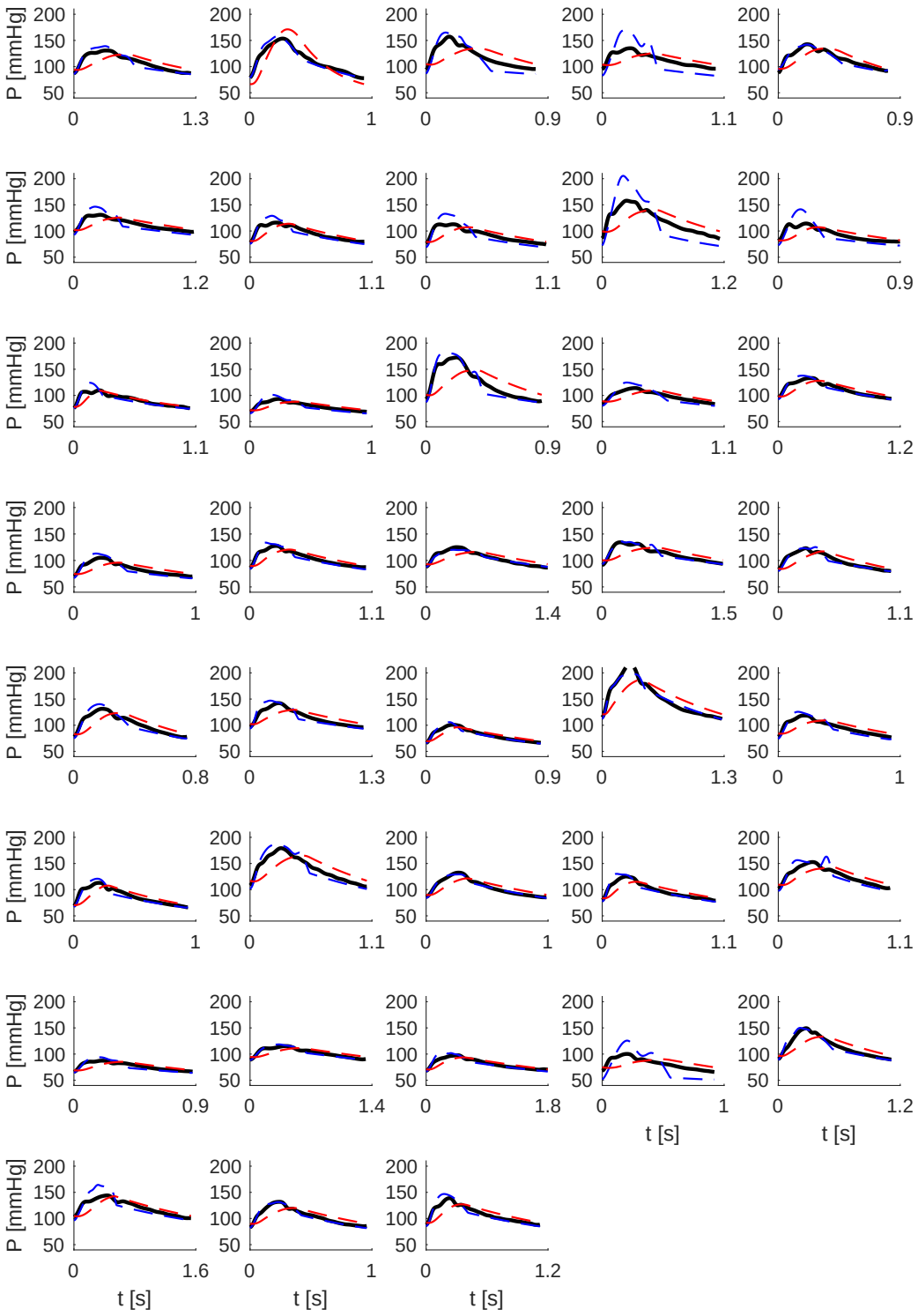

FIGURE A.9: cBP waveform estimations for Scenario 2. cBP waves calculated using the 2-element Windkessel (dashed red lines), 3-element Windkessel (dashed blue lines), and 1-D aortic (dashed black lines) cBP algorithms. They are compared against reference cBP waves from the 'Hypertensive' dataset (thick black lines).

A.3 Haemodynamics in Dilated Cardiomyopathy

This appendix contains the manuscript submitted to the *American Journal of Phisiology – Heart and Circulatory Phisiology.* The original text and American English spelling has been kept. Figures and tables have been placed at the end of the document.

Title:

Altered aortic hemodynamics and relative pressure in patients with dilated cardiomyopathy.

Authors:

David Marlevi, Jorge Mariscal-Harana, Nicholas S Burris, Julio Sotelo, Bram Ruijsink, Myrianthi Hadjicharalambous, Liya Asner, Eva Sammut, Radomir Chabiniok, Sergio Uribe, Reidar Winter, Pablo Lamata, Jordi Alastruey, David Nordsletten.

Corresponding author:

David Nordsletten

Dept. Cardiac Surgery and Biomedical Engineering, University of Michigan

Plymouth Rd, 48109

Ann Arbor, MI, USA

E-mail: david.nordsletten@gmail.com

Tel: +1 734 647 7000

Fax: +1 734 936 1905

Introduction

The heart and the vasculature are inherently coupled, and remodeling mechanisms on one side is commonly attributed to previous pathological manifestation on the other. Arterial and ventricular stiffening have been observed in heart failure patients with preserved ejection fraction(5). Pulse wave velocity and augmentation index – arterial measures related to vascular stiffness – have both been correlated to left ventricular (LV) systolic dysfunction(39). Vascular hemodynamics have also been closely coupled to ventricular function, with aortic relative pressure – the change in blood pressure over aortic segments – being linked to hypertrophic outflow tract obstruction(20), LV remodeling(6), and aortopathies (e.g., coarctation, aneurysm, or dissection)(25). Despite this, arterial function is seldom studied in cardiomyopathy patients. Instead, cardiomyopathy is typically seen as a "heart-only" disease, with diagnosis and intervention guided primarily using measures of cardiac function.

Despite clear anatomical and functional phenotypes, Dilated Cardiomyopathy (DCM) is commonly idiopathic with associated poor prognosis(12). Refined prognostic and diagnostic biomarkers are thus merited, and herein, ventricular-vascular interaction has been hypothesized as a key component in understanding disease progression. An increased aortic stiffness has been identified in DCM(4), and vascular hemodynamics have been linked to disease development, with pulmonary and systemic hypertension correlated to DCM mortality(1). Interestingly, the prognosis following cardiac resynchronization of heart failure patients (including DCMs)(42), as well as the ability to induce left ventricular reverse remodeling (experienced in up to 40% of all DCM patients(28)) have been related to arterial behavior, highlighting the importance of the vasculature.

To date, the clinical assessment of cardiovascular function has been largely based on medical imaging. In addition to diagnosing DCM by means of LV size and function, myocardial tissue characterization by cardiac magnetic resonance imaging (MRI) (using T1 or T2 mapping) is being increasingly used in clinical assessment(18). To this, phase-contrast (PC-) MRI methods such as 2D or 4D flow MRI(15) now permit comprehensive evaluation of blood flow in the cardiovascular system. 4D flow MRI in particular has uncovered altered diastolic ventricular flow routes in DCM(16), quantified aortic relative pressure in association with ventricular remodeling(6), and has enabled accurate estimation of relative pressure *in vivo*(13, 27). MRI flow imaging has been suggested as a possible tool for assessing ventricular-vascular behavior

in chronic heart failure(10), and right-ventricular-pulmonary coupling(26). Thus, 4D flow MRI can provide a more comprehensive evaluation of cardiac and vascular behavior, and may allow for refined understanding of ventricular-vascular interaction in DCM patients.

The aim of this study was to examine aortic hemodynamic changes in a DCM cohort, utilizing 4D flow MRI, to non-invasively assess vascular alterations in cardiac disease. Specifically, aortic relative pressure was derived from the 4D flow MRI data, utilizing the fact that changes in relative pressure are coupled to both cardiac function and reservoir status(6, 20, 25) to assess overall vascular response to myocardial dysfunction. Furthermore, given the challenges of studying isolated effects of arterial and ventricular perturbations in patients due to their physiologic interdependence, we developed a computational virtual cohort(40) (representing a model equivalent of the blood flow in the larger systemic arteries) to understand the impact of cardiovascular properties on aortic relative pressure. Using this combination of advanced blood flow imaging and computational cardiovascular simulations techniques, we aim to map aortic and cardiac hemodynamic function, and uncover possible signs of ventricular-vascular interplay in DCM.

Methods

Figure 1 shows an overview of all utilized data sources. Additionally, extracted quantities are specified, showing the spectrum of cardiac and aortic parameters analyzed.

Study population

Adult subjects were recruited at St Thomas' Hospital, King's College London, through the British Heart Foundation Integrated Mathematical Modelling and Imaging (BHF-IMMI) project, with data acquired during March 2013 – April 2014. The inclusion criteria for the patient cohort were age > 18 years, and diagnosed non-ischemic symptomatic (NYHA class III) DCM-related heart failure. The exclusion criteria were known airway disease, pregnancy, renal or hepatic impairment, previous history of angina or cardiac arrhythmias for which continuous administration of beta blockers was deemed necessary, as well as contraindications to MRI. In addition to patients, the BHF-IMMI project also recruited healthy control subjects without any known cardiovascular, pulmonary, renal, hepatic, diabetic, or other systemic diseases.

In this retrospective study, 14 patients and 16 healthy controls were included. Patient treatment followed guideline medical management for heart failure, specifically including beta blocker administration. At the time of MRI, a subgroup of DCM patients presented with preserved LV function following medical therapy. Consequently, the DCM cohort was divided into two subgroups: subjects with reduced LV function (DCM_{red}, LV ejection fraction (EF) < 50%, n = 9) and subjects with preserved LV function (DCM_{pres}, EF ≥ 50%, n = 5). Prior to data collection, the entire patient cohort had their beta blocker treatment discontinued for 48 hours to examine native cardiovascular function.

All subjects provided informed consent, with data collection approved by the Regional Ethics Committee, South East London, UK (REC, 12/LO/1456). Subject demographics are shown in Table 1.

Imaging, data collection, and post-processing

a) Cardiac functional imaging

MRI was performed at 1.5T (Philips ACHIEVA) using a 32-channel cardiac coil. Cardiac function and characteristics were assessed using cine steady-state free precession (SSFP) MRI of stacked short axis, and three long axis view planes. Left and right ventricular end-systolic and end-diastolic volumes, along with cardiac output metrics (EF, stroke volume (SV), cardiac output (CO), cardiac index (CI)) were obtained from all subjects (imaging and processing details are provided in Supplementary Material).

b) Vascular flow imaging and aortic relative pressure estimation

All subjects were imaged using 4D flow MRI (8-fold acquisition using the k-t PCA technique(32) in combination with a sparsifying transform(24), spatial resolution ~2.5 mm^3, temporal resolution ~33 ms, prospective ECG gating, velocity encoding range ~120-190 cm/s). The thoracic aorta was segmented using an in-house software. Aortic relative pressure was computed from the left ventricular outflow tract (LVOT) to the diaphragm level of the descending aorta using a validated virtual work-energy approach (see Marlevi et al(27) and Supplementary Material). From each relative pressure trace, maximum and minimum relative pressure were derived. Additionally, time-to-peak relative pressure (TTP) was computed, given as the time from acquisition onset (triggered at ECG R-wave) to maximum relative pressure. These three metrics were chosen to represent aortic hemodynamic behavior, with positive and negative relative pressure relating to the acceleration and deceleration of blood through the aorta, and with TTP relating to ventricular conduction(36) and myocardial contractility(35). An illustration of the derived metrics is given in Figure 2.

Aortic pulse wave velocity (PWV) was derived using a validated cross-correlation method(19), assessing the flow transit time between prescribed inlet and outlet. Aortic stiffness was subsequently calculated using the Moens-Korteweg equation(29).

c) Central blood pressure estimation

Central blood pressure (CBP) estimates were derived from brachial sphygmomanometer cuffing acquired prior to imaging, using dedicated equipment (CENTRON cBP301, SunTech Medical Inc., Morrisville, NC, USA) where brachial pressures are converted into CBP by means of validated transfer functions(7).

Virtual cohort

Structural and functional cardiovascular characteristics can be studied by means of non-invasive imaging. However, the intertwined nature of ventricular-vascular behavior makes it difficult to isolate independent factors that impact cardiovascular function. Computational modeling, however, allows for the study of the physiological effects of specific parameters on the cardiovascular system in an isolated fashion(9). To understand aortic relative pressures, a virtual cohort was thus created, solving 1D blood flow equations through a systemic circulatory model, all based on the models described in Willemet et al(40) and Alastruey et al(2). Importantly, such models have been extensively validated and verified to accurately represent 1D arterial hemodynamic behavior through the larger arterial system(31, 33).

The virtual cohort was adjusted to match clinical characteristics (arterial peripheral resistance, SV, cardiac period, aortic area, aortic stiffness), with both DCM_{red} and DCM_{pres} having a corresponding virtual subgroup. By varying isolated parameters around a subgroup baseline, the independent influence of these defined clinical characteristics was assessed. Virtual relative pressures were derived from the LVOT to the descending aorta, with outputs normalized over aortic length. Technical details of the virtual cohort are provided in Supplementary Material.

Statistical analysis

Statistical differences in subject characteristics, cardiac metrics, and aortic outputs were evaluated using a Mann-Whitney U-test for continuous data, and a χ^2 test for nominal data (significance inferred at $p < 0.05$). Outliers were evaluated by Tukey's fences.

The Pearson correlation coefficient was evaluated to assess potential correlations between subject characteristics and output metrics. Correlation was inferred for $|R| > 0.5$ and $p < 0.002$ (determined from $p < 0.05$ together with a Bonferroni correction for $m = 21$ tested correlates, introduced to account for the multiple comparisons).

All evaluations were performed using MATLAB R2016a (MathWorks, Natick, MA, USA).

Results

Based on the acquired image data, one DCM subject with reduced LV function was excluded following the identification of mild aortic stenosis (maximum aortic outflow velocity = 1.8 m/s versus group mean = 0.8 ± 0.3 m/s, falling beyond the outer Tukey fence), and a significantly altered aortic geometry (aortic diameter = 1.0 cm versus a group mean = 1.6 ± 0.2 cm, LVOT cross-sectional area = 1.5 cm^2 versus a group mean = 5.9 ± 2.9 cm^2).

Clinical data and subject characteristics

Complete characteristics and data output are provided in Table 1. The DCM_{red} group showed significantly higher body mass index (BMI) and LV volumes, and significantly lower LV EF, LV cardiac index (CI), as well las right ventricular (RV) CI. Systolic and mean blood pressure were also elevated.

Aortic relative pressure in dilated cardiomyopathy patients

Aortic relative pressure characteristics are provided in Table 2, with Figure 3 showing comparisons of flow-derived markers.

The DCM_{red} group showed a significantly decreased maximum aortic relative pressure, with an average reduction of 22% (61.6 ± 10.0 mmHg/m vs. 78.9 ± 18.0 mmHg/m, p = 0.022). However, this difference was not reflected for the minimum relative pressure, where similar values were obtained as for the control group.

A markedly prolonged TTP was seen in both DCM_{red} and DCM_{pres} groups. Strong statistical differences in group means were seen between the control group and both DCM groups ($p \leq 0.01$), with the DCM patients requiring twice as much time to reach maximum relative pressure (109 ± 22 and 108 ± 38 ms vs. 55 ± 22 ms).

The DCM_{red} group showed a higher aortic PWV compared to the control group, with an increase of 47% (11.0 ± 4.6 m/s vs. 7.5 ± 2.5 m/s, p = 0.034). Increased PWV was not noted in the DCM_{pres}. Similar results were observed for derived aortic stiffness, where the DCM_{red} group had a significantly higher aortic stiffness, with an increase of 130% (14.5 ± 12.0 kPa vs 6.3 ± 5.1 kPa, p = 0.035).

Correlation of aortic relative pressure with clinical, structural, and central blood pressure metrics

Complete correlation results are provided in Supplementary Table 2. In short, for the DCM_{red} and DCM_{pres} groups, no correlations could be inferred between any clinical parameter and the derived aortic metrics, including central blood pressures. For the control group, similar behavior was observed, with only BSA and BMI correlated to minimum relative pressure and aortic stiffness, respectively.

Influence of isolated cardiovascular properties on aortic relative pressure

The individual influence of cardiovascular properties on aortic relative pressure was analyzed using the virtual cohort. Aortic relative pressure for each virtual subgroup, together with corresponding clinical traces, is shown in Figure 4.

For the virtual cohort, aortic maximum relative pressure varied between 23.9 – 56.5, 28.3 – 62.5, and 30.4 – 72.1 Pa/m for the DCM_{red}, DCM_{pres}, and control groups, respectively. For reference, the clinical cohort varied between 42.4 – 72.8, 62.2 – 102.7, and 57.3 – 121.4 Pa/m within the same three groups, respectively. Individual variations as a function of isolated variables are given in Supplementary Table 3.

For the virtual cohort, aortic stiffness and aortic area were the two dominant properties influencing aortic relative pressure. Specifically, variations in aortic stiffness alone recovered 47% of the total variations observed in maximum relative pressure in the DCM_{red} subgroup, 63% of the total variations observed in the DCM_{pres} group, and 100% of the total variations in the control group. Similarly, variations in aortic area alone recovered 87, 91, and 73% of the total observed variations in maximum relative pressure in the same three groups, respectively. In contrast, cardiac parameters (SV, cardiac period) had a comparatively smaller influence.

For minimum relative pressure, similar behavior could be observed where aortic stiffness and aortic area were the two major contributors to the observed variations (aortic stiffness equaling 70, 63, and 94% of the total variations, compared to aortic area equaling 95, 100, and 92%, again reported for the DCM_{red}, DCM_{pres}, and control groups, respectively).

Discussion

In this study we have used 4D flow MRI to evaluate aortic hemodynamic changes in patients with DCM. We identified clear evidence of vascular modifications in the patients with reduced LV function, with decreasing maximum aortic relative pressure, and increased aortic stiffness estimates evident from the flow-based analysis. We also inferred potential signs of ventricular conduction delay from the aortic analysis, with prolonged TTP evident in all patients, independent of LV function. Furthermore, our computational virtual cohort showed that these aortic hemodynamic metrics are predominantly governed by arterial behavior (aortic size and stiffness), indicating an active role of the vasculature in the development and manifestation of DCM. With previous observations linking both cardiac disease and interventional outcome success to arterial behavior(28, 42), our results highlight how highlight how vascular evaluation could complement the clinical assessment of DCM patients, and provide insights into the pathophysiological interactions between cardiac and arterial function.

Changes in aortic relative pressure – relation to cardiac and aortic physiology

The DCM_{red} group showed a significantly reduced maximum aortic relative pressure, being on average 22% lower than the control group. Conversely, the DCM_{pres} group did not differ significantly from the control, maintaining maximum aortic relative pressure. While the DCM_{red} and DCM_{pres} groups are defined on the basis of cardiac function, the observed differences in aortic relative pressure show how changes in cardiac function are reflected on the vascular side. In previous studies, DCM has been associated with a reduction in peak aortic outflow acceleration(22), and deteriorating cardiovascular status has been correlated to a decrease in LVOT outflow gradients(3), highlighting how ventricular dilation affects vascular hemodynamics. Given that aortic relative pressure has been correlated to LV remodeling(6), our findings suggest that vascular response could be important for better understanding disease progression in DCM.

In contrast, no significant differences could be inferred for minimum aortic relative pressure, where both DCM_{red} and DCM_{pres} groups showed similar values to the control group. Minimum aortic relative pressure – an entity related to the deceleration of blood during late systole – has been less studied in conjunction to cardiac disease, and has instead been linked to aortic reservoir function(34). However, with apparent differences in aortic stiffness estimates

inferred between DCM_{red} and DCM_{pres} groups, this instead indicates a possible intertwined relationship between cardiac status, aortic function, and relative pressure. In other disease (e.g. bicuspid aortic valve, or aortic dissection), aortic relative pressure has been related to both cardiac and aortic physiology(25), supporting the role of coupled cardiac and vascular hemodynamic behavior.

In comparison to the above, TTP is an entity coupled to the contractility of the left ventricle: the shorter the TTP the faster the ventricular contraction. In our study, a significant delay in TTP was observed in both DCM groups relative to controls, with an almost doubling of the time required to reach peak relative pressure. Ventricular conduction delay is commonly reported for DCM(23), and although conduction abnormalities were not assessed in our study, prolonged QRS duration has been correlated to a reduction in maximum intraventricular relative pressure(41) – in-line with our findings on TTP. Especially noteworthy is the fact that the entire DCM group exhibited prolonged TTP, regardless of LV status. That is, even though ventricular function was decreased in some and preserved in others, an underlying electrophysiological pathology could be possibly indicated in both groups. In DCM, ventricular conduction delay has shown to be one of the most powerful predictors of prognosis(38), and our results seem to indicate a persistent conduction abnormality despite medical management and preserved LV ejection fraction. Idiopathic DCM is connected to the long-term development of heart failure(17), and latent subclinical contractile abnormalities could have detrimental long-term ramifications even in groups where short-term improvement in cardiac function is observed.

A significant increase in PWV and aortic stiffness estimates were obtained in the DCM_{red} group, with aortic stiffness estimates increasing by a factor of almost 2.3 compared to the control group. On the contrary, the DCM_{pres} group did not differ significantly from the control group. Arterial stiffening in DCM patients has been described previously(4) and reduced maximum relative pressure was recently reported in an elderly cohort(6), in sorts similar to how our clinical findings connect reduced relative pressure with increased estimated aortic stiffness. In general, arterial stiffening is a commonly ascribed vascular response mechanism in cardiovascular disease where – in the case of impaired ventricular efficiency – increased arterial stiffening may contribute to maintaining necessary forward-flow of blood into the peripheral circulation.

Lastly, the DCM_{red} group showed significantly increased systolic blood pressure compared to the control group. This increase in afterload is however not coupled to any significant differences in SV, suggesting that increased ejection force is required to maintain systemic circulation in the DCM_{red} group. Furthermore, the simultaneous increase in mean blood pressure indicates elevated systemic resistance in the DCM_{red} group, however, this is slightly opposed by unaltered diastolic blood pressure. In general, the development of hypertension is common in DCM(12) and originates in part from increased neurohormonal activation(8). It highlights a persistent detrimental remodeling feedback loop, in which long-term congestion leads to increased afterload due to sympathetic activation,. The chronic overload of the ventricle thus in turn leads to worsening contractile properties.

Correlation to aortic relative pressure – independent role of aortic hemodynamics

The correlation analysis revealed a general lack of defined relationships between aortic hemodynamics and standard volumetric and functional metrics for the entire DCM cohort. This should be contrasted to the clear differences in the DCM_{red} group seen with the derived aortic metrics. In other words, the assessment of aortic relative pressure may be a useful parameter for assessing function in DCM patients beyond standard EF assessment, and may have independent value given the lack of strong correlation with other conventional functional, volumetric, and hemodynamic parameters. Others have indicated the independent association between aortic relative pressure and LV remodeling(6), highlighting relative pressure as a complementary and independent biomarker for refined cardiac diagnosis.

The role of cardiac and aortic function on relative pressure – isolated virtual cohort study

Out of the evaluated metrics in the virtual cohort analysis, estimated aortic stiffness and mean cross-sectional area were the main counteracting determinants of aortic relative pressure: while positive changes in stiffness increase relative pressure magnitudes, positive changes in area decrease them. Such balancing reservoir behavior could explain the maintained minimum relative pressure; however would not completely clarify the corresponding net decrease in maximum relative pressure. This reduction could instead be attributed to cardiac changes such as modified contractility(21), lack of contractile coordination(23), or coupled reservoir

behavior. Regardless, the combination of clinical and computational results indicates both modified reservoir and altered cardiac function, both mutually present in DCM.

Aortic change in DCM – clinical implications of image-based findings

In our study, a number of aortic hemodynamic changes have been inferred for DCM. In particular, the aortic response differed between DCM_{red} and DCM_{pres}. With the two groups following similar guideline therapeutic management, the separation could indicate how cardiac treatment efficacy may be, at least in part, coupled to vascular adaption abilities.

Antihypertensive medications have been shown to reduce arterial stiffness(14), being part of a general strategy to hinder continuous dilation through ventricular unloading. In the DCM_{red} group, however, modified vascular adaption could render an ineffective response, where – despite treatment – increased blood pressure and aortic stiffness require excessive myocardial work to maintain systemic perfusion. Furthermore, with hypertension correlated to aortic dilation(30), and with an increased aortic cross-sectional area decreasing relative pressure, the DCM_{red} will experience decreased acceleration of the ejected blood being potentially impactful for long-term stability of the systemic circulation. If, at this stage, an additional medication could decrease aortic stiffness or blood pressure, an additional unfavorable depression of relative pressure could follow. This suggests that due to poor vascular adaption, the standard treatment may potentially fail to unload the heart, instead pushing it further down a pathological remodeling spiral. While using arterial function as a measure of drug effectiveness is not a new concept(11), our study indicates that unloading the heart requires a unified look at cardiac, aortic, and systemic function.

Clinical outlook - non-invasive imaging for the assessment of ventricular-vascular function

Advanced MRI blood flow imaging permits detailed hemodynamic analysis. As evident from our study, aortic hemodynamics are altered in cardiac disease, and aortic relative pressure may be directly connected to cardiac and vascular function, going beyond what can be inferred by conventional cardiac assessment (using e.g. EF, SV, or ventricular volumes). With physics-based image processing allowing for relative pressure to be derived directly from acquired image data, the proposed biomarkers can thus be added as a complement to the traditional diagnostic information. Several examples exist of where volumetric flow imaging improves

the assessment of cardiovascular disease: quantifying 4D intraventricular flow in relation to heart failure severity(37), providing accurate estimates of relative pressure(13, 27) or assessing aortic hemodynamics in conjunction to ventricular remodeling(6). Our study underlines this clinical impact of advanced flow imaging, with arterial alterations indicating active vascular response to manifested cardiac disease. Further studies are required to uncover the initiation and sequential order of the remodeling response, however, imaging has the potential to play a key role in studying such behavior in a non-invasive setting.

Limitations

A fairly small sample size was used, and the generalization of these findings to a global DCM population requires further investigation. Instead, our results can be seen as an example of how advanced flow imaging together with biophysical modelling can provide novel insights into pathophysiological developments, specifically addressing the concept of aortic hemodynamic response in cardiac disease.

For the virtual cohort, the analysis was limited to a selection of key cardiovascular properties, chosen based on their conventional use in cardiovascular practice. The virtual cohort showed slightly lower relative pressure compared to the retrieved clinical data in all three subgroups. As is common in 1D cardiovascular simulations, systemic baseline characteristics (peripheral resistance, systemic variations in PWV, segment diameters etc.) were retrieved from published literature values on healthy subjects, with only conventionally assessable metrics (SV, heart rate) tailored to reflect certain pathologies. Consequently, these underlying baseline characteristics might not be entirely reflective of the assessed clinical cohort and might cause the observed bias. However, with virtual and clinical cohorts showing similar trends with respect to aortic relative pressure (decreasing relative pressure with increasing LV impairment), there are reasons to believe that the isolated influence of evaluated cardiovascular parameters on the virtual cohort is reflective of similar behavior on the clinical side.

Conclusion

In this study a combination of non-invasive MRI blood flow imaging and computational modeling were used to study aortic relative pressure in DCM. Significant aortic hemodynamic changes were observed, relating to specific physiological aspects of the disease: decreased maximum relative pressure indicating impaired ventricular ejection (DCM_{red} group); prolonged TTP indicating conduction delay (both DCM groups regardless of LV status); and increased aortic stiffness and systolic blood pressure indicating compensatory arterial remodeling (DCM_{red} group). Given that the aortic response was different between the patients with preserved and reduced LV function, vascular adaption could be a novel complementary marker for assessing disease severity and treatment efficacy in DCM. Further, with the 4D flow derived hemodynamic parameters not correlated to conventional cardiac metrics (e.g., EF, SV or ventricular volumes), the aortic assessment could provide additional diagnostic and prognostic value. Overall, this study highlights the important role of vascular adaption in the pathogenesis and progress of DCM, and also demonstrates how ventricular-vascular abnormalities can be effectively studied using 4D flow imaging and advanced biophysical image processing.

References

[1] Abramson SV, Burke JF, Kelly JJ, Kitchen JG, Dougherty MJ, Yih DF, McGeehin FC, Shuck JW, and Phiambolis TP. Pulmonary hypertension predicts mortality and morbidity in patients with dilated cardiomyopathy. *Annals of internal medicine* 116: 888-895, 1992.

[2] Alastruey J, Parker KH, and Sherwin SJ. Arterial pulse wave haemodynamics. *11th International Conference on Pressure Surges*. Virtual PiE Led t/a BHR Group Lisbon, Portugal, 2012, p. 401-442.

[3] Avramides D, Perakis A, Voudris V, and Gezerlis P. Noninvasive assessment of left ventricular systolic function by stress-shortening relation, rate of change of power, preload-adjusted maximal power, and ejection force in idiopathic dilated cardiomyopathy: prognostic implications. *Journal of the American Society of Echocardiography* 13: 87-95, 2000.

[4] Bonapace S, Rossi A, Cicoira M, Golia G, Zanolla L, Franceschini L, Conte L, Marino P, Zardini P, and Vassanelli C. Aortic stiffness correlates with an increased extracellular matrix turnover in patients with dilated cardiomyopathy. *American heart journal* 152: 93. e91-93. e96, 2006.

[5] Borlaug BA and Kass DA. Ventricular–vascular interaction in heart failure. *Cardiology clinics* 29: 447-459, 2011.

[6] Bouaou K, Bargiotas I, Dietenbeck T, Bollache E, Soulat G, Craiem D, Houriez-Gombaud-Saintonge S, De Cesare A, Gencer U, and Giron A. Analysis of aortic pressure fields from 4D flow MRI in healthy volunteers: Associations with age and left ventricular remodeling. *Journal of Magnetic Resonance Imaging* 50: 982-993, 2019.

[7] Brett SE, Guilcher A, Clapp B, and Chowienczyk P. Estimating central systolic blood pressure during oscillometric determination of blood pressure: proof of concept and validation by comparison with intra-aortic pressure recording and arterial tonometry. *Blood pressure monitoring* 17: 132-136, 2012.

[8] Bristow MR. The adrenergic nervous system in heart failure: Mass Medical Soc, 1984.

[9] Chabiniok R, Wang VY, Hadjicharalambous M, Asner L, Lee J, Sermesant M, Kuhl E, Young AA, Moireau P, and Nash MP. Multiphysics and multiscale modelling, data–model fusion and integration of organ physiology in the clinic: ventricular cardiac mechanics. *Interface Focus* 6: 20150083, 2016.

[10] Chirinos JA and Sweitzer N. Ventricular-Arterial Coupling in Chronic Heart Failure. *Cardiac failure review* 3: 12-18, 2017.

[11] Cohn JN, Duprez DA, and Grandits GA. Arterial elasticity as part of a comprehensive assessment of cardiovascular risk and drug treatment. *Hypertension* 46: 217-220, 2005.

[12] Dec GW and Fuster V. Idiopathic dilated cardiomyopathy. *New England Journal of Medicine* 331: 1564-1575, 1994.

[13] Donati F, Myerson S, Bissell MM, Smith NP, Neubauer S, Monaghan MJ, Nordsletten DA, and Lamata P. Beyond Bernoulli. *Circulation: Cardiovascular Imaging* 10: e005207, 2017.

[14] Dudenbostel T and Glasser SP. Effects of antihypertensive drugs on arterial stiffness. *Cardiology in review* 20: 1-11, 2012.

[15] Dyverfeldt P, Bissell M, Barker AJ, Bolger AF, Carlhäll C-J, Ebbers T, Francios CJ, Frydrychowicz A, Geiger J, and Giese D. 4D flow cardiovascular magnetic resonance consensus statement. *Journal of Cardiovascular Magnetic Resonance* 17: 1, 2015.

[16] Eriksson J, Bolger AF, Ebbers T, and Carlhäll C-J. Four-dimensional blood flow-specific markers of LV dysfunction in dilated cardiomyopathy. *European Heart Journal-Cardiovascular Imaging* 14: 417-424, 2013.

[17] Felker GM, Thompson RE, Hare JM, Hruban RH, Clemetson DE, Howard DL, Baughman KL, and Kasper EK. Underlying causes and long-term survival in patients with initially unexplained cardiomyopathy. *New England Journal of Medicine* 342: 1077-1084, 2000.

[18] Ferreira VM, Piechnik SK, Robson MD, Neubauer S, and Karamitsos TD. Myocardial tissue characterization by magnetic resonance imaging: novel applications of T1 and T2 mapping. *Journal of thoracic imaging* 29: 147, 2014.

[19] Gaddum N, Alastruey J, Beerbaum P, Chowienczyk P, and Schaeffter T. A technical assessment of pulse wave velocity algorithms applied to non-invasive arterial waveforms. *Annals of biomedical engineering* 41: 2617-2629, 2013.

[20] Gersh BJ, Maron BJ, Bonow RO, Dearani JA, Fifer MA, Link MS, Naidu SS, Nishimura RA, Ommen SR, and Rakowski H. 2011 ACCF/AHA guideline for the diagnosis and treatment of hypertrophic cardiomyopathy: a report of the American College of Cardiology Foundation/American Heart Association Task Force on practice guidelines. *Journal of the American College of Cardiology* 58: e212-e260, 2011.

[21] Hasenfuss G, Mulieri L, Leavitt B, Allen P, Haeberle J, and Alpert N. Alteration of contractile function and excitation-contraction coupling in dilated cardiomyopathy. *Circulation research* 70: 1225-1232, 1992.

[22] Isaaz K and Pasipoularides A. Noninvasive assessment of intrinsic ventricular load dynamics in dilated cardiomyopathy. *Journal of the American College of Cardiology* 17: 112-121, 1991.

[23] Kerwin WF, Botvinick EH, O'Connell JW, Merrick SH, DeMarco T, Chatterjee K, Scheibly K, and Saxon LA. Ventricular contraction abnormalities in dilated cardiomyopathy: effect of biventricular pacing to correct interventricular dyssynchrony. *Journal of the American College of Cardiology* 35: 1221-1227, 2000.

[24] Knobloch V, Boesiger P, and Kozerke S. Sparsity transform k-t principal component analysis for accelerating cine three-dimensional flow measurements. *Magnetic resonance in medicine* 70: 53-63, 2013.

[25] Lamata P, Pitcher A, Krittian S, Nordsletten D, Bissell MM, Cassar T, Barker AJ, Markl M, Neubauer S, and Smith NP. Aortic relative pressure components derived from four-dimensional flow cardiovascular magnetic resonance. *Magnetic resonance in medicine* 72: 1162-1169, 2014.

[26] Lee N, Taylor MD, and Banerjee RK. Right ventricle-pulmonary circulation dysfunction: a review of energy-based approach. *Biomedical engineering online* 14: S8, 2015.

[27] Marlevi D, Ruijsink B, Balmus M, Dillon-Murphy D, Fovargue D, Pushparajah K, Bertoglio C, Colarieti-Tosti M, Larsson M, Lamata P, Figueroa CA, Razavi R, and Nordsletten D. Estimation of Cardiovascular Relative Pressure Using Virtual Work-Energy. *Scientific reports* 9: 1375, 2019.

[28] Merlo M, Caiffa T, Gobbo M, Adamo L, and Sinagra G. Reverse remodeling in dilated cardiomyopathy: insights and future perspectives. *IJC heart & vasculature* 18: 52-57, 2018.

[29] O'Rourke MF. Arterial aging: pathophysiological principles. *Vascular medicine* 12: 329-341, 2007.

[30] O'Rourke MF and Nichols WW. Aortic diameter, aortic stiffness, and wave reflection increase with age and isolated systolic hypertension. *Hypertension* 45: 652-658, 2005.

[31] Olufsen MS, Peskin CS, Kim WY, Pedersen EM, Nadim A, and Larsen J. Numerical simulation and experimental validation of blood flow in arteries with structured-tree outflow conditions. *Annals of biomedical engineering* 28: 1281-1299, 2000.

[32] Pedersen H, Kozerke S, Ringgaard S, Nehrke K, and Kim WY. k-t PCA: temporally constrained k-t BLAST reconstruction using principal component analysis. *Magnetic Resonance in Medicine: An Official Journal of the International Society for Magnetic Resonance in Medicine* 62: 706-716, 2009.

[33] Reymond P, Bohraus Y, Perren F, Lazeyras F, and Stergiopulos N. Validation of a patient-specific one-dimensional model of the systemic arterial tree. *American Journal of Physiology-Heart and Circulatory Physiology* 301: H1173-H1182, 2011.

[34] Reymond P, Westerhof N, and Stergiopulos N. Systolic hypertension mechanisms: effect of global and local proximal aorta stiffening on pulse pressure. *Annals of biomedical engineering* 40: 742-749, 2012.

[35] Ruijsink B, Zugaj K, Wong J, Pushparajah K, Hussain T, Moireau P, Razavi R, Chapelle D, and Chabiniok R. Dobutamine stress testing in patients with Fontan circulation augmented by biomechanical modeling. *PloS one* 15: e0229015, 2020.

[36] Sermesant M, Chabiniok R, Chinchapatnam P, Mansi T, Billet F, Moireau P, Peyrat J-M, Wong K, Relan J, and Rhode K. Patient-specific electromechanical models of the heart for the prediction of pacing acute effects in CRT: a preliminary clinical validation. *Medical image analysis* 16: 201-215, 2012.

[37] Stoll VM, Hess AT, Rodgers CT, Bissell MM, Dyverfeldt P, Ebbers T, Myerson SG, Carlhäll C-J, and Neubauer S. Left ventricular flow analysis: novel imaging biomarkers and predictors of exercise capacity in heart failure. *Circulation: Cardiovascular Imaging* 12: e008130, 2019.

[38] Unverferth DV, Magorien RD, Moeschberger ML, Baker PB, Fetters JK, and Leier CV. Factors influencing the one-year mortality of dilated cardiomyopathy. *The American journal of cardiology* 54: 147-152, 1984.

[39] Weber T, Auer J, Lamm G, O'Rourke MF, and Eber B. Arterial stiffness, central blood pressures, and wave reflections in cardiomyopathy—implications for risk stratification. *Journal of cardiac failure* 13: 353-359, 2007.

[40] Willemet M, Chowienczyk P, and Alastruey J. A database of virtual healthy subjects to assess the accuracy of foot-to-foot pulse wave velocities for estimation of aortic stiffness. *American Journal of Physiology-Heart and Circulatory Physiology* 309: H663-H675, 2015.

[41] Xiao HB, Brecker SJ, and Gibson DG. Effects of abnormal activation on the time course of the left ventricular pressure pulse in dilated cardiomyopathy. *Heart* 68: 403-407, 1992.

[42] Zanon F, Aggio S, Baracca E, Pastore G, Corbucci G, Boaretto G, Braggion G, Piergentili C, Rigatelli G, and Roncon L. Ventricular-arterial coupling in patients with heart failure treated

with cardiac resynchronization therapy: may we predict the long-term clinical response? *European Journal of Echocardiography* 10: 106-111, 2008.

Figures

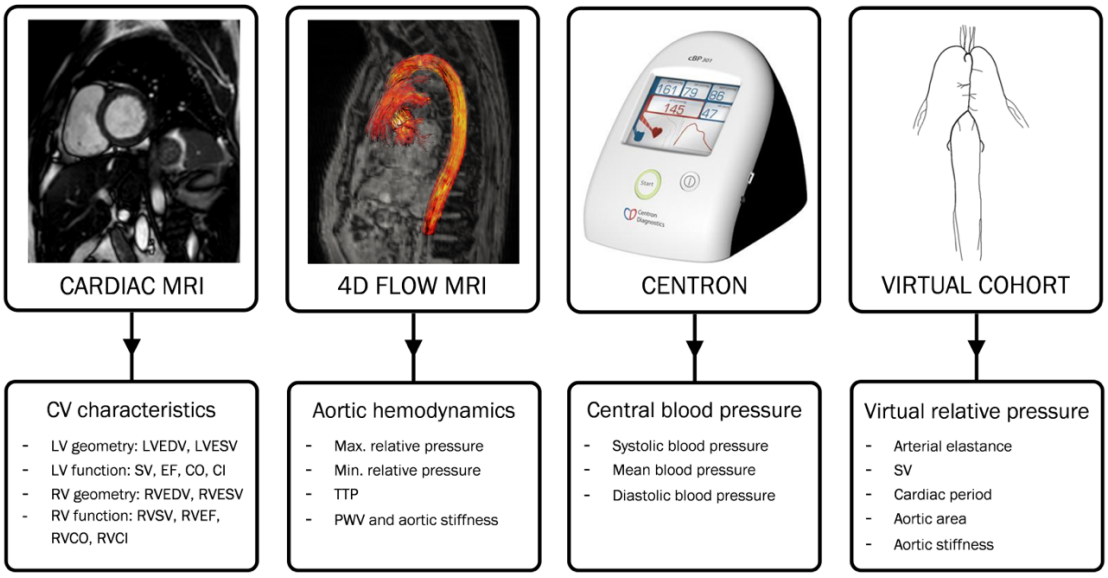

FIGURE 1: Overview of assessed study metrics. Overview of the assessed metrics of the study, with cardiovascular (CV) characteristics given by cardiac MRI, aortic hemodynamics from 4D flow MRI, and central blood pressure from sphygmomanometer measures. The isolated influence of listed cardiovascular properties on aortic relative pressure is determined using a computational virtual cohort. LV = Left ventricle. RV = Right ventricle. EDV = End-diastolic volume. ESV = End-systolic volume. SV = Stroke volume. EF = Ejection fraction. CO = Cardiac output. CI = Cardiac index, PWV = Pulse wave velocity. TTP = Time-to-peak relative pressure.

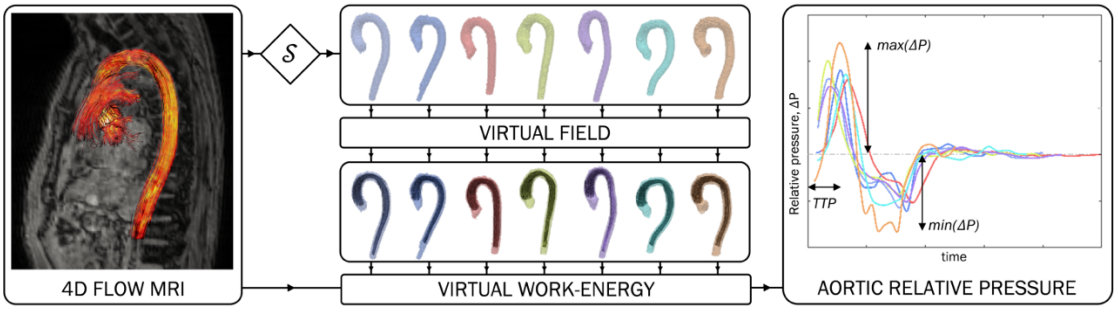

FIGURE 2: Overview of the virtual work-energy principle. Overview of the virtual work-energy principle to derive aortic relative pressure from 4D flow MRI (left). Aortic segmentations (*S*, upper mid-portion) are shown together with corresponding virtual fields (lower mid-portion), used to isolate aortic relative pressure. Maximum relative pressure, minimum relative pressure, and time-to-peak relative pressure (TTP) are derived (right). Each case is processed individually, with the color coding of the segmentations corresponding to the ones of the relative pressure traces.

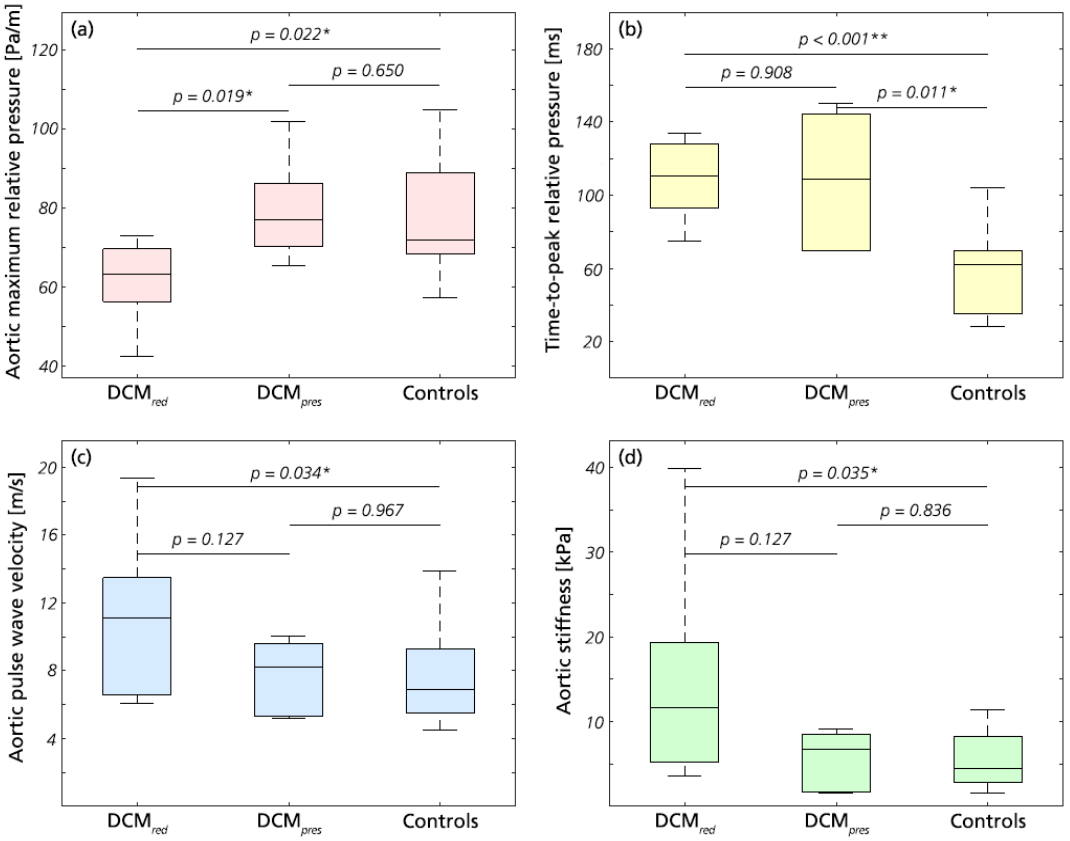

FIGURE 3: Key results from aortic relative pressure analysis. (a) Maximum relative pressure, (b) TTP, (c) PWV, and (d) aortic stiffness for DCM_{red}, DCM_{pres}, and the control groups, respectively. p-values are reported throughout with significance indicated by * ($p<0.05$) or ** ($p<0.01$).

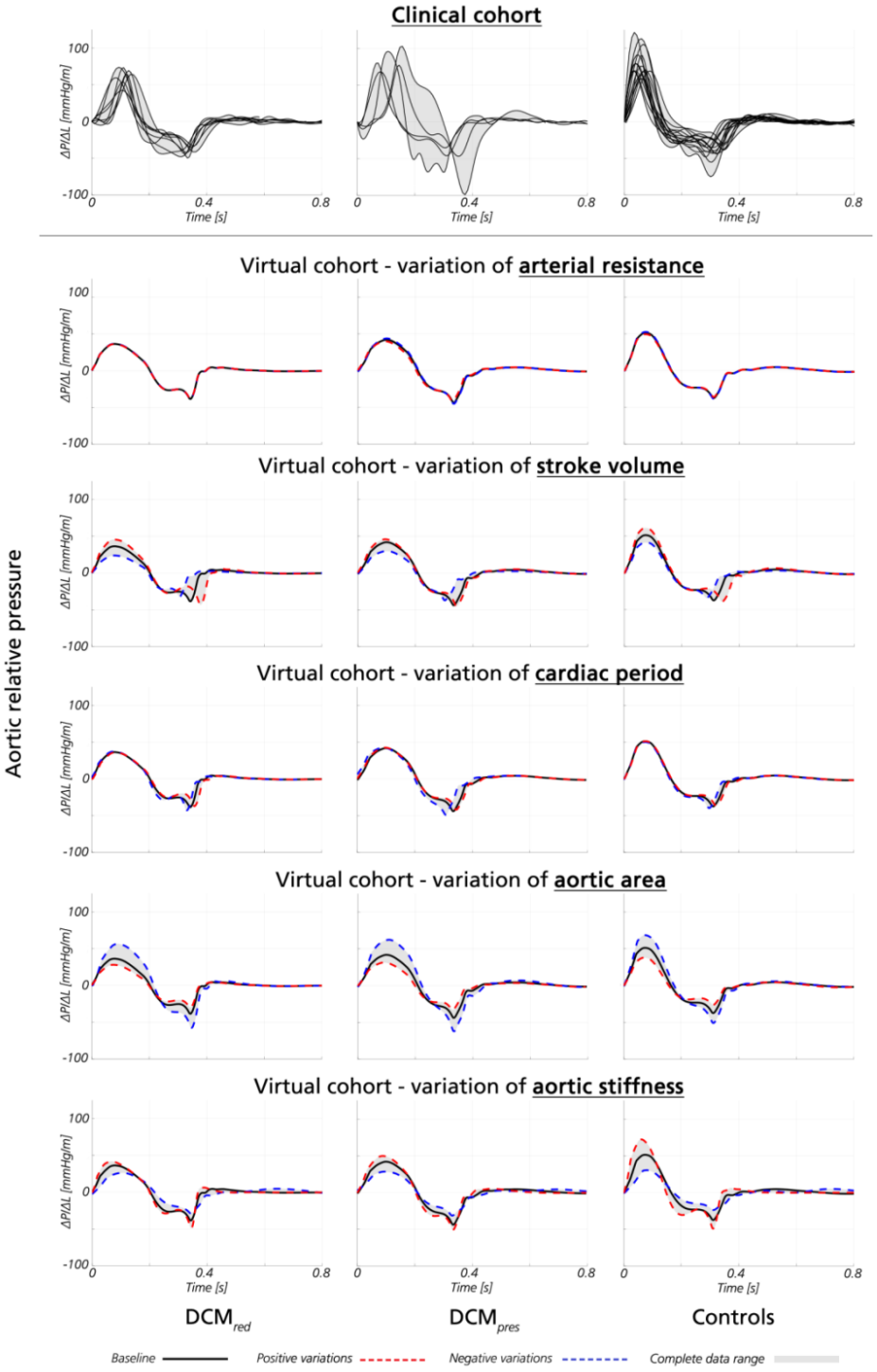

FIGURE 4: Aortic relative pressure traces from clinical and virtual analysis. Aortic relative pressure traces from the clinical (top row) and virtual cohort (remaining rows), presented as a function of isolated variations of arterial resistance, stroke volume, cardiac period, aortic area, and aortic stiffness, respectively. Relative pressure is shown for DCM_{red} (left), DCM_{pres} (middle), and controls (right). For the clinical data, each individual subject is given in black. For the virtual data, isolated variations around baseline (black) are given as positive variations (red) and negative variations (blue), respectively, superimposed on the data range (grey).

Tables

TABLE 1: Data and subject characteristics. Data and subject characteristics for the DCM_{red}, DCM_{pres}, and control groups, respectively. Intragroup p-values are reported with significant differences indicated by * ($p<0.05$), ** ($p<0.01$), or *** ($p<0.001$), as well as with the color coding. Volumes are normalized by body surface area (BSA).

Variable	**DCM_{red} (n = 8)**	**DCM_{pres} (n = 5)**	**Controls (n = 16)**	**p-value, DCM_{red} vs. Controls**	**p-value, DCM_{pres} vs. Controls**	**p-value, DCM_{red} vs. DCM_{pres}**
Subject demographics						
Age [yrs]	50.9 ± 5.5	42.8 ± 15.5	42.4 ± 12.4	0.080	0.967	0.524
BMI [kg/m²]	30.2 ± 6.8	26.6 ± 7.6	23.8 ± 3.7	**0.011***	0.458	0.429
BSA [m²]	2.05 ± 0.22	1.83 ± 0.35	1.85 ± 0.23	0.053	0.965	0.284
Male / Female [n]	4 / 4	3 / 2	9 / 7	0.772	0.882	0.724
HR [beats/min]	66 ± 10.5	75.2 ± 15.8	68.3 ± 8.0	0.401	0.382	0.331
Cine SSFP MRI						
LVEDV/BSA [mL/m²]	109.6 ± 38.9	86.7 ± 21.5	78.5 ± 9.4	**0.032***	0.687	0.435
LVESV/BSA [mL/m²]	69.2 ± 33.1	37.2 ± 11.9	28.8 ± 6.6	**0.0003*****	0.186	**0.045***
SV/BSA [mL/m²]	46.1 ± 10.9	47.0 ± 6.2	49.6 ± 5.5	0.562	0.500	0.943
EF [%]	41.6 ± 5.7	56.6 ± 6.1	63.9 ± 5.9	**0.0001*****	0.049*	**0.002****
CO [l/min]	6.1 ± 1.1	6.3 ± 1.1	6.2 ± 1.0	0.674	0.965	0.833
CI [l/(min/m²)]	2.9 ± 0.4	3.5 ± 0.4	3.4 ± 0.5	**0.032***	0.622	**0.045***
RVEDV/BSA [mL]	86.0 ± 28.5	76.9 ± 13.1	84.7 ± 8.6	0.973	0.298	0.833
RVESV/BSA [mL]	44.3 ± 9.4	29.6 ± 7.7	36.0 ± 5.3	0.811	0.070	0.524
RVSV/BSA [mL]	44.3 ± 9.4	47.1 ± 6.1	49.5 ± 5.5	0.207	0.559	0.524
RVEF [%]	53.3 ± 8.2	61.8 ± 4.7	58.3 ± 4.1	0.258	0.204	0.118

RVCO [l/min]	5.9 ± 1.1	6.3 ± 1.1	6.2 ± 1.0	0.457	1.000	0.499
RVCI [l/(min/m^2)]	2.9 ± 0.4	3.5 ± 0.4	3.4 ± 0.5	**0.019***	0.687	**0.030***
Aortic curvature [-]	0.5 ± 0.1	0.5 ± 0.0	0.5 ± 0.1	0.927	0.967	0.524
Aortic length [cm]	27.8 ± 4.8	26.9 ± 3.1	25.5 ± 2.1	0.426	0.710	0.833
Aortic diameter [cm]	1.6 ± 0.2	1.3 ± 0.2	1.5 ± 0.2	0.150	0.083	**0.030***
Central blood pressure						
SBP [mmHg]	125.3 ± 8.8	116 ± 10.2	116.9 ± 8.8	**0.022***	0.985	0.165
DBP [mmHg]	75.5 ± 5.6	69.6 ± 7.3	71.4 ± 5.8	0.122	0.431	0.107
MBP [mmHg]	86.8 ± 4.9	79.6 ± 7.8	81.3 ± 6.3	**0.034***	0.514	0.064

TABLE 2: Aortic flow analysis. Aortic relative pressure metrics for the DCM_{red}, DCM_{pres}, and control groups, respectively. Intragroup p-values are reported with significant differences indicated by * ($p<0.05$), ** ($p<0.01$), or *** ($p<0.001$), as well as with the color coding.

Variable	**DCM_{red} (n = 8)**	**DCM_{pres} (n = 5)**	**Controls (n = 16)**	**p-value, DCM_{red} vs Controls**	**p-value, DCM_{pres} vs Controls**	**p-value, DCM_{red} vs DCM_{pres}**
4D flow MRI						
Maximum relative pressure [mmHg/m]	61.6 ± 10.0	79.4 ± 13.8	78.9 ± 18.0	**0.022***	0.650	**0.019***
Minimum relative pressure [mmHg/m]	-41.3 ± 5.6	-58.3 ± 25.9	-39.4 ± 12.3	0.232	0.063	0.171
Time-to-peak relative pressure [ms]	109 ± 22	108 ± 38	55 ± 22	**0.0002*****	**0.011***	0.908
Pulse wave velocity [m/s]	11.0 ± 4.6	7.5 ± 2.5	7.5 ± 2.6	**0.034***	0.967	0.127
Aortic stiffness [kPa]	14.5 ± 12.0	5.5 ± 3.6	6.3 ± 5.1	**0.035***	0.836	0.127

A.4 Supplementary Material

This appendix contains the supplementary material submitted to the *American Journal of Phisiology – Heart and Circulatory Phisiology*. The original text and American English spelling has been kept. Supplementary tables have been placed at the end of the document.

Title:
Supplementary material.

Authors:
David Marlevi, Jorge Mariscal-Harana, Nicholas S Burris, Julio Sotelo, Bram Ruijsink, Myrianthi Hadjicharalambous, Liya Asner, Eva Sammut, Radomir Chabiniok, Sergio Uribe, Reidar Winter, Pablo Lamata, Jordi Alastruey, David Nordsletten.

Corresponding author:
David Nordsletten
Dept. Cardiac Surgery and Biomedical Engineering, University of Michigan
Plymouth Rd, 48109
Ann Arbor, MI, USA
E-mail: david.nordsletten@gmail.com
Tel: +1 734 647 7000
Fax: +1 734 936 1905

Supplementary methods

Structural magnetic resonance protocol and analysis

For structural analysis, cine SSFP MRI (retrospective ECG gating, spatial resolution ~2x2x8 mm^3, temporal resolution ~20 ms) and 3D tagged MRI (prospective ECG triggering, spatial resolution ~3.4x3.4x7.7 mm^3, temporal resolution ~30 ms) was acquired, all using a 1.5T Philips ACHIEVA system (Philips Healthcare Best, The Netherlands).

Left and right ventricular volumes (end-diastolic volumes (LVEDV, RVEDV) end-systolic volumes (LVESV, RVESV)), as well as left and right ventricular output metrics such as ejection fraction, stroke volume and cardiac output (EF, SV, CO, RVEF, RVSV, RVCO) were calculated by manually identifying end-diastolic and end-systolic segmentations of the short-axis images (CVI software, Circle Cardiovascular Imaging Inc, Alberta, Canada).

Mathematical details of the derivation of relative pressure from 4D flow MRI

From the 4D flow MRI data, relative pressure was derived using a virtual work-energy approach – νWERP – originally presented and validated against invasive catheter measurements in Marlevi et al(1). The method originates from the Navier-Stokes equation, in which the conservation of mass and momentum are used to constrain the 3D movement of Newtonian fluid over time. From such, νWERP estimates the relative pressure Δp across an arbitrary vascular section Ω with inlet plane Γ_i and outlet plane Γ_o as

$$\Delta p = -\frac{1}{Q}\left(\frac{\partial}{\partial t}K_e + A_e + V_e\right). \qquad \text{(A)}$$

Each entry in equation (A) now represents separated *virtual* energy components of an introduced *virtual* field, created in conjunction to the acquired 4D flow MRI. Specifically Q is the virtual flow through the inlet, K_e the virtual kinetic energy held within the fluid, A_e the rate at which virtual kinetic energy changes within the field, and V_e the rate of virtual viscous energy dissipation by the field.

With the above, νWERP acts directly on the non-invasively acquired 4D flow MRI data, and does not require any additional measurements to compute Δp. Specific details on data

post-processing of the acquired velocity field, $\boldsymbol{v}$, as well as the creation of the auxiliary virtual field, $\boldsymbol{w}$, are all described using an identical setup in Marlevi et al(1).

Virtual cohort creation and analysis

A virtual cohort was utilized based on Willemet et al(2), where blood pressure, blood flow, and arterial area waveforms could be simulated using a validated one-dimensional (1D) computational model of arterial hemodynamics consisting of the 55 larger arteries of the human systemic circulation(3). The virtual cohort was adapted to match the clinical characteristics, creating three virtual subgroups: one virtual DCM_{red} group, one virtual DCM_{pres} group, and one virtual control group, respectively. Specific cardiovascular parameter values (all originating from the clinical acquisitions) are defined in Supplementary Table 1.

For each subgroup, a baseline virtual subject was created to match the mean of the clinical characteristics. The independent influence of certain cardiovascular properties was then assessed by creating a set of virtual subjects for each defined property, varying that specific entity within the clinical subgroup range whilst keeping the rest of the properties at baseline level. By doing so, the isolated influence on aortic relative pressure from SV, heart rate, arterial peripheral resistance (calculated from mean blood pressure and cardiac output), aortic stiffness, and aortic area was evaluated. Similarly, virtual flow profiles were generated based on through-plane LVOT flows from the 4D flow MRI of each subgroup, respectively. For each virtual subject, aortic relative pressure was calculated from the LVOT to the end of the thoracic aorta, with relative pressure normalized by aortic length to match the derived clinical data. Note that the LVOT level was assigned at the aortic root, with no valvular influence included in the simulated output (assuming normal valvular function for the entire virtual cohort).

General cardiovascular parameter values, which were kept constant over all virtual subjects, were taken from Willemet et al(2) and modified when appropriate. The parameters and their corresponding values were: blood density (1050 kg/m^3), blood viscosity (0.0025 Pa·s), velocity profile coefficient (1.33, corresponding to a Poiseuille flow), and outflow pressure (0 Pa).

Aortic stiffness was calculated ensuring that PWV in the virtual subjects was equal to the mean PWV values extracted from each clinical subgroup. With the exact length of the clinical subject aortas unknown, virtual aortic lengths were taken from Willemet et al(2). Aortic diastolic areas were also extracted from the same reference, and scaled according to the ratio of the clinical to virtual average aortic areas.

For each virtual subgroup, mean values of left-ventricular ejection time (LVET) and time-to-peak flow were calculated from the corresponding clinical subgroup flow data. A spline interpolation was performed to smooth each flow waveform. LVET was then extracted using an in-house algorithm. Time-to-peak flow was extracted as the time of maximum flow. For each subgroup, the average values of LVET and time-to-peak flow were used to generate the virtual flow profiles.

1D simulations were run for a total of 20 s with a 0.1 ms time step to ensure numerical convergence. A visual check of all virtual pressure waveforms at the ascending and abdominal aorta was additionally employed to confirm convergence.

Supplementary results

Correlation analysis

Pearson correlation coefficients for a few maximum relative pressure, minimum relative pressure, time-to-peak relative pressure, pulse wave velocity, and aortic stiffness are all provided in Supplementary Table 2. Condensed key results are provided in the main manuscript, however for completeness here follows a detailed description of the obtained correlation results:

For the aortic maximum relative pressure, no significant correlation could be identified with any of the subject characteristics in the DCM cohort.

For the aortic minimum relative pressure, similar behavior could be observed: for the DCM patients no correlations could be inferred with any of the evaluated clinical parameters. For the control group however, slight negative correlation could be inferred between minimum aortic relative pressure and body surface area ($R=-0.73$, $p=0.002$).

For TTP no correlation could be inferred for any of the clinical groups at the set significance level.

Lastly, for PWV and derived arterial stiffness, only body mass index was correlated to arterial, stiffness ($R=0.755$, $p = 0.001$), however only inferable for the control group.

As noted in the main manuscript, absolute systolic, diastolic, and central blood pressure (SBP, DBP or CBP) did not correlate with any of the evaluated aortic relative pressure metrics.

References

[1] Marlevi D, Ruijsink B, Balmus M, Dillon-Murphy D, Fovargue D, Pushparajah K, Bertoglio C, Colarieti-Tosti M, Larsson M, Lamata P, Figueroa CA, Razavi R, and Nordsletten D. *Estimation of Cardiovascular Relative Pressure Using Virtual Work-Energy*. Scientific reports 9: 1375, 2019.

[2] Willemet M, Chowienczyk P, and Alastruey J. *A database of virtual healthy subjects to assess the accuracy of foot-to-foot pulse wave velocities for estimation of aortic stiffness*. American Journal of Physiology-Heart and Circulatory Physiology 309: H663-H675, 2015.

[3] Alastruey J, Parker KH, and Sherwin SJ. Arterial pulse wave haemodynamics. *11th International Conference on Pressure Surges*. Virtual PiE Led t/a BHR Group Lisbon, Portugal, 2012, p. 401-442.

Supplementary tables

SUPPLEMENTARY TABLE 1: Parameter variation for virtual cohort. Parameter variations for each virtual cohort with all data derived from the *in vivo* imaging. For each subgroup, the baseline virtual subject corresponded to the mean parameter value. Each additional virtual subject within that subgroup corresponded to the variation of a single, isolated parameter (varied from minimum to maximum, one at a time).

CV parameters	**Virtual DCM$_{red}$**			**Virtual DCM$_{pres}$**			**Virtual controls**		
	min	***mean***	***max***	***min***	***mean***	***max***	***min***	***mean***	***max***
Peripheral resistance, [mmHg s/mL]	0.69	0.77	0.84	0.64	0.89	1.20	0.61	0.78	1.04
Stroke volume, [mL]	55.0	95.5	132.0	53.0	86.0	100.0	66.3	91.7	122.9
Cardiac period, [s]	0.75	0.91	1.13	0.59	0.80	1.00	0.70	0.88	1.03
Aortic area, [cm^2]	1.86	2.96	3.87	1.21	1.96	2.72	1.72	2.49	3.66
Aortic PWV, [m/s]	6.10	11.00	19.40	5.20	7.70	10.00	4.50	7.50	13.90

SUPPLEMENTARY TABLE 2: Complete Pearson correlation coefficient table. Pearson correlation coefficient, for the evaluation of aortic relative pressure measurements. Correlation is evaluated against maximum relative pressure, minimum relative pressure, time to peak relative pressure, pulse wave velocity, and aortic stiffness, respectively. Data is also separated for DCM with reduced LV function (n=8), DCM with preserved LV function (n=5), and control group (n=16), respectively. If a correlation is statistically significant with Bonferroni correction ($|R| > 0.5$ and $p < 0.002$, m=21) this is indicated by * (correlations removed by Bonferroni correction indicated by +). Significance is also indicated by the color coding.

	Max. relative pressure			Minimum relative pressure			TTP			PWV			Aortic stiffness		
	DCM_{red}	DCM_{pres}	Controls	DCM_{red}	DCM_{pres}	Controls	DCM_{red}	DCM_{pres}	Controls	DCM_{red}	DCM_{pres}	Controls	DCM_{red}	DCM_{pres}	Controls
Age	-0.34	-0.62	0.04	0.00	0.66	0.06	-0.18	-0.30	-0.26	0.24	0.69	0.44	0.23	0.71	0.43
BMI	-0.64	-0.02	0.68+	0.87+	0.70	0.55+	-0.18	-0.43	0.18	0.22	0.88	0.63	0.10	0.88+	0.755*
BSA	-0.55	-0.28	0.67+	0.67	0.79	-0.73*	-0.54	-0.41	0.32	0.02	0.96+	0.47	-0.01	0.98+	0.57+
LVEDV/BSA	0.10	0.78	0.2	-0.06	-0.71	-0.47	-0.41	0.72	0.47	-0.17	-0.38	-0.31	-0.05	-0.32	-0.18
LVESV/BSA	-0.13	0.59	0.22	0.04	-0.62	-0.48	-0.40	0.76	0.42	-0.11	-0.33	-0.03	0.01	-0.28	0.10
SV/BSA	-0.35	0.83	0.07	0.28	0.51	-0.22	-0.37	0.53	0.29	-0.17	-0.12	-0.50	-0.07	-0.06	-0.44
EF	-0.06	-0.29	-0.21	0.20	0.56	0.37	0.24	-0.74	-0.24	-0.04	0.39	-0.09	-0.18	0.36	-0.18
CO	-0.53	-0.36	0.30	0.49	0.75	-0.57+	-0.39	-0.05	0.32	0.23	0.88+	-0.09	0.30	0.86	-0.05
CI	-0.36	-0.15	-0.22	0.24	-0.19	-0.01	-0.16	0.55	0.09	0.32	-0.34	-0.45	0.45	-0.40	-0.48
RVEDV/BSA	-0.60	0.64	0.16	0.41	-0.24	-0.43	-0.47	0.36	0.47	-0.14	-0.15	-0.46	-0.07	0.22	-0.36
RVESV/BSA	-0.57	0.44	0.12	0.35	-0.01	-0.53	-0.59	0.20	0.10	-0.19	-0.37	-0.32	-0.13	0.43	-0.20
RVSV/BSA	-0.60	0.83	0.07	0.49	-0.49	-0.20	-0.15	0.51	0.20	0.00	-0.11	-0.49	0.08	-0.04	-0.43
RVEF	0.37	-0.13	-0.03	-0.19	-0.32	0.30	0.72+	0.08	0.23	0.38	-0.64	0.04	0.32	-0.69	-0.02
RVCO	-0.67	-0.35	0.29	0.63	0.77	-0.58+	-0.12	-0.07	0.28	0.39	0.89+	-0.14	0.42	0.88+	-0.09
RVCI	-0.54	-0.15	-0.23	0.41	-0.16	-0.03	0.22	0.53	0.07	0.53	-0.32	-0.47	0.60	-0.38	-0.48
HR	0.37	-0.53	-0.30	-0.41	0.12	0.18	0.45	0.00	-0.21	0.38	-0.23	-0.12	0.34	-0.30	-0.20
SBP	0.62	0.00	0.13	-0.58	0.51	-0.24	-0.59	0.07	0.13	-0.28	0.80	0.13	-0.23	0.82	0.13
DBP	0.45	-0.54	-0.08	-0.53	0.57	0.08	-0.56	0.10	-0.09	-0.20	0.59	0.11	-0.18	0.58	0.09
MBP	0.65	-0.41	-0.03	-0.69	0.57	0.01	-0.49	0.12	-0.03	-0.47	0.67	0.12	-0.41	0.67	0.11
Curvature	-0.22	0.85	0.01	0.50	-0.54	-0.34	0.16	0.72	0.55+	0.26	-0.33	-0.02	0.11	-0.34	0.01
Radius	-0.07	-0.30	0.39	-0.21	0.64	-0.34	-0.31	-0.41	-0.02	-0.24	0.80	0.40	-0.06	0.84	0.48

SUPPLEMENTARY TABLE 3: Maximum relative pressure variations from the virtual cohort analysis. Results from the virtual cohort analysis, showing variations in aortic maximum relative pressure per unit length as a function of isolated variations of peripheral resistance, stroke volume, cardiac period, aortic area, and aortic stiffness, respectively. Data provided for baseline, minimum and maximum range, with all values reported in mmHg/m. The bottom row shows the complete range of aortic maximum relative pressure over all variations.

Variation variable	**Virtual DCM$_{red}$**			**Virtual DCM$_{pres}$**			**Virtual controls**		
	min	***baseline***	***max***	***min***	***baseline***	***max***	***min***	***baseline***	***max***
Peripheral resistance	36.3	36.5	36.7	39.8	42.0	43.8	49.4	51.3	52.5
Stroke Volume	23.9	36.5	45.6	30.1	42.0	46.0	41.5	51.3	60.8
Cardiac period	35.9	36.5	37.2	42.7	42.0	42.9	50.2	51.3	51.3
Aortic area	28.1	36.5	56.5	31.5	42.0	62.5	38.1	51.3	68.5
Aortic stiffness	26.5	36.5	41.9	28.3	42.0	49.7	30.4	51.3	72.1
Total range	23.9	36.5	56.5	28.3	42.0	62.5	30.4	51.3	72.1

SUPPLEMENTARY TABLE 4: Minimum relative pressure variations from the virtual cohort analysis. Results from the virtual cohort analysis, showing variations in aortic minimum relative pressure per unit length as a function of isolated variations of peripheral resistance, stroke volume, cardiac period, aortic area, and aortic stiffness, respectively. Data provided for baseline, minimum and maximum range, with all values reported in mmHg/m. The bottom row shows the complete range of aortic maximum relative pressure over all variations.

Variation variable	**Virtual DCM$_{red}$**			**Virtual DCM$_{pres}$**			**Virtual controls**		
	min	***baseline***	***max***	***min***	***baseline***	***max***	***min***	***baseline***	***max***
Peripheral resistance	-38.4	-38.5	-38.7	-45.2	-43.8	-41.9	-38.5	-37.5	-36.1
Stroke Volume	-42.8	-38.5	-32.2	-45.0	-43.8	-37.2	-38.9	-37.5	-34.1
Cardiac period	-43.0	-38.5	-37.1	-49.0	-43.8	-42.0	-39.8	-37.5	-36.4
Aortic area	-57.8	-38.5	-30.2	-62.2	-43.8	-33.2	-51.1	-37.5	-26.5
Aortic stiffness	-49.0	-38.5	-28.9	-50.7	-43.8	-31.4	-49.2	-37.5	-23.9
Total range	-57.8	-38.5	-28.9	-62.2	-43.8	-31.4	-51.1	-37.5	-23.9